Mixing of Two Miscible Liquids with High Viscosity and Density Difference in Semi-Batch and Batch Reactors – CFD Simulations and Experiments

(Mischen von zwei vollständig mischbaren Flüssigkeiten mit großen Viskositäts- und Dichte-Unterschieden in Semi-Batch- und Batch Reaktoren – CFD Simulationen und Experimente)

by

Fawzi A. Hamadi Al-Qaessi

Thesis submitted to the Department of Chemistry of
Universität Duisburg-Essen, in partial fulfilment of
the requirements of the degree of
Dr. rer. nat.

Approved by the examination committee on December 17, 2007:

Chair : Prof. Dr. Georg Jansen

Advisor : Prof. Dr. Axel Schönbucher

Reviewer : Prof. Dr. Mathias Ulbricht

Essen, 2007

Declaration

I declare here that I have written this thesis on my own. The literature and technical aids used have been completely indicated.

Essen, 14.11.2007 Signature:

Acknowledgements

First, I wish to express my deep gratitude and appreciation to my advisor Prof. Dr. Axel Schönbucher for accepting me as a Ph.D. student in his Institute of Chemical Engineering (Institut für Technische Chemie I, Universität Duisburg-Essen), and for his guidance and support in the course of this work. He has given me helpful advice on approaching and performing challenging tasks. This research would not have been possible without his prominent views and discussions.

I am very grateful to Prof. Dr. Mathias Ulbricht, Institut für Technische Chemie II, Universität Duisburg-Essen, for his accepting the task of co-examiner of this thesis and for his valuable remarks.

A special thank goes to Dr. Wolfgang Laarz for his engaged support and the helpful discussions as well as for the use of his provided technical devices, with which the light cut photographs and the video photographs could be accomplished.

A warm thank goes to all Ph.D. students at the Institute for all the professional and personal communications, and the very enjoyable time we have spent together; with a special thank to my working group, Christian Kuhr, Iris Vela, Peter Sudhoff and Markus Gawlowski. Another special thank goes to Rafael Tarnawski at the Institut für Technische Chemie II, Universität Duisburg-Essen, who has helped me in evaluating the experimental data.

Especial thanks are extended to Mrs. Lieselotte Schröder for her advisement, support and endless help in the communication with the DAAD office and foreign office. I appreciate her kindness and cooperation.

All thanks are extended to Dieter Jacobi, Gerd Joppich, Anja Schröder, and the staff of the Institute for their help during different stages of this work.

My most hearty thank and gratitude to my wife Laila Abu-Farah for her endless support and patience. Also, our sons Sadid and Noor for providing me so much love. I was always glad to know that they are with me.

I want to thank my parents, brothers and sisters for giving me support in any way I needed it before and during the time this work has been done. Their love and strong belief in me has always strengthened my self-confidence.

Finally, I wish to gratefully acknowledge the financial support by the DAAD (Deutscher Akademischer Austausch Dienst) in Bonn - Germany, having made this work possible.

Abstract

The mixing behavior of two liquids with different viscosities and different densities is investigated experimentally in a glass SBR and BR as well as by CFD simulation.

With a torque method, the mixture viscosity $\eta_m(t)$ of ethanol and glycerol is measured as a function of time. From $\eta_m(t)$ it is determined the mixing time t_m at which the mixture viscosity begins to remain constant.

In addition the mixing time t_m is measured directly by a decolorisation method using the iodine sodium thiosulfate reaction.

The dynamic mixing behavior of the ethanol and glycerol mixtures in a SBR and a BR is analysed by video visualisation of the flow field with a light cut procedure. In a BR a pan cake effect of an ethanol layer is observed.

The definition of mixing, the scales of mixing, some important mixing characteristics and overview of types of stirrers as well as some essentials of computational fluid dynamics (CFD) are discussed within the theoretical background given in this work.

For a quantitative description of the measured dynamic mixing behaviour of ethanol and glycerol, a CFD simulation is carried out by using the Ansys CFX-10 tool. The used models are an isothermal, multiphase, multicomponent, modified algebraic slip model and the following submodels: A homogeneous standard free surface flow model for air/liquid interface, a sliding mesh model and a laminar buoyant flow model for the liquid mixture.

With Ansys ICEM CFD 5.1 an unstructured mesh with tetrahedron cells is used. It is found that the computational time of simulation (CPU time) can

be reduced from 20 to 2 days if the number of tetrahedron cells will be reduced from 600,000 to 26,000. Then the cell size increases from 0.001 m to 0.015 m, without remarkable change in the calculated results.

From the CFD simulations with a half geometry in a SBR, it is found that the mesh refinement at the interface between the mixture phase and the air changes from 0.015 m to 0.00375 m gives a sharper interface and better resolution.

When the dosage time for ethanol increases from 1 s to 5 s and the inlet tube diameter increases from 0.023 m to 0.05 m, the mixing time increases with a factor of 2. When the velocity of the anchor impeller increases from 25 rpm to 400 rpm, then the mixing time decreases with a factor of 6. The stirrer velocity has a greater effect on the secondary axial flow than on the primary tangential flow. When the width of the horizontal blade of the anchor impeller increases from 0.012 m to 0.015 m the mixing time decreases with a factor of 2.

The effect of different mixture ratios of glycerol and ethanol on the flow field is studied in a BR. It is predicted from the CFD simulation of the flow field that pure ethanol shows mainly axial flow with no circulations in the domain between the shaft and anchor impeller. A secondary flow with an axial circulation is predicted behind (down stream) the rotating anchor impeller in the case of the mixing of pure glycerol or of ethanol/glycerol.

From the CFD simulations with a full geometry it is derived a new method to determine the mixing time t_m, by calculation the ethanol mass fraction in a SBR and a BR at nine different positions as a function of time. The mixing time and a homogeneous mixture are obtained when the ethanol mass fractions are constant at all nine positions. It is found that the ethanol

mass fraction near the stirrer reaches a constant value earlier than that near the shaft of the stirrer.

The new developed modified algebraic slip model (MASM) which includes the ethanol droplets break up $d_p(t)$ as a function of time t by modeling with a validated step function, gives the real mixing behaviour, i.e. $\eta_m(t)$ and mixing times t_m in a good agreement with the experimental results in a SBR and a BR. Also the prolongation of the mixing time t_m by a factor of 1.5 caused by the pan cake effect is predicted by the MASM. The often used algebraic slip model (ASM) and transport model (TRM) give an unrealistic prediction of the experimental mixing behavior in the case of ethanol and glycerol.

Table of Contents

Nomenclature

Latin letters

$A_{\alpha\beta}$	[1/m]	Interfacial area density
C_D	[–]	Drag coefficient
D_i	[m^2/s]	Diffusion coefficient of component i
d	[m]	Stirrer diameter
d_v	[m]	Vessel diameter
d_p	[m]	Mean diameter of droplets
F_α	[N/m^3]	Volumetric buoyancy force
g	[m/s^2]	Acceleration due to gravity
h_{tot}	[J/kg]	Total specific enthalpy of the liquid mixture
H	[m]	Vessel height
H_E	[m]	Ethanol height
H_G	[m]	Glycerol height
H_i	[m]	Impeller height
H_l	[m]	Total liquid height
H_t	[m]	Inlet tube length
l_k	[s]	Kolmogoroff's length scale of turbulence
M	[Nm]	Torque of the shaft of the anchor impeller
M_α^i	[N/m^3]	Momentum transfer with other phases
$\tilde{M}_i$	[kg/kmol]	Molar mass of the components i = A, B, … N
$\tilde{M}_m$	[kg/kmol]	Molar mass of mixture
N	[–]	Total number of components
N_P	[–]	Total number of phases
P	[W]	Power of the impeller

p	[Pa]	Pressure
r_α	[-]	Volume fraction of phase α
$S_{A\alpha}$	[kg/(m^{3}s)]	Source term in multicomponent multiphase flow
S_E	[W/m^3]	Source term in energy equation
S_M	[kg/(m^{2}s^2)]	Source term in momentum equation
$S_{MS\alpha}$	[kg/(m^{3}s)]	Source term in continuity equation in phase α
S_i	[kg/(m^{3}s)]	Reaction source of component i
T	[K]	Temperature
t	[s]	Time
t_d	[s]	Ethanol dosage time
t_{df}	[s]	Final ethanol dosing time
t_{di}	[s]	Initial ethanol dosage time
t_k	[s]	Kolmogoroff time scale of turbulence
t_m	[s]	Mixing time
$t_{m,L}$	[s]	Mixing time for a level of uniformity L
U	[m/s]	Vector of velocity $\begin{pmatrix} u_x \\ u_y \\ u_z \end{pmatrix}$ in bulk liquid
U_α	[m/s]	Vector of velocity $\begin{pmatrix} u_x \\ u_y \\ u_z \end{pmatrix}$ in phase α
U_{Wall}	[m/s]	Velocity at the wall
$\tilde{U}_{ij}$	[m/s]	Mass averaged velocity of component i through coordinate j
$\tilde{U}_j$	[m/s]	Mass averaged velocity through coordinate j
u_E	[m/s]	Velocity of ethanol feed

u_m	[m/s]	Flow velocity of the liquid mixture (mixture velocity)
$\begin{pmatrix} u_x \\ u_y \\ u_z \end{pmatrix}$	[m/s]	Velocity in the coordinate directions x, y, z
u_C^i	[m/s]	Velocity of component i in continuous phase C
$u_{D\alpha}^i$	[m/s]	Drift velocity of component i in phase α
u_m^i	[m/s]	Velocity of component i in the mixture m
$u_{S\alpha}^i$	[m/s]	Slip velocity of component i in phase α
u_α^i	[m/s]	Velocity of component i in phase α
V	[m^3]	Volume of the liquid mixture in the vessel
$\dot{V}_E$	[m^3/s]	Ethanol volumetric flow rate
w_h	[m]	Horizontal blade width of anchor impeller
x, y, z	[m]	Cartesian coordinates
Y_i	[kg/kg]	Mass fraction of component i
$\tilde{Y}_i$	[kg/kg]	Averaged mass fraction of component i
y_v	[V]	Voltage of the impeller momentum
$y_{v,0}$	[V]	Blind voltage of the impeller momentum
$y_{v,net}$	[V]	Net voltage of the impeller momentum
$\tilde{y}_v$	[V]	Averaged voltage of the impeller momentum

Greek letters

ε	[W/kg]	Energy dissipation
φ	[–]	Volume ratio
η	[Pa s]	Mixture dynamic viscosity

λ	[W/(m K)]	Thermal conductivity of the liquid mixture
ν	[m^2/s]	Kinematic viscosity
$\tilde{\nu}$	[m^2/s]	Average kinematic viscosity
ϑ	[°C]	Temperature
ρ	[kg/m^3]	Density
ρ_i	[kg/m^3]	Density of the component i
ρ_L	[kg/m^3]	Density of the less dense liquid
ρ_α	[kg/m^3]	Density of phase α
$\tilde{\rho}_i$	[kg/m^3]	Averaged mass density of component i
$\overline{\rho}$	[kg/m^3]	Time averaged density
$\tilde{\rho}$	[kg/m^3]	Average density
$\Delta\rho$	[kg/m^3]	Density difference between the pure components
τ	[N/m^2]	Shear stress
ω	[1/s]	Stirrer velocity

Indices

α	Phase α
β	Phase β
abs	Absolute
ax	Axial
D	Drift
E	Ethanol
e	End mixing
G	Glycerol
i	Components i = A, B, … N

j	x,y,z- coordinates
m	Mixture
ref	Reference state (for density and pressure)
s	Start mixing
tot	Total
v	Voltage

Abbreviations

ASM	Algebraic slip mixture model
BR	Batch reactor
CAM	Video camera
CEL	Command expression language for the step function
CFD	Computational fluid dynamics
F	Flex point
FD	Finite difference method
FE	Finite element method
FV	Finite volume method
L1, L2	Level of uniformity 1 and 2
MASM	Modified Algebraic slip model
PC	Personal computer
PDE	Partial differential equation
rpm	Revolution per minute
SBR	Semibatch reactor
TM	Transport model
T	Thermostat

Dimensionless numbers

Ar	Archimedes number (s. Eq. 2-7)
Re	Impeller Reynolds number (s. Eq. 2-6)
Re*	Modified impeller Reynolds number (s. Eq. 2-9)
Ri	Richardson number (s. Eq. 2-5)

1. INTRODUCTION

The mixing process is a common and important operation in a wide range of industries such as polymer processing, petrochemicals, food, biotechnology, cosmetics and paints. Insufficient understanding of these processes causes the continuous loss of a large amount of money. The fluids used in these processes are often highly viscous and have different viscosities and densities. They are mixed in a semibatch or batch mode.

The literature dealing with the mixing effects of these fluids are mostly limited to the case of mixing two large volume layers of liquids at the beginning of the process (Batch mixing process). But, it is much interesting in the process industry to mix small quantities of the inlet liquid with that in the vessel while stirring is in progress for fast mixing and/or reactions (Semibatch mixing process) rather than to begin mixing with large liquids volumes. Present investigations study the mixing of liquids with density differences and not consider the viscosity differences and the large volume inlet liquid in case of semibatch mixing.

Mixing operation may involve difficulties in predicting the mixing time, whereas high product quality control with a minimum mixing time is needed. In many investigations of the mixing time in the past, the effects of differences in viscosity or density have not been taken into account. It is often not clear whether mixing problems like the scale of homogeneity and the time available to accomplish mixing are caused by viscosity differences or by density differences. These can yield unexpectedly long mixing times. A series of experiments proved the dependence of mixing time on a combination of viscosity and density differences.

Anchor impellers are often used for mixing high viscosity fluids in the

range 1-10 Pa s. Very few investigations study these impellers and a little is done by computational fluid dynamics (CFD) simulations. Anchor impellers are especially preferred for mixing operations because they generate both tangential and axial motion, which enhances the mixing efficiency and to avoid the stagnation of the products at the vessel walls, since the anchor blades work as a scraper.

The primary tangential flow using a two dimensional grid has been studied; it is caused by the rotation of the horizontal blade of the anchor impellers. Three dimensional flow patterns inside the vessel are important to understand the state of flow of the fluids and the mechanisms responsible for homogenization and transport processes. Secondary flow is the flow generated by the action of the inertial forces due to the movement of the anchor blades; it is generated by the rotation of the vertical blade of the anchor impeller as well as the hydrodynamic conditions. It is necessary to get more insight about the detailed picture of the secondary flow to determine ways in which the mixing process can be improved. The great majority of computational work for vessels with anchor stirrers presents computational studies for the primary flow and very coarse grid was used, but a little is known for the secondary flow and fine grid.

In this work the following topics will be investigated:

1. It should be described the theoretical back ground of the mixing process of liquids with very high density and viscosity differences. A mixture of high viscosity glycerol and low viscosity ethanol will be used as a test mixing process in a semibatch reactor (SBR) and a batch reactor (BR) with anchor impeller.
2. Viscosity of the liquid-liquid mixture should be measured as a function of time. The mixing time in the case of a SBR and a BR will be measured.

Different dosage times will be used in a SBR. The total height of the liquid mixture will be varied in a BR. Flow field patterns of the dynamic mixing behaviour will be visualised by a video camera.

3. The mixing phenomena should be described with transient 3D computational fluid dynamics (CFD) simulations. The commercial program Ansys CFX-10 will be used for solving the Navier-Stokes equations. It should be found which kind of submodels must be included to predict the mixing times. It should be proved to give prediction of the mixing phenomena with the used liquids in a SBR and a BR.
4. It should be varied the size and the number of the cells by using ICEM CFD program. The mixing process in a SBR will be calculated at different dosage times, inlet tube diameters and anchor velocities. It should be varied the dimensions of the anchor impeller. Different types of liquids will be used such as pure ethanol, pure glycerol and mixture of ethanol and glycerol at different compositions in a BR.
5. The time dependent dynamic viscosity of the liquid mixtures, the mixing times and the flow field patterns should be determined based on CFD simulations in a SBR and a BR. It will be proved the homogeneity of the final liquid mixture in these reactors.

2. THEORETICAL BACKGROUND

2.1 Mixing definition and perspective

Mixing is understood to be any operation used to change a non-uniform system into a uniform one. A quantity of matter may be called uniform or homogeneous when the composition of a volume element of appropriate size does not deviate by more than a fixed amount from the average composition of the entire system. Mixing is very often part of a chemical or physical process, such as blending, dissolving, emulsification, heat transfer and chemical reactions. Chemical engineering recognizes it as one of the unit operations.

Mixing can be classified according to the various combinations between the phases gas, liquid, and solid. Liquid-liquid mixing, for instance, is understood to be the mixing of two miscible or immiscible liquids. Important methods of mixing are: flow mixing, e.g. circulation by pumping, injection; vibrational mixing, e.g. by ultrasonic; mixing by rotating stirrers. In mixing miscible liquids, the molecular diffusion also contributes to the ultimate homogeneity of the system to be mixed [2] [57].

Mixing is the reduction of inhomogeneity in order to achieve a desired process result. The inhomogeneity can be one of concentration, phase, or temperature. Secondary effects, such as mass transfer, reaction, and product properties are usually the critical objectives. Mixing process objectives are critical to the successful manufacturing of a product. If the mixing scale-up fails to produce the required product yield, quality, or physical attributes, the costs of manufacturing may be increased significantly, and perhaps more important, marketing of the product may be delayed or even canceled in view of the cost and time required to correct the mixing problem. Failure to

provide the necessary mixing may result in severe manufacturing problems on scale-up, ranging from costly corrections in the plant to complete failure of a process. The costs associated with these problems are far greater than the cost of adequately evaluating and solving the mixing issues during process development. Conversely, the economic potential of improved mixing performance is large [75].

Mixing equipment design must go beyond mechanical and costing considerations, with the primary consideration being how best to achieve the key mixing process objectives [26]. Useful methods for mixing process development effort have been evolving in academic and industrial laboratories over the past several decades. They include improvements to traditional correlations as well as increasingly effective methods both for experiments and for simulation and modeling of complex operations. The combination of these approaches is providing industry with greatly improved tools for development of scalable operations [75].

Good experimental design based on an understanding of mixing mechanisms is critical to obtaining useful data and right solutions. The two principal tools used to investigate mixing phenomena and evaluate mixing equipment: laboratory experiments and computational fluid dynamics (CFD) [5]. A wide range of mixing equipment is now available like traditional stirred tanks, baffling, the full range of impellers, and other tank internals and configurations. Some study focuses on rotor-stators, which have been used for many years [75].

Mixtures are different from single components because [77]:

(1) There is a new property, composition, associated with a mixture.

(2) Properties may not be a simple combination of those of the constituents.

(3) If two or more phases are formed from a mixture, these have in general different compositions.

(4) Reactions are associated with mixtures as there will be at least two species present.

(5) Mixtures can be ideal when most properties combine in a readily predictable manner or nonideal when they do not. In ideal mixture each component is assumed to behave as it would in the absence of other chemical species. If there is any form of chemical interaction between the species, the mixture will be nonideal and properties cannot be simply combined, this happens when the substances which are polar and substances in a mixture have different functional groups.

2.2 Scales of mixing

- *Macromixing* is a mixing driven by the largest scales of motion in the fluid.
- *Mesomixing* is a mixing on a scale smaller than the bulk circulation (or the vessel diameter) but larger than the micromixing scales, where molecular and viscous diffusion become important. Mesomixing is most frequently evident at the inlet tube of semibatch reactors.
- *Micromixing* is a mixing on the smallest scales of motion and at the final scales of molecular diffusivity. It is the limiting step in the progress of fast reactions, because micromixing dramatically accelerates the rate of formation of interfacial area available for diffusion. This is the easiest way to enlarge contact area at the molecular level, since the molecular diffusivity remains more or less constant [75].

2.3 Mixing of liquid-liquid system

Liquid-liquid mixing is one of the most difficult and least understood mixing problems. Mixing in vessels is an important area when considering the number of processes which are accomplished. Essentially, any physical or transport process can occur during mixing [132]. Qualitative and quantitative observations, experimental data, and flow regime identifications are needed and should be emphasized in any experimental pilot studies in mixing [141].

Fluid mechanics and geometry are key points to understand mixing. The fluid mechanics transports the liquid in the vessel, whereas the geometry determines the fluid mechanics [137]. Liquid-liquid dispersion is very much dependent on the shape of the tank bottom, the geometry of the impeller, the relative size of the vessel to the impeller and power draw on the impeller geometry [142].

Mixing efficiency in a stirred vessel is affected by e.g. baffles, impeller speed, impeller type, clearance, vessel geometry and position of the impeller [147]. Mixing, mass and heat transfer between phases or external surfaces can be accomplished by stirring. The operation of stirring, which includes mixing as a special case, is now well established as an important and in a wide variety of chemical processes [149]. Specifically, stirrers are applied to three general classes of problems [56]:

(1) To produce static or dynamic uniformity in multicomponent multiphase systems.

(2) To facilitate mass or energy transfer between the parts of a system not in equilibrium.

(3) To promote phase changes in multicomponent systems with or without a change in composition.

Stirring plays a controlling role in the liquid-liquid systems. It controls the breakup of drops (dispersion), the combining of drops (coalescence) and the suspension of drops within the system [135]. The magnitude and direction of convective flows produced by a stirrer affect distribution and uniformity throughout the vessel as well as the kinetics of dispersion. Stirring intensity is important, because the intense turbulence found near the impeller leads to drop dispersion, not coalescence [25]. Lower turbulence or laminar/transitional conditions found elsewhere in the vessel promote coalescence by enabling drops to remain in contact long enough for them to coalesce. Laminar shear also leads to drop dispersion [143]. If a drop is stretched beyond the point of critical elongation, it breaks. If not, it returns to its prestressed state [75]. Liquid mixing problems in laminar flow tend to be very difficult in the pharmaceutical, food, polymer, and biotechnological processes. They are carried out at low velocities or involve high viscosity substances, such as detergents, ointments, creams, suspensions, antibiotic fermentations, and food emulsions [72]. Both the mixing system and duration of mixing have an important effect on drop size distribution, drop breakup, and coalescence [75].

2.4 Miscible and immiscible liquids

Blending is the mixing of two or more miscible liquid components into a more uniform mass [62]. Poor blending leads to concentration and temperature gradients, which affect the product quality and yield. The blending of miscible liquids is carried out for many purposes: to adjust the pH in fermentation, viscosity in diluting or thickening and temperature in sterilization to blend ingredients; to promote reactions in polymerization; to avoid stratification in storage tanks [97]. Miscible liquid blending is the

easiest mixing task. The miscible blending requires two things: The streams must be completely soluble, and there must be no resistance to dissolution at the fluid interface [75]. As soon as the two miscible liquids come into contact, diffusion will produce a region of intermediate viscosity between the bulk liquids. Although there may be considerable differences in the free energy of the bulk materials, there is no phase discontinuity to give rise to localized forces equivalent to an interfacial tension [69].

The term miscible refers to the property of various substances, particularly liquids, that allows them to be mixed together and form a single homogeneous phase [133]. For example, water and ethanol are miscible in all proportions. By contrast, substances are said to be immiscible if they cannot be mixed together, for example, oil and water. In organic compounds, the length of the carbon chain often determines miscibility relative to members of the homologous series. For example, in the alcohols, ethanol has two carbon atoms and is miscible with water, whereas octanol has eight carbon atoms and is not miscible with water. Miscibility can arise for a number of reasons. In the alcohol examples above, the OH-group can form hydrogen bonds with water molecules [81].

The term immiscible liquid-liquid system refers to two or more insoluble liquids present as separate phases. These phases are referred to as the dispersed or drop phase and the continuous phase. The dispersed phase is usually smaller in volume than the continuous phase, but under certain conditions, it can represent up to 99% of the total volume of the system [136]. In dispersion, a two-phase system in which one phase is broken into discrete particles which are completely surrounded by the second phase. Particles may be solid, liquid or gas. For mixing purposes, the second phase is generally a liquid [75] [62].

2.5 Details of the mixing process

The history of added liquid to a liquid in a stirred tank is determined by a combination of factors. Depending on the conditions in the vessel, the properties of the liquids and the position of the addition point. The added liquid may pass through several of four main zones: the stirrer region; the free surface, the bottom of the vessel and the bulk. In each zone there is a chance that the liquid drops will be divided into smaller drops or mixed into the bulk liquid. In addition, in each zone the liquid drops have a chance to move to another zone. If all these chances are known, a prediction of the mixing time and of its expected standard deviation can be made. The impeller's energy input is divided between large-scale flow and turbulence, depending on the type of impeller. The distribution of these two flow types over the regions in the vessel are also determined by the stirrer. Thus, each region makes its own characteristic contribution to the process of mixing, depending on the type of impeller and the flow conditions in the vessel [55]:

(1) In the stirrer region the turbulence intensities as well as the shear forces are high, so that drops have a good chance of breaking up. Especially when the viscosity of the added liquid is high compared to that of the bulk, these shear forces are very important for the mixing process, because in other parts of the vessel the shear forces may be too weak to cause break-up. Drops may also be divided by physical contact with the stirrer. The circulation time is the time between two passages of a liquid volume through the impeller, is determined by the large scale flow. If a drop is not broken up during a passage through the impeller, the mixing time will be increased by circulation time before the drop will pass the stirrer again.

(2) In the bulk, the shear stresses and the level of turbulence are lower, but

deformed drops may be deformed further or be mixed completely.

(3) The large scale flow combined with the net force, resulting from density differences, determines whether a drop reaches the free surface or the bottom of the tank. If this happens, the added liquid will generally remain there provided the net force is in the appropriate direction. The liquid can then reenter the bulk by turbulent eddies or disappear by means of diffusion. Both mechanisms yield relatively long mixing times.

2.6 Mixing characteristics

2.6.1 Mixing Time

The mixing time is defined as the required time to achieve certain degree of homogeneity and to get a uniform mixture of two miscible liquids [46] [62]. The prediction of mixing time is important and needed e.g. for the purpose of quality control [32]. The mixing time for liquids of very different physical properties can be long [123]. The added material has a tendency to float at the surface or go to the vessel base due to the density difference. Similarly, if the viscosity of the added material is much higher, due to resistance to deformation, the mixing time will be much longer than for liquids of similar properties [57] [55] [97].

2.6.1.1 Determination

The mixing time or homogenizing time designates the time which the stirrer needs in order to obtain a desired homogeneity degree. There are different measuring methods to determine the mixing time like [41] [85]:

(1) *Probe methods*.

(2) *Schlieren method*.

(3) *Chemical methods*.

The determination of the mixing time by means of *Probe methods* usually takes place with conductivity electrodes or photoelectric probes. The advantage of this method is a relatively precise measurement of the homogeneity degree within fluids of the medium. Since the homogeneity degree is not reached at the same time at each place in the vessel, only a partial mixing can be measured with several probes. The same problem results also in the case of the measurement of pH values and temperature by means of probes. Additionally the influence of diffusion is no longer negligible.

The *Schlieren method* is an optical used technique to determine the moment at which uniformity is reached**.** Optical inhomogenieties of the liquid in the mixing vessel, in the form of gradients in refractive indices, will produce Schlieren, whereas absence of the latter indicates homogeneity of the liquid mixture. The mixing time is the time between the instant when the stirrer starts mixing and the instant of disappearance of the Schlieren [57].

The *chemical method* is a measuring procedure developed by Käppel [87] with which one of the liquids to be mixed is colored by an iodine solution; the other transparent one contains a stoichiometric quantity of sodium thiosulfat. The iodine liquid mixture is decolorised after the following reaction with sodium thiosulfate [30] [31]:

$$I_2 + 2Na_2S_2O_3 \rightarrow 2NaI + Na_2S_4O_6$$

During most past investigations of the mixing time the liquids differed only in the added chemical components (e.g. sulfuric acid/caustic solution with phenolphthalein as indicator or sodium thiosulfate/iodine with starch as indicator), the mixing time was determined when the reaction is completed and determined by the indicator change with time (so called chemical

decolorisation method) [58]. This technique can be followed by visual observations using a video camera to see the color change during the reaction. When the mixed liquids have negligible density and viscosity differences, then the mixing time is determined from the number of revolutions, the stirrer diameter and the kinematic viscosity of the medium. The dimensionless mixing time is the product of the impeller speed and mixing time, its value represents the number of revolutions an impeller must make to blend the liquid [97].

2.6.1.2 Correlations

Hoogendoorn et al. [67] used several ways to represent their experimental mixing time t_m data in graphs. When comparing similar types of impellers they plot the dimensionless mixing time against the impeller Reynolds number. The value of dimensionless mixing time can be interpreted as the number of stirrer revolutions needed for homogenization. They introduced two dimensionless groups:

$$\frac{P\, t_m^2}{\eta\, d_v^3} = f\left(\frac{\rho\, d_v^2}{\eta\, t_m}\right). \qquad (2\text{-}1)$$

The left hand side of the equation (2-1) is a function of a modified impeller Reynolds number which can be given in a form of diagram for different types of stirrers as can be seen in Fig. 2.1. Also, the left hand side of the equation (2-1) can be interpreted as [55]:

$$\frac{P\, t_m^2}{\eta\, d_v^3} = \frac{P}{\rho\, d_v^3}\frac{1}{\nu}t_m^2 \propto \frac{\varepsilon}{\nu}t_m^2 = \frac{t_m^2}{t_k^2}. \qquad (2\text{-}2)$$

Where t_k is Kolmogoroff's time scale of turbulence = $(\nu/\varepsilon)^{0.5}$. The left hand side group ranges from 10^4 to 10^8, so t_m / t_k ranges from 10^2 to 10^4.

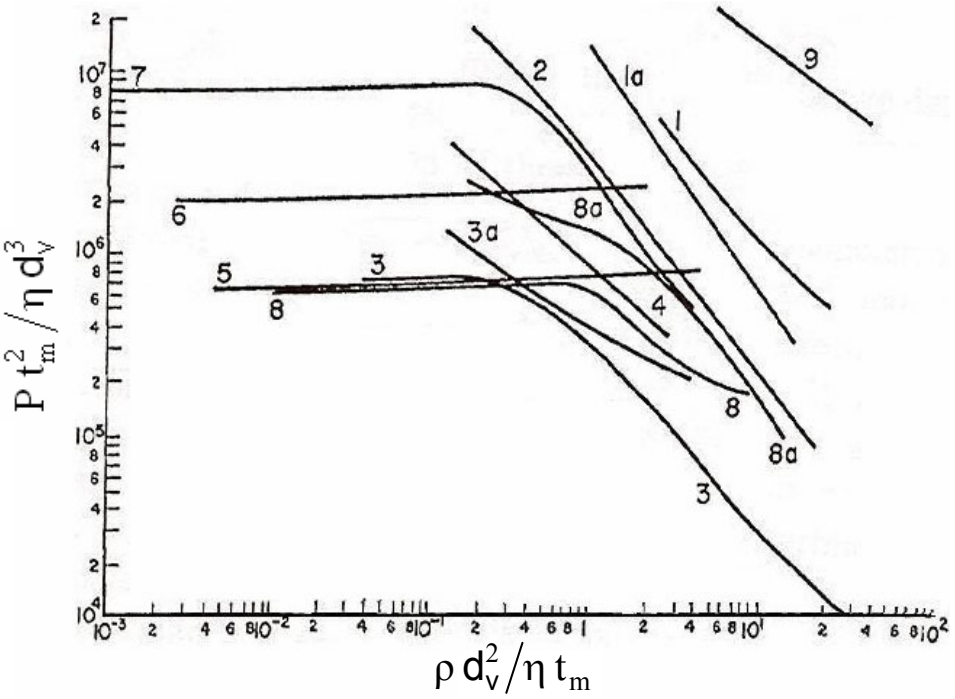

Figure 2.1: The dimensionless group $P\,t_m^2/(\eta\,d_v^3)$ as a function of modified impeller Reynolds number $\rho\,d_v^2/(\eta\,t_m)$ for different types of stirrers [67]. 1: Turbine + baffles, 1a: Turbine, 2: 3 inclined-blade paddles, 3: 3 inclined-blade paddles + draught tube, 3a: 1 inclined-blade paddles + draught tube, 4: Screw, 5: Screw + draught tube, 6: Ribbon, 7: Propeller A + draught tube, 8: Propeller B + draught tube, 8a: Propeller B, 9: Anchor.

Zlokarnik [155] also used the above mentioned groups, and added a new relationship to represent the mixing time:

$$\frac{\rho^2\,P\,d_v}{\eta^3} = f\left(\frac{\eta\,t_m}{\rho\,d_v^2}\right). \tag{2-3}$$

The left hand side of the equation (2-3) is drawn as a function of $\eta\,t_m/(\rho\,d_v^2)$ for different types of stirrers as can be seen in Fig. 2.2. Also, the left hand side of the equation (2-3) can be interpreted as [55]:

$$\frac{\rho^2\,P\,d_v}{\eta^3} = \frac{P}{\rho\,d_v^3}\frac{\rho^3}{\eta^3}d_v^4 \propto \frac{\varepsilon}{\nu^3}d_v^4 = \frac{d_v^4}{l_k^4}. \tag{2-4}$$

Where l_k is Kolmogoroff's length scale of turbulence = $(\nu^3/\varepsilon)^{0.25}$. In the turbulent region d_v / l_k ranges from 10^2 to 10^4.

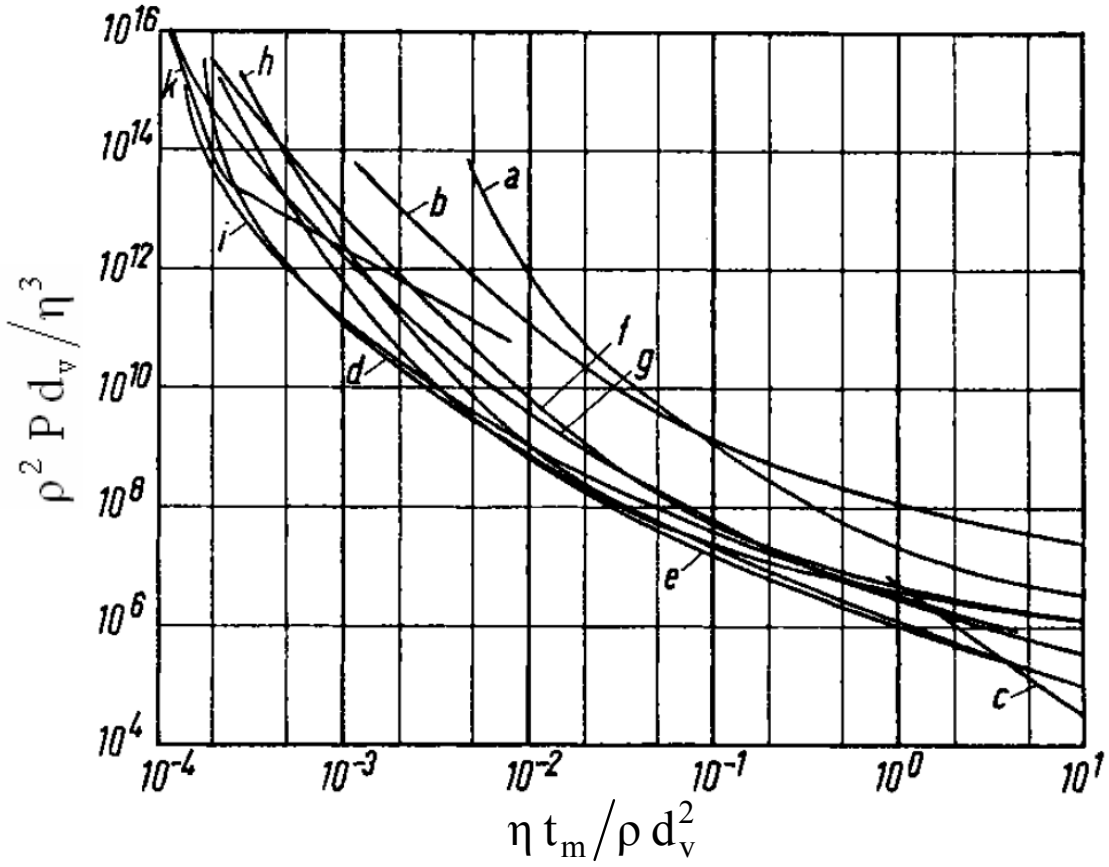

Figure 2.2: The dimensionless group $\rho^2 P d_v / (\eta^3)$ as a function of $\eta t_m / (\rho d_v^2)$ for different types of stirrers [155]. a: Anchor with 4 blades, b: Anchor with 2 blades, c: Spiral, d: Flat-blade with alternative current, e: Flat-blade without alternative current, f: Cross bar without alternative current, g: Cross bar with alternative current, h: Lattice without alternative current, i: Lattice with alternative current, k: Propeller stirrer.

The above two literatures did not consider the effect of viscosity or density differences. Rielly et al. [156] examined the mixing of two layers of different viscosity, initially stratified as a result of a density difference in a batch mixing situation. The mixing time correlation can be found from drawing the dimensionless mixing time as a function of Richardson number Ri which is defined as:

$$Ri = \frac{\Delta\rho \, g H_l}{\rho_L \, \omega^2 d^2} \quad . \tag{2-5}$$

Where d is the stirrer diameter, H_l is the liquid height and $\Delta\rho = \rho_1 - \rho_2$.

2.6.2 Density differences and viscosity differences

Blending miscible liquids of different viscosities or densities is a common operation in the process industries. This operation may involve difficulties in predicting the mixing time [145]. Because is often not clear whether mixing problems arising in these cases are caused by viscosity differences or by density differences [73]. Moreover, in many investigations in the past the effects of differences in viscosity or density have not been taken into account [55]. The main problem with micromixing of liquids of different viscosities is concerned with a proper modeling of deformation of fluid elements, which generates the contact surface between the mixed materials [134]. Any differences in viscosity of mixed liquids produce discontinuity of the velocity gradients at an intermaterial surface, which may lead to destabilization of laminar flow during mixing [54].

Rożeń et al. [53] investigated the mixing of two miscible liquids of different viscosities in Couette flow (refers to the laminar flow of a viscous liquid in the space between two surfaces, one of which is moving relative to the other) by means of a single decolorization reaction to visualize mixing and flow destabilization. They found that the simple laminar flow becomes unstable when the contacted liquids have different viscosities. This destabilization leads to formation of small streak and structures consisting elements of one liquid, which remain segregated from the surrounding liquid; for example an elongated filaments or a drop like inclusion are transformed into a set of ellipsoidal or more complex structures, also the flow becomes completely irregular.

Bouwmans et al. [55] studied the effect of density and viscosity differences of different liquids on the mixing time when they are mixed under different conditions like the type and speed of the stirrer, also the

point of liquid addition to the second liquid in the vessel. They found that the roll of the density and viscosity differences depends on the way the energy input of the impeller is divided and distributed in the vessel depending on the produced flow type. Also, when a liquid less dense than the bulk liquid is added near the surface buoyancy effects, large mixing time is obtained [146]. Low stirrer speeds yields long mixing time. When liquid is added near the impeller, the mixing time is not affected by the density and viscosity differences.

Smith et al. [69] carried out blending experiments of small quantities of high viscosity additives into a turbulent low viscosity liquid. Mixing times were measured by using conductivity method. They found that the higher viscosity does not itself retard the later stages of blending and the addition near the impeller shaft on the free surface is generally reliable and efficient, also higher impeller speeds reduce the danger of settling out and adhesion of the viscous material to arbitrary surfaces.

Bouwmans et al. [68] made measurements with very small quantities of additions to viscous bulks; they found that density differences are more likely to cause longer mixing times than viscosity differences.

2.6.2.1 Influence on the mixing time

Zlokarnik [58] [45] [83] determined the influence of density and viscosity differences on the mixing time. The investigations were made with cross bar stirrer in reinforced containers, so that with high viscosity differences the two phases do not together-slide and/or with large density variations no centrifugation effects arise. When homogenizing liquids without density and viscosity differences in the vessel with a given type of stirrer and installation, the mixing time t_m is dependent on the stirrer

velocity ω, the stirrer diameter d, the density ρ of the liquid, kinematic viscosity ν and acceleration of gravity g.

When homogenizing liquids with different density and viscosity, the mixing time is affected by the density ρ_2 and kinematic viscosity ν_2 of the second mixing component which have the low density and viscosity value as well as by the volume ratio $\varphi = V_2/V_1$ of the pure liquids which will be homogenized (where V_2 is the volume of the second mixing component which have low density and viscosity value) , also the connection of g with the density difference $\Delta\rho = \rho_1 - \rho_2$ between the pure components with the term $\Delta\rho$ g has an influence on the mixing time. He used a similarity theory to correlate the dimensionless mixing time as a function of impeller Reynolds number Re and Archimedes number Ar which are defined as:

$$Re = \omega d^2 / \tilde{\nu}. \tag{2-6}$$

$$Ar = d^3 \Delta\rho g / (\tilde{\nu}^2 \tilde{\rho}). \tag{2-7}$$

Where $\tilde{\nu}$ and $\tilde{\rho}$ are the average kinematic viscosity and density of the mixed components, respectively. When homogenizing two soluble liquids with a small density difference of $\Delta\rho \leq 0.5$ g/cm^3, then $\Delta\rho$ has no influence on ωt_m. Zlokarnik found from the similarity theory and the experimental measurements the following mixing time correlation:

$$\sqrt{\omega t_m} = 51.6\ Re^{-1}\ (Ar^{1/3} + 3). \tag{2-8}$$

Equation (2-8) is valid for $10^1 < Re < 10^5$, $10^2 < Ar < 10^{11}$, $1 < \nu_1/\nu_2 < 5300$, $0.1 < \varphi < 1$ and $\Delta\rho > 0.5$ g/cm^3.

The effect of density difference on the mixing time when the second liquid component is added at different injection positions in SBR is studied

by Bouwmans et al. [55]. They have considered two cases based on $\Delta\rho = \rho_1 - \rho_2$:

Case 1: $\Delta\rho \geq 0$

In this case the difference between the densities of the added liquid (ρ_1) and that of the bulk (ρ_2) was always positive or zero. This causes the tracer liquid to be drawn into the stirrer in all injection cases, so that injection of the tracer near the surface results in the same mixing times as injection near the stirrer, provided that the added liquid does not adhere to the vessel.

Case 2: $\Delta\rho \leq 0$

(a) Injection near the surface: When tracer liquid is injected about 1 cm below the free surface the mixing time is strongly influenced by density differences.

(b) Injection in the stirrer plane: When tracer liquid is added near the stirrer, in a region where both shear stresses and turbulence intensities are high, the mixing time is low and practically constant and the relative standard deviation is small.

The effect of both density and viscosity differences of the miscible liquids and the buoyant additions of small quantities of the liquids on the mixing time measurements in turbulently stirred vessels are studied by Bouwmans et al. [68]. They defined the Richardson number which includes the density difference between the mixed liquids (see equation 2-5). Three control regimes for buoyant additions based on a Richardson number were determined:

(1) The stirrer regime when the liquid is added near the stirrer and when the bulk flow succeeds in transporting all of the added liquid to the stirrer, then the homogenization time depends on the rate of distribution of the

added liquid over the vessel. The mixing time is independent on the viscosity ratio, the location of the injection and the added liquid volume for small volume ratio between the added and the bulk liquids, the mixing times are equal to those for liquids of equal properties [148].

(2) The gravity regime when the liquid is added at the surface. The mixing time is dependent on the viscosity and density differences, very long mixing times can result.

(3) The intermediate regime when only part of the added liquid is transported to the stirrer. The mixing time is unpredictable and can be any where between the stirrer controlled mixing time and the gravity controlled mixing time, and strongly depends on the amount of liquid that is added at the surface.

The effect of viscosity differences when adding a small quantity of a viscous liquid to water in a turbulently stirred vessel on the mixing time at different impeller types and sizes and at different diameters of the stirred vessels are studied by Pip et al. [98]. They considered a modified Reynolds number (Re^*), that incorporates the ratio of bulk to added viscosities (η_2 / η_1), to identify the operating regime over which the addition of the liquid has an effect on the mixing time:

$$Re^* = \frac{\omega d^2 \rho_2}{\eta_2} \left(\frac{\eta_2}{\eta_1} \right) . \qquad (2\text{-}9)$$

The stirrer regime when $Re^* > 10^2$ is considered, where the following mixing time correlation for similar property liquids can be used to calculate mixing time for a given level of uniformity L1 ($0 < L1 < 1$) from a measured value of mixing time for another level of uniformity L2:

$$\frac{t_{m,L1}}{t_{m,L2}} = \frac{\ln(1.0 - L1)}{\ln(1.0 - L2)} \quad . \tag{2-10}$$

The added liquid regime when $Re^* < 10^2$ is considered, in which the blending process is considerably slower, mixing time depends on the physical property differences as well as the impeller speed and the method and location of addition. They found when the turbulent Reynolds or shear stresses of the bulk liquid is higher than the viscous shear stress of the added liquid, then the added liquid will be deformed and mixed rapidly. Also, large viscosity differences require much longer mixing times which need to be considered carefully in terms of product quality and energy requirements of the process, the extent to which the mixing time is increased depends on the operating conditions. The effect of the viscosity difference is more important in small scale vessels. Increasing the ratio of the impeller diameter to the vessel diameter or increasing the input power can reduce the mixing time in the stirrer regime for similar property liquids. Using a small diameter and/or low power number impeller gives shorter mixing times at a given power input. They proposed the following correlation to calculate the mixing time for turbulent mixing is:

$$t_m = 5.91\, d_v^{2/3} \left(\frac{\rho V}{P}\right)^{1/3} \left(\frac{d_v}{d}\right)^{1/3} \quad . \tag{2-11}$$

The influence of the radial position of addition point of the tracer when using sliding mesh model via CFX on the simulated flow field and mixing times in the high transitional and turbulent flow regime for a vessel stirred by a Rushton turbine are investigated by Bujaski et al. [44]. They found that the radial distance from the wall of the vessel had a very big effect on both mixing time and the development of the concentration field. When the

addition point was close to the sliding mesh surface, the simulation was in a good agreement with the empirical predictions whilst that for a point close to the wall was much too longer. They proposed the following correlation to calculate the mixing time for any level of uniformity L, where $0 < L < 1$:

$$t_{m,L} = \frac{-\ln(1-L)}{1.06\left(\frac{d}{d_v}\right)^{2.17}\left(\frac{d_v}{H}\right)^{0.5}} \quad . \tag{2-12}$$

The effects of turbulence model and different tracer adding and detecting positions on the macro-mixing and mixing time in a baffled stirred vessel with Rushton turbine are studied by Guozhong et al. [154]. 3D simulation was done using the CFD package CFX-4.3. A sliding mesh model was used to account for the relative movement impeller and baffles. The calculated mixing times from CFD were compared with those obtained from tracer experiments at different adding positions. They found that different tracer adding position gives different mixing times. Mixing simulation highly rely on the flow field prediction from different turbulence models.

The effects of various geometrical parameters of the mixing equipment (e.g. wall-clearance and blade width) on the overall homogenization process to optimize the mixing efficiency when mixing Newtonian viscous fluids with a helical ribbon impeller are studied by Delaplace et al. [153]. The degree of homogeneity is followed using a conductivity method after a tracer injection. They showed that using the time-dependent stirrer velocity during the mixing process allows energy saving. The mixing times have been determined from tracer method.

2.6.3 Flow patterns

Mixing by stirring of liquids involves the transfer of momentum from the moved stirrers to the liquid. According to the way in which this occurs, stirrers may be divided into two categories [57]:

(1) The momentum is transferred by *shearing stress*, i.e. the transfer is perpendicular to the direction of flow. This category includes the cone stirrer, the bulb stirrer and the rotating disc.

(2) The momentum is transferred by *normal stress*, i.e. the transfer is in the direction of flow. This category includes the paddle stirrer, the turbomixer and the propeller.

Flow patterns are influenced by the type of impellers. There exists four categories axial, radial, tangential and secondary flow [13] [14]:

(a) *Axial flow*: Is the movement of a fluid from the bottom to the top of the vessel. This movement of the fluid coincides with the axis of impeller shaft, so when the impeller operates in an up pumping mode, the flow collides with the bottom of the tank and spreads out in all radial directions toward the wall. The flow rises along the walls up to the liquid surface and is pushed radial to the impeller. Since axial flow impeller produce only one loop right and left to the shaft as shown in Fig. 2.3, fluids mix faster and mixing time is reduced compared to radial flow impellers with two loops. The power consumption of these flow impellers is less than that of radial flow impellers at the same stirrer velocity and diameter. Axial flow is found with propeller type stirrers and pitched blade turbine [75] [62] [56] [57].

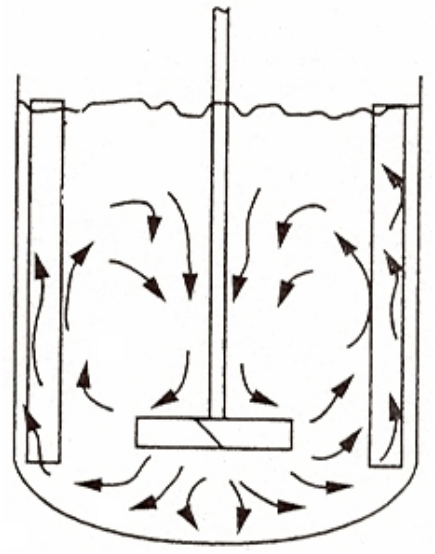

Figure 2.3: Axial flow pattern of pitched blade turbine [75].

(b) *Radial flow*: Is parallel to the impeller radius toward to the vessel wall. If a radial impeller is not positioned close to the vessel wall or bottom, the flow will split into two streams upon collision with vessel wall. Each flow loop will continue along the wall and then return to impeller as shown in Fig. 2.4. The movement of a fluid is generally from the center of the vessel to the wall. Radial flow is found with a turbine type or a paddle stirrer [75] [62] [56] [57].

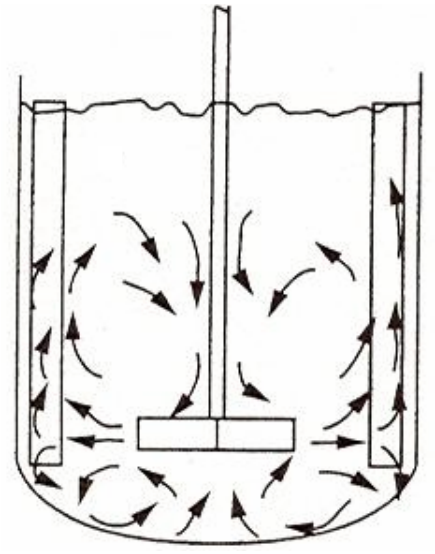

Figure 2.4: Radial flow pattern of flat-blade turbine [75].

(c) *Tangential flow*: Is naturally induced by swirling or vortexing flow. It offers very little mixing because the velocity gradients are very small. Tangential flow (Fig. 2.5) is found with all normal rotating stirrers if no baffles or deflecting blades are present and the stirrer is placed centrally. The tangential flow does not contribute to the mixing in a vertical direction. It is always converted into radial flow by the centrifugal force. In the unbaffled vessel with the impeller rotating in the center, centrifugal force acting on the fluid raises the fluid level near the wall and lowers the level at the shaft [56] [57].

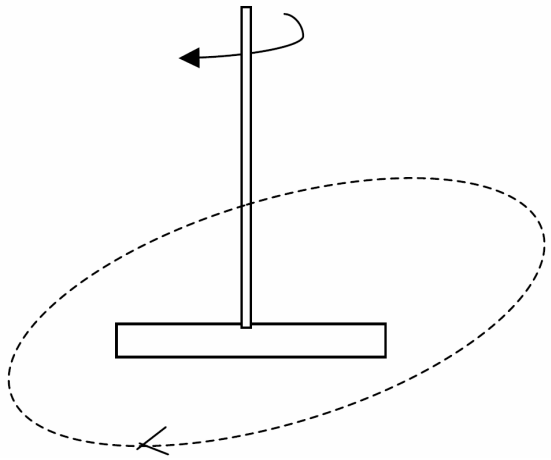

Figure 2.5: Tangential flow pattern of pitched blade turbine.

(d) *Secondary flow*: By transferring energy to the liquid, the rotating stirrer produces a rotational motion which is referred to the primary flow (Fig. 2.6-left). Due to the rotational primary flow a centrifugal force results which produce the secondary flow. This force drives the liquid outwards in a radial direction. The liquid flows at the vessel wall either upwards or downwards forming vortex rings (Fig. 2.6-right). A vortex is produced due to the centrifugal force acting on the rotating liquid. The depth and the shape of the vortex depend on impeller and vessel dimensions as well as on stirrer velocity. The secondary flow consists of radial and axial velocity

components which are required in the mixing process. Primary fluid flow may be considered as an energy reservoir for the secondary flow [56] [79].

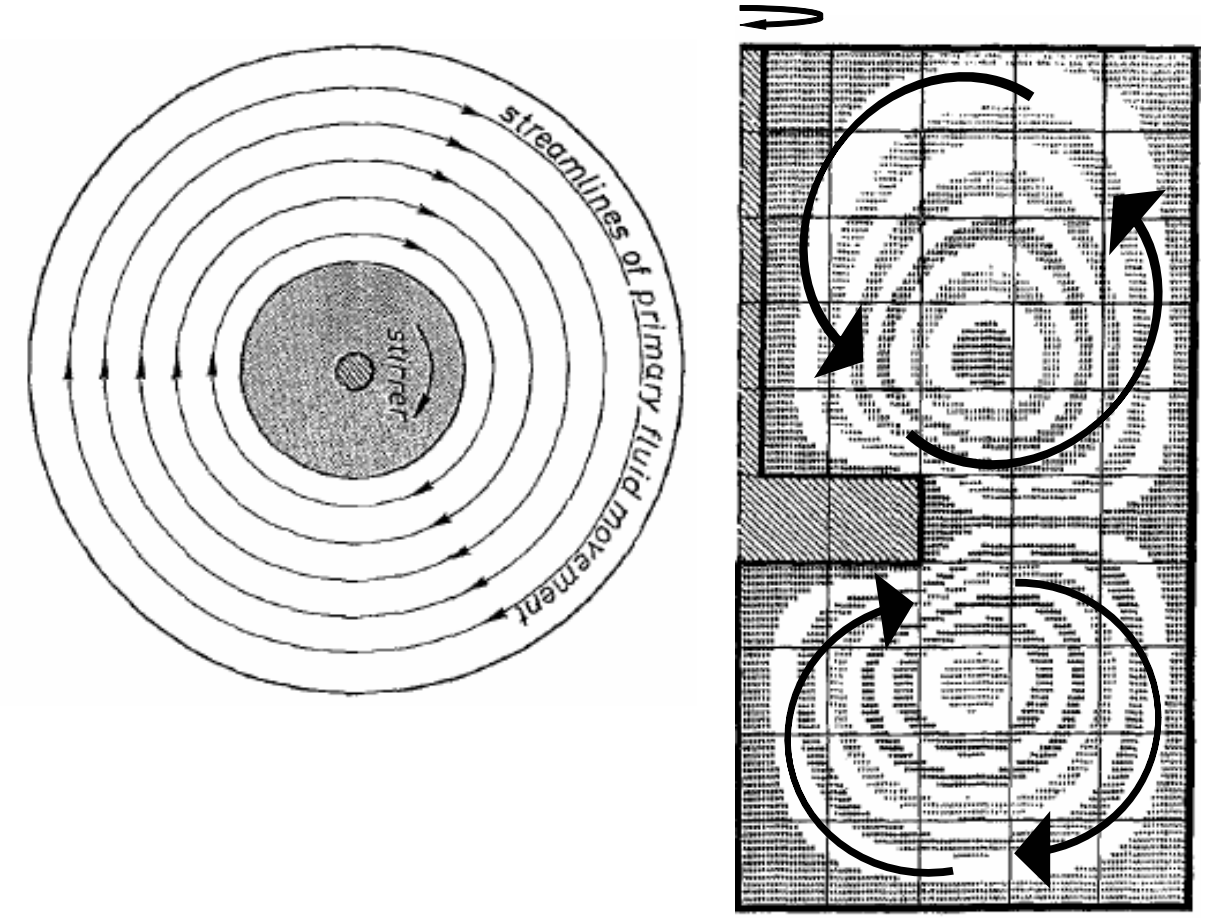

Figure 2.6: Primary flow from top view (left) and Secondary flow from front view (right) of a liquid fluid.

Three dimensional flow patterns inside the vessel are important to get a better understanding of the state of flow of the fluids and of the mechanisms responsible for homogenization and transport processes [4]. Flows in industrial mixing vessels have many complications arising from the complex design of the impeller/vessel arrangement (small clearance B, s. Fig. 3.1) and from the complex rheological behavior of the stirred fluid [10].

In the case of small clearance B when using a laser beam [1], no experimental data can be measured and consequently it is impossible to obtain the velocity profile at whole stage during a cycle (a cycle is the required time for impeller to rotate one revolution), although a detailed characterization of the three dimensional flow pattern inside the vessel is important to get a better understanding of the flow state of the fluids and of the mechanisms responsible for homogenization and transport processes.

Ohta et al. [54] proposed the numerical study for a Newtonian fluid mixing in stirred vessels having different diameters. They studied a two dimensional model for secondary flow to express the flow field in the vertical plane of an anchor stirred vessel, the anchor has only long vertical blade without horizontal blade. The effect of the clearance and the anchor velocity on the flow field was studied. They found that two vortices are formed in the upper and lower region of the vessel. The number and flow rate of axial circulations become greater with an increase of the anchor velocity. The stirrer velocity has a greater effect on the secondary axial flow than on the primary tangential flow. The centre of the vortex seems to be poorly mixed region.

Abid et al. [52] studied a three dimensional model applied to the flows generated in a vessel by anchors stirrers in a laminar flow regime. Long anchor stirrer without horizontal shaft and short anchor stirrer with horizontal shaft are used for comparison of the mixing efficiency. The secondary flows induced by anchor stirrer are investigated. The effects of clearance B or the ratio of B/d_v, the height H_i (s. Fig. 3.1) of the vertical blades or the ratio H_i/H_l on the flow field and mixing were studied. They found that the horizontal blades enhance the axial circulation and the vertical blades are more efficient if their tips are slightly below the liquid level.

Secondary flows are created between the blades and the central shaft when short anchor stirrer with horizontal shaft is used, this enhance the mixing in the vessel, by producing new axial circulations. Velocity of the stirrer or Reynolds number influence the appearance of more or less recirculation loops behind the blades, but does not change the flow structures. A large upward axial flow is generated, and the radial movement increases, compared with the long anchor for the same liquid level in the vessel. A big recirculation is noted behind the crossing of the two blades below the stirrer, near the bottom of the vessel. Primary tangential flow is created by the rotation of the horizontal blade. They found that short anchor with the horizontal blade is the best to use because it requires lower power consumption and produces axial circulations; this achieves a best mixing at a low price.

Peters et al. [49] [43] studied experimentally the flow patterns, velocity profiles and mixing times in anchor stirred vessels. The effect of the anchor velocity and blade-to-wall clearance on the velocity profiles and vortex formation were determined. A dye coloration and decolorization technique is used in the first experiment to measure the mixing time which is defined as the time required to disperse the dye. The motion of the fluid was followed by taking a cine record of the movement of small suspended polyethylene and polystyrene beads in the second experiment. They found that as the anchor velocity and Reynolds number increase, the flow reversal behind the blade tip increases, also longer and larger vortices are formed. Decreasing the clearance causes the vortices to be formed at lower Reynolds number because of the greater amount of fluid flowing around the inside edge of the blade at a higher velocity than at higher clearance. As the stirrer velocity increases, the mixing rate increases up to a certain limit, then it decreases

again. Vertical vortices are formed between the blades and the centre shaft. The vortex core is the last region to be mixed. The vertical circulations are resulting in a greater degree of homogenization. The primary flow of the anchor impeller is attributed to horizontal blade and the secondary flow to the vertical blades as well as the hydrodynamic conditions.

Peixoto et al. [8] studied the behavior of the stirred vessels with anchor impellers using a computational fluid dynamics approach. CFX-4.2 software tool was used to calculate the flow generated by the anchor impeller using three dimensional and finite volume methods. A mesh independent study was carried out, the radial and axial velocities for two mesh densities of 5492 and 13080 cells were calculated, and very similar results were found. A single axial recirculation zone centered near the curve separating bottom and vessel walls, a little bit above the curve of the anchor blade. As the velocity of the impeller increases, the fluid circulation increases and the low velocity region near the free surface is eliminated.

Delaplace et al. [10] [42] [1] studied the laminar and transient flow field patterns of Newtonian and non- Newtonian fluids in a rounded bottom vessel stirred by anchor and helical ribbon impellers experimentally and with CFD simulations. Tracer experiments were done. For Newtonian fluid, they found that the tangential flow is dominant and becomes smaller with radial distances away from the impeller. For non-Newtonian fluid, the flow field of yield stress fluids is quite similar to those obtained with high shear thinning fluids. Also the tangential, axial and radial components of the velocity away from the blades are smaller than the corresponding values obtained for Newtonian fluids. They found that the used impellers generate an axial flow and the maximum shear rates are along the vertical arms and helical ribbons.

Espinosa et al. [151] studied the effect of wall and bottom clearance on power consumption for anchors by considering the variations in the flow patterns. They found that when the bottom clearance to the vessel diameter ratio increases, then the necessary power input decreases. Changing the bottom clearance produces axial flows which affect the primary flow patterns and thus the power consumption.

Kampinoyama et al. [152] analyzed the three dimensional flow of a Bingham fluid in an anchor impeller numerically using the equations of continuity, motion and the Bingham model equation for the rheological characteristics. They found that the apparent viscosity of the liquid strongly increases in the region between the wall of the vessel and the impeller. The downward fluid circulations are generated near the bottom of the vessel by the lower part of the vertical blade. The rotation of the impeller generates a strong upward flow with increasing the distance from the bottom of the vessel. The circumferential velocity distribution varied in the region of high shear rate next to impeller, and the velocity components have uniform distribution in the region of low shear rate away from the impeller. The circumferential velocity component increases from the axis of rotation to the edge of the impeller, while the radial and axial velocity components are almost constant.

2.6.3.1 Calculation methods

Computational fluid dynamics models are used to calculate the flow patterns in stirred reactors. To model the impeller, it is common to describe experimentally obtained velocity data in the outflow of the impeller. This has the disadvantage that it is often necessary to extrapolate the data to situations for which no experiments can be performed. Only recently new

methods are available to calculate the flow pattern around the impeller blades without describing any experimental data [157]. These methods are following:

2.6.3.1.1 Sliding mesh model

It is a time dependent solution approach in which the grid surrounding the rotating components physically moves during the solution. The velocity of the impeller and shaft relative to the moving mesh region is zero, as the velocity of the vessel and other internals in the stationary mesh region. The motion of the impeller is realistically modeled because the grid surrounding it moves as well as giving rise to a time accurate simulation of the impeller-wall interaction as shown in Fig. 2.7. After each such motion, the set of conservation equations is solved in an iterative process until convergence is reached. The grid moves again, and convergence is once again obtained from an iterative calculation. During each of these quasi-steady calculations, information is passed through the interface from the rotating to the stationary regions and back again [75].

In order to rotate one mesh relative to another, the boundary between the meshes needs to be a surface of revolution. When it is initially in non rotated position, the grid on this boundary must have two surfaces. During the solution, one will remain with the rotating mesh region, and the other will remain with the stationary mesh region. When information is passed between the rotating and stationary grid regions, interpolation is required to match each cell with its many neighbors across the interface [80].

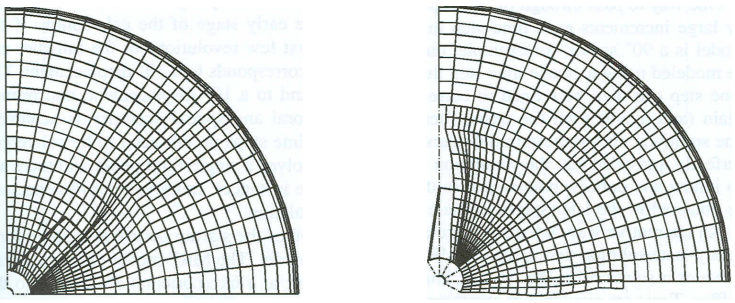

Figure 2.7: Sliding mesh in two orientations (shown in 2D).

2.6.3.1.1.1 Solution procedures

For transient model involving the motion of the impeller, starting the simulation with the impeller at rest is required. After a period of time the flow field reaches periodic steady state, but this period of time needs lot of revolutions. If the goal of the simulation is to study the periodic steady state conditions, minimizing the time spent to reach this state is desirable. One way to pass through the startup conditions rapidly is to move the impeller by large increments each time step in the early stage of the calculation. If the model is a 90° sector, for example, the first few revolutions of the impeller can be modeled using a large time step that corresponds to a 30° displacement. The time step can be reduced to correspond to a 10° displacement, and reduced again until the desired accuracy is achieved. The solutions during these initial large time steps do not need to be converged perfectly. Improved convergence can be obtained in the later stages of the calculation [75].

2.6.3.1.1.2 Validation

Bakker et al. [80] presented the validation of the sliding mesh model in a baffled stirred tank with a pitched blade turbine under laminar conditions. The flow patterns were experimentally predicted by LDV (laser-Doppler

velocimetry) [3]. They found that this method is suitable to predict the flow patterns of the impellers without needing any experimental data and a good agreement with the experimental data was found. The flow patterns were shown by means of velocity vectors [9] [12]. Two circulation loops formed, above and below the impeller. The length of the vectors is proportional to the magnitude of the liquid velocity [11]. They found also as Reynolds number increases, the flow changes from the radial to the axial.

2.6.3.1.2 Rotating frame model

The rotating frame model solves the momentum equations for the entire domain in a rotating frame. Problems solved in a rotating frame typically use the angular velocity of the primary rotating component as the angular velocity of the frame. In stirred tanks, the impeller serves this purpose, so the frame is assumed to rotate with the impeller. The tank, however, rotates in the opposite direction, so must have a rotational boundary condition of negative angular velocity value. The approach is therefore only useful for unbaffled tanks with smooth tank walls that are geometrically equivalent to a perfect surface of revolution. Thus an unbaffled cylindrical tank with an axisymmetric bottom shape and no angular-dependent internals could be simulated in this manner [75].

2.6.3.1.3 Multiple reference frames model

A modification of the rotating frame model is the multiple reference frames (MRF) model. The modification is that more than one rotating or non rotating reference frame can be used in a simulation. This steady state approach allows for the modeling of baffled stirred tanks and tanks with other complex rotating or stationary internals. A rotating frame is used for

the region containing the rotating components while a stationary frame is used for regions that are stationary. In the rotating frame containing an impeller, the impeller is at rest. In the stationary frame containing the tank walls and baffles, the walls and baffles are at rest [75].

2.7 Types of stirrers

Stirrer is a device consisting of at least a power package, a shaft and an impeller to provide stirring of the contents of a vessel [62]. Basic types of stirrers are shown in Figs. 2.8 and 2.9 [78] [65].

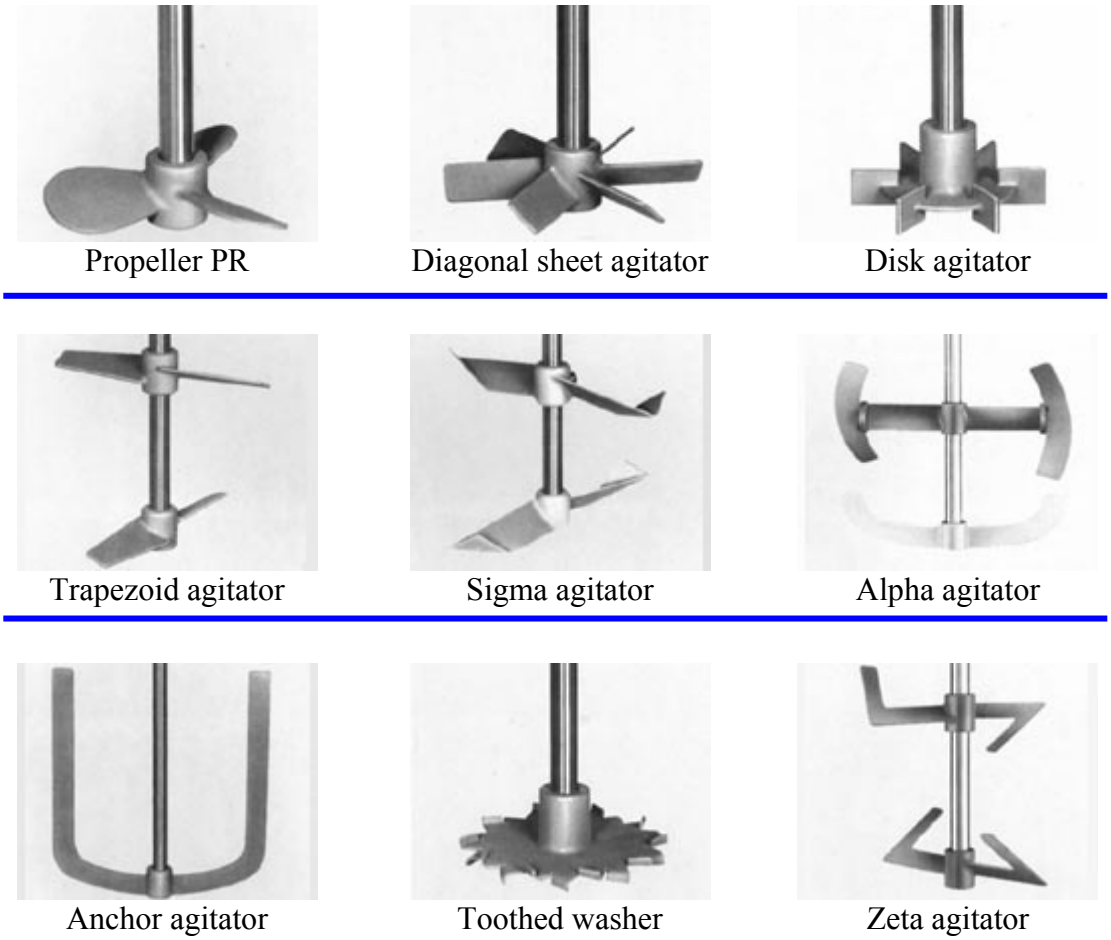

Figure 2.8: Types of stirrers.

Pitched Blade Turbine  The pitched blade turbine is suited for high speed liquid/solid applications where vessel baffles may be impractical. The pitch angle varies between 0 and 90 degrees from the vertical. It gives axial flow.	**Straight Blade Turbine**  It is known as Rushton Turbine, this impeller is suited for gas/liquid applications requiring high speeds. It gives radial flow.
Helical Impeller - Outer Flight  This impeller is used for very viscous materials. They operate with minimal clearance at the vessel wall and provide axial flow at low speed.	**Anchor Impeller**  Best suited for high viscosity fluid. This impeller provides tangential flow and improved heat transfer as relatively low speed.

Figure 2.9: Types of stirrers and flow fields.

There are other types of impellers and stirrers as follow [63] [140] [144]:

(1) *High-Viscosity impellers:* These impellers are described below and shown in Fig. 2.10 [64] [111 – 113]:

(a) *Double Helical Ribbon*: It is proven as the best high viscosity over 30,000 mPa s, laminar flow impeller, highly effective in heat transfer and efficiently incorporates surface liquids and solids [84].

(b) *Anchor*: It is most economical laminar flow impeller with horizontal flow well suited for low liquid level geometries. It solves heat transfer fouling problems with optional wall scrapers.

(c) *Screw (Auger)*: It is ideal for shear sensitive, uniform blending applications (polymers), excellent top to bottom turnover flow characteristics, and used in mildly pseudo-plastic applications with power law indexes as low as 0.5.

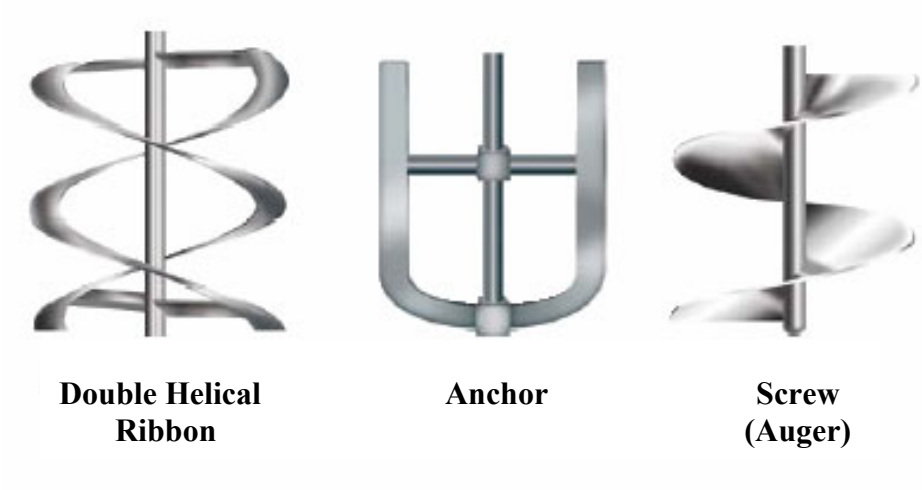

Figure 2.10: High-Viscosity impellers.

(2) *Turbine type impellers*: It is produced an excellent mixing action over the range of stirring speeds. These impellers (Fig. 2.11) are made in four-blade and six-blade styles, the smaller four-blade impellers are used only on micro and mini reactors [48]. These impellers generally provide excellent mixing for systems with effective viscosities up to 50 Pa s.

Figure 2.11: Turbine type impeller.

(3) *Spiral stirrers*: Can be installed in any 1 liter or 2 liter reactor to produce a positive down or upward force action when working with viscous polymers or other high viscosity mixtures. They work best in floor stand reactors with adjustable speed, heavy duty drive systems as shown in Fig. 2.12.

Figure 2.12: Spiral stirrers.

(3) *Gas entrainment impellers*: are used to obtain maximum gas dispersion into a liquid system. This is obtained with a unique impeller attached to a hollow stirring shaft through which gases are continuously recirculated from the head space above the liquid through the impeller into the liquid phase as shown in Fig. 2.13. Gas entrainment impellers operate best in the 1000 - 1200 rpm range.

Figure 2.13: Gas entrainment impeller.

2.7.1 Anchor impeller

Impeller is the portion of the agitator imparting force to the material being mixed. The anchor impeller is a double-armed agitator in the form of an anchor as shown in Fig. 2.14. The impeller sheet is adapted near wall and ground shape. The primary promotion direction is tangential. The speed of the anchor is in the range between 1 and 5 m/s [61].

Mixing with anchor impellers is widely used for viscous fluids to avoid the stagnation of the products (if there is mixing with reaction) at the vessel walls, since the blades of the stirrer work as a scraper [8]. Many industries employ anchor impellers for mixing of viscous and polymer solution which are pseudo-plastic fluids [74]. Many of them are reacted in vessels agitated with anchor impellers. So the knowledge of how flow is generated in these systems has become increasingly important. Also, the knowledge of viscosity development and increase during the reaction due to the formation of more viscous product and its effect on the flow field and velocity field is of great interest [138] [139]. The anchor impeller induces a tangential liquid movement and is installed with a low wall clearance.

Figure 2.14: Anchor impeller.

The advantages of the anchor impeller are following [39]:

(1) Ideally suited for high viscosity products.

(2) Good cleaning of impeller during emptying of vessel.

(3) Clockwise or counterclockwise operation for solids incorporation / degassing.

(4) Applications: e.g. Polymerisations, cosmetics, ointments, food preparations and lubrication grease.

The velocity field around the stirrer, received from measurements, is given as boundary condition at the stirrer sheets; the tangential speed is given according to the number of revolutions. Tabs. 2.1 and 2.2 show the standard design and working area of the anchor impeller respectively [82].

Table 2.1: Limitations of using standard anchor impeller.

Designation	Geometry arrangement	Installation	Primary flow
Anchor impeller (s. Fig. 2.14)	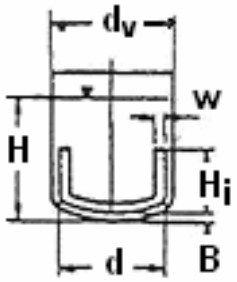 $H/d_v = 1.000$ $d/d_v = 0.960$ $B/d_v = 0.025$ $H_i/d = 0.480$ $w/d_v = 0.060$	Centrically	Tangential

Table 2.2: Work area and tasks of stirring.

d/d_v	Tip velocity [m/s]	Re	Kind of flow	Viscosity η [Pa s]
0.9 - 0.98	1 - 5	$Re > 10^2$	Laminar, Transition and turbulent	$\eta < 20$

Anchor impellers are available in several configurations for use with moderate to high viscosity materials. This type of impellers usually works best in vessels with an inside depth to diameter ratio of 1.5 to 1 or less. They are intended to operate at relatively slow speeds and generally require a heavy duty drive system capable of generating and delivering sufficient torque to the stirrer. Three basic types are shown in Fig. 2.15 [63]:

U-shaped flat bar anchor | **Flat blade paddle type anchor** | **Three-arm anchor with wiper blades**

Figure 2.15: Basic types of anchor impeller.

Murthy et al. [71] showed that the design of anchor impellers is based on an assumed linear relation between shear rate and the rotation speed of the impeller. It is shown that while the shear rate varies greatly within the mixing vessel, there exists a linear relationship between the impeller speed and the local shear rate near the tip of the impeller. The proportionality constant temperature associated with this linear relation is found to be dependent on the geometric parameters of the system, but is largely independent of the flow behavior index.

Peixoto et al. [8] gave a detailed description of the flow generated by this axial impeller with a view to indicate ways in which the design and operation of these systems can be improved.

2.8 Semibatch and batch mixing modes

Industrial mixers use a shaft, screw, blades, ribbons, impellers or propellers to mix industrial materials such as adhesives, chemicals, construction materials, minerals, coatings and paints. They are also used in food, beverage, pharmaceutical, and water treatment applications. Industrial

mixers force sediment to flow in one direction and can intensify physical and chemical processes. Most industrial mixers have three modes: batch, semibatch and continuous-feed. With continuous-feed industrial mixers, the media to mix is added continuously as mixed fluid is removed. Continuous mixers are suitable for production applications because they can run for long periods of time without being shut down [61].

The reasons for the type of reactor choice include [75]:

(1) *Complete conversion*: Reactions are generally run to achieve complete conversion of the limiting reagent-controlled by time and not subject to differences in completeness of conversion because of residence time distribution in a continuous stirred tank reactor.

(2) *Accuracy of charge*: Reagent quantities can be carefully controlled and procedures for over checks of quantities actually utilized.

(3) *Productivity*: Reactor volume is often consistent with the limited productivity requirements characteristic of this industry.

(4) *Flexibility*: Batch reactors can process a large variety of homogeneous and heterogeneous reactions successfully with little modification of internals and can be used in dedicated or multipurpose facilities. The uses of variable speed drives along with versatile impellers are key factors.

2.8.1 Semibatch operation

Semibatch reactors are very common in the specialty chemical and pharmaceutical manufacturing industries to accomplish mixing tasks [75]. Semibatch operations are typically carried out in standard type of stirred mixing vessel in both homogeneous and heterogeneous applications, although special provision is often required for fast and/or heterogeneous reactions. Their use is very flexible in that they can be quickly reconfigured

for various types of chemical reactions needed in a series of chemical synthesis steps. The blending in semibatch operation is done by feeding a particularly reactive reagent later or slower in a region of high energy dissipation, the reactant that starts in the reactor is always the limiting reactant [66]. The reactions can be forced along a more desirable path, producing a better yield of desired products. If the chemical reaction is fast enough to proceed during the addition of a chemical reactant or a catalyst, the mode is actually semibatch, and mixing effects may be present [89].

2.8.1 Batch operation

Batch mixing is the simplest mode of operation. The industrial mixer is filled with media and product mixing is allowed to proceed [153]. When mixing is complete, the vessel's contents are emptied for downstream processing. The industrial mixer is then cleaned and refilled for mixing another batch. Batch mixing of viscous fluids is widely used in the chemical and food industry, the process requires a large amount of time and energy to achieve good end product quality. If the chemical reaction is too slow, the mode is actually batch [90]. The batch reactor is very useful to investigate a wide variety of chemical reactions, particularly oscillatory reactions. The advantages of the batch process like high flexibility towards different recipes and operation procedures and the possibility to reach high conversions. It is common operation in latex producing industry. The disadvantages of batch reactors in processing should also be noted [75]:

(1) *Reaction medium*: There may exist nonuniformity of mixing intensity throughout the vessel that can lead to undesirable side reactions caused by variations in local concentrations.

(2) *Optimum conditions*: One of a reaction system may require different

conditions than another which may overlap in time (i.e., a reaction that results in precipitation of a product or by-product may require different mixing intensities for the reaction and precipitation).

(3) *Heat transfer*: High rates of heat transfer are not achievable without external pumping through a heat exchanger or by utilization of unwieldy internal coils. In these systems, heat transfer is often achieved by operating at reflux and using an external condenser to remove the heat.

(4) *Thermal hazards*: A large volume of a reacting system with highly exothermic reactions can produce large thermal hazards.

2.9 Computational fluid dynamics (CFD)

It is a computer based tool for simulating the behavior of systems involving fluid flow, heat transfer, and other related physical processes. Fluid (gas and liquid) flows are governed by partial differential equations (Navier-Stokes equations) which represent conservation laws for the mass, momentum, and energy. CFD is the method of replacing such PDE (Partial differential equations) systems by a set of algebraic equations which can be solved using digital computers. These equations are solved over a region of interest, with specified conditions on the boundary of that region [86] [102].

2.9.1 Developments

Computers have been used to solve fluid flow problems for many years. Numerous programs have been written to solve either specific problems, or specific classes of problem. From the mid-1970's the complex mathematics required to generalize the algorithms began to be understood, and general purpose CFD solvers were developed. These began to appear in the early 1980's and required powerful computers as well as knowledge of fluid

dynamics, and large amounts of time to set up simulations. Consequently, CFD was a tool used almost exclusively in research [122].

Recent advances in computing power, together with powerful graphics and interactive three dimensions manipulation of models have made the process of creating a CFD model and analyzing results much less labor intensive, reducing time and hence cost. Advanced solvers contain algorithms which enable right solution of the flow field in a reasonable time. As a result of these factors, Computational Fluid Dynamics is now an established industrial design tool, helping to reduce design timescales and improve processes throughout the engineering world. CFD provides a cost effective and accurate alternative to scale model testing, with variations on the simulation being performed quickly, offering obvious advantages [102].

2.9.2 Applications

CFD provides a qualitative (and sometimes even quantitative) prediction of fluid flows by means of [124]:

(1) Mathematical modeling (partial differential equations).

(2) Numerical methods (discretisation and solution techniques).

(3) Software tools (solvers, pre- and postprocessing utilities).

CFD enables scientists and engineers to perform numerical experiments (computer simulations) in a real experiment CFD simulation. It is attractive for two reasons. Firstly, the desire to be able to model physical fluid phenomena that cannot be easily simulated or measured with a physical experiment, for example weather systems or hypersonic aerospace vehicles. Secondly, the desire to be able to investigate physical fluid systems more cost effectively and more rapidly than with experimental methods [35] [36].

CFD computer codes, both commercial and in-house are now considered to be standard numerical tools, widely utilized within industry for design and development. Numerical simulations of fluid flow will enable [24] [34] [40] [131]:

(a) Architects to design comfortable and safe living environments.

(b) Designers of vehicles to improve the aerodynamic characteristics.

(c) Chemical engineers to maximize the yield from their equipment.

(d) Petroleum engineers to devise optimal oil recovery strategies.

(e) Surgeons to cure arterial diseases (computational hemodynamics).

(f) Meteorologists to forecast the weather and warn of natural disasters.

(g) Safety experts to reduce health risks from radiation and other hazards.

2.9.3 Analysis steps

The following steps are used by CFD for analysis and investigation problems in a wide variety of applications [15] [16]:

(1) Problem statement information about the flow.

(2) Mathematical model.

(3) Mesh generation nodes/cells, time instants.

(4) Space discretisation coupled ordinary differential equations systems.

(5) Time discretisation algebraic system.

(6) Iterative solver discrete function values.

(7) CFD software implementation.

(8) Simulation runs parameters, stopping criteria.

(9) Post processing visualization, analysis of data.

(10) Verification model, validation / adjustment.

2.9.4 Mathematical model

A mathematical model is used to describe the process as in the following:

(1) Choose a suitable flow model and reference frame.

(2) Identify the forces which cause and influence the fluid motion.

(3) Define the computational domain in which to solve the problem.

(4) Formulate conservation laws for the mass, momentum, and energy.

(5) Simplify the governing equations to reduce the computational effort:

(a) Use available information about the flow regime.

(b) Check for symmetries and predominant flow directions.

(c) Neglect the terms which have little or no influence on the results.

(d) Model the effect of small scale fluctuations that cannot be captured.

(e) Incorporate knowledge of the measurement data and CFD results.

(6) Add constitutive relations and specify initial/boundary conditions.

2.9.5 Numerics

The set of equations which describe the processes of momentum, heat and mass transfer are known as the Navier Stokes equations. These partial differential equations were derived in the early nineteenth century and have no known general analytical solution but can be discretised and solved numerically [92]. Equations describing other processes, such as combustion, can also be solved in conjunction with the Navier Stokes equations [91]. Often, an approximating model is used to derive these additional equations, turbulence models being a particularly important example. There are a number of different solution methods which are used in CFD codes [93]. The most common and the one on which CFX is based, is known as the finite volume technique. In this technique, the region of interest is divided into small sub-regions, called control volumes. The equations are discretised

and solved iteratively for each control volume. As a result, an approximation of the value of each variable at specific points throughout the domain can be obtained. In this way, a full picture of the behavior of the flow can be derived [102].

2.9.5.1 Discretisation method

After selecting the mathematical model, a suitable discretisation method should be chosen, i.e. a method of approximating the differential equations by a system of algebraic equations for the variables at some set of discrete locations in space and time. There are many approaches, but the most important of which are: finite difference (FD), finite volume (FV) and finite element (FE) methods. Other methods, like spectral schemes, boundary element methods, and cellular automata are used in CFD but their use is limited to special classes of problems. Each type of method yields the same solution if the grid is very fine. However, some methods are more suitable to some classes of problems than others. The preference is often determined by the attitude of the developer [51].

2.9.5.1.1 Finite difference method

This is the oldest method for numerical solution of PDE's has been introduced by Euler in 18th century. It is also the easiest method to use for simple geometries. The starting point is the conservation equation in differential form. The solution domain is covered by a grid. At each grid point, the differential equation is approximated by replacing the partial derivatives by approximations in terms of the nodal values of the functions. The result is one algebraic equation per grid node, in which the variable value at this node and a certain number of neighbor nodes appear as

unknowns. The FD method can be applied to any grid type; it has been applied to structured grids. The grid lines serve as local coordinate lines. Taylor series expansion or polynomial fitting is used to obtain approximations to the first and second derivatives of the variables with respect to the coordinates. On structured grids, the FD method is very simple and effective. It is especially easy to obtain higher order schemes on regular grids. The disadvantage of FD methods is that the conservation is not enforced unless special care is taken. Also, the restriction to simple geometries is a significant disadvantage in complex flows [51].

2.9.5.1..2 Finite element method

The FE method is similar to the FV method in many ways. The domain is broken into a set of discrete volumes or finite elements that are generally unstructured; in two dimensions, they are usually triangles or quadrilaterals, while in three dimensions, tetrahedral or hexahedra are most often used. The distinguishing feature of FE methods is that the equations are multiplied by a weight function before they are integrated over the entire domain. In the simplest FE methods, the solution is approximated by a linear shape function within each element in a way that guarantees continuity of the solution across element boundaries. Such a function can be constructed from its values at the corners of the elements. The weight function is usually of the same form. This approximation is then substituted into the weighted integral of the conservation law and the equations to be solved are derived by requiring the derivative of the integral with respect to each nodal value to be zero; this corresponds to selecting the best solution within the set of allowed functions (the one with minimum residual). The result is a set of non-linear

algebraic equations. An important advantage of finite element methods is the ability to deal with arbitrary geometries [51].

2.9.5.1.3 Finite volume method

The FV method uses the integral form of the conservation equations as its starting point. The solution domain is subdivided into a finite number of continuous control volumes, and the conservation equations are applied to each control volume. At the centroid of each control volume lies a computational node at which the variable values are to be calculated. Interpolation is used to express variable values at the control volume surface in terms of the nodal (control volume-center) values. Surface and volume integrals are approximated using suitable quadrate formula. As a result, an algebraic equation is obtained for each control volume, in which number of neighbor nodal values appear. The FV method can accommodate any type of grid, so it is suitable for complex geometries. The grid defines only the control volume boundaries and need not be related to a coordinate system. The method is conservative by construction, so long as surface integrals (which represent convective and diffusive fluxes) are the same for the control volume sharing the boundary. The FV approach is the simplest to understand and to program. All terms that need be approximated have physical meaning which is why it is popular with engineers. The disadvantage of FV methods compared to FD schemes is that methods of order higher than second are more difficult to develop in three dimensions. This is due to the fact that the FV approach requires two levels of approximation: interpolation and integration [51].

2.9.5.2 Iterative solution strategy

The coupled nonlinear algebraic equations must be solved iteratively [130]:

(1) Outer iterations: the coefficients of the discrete problem are updated using the solution values from the previous iteration so as to:
   (a) Get rid of the nonlinearities by a Newton-like method.
   (b) Solve the governing equations in a segregated fashion.

(2) Inner iterations: the resulting sequence of linear sub problems is typically solved by an iterative method (conjugate gradients, multigrid) because direct solvers (Gaussian elimination) are expensive.

(3) Convergence criteria: it is necessary to check the residuals, relative solution changes and other indicators to make sure that the iterations converge.

As a rule, the algebraic systems to be solved are very large (millions of unknowns) but sparse, i.e., most of the matrix coefficients are equal to zero.

2.9.5.3 Uncertainty and error

Whether or not the results of a CFD simulation can be trusted depends on the degree of uncertainty and on the cumulative effect of various errors [130]:

(1) Uncertainty is defined as a potential deficiency due to the lack of knowledge (turbulence modeling is a classical example).

(2) Error is defined as a recognizable deficiency due to other reasons:
   (a) Acknowledged errors have certain mechanisms for identifying, estimating and possibly eliminating or at least reducing them.

(b) Unacknowledged errors have no standard procedures for detecting them and may remain undiscovered causing a lot of harm.

(c) Local errors refer to solution errors at a single grid point or cell.

(d) Global errors refer to solution errors over the entire flow domain.

Local errors contribute to the global error and may move throughout the grid. The acknowledged errors are classified as:

(1) Physical modeling error due to uncertainty and simplifications.

(2) Discretisation error approximation of PDEs by algebraic equations:

(a) Spatial discretisation error due to a finite grid resolution.

(b) Temporal discretisation error due to a finite time step size.

(3) Iterative convergence error which depends on the stopping criteria.

(4) Round-off errors due to the finite precision of computer arithmetic Unacknowledged errors.

(5) Computer programming error due to coding and logical mistakes.

(6) Usage error: wrong parameter values, models or boundary conditions.

Knowledge of these error sources and an ability to control the error are important prerequisites for developing and using CFD software.

2.9.5.4 Verification of CFD codes

Verifications (i.e. if the equations are solved right) to looking for errors in the implementation of the models are done through [130]:

(1) Examine the computer programming by visually checking the source code, documenting it and testing the underlying subprograms individually.

(2) Examine iterative convergence by monitoring the residuals, relative changes of integral quantities and checking if the prescribed tolerance is attained.
(3) Examine consistency (check if relevant conservation principles are satisfied).
(4) Examine grid convergence: as the mesh and/or the time step are refined, the spatial and temporal discretization errors, respectively, should approach zero (in the absence of round-off errors).
(5) Compare the computational results with analytical and numerical solutions for standard configurations (representative test cases).

2.9.5.5 Validation of CFD models

Validations (i.e. if the right equations are solved) to check if the model itself is suitable for practical purposes are done by [94] [95] [130]:

(1) Verify the code to make sure that the numerical solutions are correct.
(2) Compare the results with available experimental data to check if the reality is represented accurately enough.
(3) Perform sensitivity analysis and a parametric study to assess the inherent uncertainty due to the insufficient understanding of physical processes.
(4) Try using different models, geometry, and initial/boundary conditions.
(5) Report the findings, document model limitations and parameter settings.

The goal of verification and validation is to ensure that the CFD code produces reasonable results for a certain range of flow problems.

2.9.6 Simulation by CFX-10 software

The process of performing a single CFD simulation is split into four components:

There are many CFD software packages are based on this simulation structure like CFX-10 software [102].

2.9.6.1 Introduction

CFX-10 is a general purpose Computational Fluid Dynamics (CFD) code, combining an advanced solver with powerful pre and post-processing capabilities. CFX-10 includes the following features [102]:

(1) An advanced coupled solver which is both reliable and correct.

(2) Full integration of problem definition, analysis and results presentation.

(3) An intuitive and interactive setup process, using advanced graphics.

(4) Detailed online help.

2.9.6..2 Structure

CFX-10 consists of five software modules which are linked by the flow of information required to perform a CFD analysis [102]:

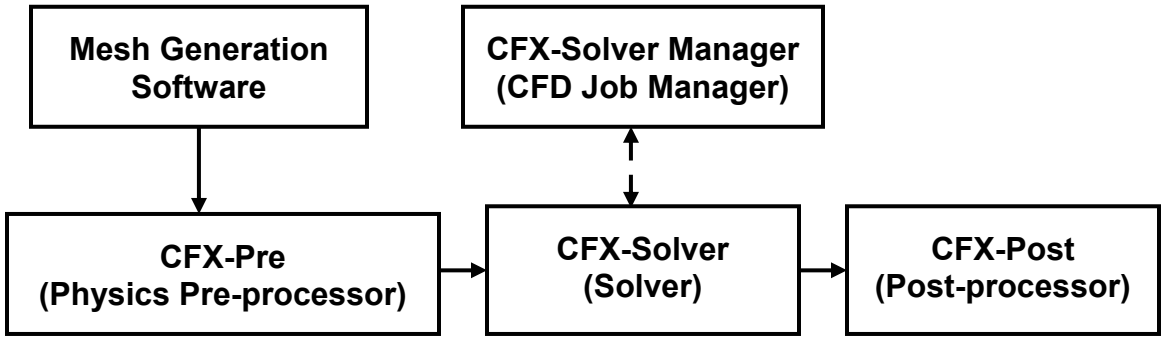

CFX-10 is capable of modeling steady-state and transient flows, laminar and turbulent flows, subsonic, transonic and supersonic flows, heat transfer and thermal radiation, buoyancy, non-Newtonian flows, transport of non-reacting scalar components, multiphase flows, combustion, flows in multiple frames of reference and particle tracking.

2.9.6.2.1 Geometry and mesh generation

This interactive process is the first pre-processing stage. The objective is to produce a mesh for input to the physics pre-processor. Before a mesh can be produced, a closed geometric solid is required. The geometry and mesh can be created by using ICEM CFD or any of the other geometry/mesh creation tools. The basic steps involve [102]:

(1) Defining the geometry of the region of interest.

(2) Creating regions of fluid flow, solid regions and surface boundary names.

(3) Setting properties for the mesh.

Different types of grids can be generated with CFX [20]:

(a) *Structured grid*: It is defined as a mesh where all the nodes have the same number of elements around it. This makes that the matrix of algebraic equations system has a regular structure. There are a large number of efficient solvers applicable only to structured grids. Disadvantages are only for geometrically simple domains, difficult to control distribution of grid points.

(b) *Unstructured grid*: For very complex geometries, can fit arbitrary boundaries. Grids made of triangles or quadrilaterals in two dimensions and tetrahedral or hexahedra in three dimensions are the most often used. Such grids can be generated automatically by existing algorithms.

Disadvantages are irregularity of the data structure. The solvers for the algebraic equation system are usually slower than those for structured grids. Development of unstructured and hyprid meshing techniques has allowed the representation of more complicated geometries often found in laminar flow mixing [1].

(c) *Block-structured grid*: It is a structured grid inside each block, but the order of blocks is irregular.

2.9.6.2.1.1 Cell types

There are four types of elements, which are identified by the number of nodes: Tetrahedrons (4 nodes), pyramids (5 nodes), wedges or prisms (6 nodes) and hexahedrons (8 nodes). The vertex ordering for the elements follows Patron Neutral File element conventions, and is shown in Fig. 2.16 [103].

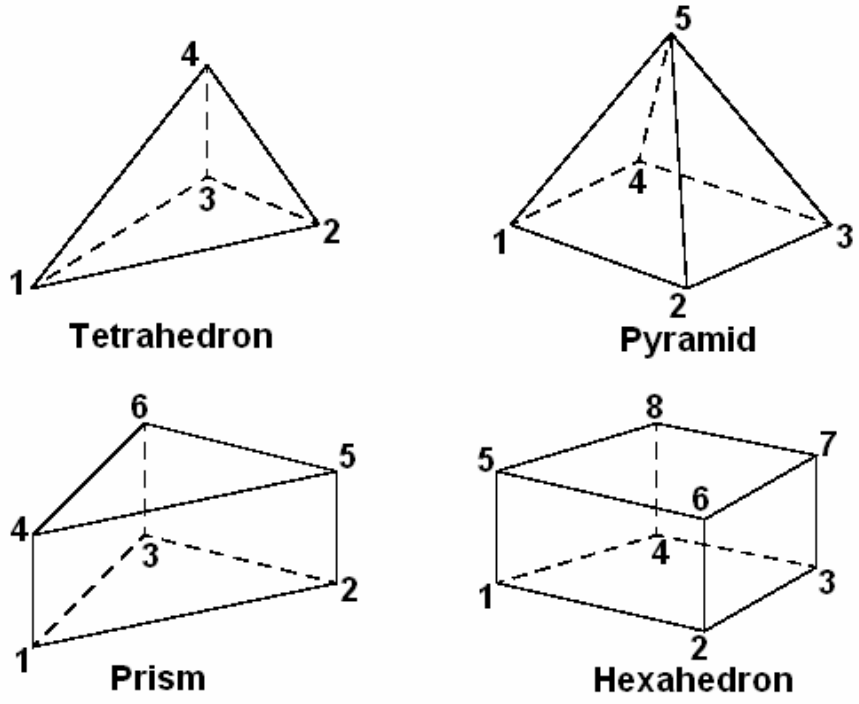

Figure 2.16: Cell types and vertex ordering.

2.9.6.2.2 CFX-pre

This interactive process is the second pre-processing stage and is used to create input required by the solver. It is the physics definition pre-processor part of CFX-10. It is used to import meshes produced in mesh generation software packages and to select physical models used in the CFD simulation [88]. Flow physics, fluid properties, initial values and solver parameters are specified in CFX-pre. A full range of boundary conditions, including inlets, outlets and openings, together with boundary conditions for heat transfer models and periodicity are all available in CFX-pre which has different modes of operations [102]:

(1) *General*: this can be used for all cases.

(2) *Turbo*: It simplifies the set up of some turbomachinery simulations.

(3) *Quick setup*: this provides fewer model options and is suitable for more simple cases. It allows setting up simple physics cases very quickly.

(4) *Model library*: It is used to import predefined library files for more complex simulations. This will set up the physics required for a particular case.

2.9.6.2.3 CFX-solver

The solver is the component which solves the CFD problem. It produces the required results in a non-interactive/batch process. The CFD problem is solved as follows:

(1) The partial differential equations are integrated over all the control volumes in the region of interest. This is equivalent to applying a basic conservation law (e.g. for mass or momentum) to each control volume.

(2) These integral equations are converted to a system of algebraic equations by generating a set of approximations for the terms in the integral equations.
(3) The algebraic equations are solved iteratively.

An iterative approach is required because of the non-linear nature of the equations and as the solution approaches the exact solution it is said to converge. For each iteration, an error or residual is reported as a measure of the overall conservation of the flow properties. How close the final solution is to the exact solution depends on a number of factors, including the size and shape of the control volumes and the size of the final residuals. The solver produces a results file which is then passed to the post-processor. CFX-solver solves all the solution variables for the simulation for the problem specification generated in CFX-pre [102].

2.9.6.2.3.1 Manager

The CFX-solver manager is a part that provides greater control to manage the CFD task, it is a graphical user interface that allows setting attributes for the CFD calculation, controlling the CFX-solver interactively, and viewing information about the emerging solution. Its major functions are [102] [107]:
(1) Specify the input files to the CFX-solver.
(2) Start/stop the CFX-solver.
(3) Monitor the progress of the solution.
(4) Set up the CFX-solver for a parallel calculation.

2.9.6.2.3.2 Modeling

Descriptions of more advanced physical models and how the basic models extend to more complex cases are provided in modeling multiphase flow, turbulence, domain interface, particle transport, combustion, radiation and real fluid properties [101].

2.9.6.2.3.3 Numerical discretisation

Analytical solutions to the Navier-Stokes equations exist for only the simplest of flows under ideal conditions. To obtain solutions for real flows a numerical approach must be adopted whereby the equations are replaced by algebraic approximations which may be solved using a numerical method. The domain is discretised into finite control volumes using a mesh. The governing equations are integrated over each control volume and solved with the initial and boundary conditions. Resolution of the algebraic equations is carried out using high resolution advection and second order backward Euler transient schemes. Fig. 2.17 shows a typical mesh in two-dimension on which one surface of the finite volume is represented by the shaded area; each node is surrounded by a set of surfaces which contain the finite volume. All the solution variables and fluid properties are stored at the element nodes [100].

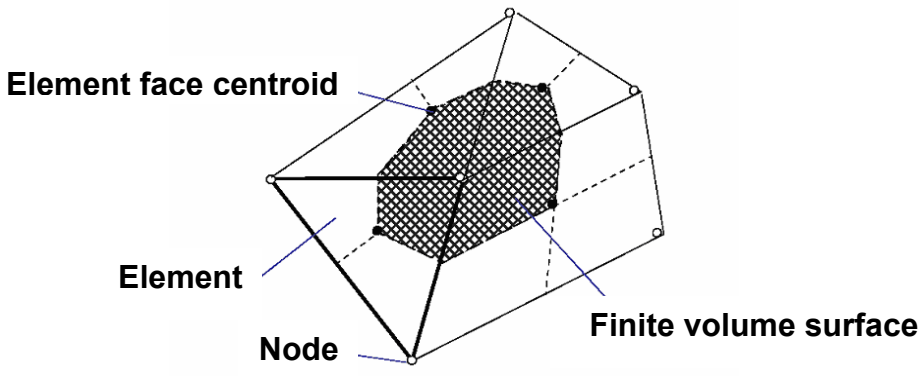

Figure 2.17: Finite volume surface.

2.9.6.2.3.4 Coupled solver

It is one of the most important features of CFX-10 in which all the hydrodynamic equations are solved as a single system simultaneously. The coupled solver is faster than the segregated solver and less iteration are required to obtain a converged flow solution [102]. This solution approach uses a fully implicit discretisation of the equations at any given time step.

The linear sets of equations that arise by applying the finite volume method to all elements in the domain are discrete conservation equations. The system of equations can be written in the form:

$$\sum_{nb_i} a_i^{nb} \phi_i = b_i \,. \tag{2-13}$$

Where ϕ_i is the variable vector, b here is the solution, a is the coefficient matrix of the equation, i here is the identifying number of the finite volume or node in question, and nb is the central coefficient multiplying the solution at the ith location. This method is applicable to both structured and unstructured meshes. The set of these, for all finite volumes constitutes the whole linear equation system. For the coupled, three dimensions mass-momentum equation set, they can be expressed as (4 x 4) matrix and (4 x 1) vector as in the following:

$$a_i^{nb} = \begin{bmatrix} a_{uu} & a_{uv} & a_{uw} & a_{up} \\ a_{vu} & a_{vv} & a_{vw} & a_{vp} \\ a_{wu} & a_{wv} & a_{ww} & a_{wp} \\ a_{pu} & a_{pv} & a_{pw} & a_{pp} \end{bmatrix}_i^{nb} \quad \text{and} \quad \phi_i = \begin{bmatrix} u \\ v \\ w \\ p \end{bmatrix}_i \quad , \quad b_i = \begin{bmatrix} b_u \\ b_v \\ b_w \\ b_p \end{bmatrix}_i$$

The advantages of such a coupled treatment over a non-coupled or segregated approach are efficiency, generality and simplicity. These advantages all combine to make the coupled solver an extremely powerful feature of any CFD code.

2.9.6.2.4 CFX-post

It is a flexible interactive post-processor graphics tools for CFX-10. It is designed to allow easy visualization, analyzing, presenting and quantitative post-processing the results of CFD simulation. Post-processing includes anything from obtaining point values to complex animated sequences. Examples of some important features of post-processors are [102] [108]:

(1) Visualization of the geometry and control volumes.

(2) Vector plots showing the direction and magnitude of the flow.

(3) Visualization of the variation of scalar variables which have only magnitude not direction such as temperature and velocity in the domain.

(4) Visualization for representation of numbers of images:

  (a) One dimension: function values connected by straight lines.

  (b) Two dimensions: streamlines, contour levels, color diagrams.

  (c) Three dimensions: cutlines, cutplanes, isosurfaces and isovolumes.

  (d) Arrow plots, particle tracing and animations.

(5) Quantitative numerical calculations.

(6) Charts showing graphical plots of variables and hardcopy output.

(7) Calculation of derived quantities such as stream function and vorticity.

(8) Calculation of integral parameters like lift, drag and total mass.

(9) Systematic data analysis by means of statistical tools.

(10) Verification and validation of the CFD model.

3. EXPERIMENTS

Mixing of liquids of different densities and different viscosities is carried out in a non-baffled glass SBR and glass BR with anchor impeller at a constant temperature. The effect of the dosage time in a SBR mixing process and the total liquid mixture height or total liquid volume in a BR mixing process on the transient mixing behavior is studied. The dynamic mixing of the used liquids is characterized by measuring the mixing time and the transient mixture viscosities. These measurements are done by applying a torque method and decolorisation reaction, respectively.

3.1 Mixture components

Glycerol is a colorless, odorless, hygroscopic, and sweet-tasting viscous liquid. It is a sugar alcohol and has three hydrophilic alcoholic hydroxyl groups (-OH) that are responsible for its solubility in water [60].

Ethanol is a flammable, tasteless and colorless. At the molecular level, liquid ethanol consists of hydrogen-bonded pairs of ethanol molecules; this phenomenon makes ethanol more viscous and less volatile than less polar organic compounds of similar molar mass. Ethanol is miscible with water and with most organic liquids, including nonpolar liquids such as aliphatic hydrocarbons [59]. The physical properties of glycerol and ethanol which are used in the experimental work are shown in Tab. 3.1.

Table 3.1: Some physical properties of the mixture components [47].

	$\rho_{21\,°C}$ [kg/m^3]	$\eta_{99.5\%,\,21\,°C}$ [Pa s]
Glycerol	1261.256	1.361880
Ethanol	788.560	0.001182

3.2 Experimental setup for SBR and BR

A cylindrical vessel made of glass with a rounded bottom is used. This vessel has a diameter of d_v = 0.2 m and height of H = 0.2 m. The anchor impeller has a diameter of d = 0.192 m, a thickness of k = 0.002 m and a width of w = 0.012 m. The sizes of the SBR, BR and the anchor impeller are shown in Fig. 3.1.

Vessel diameter	d_v	0.200 m
Vessel height	H	0.200 m
Liquid mixture height	H_l	0.140 m
Impeller diameter	d	0.192 m
Impeller height	H_i	0.087 m
Blade width	w	0.012 m
Blade thickness	k	0.002 m
Shaft diameter	S	0.010 m
Bottom clearance	B	0.005 m
Wall clearance	C	0.004 m
Inlet tube diameter	d_t	0.050 m

H/d_v = 0.200 m / 0.200 m = 1.000

d/d_v = 0.192 m / 0.200 m = 0.960

B/d_v = 0.005 m / 0.200 m = 0.025

H_i/d = 0.087 m / 0.192 m = 0.453

w/d_v = 0.012 m / 0.200 m = 0.060

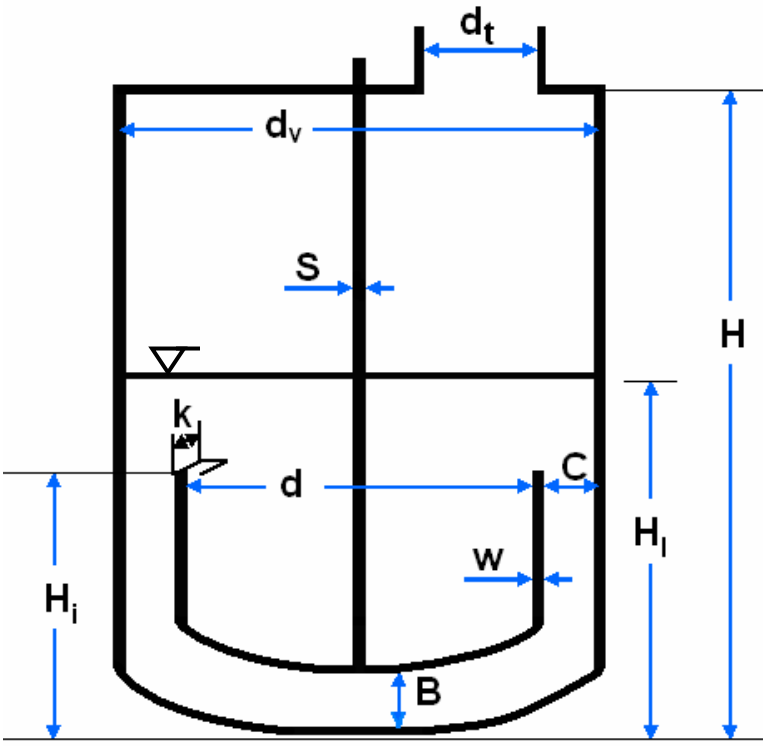

Figure 3.1: The geometric sizes of the SBR, BR and the anchor impeller with the ratios of the vessel to the anchor impeller sizes.

The shaft of the anchor is connected to the torque meter (M) which is also connected to the PC monitor to be able to read the torque values of the anchor impeller in the units of [mV] with time. The list of equipments is:

1. A glass cylindrical vessel with a rounded bottom (6 L).
2. An anchor impeller (s. Fig. 3.1) is manufactured at the Institute of Chemical Engineering (Universität Duisburg-Essen).

3. An electrical motor (Janke & Kunkel IKA-Labortechnik RE 162, 10 – 1600 1/min, made in Germany).
4. A control box (Janke & Kunkel IKA-Labortechnik RE 162 Analog, 10 – 1600 1/min, made in Germany).
5. A pump (EHEIM, type: 1030, made in Germany) has a maximum height of 4 m and volumetric flow rate of 22 L/min.
6. A Resistance Temperature Detector (RTD) (Jumo, Pt 100, made in Germany).
7. A thermostat (Julabo, type: F25 (MH), made in Germany).
8. A water bath.
9. A personal computer (PC).
10. A digital video camera (Panasonic, NV-GS280, 800,000 pixel, made in Japan).
11. A light source (500 W, home made).
12. A white screen.
13. Glass cylinders, beakers, glass rod, volumetric flasks and funnel.

3.3 Methods of measurement in SBR and BR

3.3.1 Torque method

For the torque method, a calibration curve of the pure glycerol is done. This curve represents a connection between the measured voltage and viscosity to determine the time dependent viscosity and mixing time.

3.3.1.1 Voltage / Viscosity calibration curve

A calibration curve of the pure glycerol is an important step for the viscosity measurements using the torque method to make a connection between the measured voltage and the viscosity. The viscosity values for

calibration are taken from the literature [47] in the temperature range between 10 °C and 50 °C.

A batch glass vessel (6 L) is used to stir a mass of pure glycerol 2.45 L (3089 g) with anchor impeller. This vessel as shown in Fig. 3.2 is inserted into a water bath to keep the temperature of the pure glycerol constant. The temperature is controlled by using thermostat (T), which is connected with thermocouple inside the stirred vessel.

The torque of the impeller is measured by using a voltmeter which is connected to the impeller shaft. The voltage (blank) value –which is determined when the impeller is rotating in the empty vessel–, is 154.1 mV. In each run, the temperature is adjusted to the desired value, for example ϑ = 50 °C. The stirrer velocity is adjusted to 150 rpm, and then the mixing process started until the voltage reading reached a constant value. This value corresponds to the glycerol viscosity value which is taken from the literature [47] at the same adjusted temperature. The same procedure is carried out for other temperatures in the range between 10 °C and 50 °C. As a result, for each temperature, there is a viscosity value in mPa s and a torque value in mV. A calibration curve is established by measuring of a well known viscosity solution.

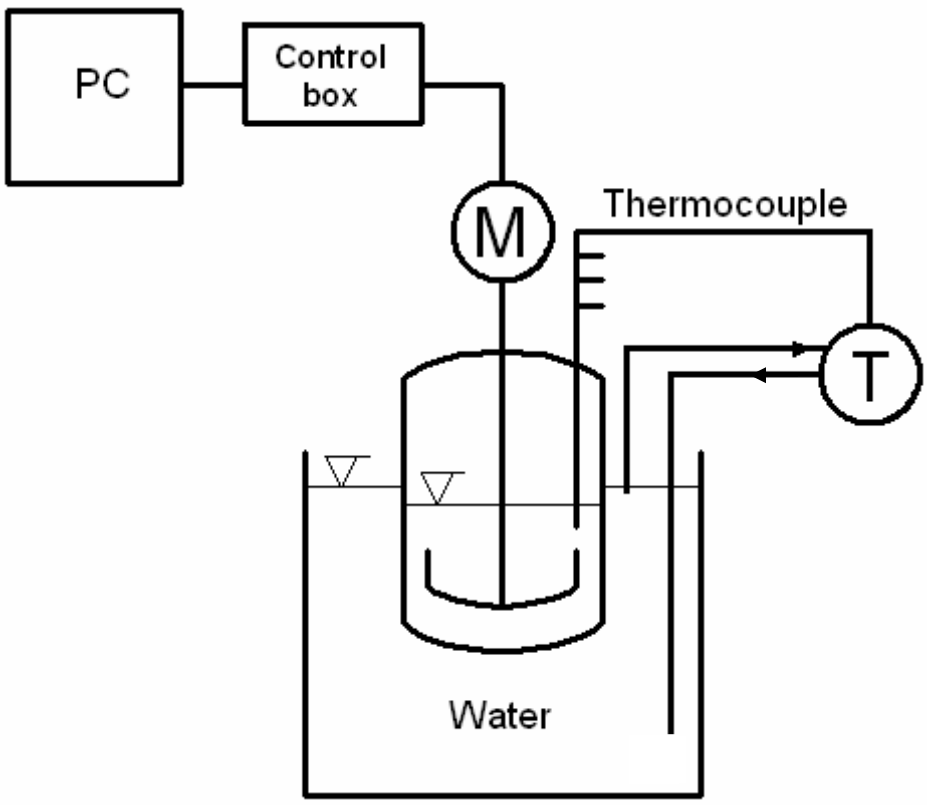

Figure 3.2: Experimental setup for the determination of the Voltage / Viscosity calibration curves.

3.3.2 Decolorisation method

The mixing time is measured by a decolorisation method. This test is done by coloring the sugar solution (64%) with 0.1 n of iodine solution (brown), and then the anchor stirrer starts the rotation at 150 rpm. Measuring the mixing time begins when a stoichiometric quantity of 0.1 n sodium thiosulfate solution is added to the sugar solution. When the color of the sugar solution disappears and a colorless solution is obtained, the mixing time is determined. The mixing time is determined for different anchor velocities. Also, different concentrations of iodine solutions are used to record the best decolorisation.

3.4 The procedure of mixing process in SBR

The experimental setup of SBR at different dosage times is shown in Fig. 3.3.

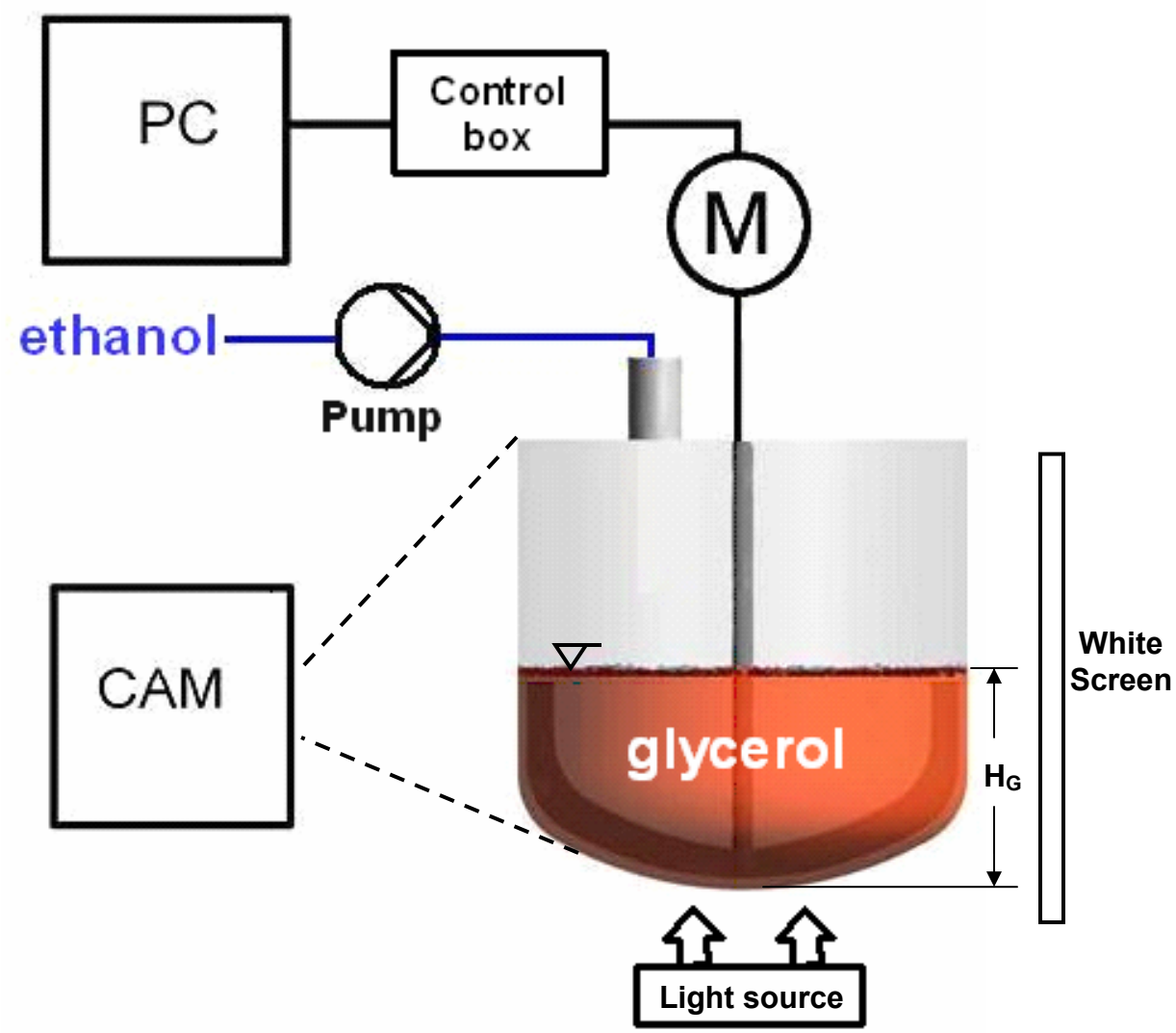

Figure 3.3: The experimental setup for the mixing process in a glass SBR at different dosage times to determine the mixing time and the transient mixing behavior.

3.4.1 t_d = 5 s (26 vol% ethanol)

This experiment is carried out according to the torque and decolorisation methods as the following steps:

(1) Put volume of glycerol 2.45 L (3089 g) at ϑ = 21 °C in the SBR, the initial height of the glycerol is H_G = 0.1 m.
(2) Add 3 ml of 0.1 n iodine solution using a syringe into glycerol.
(3) Switch on the anchor impeller at a constant velocity of ω = 150 rpm to mix the iodine solution with glycerol. A yellow solution is obtained.
(4) A volume of ethanol 0.909 L (709 g) is mixed with 3 ml of 0.1 n sodium thiosufate in a separate vessel (colorless solution). A centrifugal pump which is connected to the SBR is calibrated based on the used ethanol volumetric flow rate of 0.1818 L/s at t_d = 5 s.
(5) The time switch clock is adjusted to the required dosage time.
(6) While the anchor is rotating, switch on the centrifugal pump and start the ethanol dosage via the inlet tube which is connected to the pump. In the same time the switch clock starts.
(7) For starting the measurements, the computer begins to record the torque of the anchor impeller in mV as a function of time. Also, the camera is adjusted to visualize the mixing behavior and to recognize the disappearance of the yellow color to become colorless and then the mixing time can be determined.

3.4.2 t_d = 5 s and t_d = 10 s (33 vol% ethanol)

This experiment is carried out according to the torque method. A volume of glycerol 2.45 L (3089 g) at ϑ = 21 °C is stirred with anchor impeller at a constant rotational velocity ω = 150 rpm. A volume of ethanol 1.254 L (978.237 g) and 1.286 L (1003.2 g) for t_d = 5 s and 10 s, respectively is added to the glycerol via an inlet tube which is fixed between the stirrer and the reactor wall. While the anchor is rotating, switch on the centrifugal pump and start the ethanol dosage via the inlet tube which is connected to the

pump. The pump is calibrated to the required ethanol volumetric flow rate for t_d = 5 s is 0.251 L/s and t_d = 10 s is 0.129 L/s A stop watch is used to determine the dosage time. In the same time the computer begins to record the torque of the anchor impeller in mV as a function of time. The mixing time is determined when a constant voltage is obtained.

3.5 The procedure of mixing process in BR

A schematic diagram of the experimental setup for the batch mixing processes is shown in Fig. 3.4.

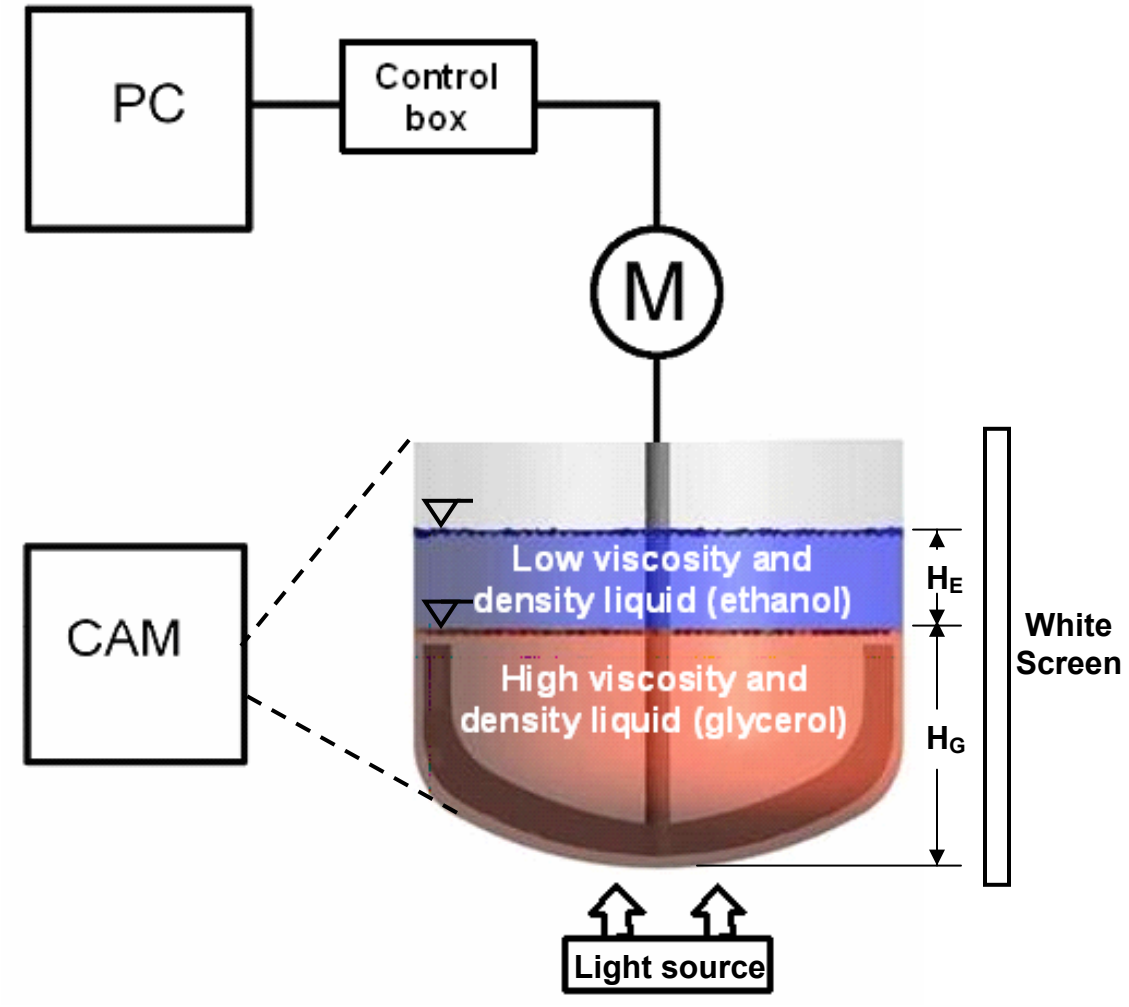

Figure 3.4: The experimental setup for the mixing process in a glass BR for the H_l = 0.14 m to determine the mixing time and the transient mixing behavior.

3.5.1 H_l = 0.14 m and H_l = 0.09 m (33 vol% ethanol)

These experiments are carried out in according to the torque and decolorisation methods as the following steps:

(1) Put the volume of glycerol at ϑ = 21 °C in the BR, the initial height of the glycerol H_G = 0.1 m for the H_l = 0.14 m and H_G = 0.07 m for H_l = 0.09 m. The volumes of glycerol and ethanol which are used in the two batch experiments are shown in Tab. 3.2.

(2) Add 3 ml of 0.1 n iodine solution using a syringe into glycerol.

(3) Stirring the solution in step 2 with the anchor impeller at a constant velocity ω = 150 rpm, a yellow solution was obtained.

(4) A volume of ethanol is mixed with 3 ml of 0.1 n sodium thiosufate solution in a separate vessel (colorless solution).

(5) Ethanol is added carefully with the help of a glass rod on the glycerin surface. Two layers are formed; one for the lighter (ethanol) and the second for the heavier (glycerol).

(6) Switch on the anchor impeller to start the mixing.

(7) For starting the measurements, the computer begins to record the torque of the anchor impeller in mV as a function of time. Also, the camera is adjusted to visualize the mixing behavior and to recognize the disappearance of the yellow color to become colorless and then the mixing time can be determined.

Table 3.2: The masses of ethanol and glycerol which are used in a BR at H_l = 0.14 m and H_l = 0.09 m

	H_l = 0.14 m (33 vol% ethanol)	**H_l = 0.09 m (33 vol% ethanol)**
Glycerol	2.45 L (3089 g)	1.25 L (1575 g)
Ethanol	1.25 L (975 g)	0.62 L (488 g)

3.6 Experimental setup for the visualization of the flow field with a light cut procedure

The experimental setup is shown in Fig. 3.5. This method is used to get a qualitative view of the flow field [27] [37]. Thus one receives a quantitative overview of the distribution of velocity in the agitating vessel from the zone of flow photographs [28] [33]. The batch vessel equipped with anchor impeller is filled with 2.45 L (H_G = 0.1 m) pure glycerol, aluminum powder which has particle sizes between 15 – 25 µm is added to the pure glycerol.

The anchor impeller started the rotation with ω = 150 rpm. A light source (500 W) is fixed under the stirred vessel in an aluminum reflector to be able to visualize the neutral zones of flow is switched on. A video camera is used to visualize these zones. The pictures from the light cut procedure are made on the CD Rome.

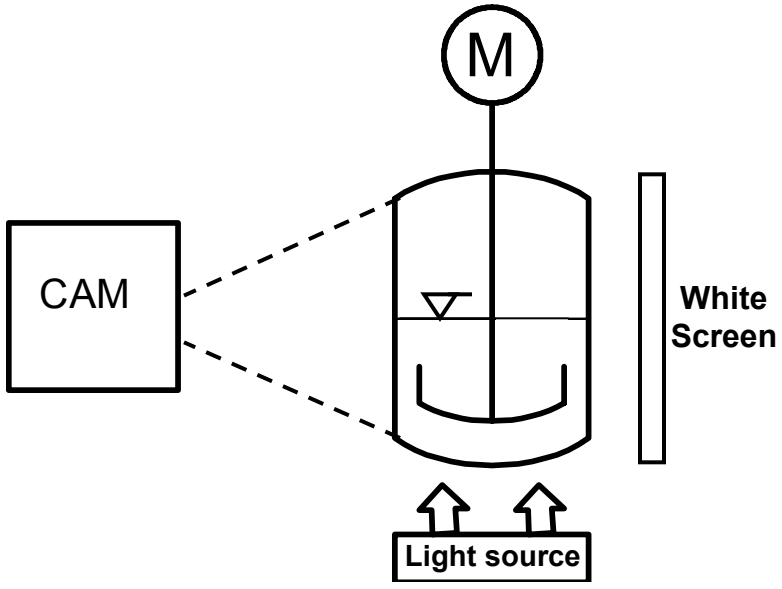

Figure 3.5: The experimental setup for the light cut procedure to visualize the flow field of the liquid mixture in glass vessel.

4. CFD SIMULATION AND SUBMODELS

This work presents a detailed CFD approach in connection with the CFX-10 software. There are only few research work studied the CFD of multicomponent mixing of the two miscible liquids ethanol and glycerol with high different viscosities and densities without reaction in a non-baffled stirred SBR and BR with anchor impeller. The effects of density and viscosity differences between the dosage and bulk liquids in case of SBR and between these liquids initially stratified in case of BR on the dynamic mixing behavior are investigated. This behavior is described by determining the mixing times, time dependent density-, viscosity- and velocity-fields as well as the flow patterns and homogeneity of the liquid mixtures. The concentration profile of the lighter liquid (ethanol) is determined at different points near the shaft and walls of the vessel to determine the homogeneity and mixing times. The mixing behavior is calculated at different dosage times of the added liquid, inlet tube diameters, anchor velocities, anchor dimensions (horizontal blade width) and the volumes of the mixed liquids.

Also, it was important to control the dosage of the lighter liquid (ethanol) to the bulk liquid (glycerol) in the reactor with a suitable speed, flow rate and dosage time by using appropriate time step functions and algebraic equation in the simulations. Different mathematical and physical models are used to describe the real mixing process like homogeneous multiphase multicomponent model. The gas phase (air) is involved in the simulations; the interaction between the gas-liquid mixture phases is modeled using the free surface model, which is used to study the deformation of the liquid at the interface and to get a sharp interface between air and liquid mixture phases, this prevents both phases to be mixed. The pressure field is assumed

to be hydrostatic in the liquid mixture phase and uniform in the air phase. The mixing of liquids is calculated by the means of multicomponent model under laminar flow [106] [109] [110].

4.1 Simulation for half geometry in SBR and BR

Half geometry is used in the simulation to reduce the required time for numerical solution (t_{CPU}) of the calculation. ANSYS ICEM CFD 5.1 is a geometry and mesh generation pre-processor module of CFX. It is used for creating and modifying the geometry of the mixing vessel and the anchor impeller. It is an interactive program which enables to generate a mesh with appropriate regions as an input to the CFX-pre.

4.1.1 Geometry building

Rounded bottom cylindrical vessel equipped with an anchor impeller is generated in three dimensions. The bottom of the vessel should be modeled curved, because the distance between the blades and vessel walls is very small. This is due to the fact that the anchor blades act as scrappers to the viscous solution.

ANSYS ICEM CFD 5.1 have different tools and options like points, curves, surfaces and build topology to build and create this vessel with dimensions according to the standard agitator dimensions which are shown in Tab. 2.1. The dimensions of the used stirred vessel with the anchor impeller and liquid mixture height in the simulation are shown in Fig. 4.1 which is the same as in the used experiments.

Vessel diameter	d_v	0.200 m
Vessel height	H	0.200 m
Liquid mixture height	H_l	0.140 m
Impeller diameter	d	0.192 m
Impeller height	H_i	0.087 m
Blade width	w	0.012 m
Blade thickness	k	0.002 m
Shaft diameter	S	0.010 m
Bottom clearance	B	0.005 m
Wall clearance	C	0.004 m
Inlet tube diameter	d_t	0.050 m

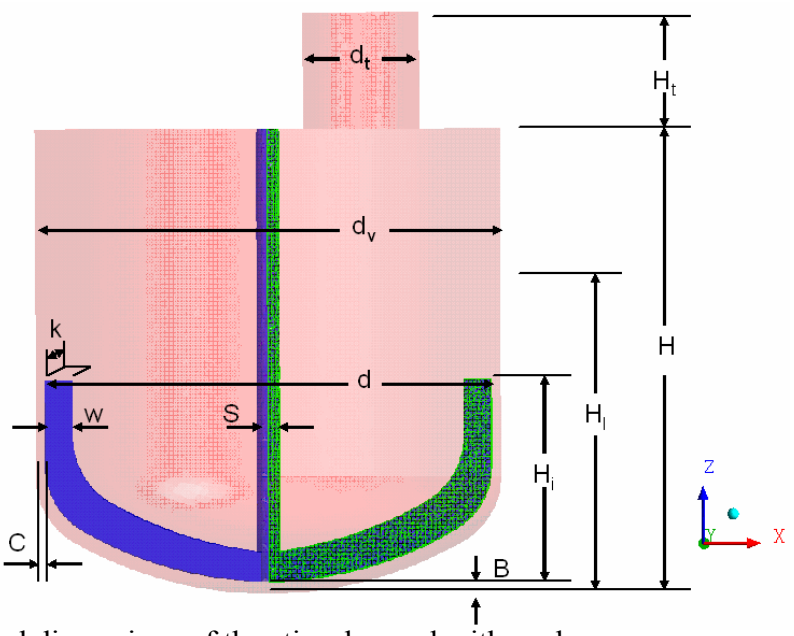

Figure 4.1: A schematic diagram and dimensions of the stirred vessel with anchor impeller.

The total volume of the constructed vessel is 6.283 L. The ratios of the vessel to the anchor impeller dimensions are used in this design are the same as in Fig. 3.1, with the standard anchor impeller dimensions in Tab. 2.1 [82].

4.1.2 Mesh generation

Unstructured tetrahedral cells are used for the created complex geometries. The meshing limitations are to optimize the CPU time of the simulation. CFX program uses a CAD-based geometry and mesh pre-processor, incorporating powerful geometry creation tools and an automatic unstructured mesh generator. The total numbers of the tested unstructured tetrahedral cells that are used in the 3D simulations with 16,000 – 600,000 cells depending on the cell size, mesh refinement, inlet tube diameters of d_t = 2.3 – 5 cm and anchor impellers with horizontal blade widths w_h = 0.015 – 0.012 m as shown in Fig. 4.2. Meshes are very refined at the

interface between air and liquid mixture phases and at the vessel walls edges with cell size of about 3.75 mm, the cells become larger above the interface with the maximum cell size of about 15 mm.

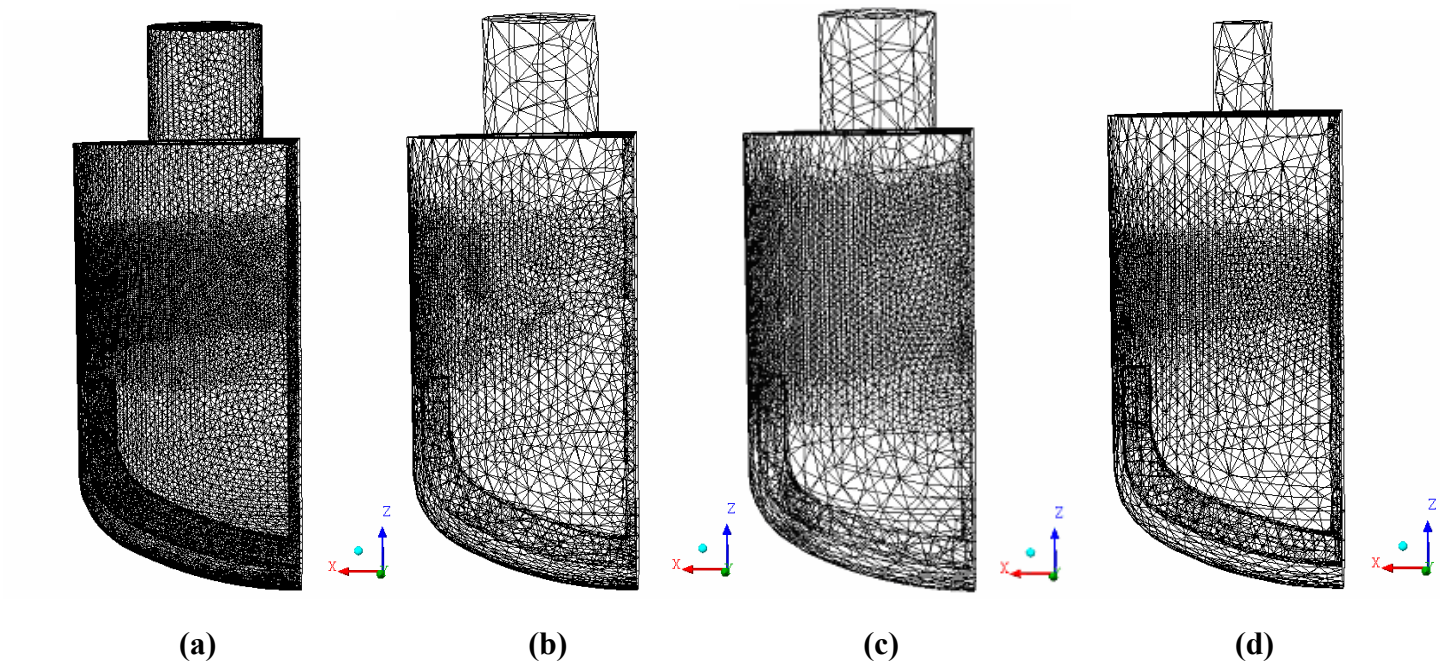

(a) **(b)** **(c)** **(d)**

Figure 4.2: The mesh of unstructured tetrahedral cells with d_t = 5 cm (a) 600,000, (b) 26,000 with w_h = 0.015 m (c) 33,000 with w_h = 0.012 m and (d) 31,000 with d_t = 2.3 cm.

4.1.3 CFX-pre

CFX-pre is the physical definition part of CFX-10. It is used to import the produced meshes in ANSYS ICEM CFD 5.1 to select the physical model which should be used in the CFD simulation. It allows multiple meshes to be imported, allowing each section of complex geometries to use the most appropriate mesh. A rotating reference of frame is used to perform the simulation. Different physical models with the appropriate initial and boundary conditions are used. Additional algebraic equations and time step functions are used to define the dosage time of the added liquid, the volumes of the used liquids and the pressure profile in the reactor. The effect of these

models on the flow and viscosity fields of the liquid mixture is performed by transient 3D-Simulations by using finite volume method. This simulation is carried out under laminar flow by using a homogeneous multiphase model to calculate the velocity and pressure fields. Multicomponent model is used to calculate the mass fractions of each component in the liquid mixture phase. Free surface model is used to calculate the phase volume fractions. Homogeneous multiphase flow is a limiting case of Eulerian-Eulerian multiphase flow where all fluids share the same velocity field and pressure profile.

The following is a detail description for the models which are used in the simulation of multicomponent liquid mixture of ethanol and glycerol with different viscosity and density in SBR and BR. The physical properties of these components are the same as those used in the experiment as shown in Tab. 3.1.

4.1.3.1 Kind of Simulation

Transient simulation is used to calculate the dynamic mixing behaviour with time and space. The time step of 0.01 s is used to get sufficient accurate and precise results.

4.1.3.2 Multicomponent modeling

A multicomponent fluid contains two or more components and its properties are calculated from those of the components. The components are assumed to be mixed at the molecular level and the properties of the fluid depend on the mass fraction of the components. The components can exist in a fixed or variable composition mixture. For fixed composition mixture, the mass fraction of each material is specified and is not allowed to change

during the course of the simulation in space or time. Fixed composition mixtures can consist of pure substances only and not other fixed composition mixtures. For variable composition mixtures, the mass fractions of each component may vary in space or time [90]. In this work, variable composition mixture is used in the simulation. With a multicomponent simulation, a single phase velocity field is calculated. Each component moves at the velocity of the fluid of which they are part with a drift velocity, arising from diffusion [125]. The properties of multicomponent fluids are calculated on the assumption that the components form an ideal mixture.

Ethanol and glycerol are assumed to be mixed at the molecular level, they share the same mean velocity-, pressure- and temperature fields, and the mass transport takes place by convection and diffusion. Multicomponent mixing flow properties in the stirred vessel with anchor impeller in SBR and BR are calculated as following described in the chapter.

4.1.3.2.1 Mixture density

The mixture density is calculated from the mass fractions Y_i. The density of each component requires knowledge of the mixture temperature, pressure and an appropriate equation of state for each component. For variable composition mixture, the density is determined by this equation [100] [105]:

$$\frac{Y_A}{\rho_A} + \frac{Y_B}{\rho_B} + \ldots + \frac{Y_N}{\rho_N} = \frac{1}{\rho_m} \quad . \tag{4-1}$$

4.1.3.2.2 Mixture viscosity

The dynamic viscosity is a measure of the drag of a fluid to shearing forces, and appears in the momentum equations. For variable composition

mixture, the dynamic viscosity can be determined by the following equations for ideal and non ideal liquid mixing.

4.1.3.2.2.1 Ideal case

In an ideal mixture the properties can be calculated directly from the properties of the components and their mass fraction in the mixture. Then for a liquid mixture of ethanol and glycerol the dynamic viscosity of this mixture is calculated by using the following equation [76] [103]:

$$\eta_{\mathrm{m}} = \sum_{i=A,B,\ldots}^{N} Y_i \, \eta_i \, . \tag{4-2}$$

4.1.3.2.2.2 Nonideal case

The viscosity of liquid mixtures in general has no linear dependence on the composition and is difficult to calculate. Arrhenius viscosity equation is proposed to predict the viscosity of the binary liquid mixtures of ethanol and glycerol by using this equation [29] [70] [96] [99] [128] [129]:

$$\ln \eta_{\mathrm{m}} = \sum_{i=A,B,\ldots}^{N} Y_i \ln \eta_i \, . \tag{4-3}$$

4.1.3.2.3 Mixture molar mass

For variable composition mixture, the molar mass is determined by using the equation [101]:

$$\frac{Y_A}{\tilde{M}_A} + \frac{Y_B}{\tilde{M}_B} + \ldots + \frac{Y_N}{\tilde{M}_N} = \frac{1}{\tilde{M}_m} \, . \tag{4-4}$$

4.1.3.2.4 Species mass fraction

In single phase multicomponent flows, the mass fraction of component $Y_{A\alpha}$ is calculated by using the transport equation [100]:

$$\frac{\partial}{\partial t}\left(r_\alpha \rho_\alpha Y_{A\alpha}\right) + \nabla \bullet \left(r_\alpha \left(\rho_\alpha U_\alpha Y_{A\alpha} - \rho_\alpha D_{A\alpha}\left(\nabla Y_{A\alpha}\right)\right)\right) = S_{A\alpha} \,. \quad (4\text{-}5)$$

Where:

$$\nabla \bullet U_\alpha = \frac{\partial u_x}{\partial x} + \frac{\partial u_y}{\partial y} + \frac{\partial u_z}{\partial z} \,.$$

This mass conservation equation provides solution to mass fraction $Y_{A\alpha}$ of the component A and their diffusion coefficient $D_{A\alpha}$ with time and space. The mass fraction of the second component e.g. B in the liquid phase is calculated by using the equation (4.32).

4.1.3.3 Multiphase flow modeling

Multiphase flow refers to the situation where more than one fluid is present. Each fluid may possess its own flow field, or all fluids may share a common flow field. Unlike multicomponent flow, the fluids are not mixed on a microscopic scale. Rather, they are mixed on a macroscopic scale, with a separate interface between the fluids. Two separate multiphase flow models are available in CFX, an Eulerian–Eulerian multiphase model and a Lagrangian Particle Tracking multiphase model. For multiphase model it is possible to use an inhomogeneous or the homogeneous model [6].

The homogeneous model is used when the interface is separate and well-defined everywhere, but when the interface is not well-defined in some locations; perhaps because one phase is entrained in the other, an

inhomogeneous model may be more appropriate. The disadvantage of the inhomogeneous models is that they require more CPU time and more memory. Multiphase flow is the more complex situation involving fluid interfaces [17] [23].

4.1.3.3.1 Homogeneous model

Modeling of free surface flow is done by using the homogeneous model. This model assumes separate phases and only one velocity field needs to be computed. The mass diffusion terms and the interfacial mechanical energy are neglected [150]. The volume fractions of the two phases are assumed separate. The volume fractions of the phases are equal to one or zero everywhere except at the interface. The surface tension is usually neglected in this model. The governing equation for isothermal motion of an incompressible and homogeneous fluid is described by the following equations [18] [19] [21] [22] [38] [100].

4.1.3.3.1.1 Continuity equation

The continuity equation is used to calculate the pressure profile and volume fraction fields:

$$\frac{\partial}{\partial t}\left(r_\alpha \rho_\alpha\right) + \nabla \bullet \left(r_\alpha \rho_\alpha U_\alpha\right) = \mathrm{S}_{MS\alpha} + \sum_{\beta=1}^{N_P} \Gamma_{\alpha\beta} \,. \tag{4-6}$$

There are no mass sources $\mathrm{S}_{MS\alpha}$ and there is no interphase mass transfer $\Gamma_{\alpha\beta}$, i.e. these terms can be neglected. The continuity equation becomes:

$$\frac{\partial\left(\rho_\alpha r_\alpha\right)}{\partial t} + \frac{\partial\left(\rho_\alpha r_\alpha u^i{}_\alpha\right)}{\partial x^i} = 0 \,. \tag{4-7}$$

Then:

$$\frac{\partial \rho_m}{\partial t} + \frac{\partial \left(\rho_m u_m^i\right)}{\partial x^i} = 0 . \tag{4-8}$$

Where:

$$\rho_m = \sum_\alpha r_\alpha \rho_\alpha \qquad \text{and} \qquad \rho_m u_m^i = \sum_\alpha r_\alpha \rho_\alpha u_\alpha^i .$$

4.1.3.3.1.2 Momentum equation

This equation is used to calculate the velocities in *x*, *y* and *z* coordinates:

$$\frac{\partial}{\partial t}(\rho \mathrm{U}) + \nabla \bullet \left(\rho \mathrm{U} \otimes \mathrm{U} - \eta\left(\nabla \mathrm{U} + (\nabla \mathrm{U})^{\mathrm{T}}\right)\right) = S_M - \nabla p . \tag{4-9}$$

Where:

$$\mathrm{U}_\alpha = \mathrm{U}, \quad 1 \le \alpha \le N_P, \quad \rho = \sum_{\alpha=1}^{N_P} r_\alpha \rho_\alpha, \quad \eta = \sum_{\alpha=1}^{N_P} r_\alpha \eta_\alpha \quad \text{and}$$

$$\tau = -\eta\left(\nabla \mathrm{U} + (\nabla \mathrm{U})^{\mathrm{T}}\right) .$$

Then:

$$\rho_\alpha r_\alpha \frac{\partial u_\alpha^i}{\partial t} + \rho_\alpha r_\alpha u_\alpha^j \frac{\partial u_\alpha^i}{\partial x^j} = -r_\alpha \frac{\partial p}{\partial x^i} + \frac{\partial \left(r_\alpha \tau_\alpha^{ji}\right)}{\partial x^j} + r_\alpha \rho_\alpha g^i + M_\alpha^i . \tag{4-10}$$

In equation (4-10), M_α^i represents momentum transfer with other phases. This term is neglected, because there is no momentum transfer with other phases, and then the equation (4-10) becomes:

$$\frac{\partial \left(\rho_m u_m^i\right)}{\partial t} + \frac{\partial \left(\rho_m u_m^j u_m^i\right)}{\partial x^j} = -\frac{\partial p}{\partial x^i} + \frac{\partial \left(\tau_m^{ji} + \tau_D^{ji}\right)}{\partial x^j} + \rho_m g^i . \tag{4-11}$$

Where:

$p_\alpha = p$ for all $\alpha = 1, ..., N_P$, $\tau_m^{ji} = \sum_\alpha r_\alpha \tau_\alpha^{ji}$ and

$\tau_D^{ji} = -\sum_\alpha r_\alpha \rho_\alpha \left(u_\alpha^i - u_m^i \right)$.

For the homogeneous model:

$u_\alpha^i = u_m^i \quad \Rightarrow \quad \tau_D^{ji} = 0$.

The viscous stresses and apparent diffusion stresses are neglected. The momentum equation becomes:

$$\frac{\partial \left(\rho_m u_m^i \right)}{\partial t} + \frac{\partial \left(\rho_m u_m^j u_m^i \right)}{\partial x^j} = -\frac{\partial p}{\partial x^i} + \frac{\partial \tau_m^{ji}}{\partial x^j} + \rho_m g^i . \qquad (4\text{-}12)$$

Accumulation | Convection | Pressure gradient | Shear stress gradient | Buoyancy

4.1.3.3.1.3 Volume fraction equation

This constraint equation is used to calculate the volume fraction of the phases remaining:

$$\sum_{\alpha=1}^{N_P} r_\alpha = 1 \ . \qquad (4\text{-}13)$$

4.1.3.3.2 Free surface flow model

Free surface models refer to flows with a distinct interface between the gas and liquid mixture phases with a large density difference. Interfacial area density $A_{\alpha\beta}$ is used to calculate this interface with equation (4-14); and no mass transfer between phases is assumed [50] [100].

$$A_{\alpha\beta} = \left|\nabla r_{\alpha}\right| \ . \tag{4-14}$$

The inertia of the gas is usually negligible due to its low density. The only influence of the gas is its pressure acting on the interface. The liquid can thus move freely, and the locations of the free surface can be determined by solving the equation (4-14). Simulation of free surface flows usually requires defining boundary and initial conditions to set up appropriate pressure profile and volume fraction fields [7].

The implementation of free surface flow model in CFX-10 need some special discretisation options to keep the interface sharp. These include:

(1) A compressive differencing scheme (High Resolution Scheme) for the advection of volume fractions in the volume fraction equations.

(2) A compressive transient scheme (Second Order Backward Euler) for the volume fraction equations.

(3) Special treatment of the pressure gradient and gravity terms to ensure that the flow remain sharp at the interface.

4.1.3.4 Submodels

4.1.3.4.1 Fluid buoyancy model

Buoyancy is a natural and mixed convection flows in which gravity is important. Natural convection happens when the fluid is driven only by local density variations. Convection in the mixture occurs when the fluid is driven by both a pressure gradient and buoyancy forces. Buoyancy is driven by variations in density which can arise from a number of sources:

(1) Natural convection.

(2) In multicomponent flows, variations in the mass fraction cause density

variations since each component usually has a different density.

(3) In multiphase flows, including particle transport modeling, the difference in density between the phases results in a buoyancy force.

(4) If density is variable for a general fluid (i.e., defined by an expression), a buoyancy force will arise.

(5) For ideal gases and real fluids, local pressure variations also cause changes in density. These changes are often small and the buoyancy effect is usually not important in the flow.

In the buoyancy calculations, the gravity vector components in x, y and z are set in the Cartesian coordinate. Buoyancy is simulated in this work by using the density difference buoyancy model.

4.1.3.4.1.1 Density difference between two liquids

For single phase flows, this model is used when the fluid density is a function of temperature or pressure (which includes ideal gases and real fluids) and when a multicomponent fluid is used. For Eulerian multiphase or particle tracking, it is also set even if all phases have constant density. Significant density variations with temperature occur for most gases. A buoyancy reference density as an approximate average value of the expected domain density is specified for the lower density phase. In multiphase simulations, fluid buoyancy model with density difference is also used. The volumetric buoyancy force F_α is modeled by considering the difference in density between phases with the equation:

$$F_\alpha = \left(\rho_\alpha - \rho_{ref}\right) g . \tag{4-15}$$

4.1.3.4.1.2 Pressure gradient between two liquids

The hydrostatic pressure is responsible for driving the flow. It depends on the density of the liquid mixture and buoyancy forces. Initial and boundary conditions are defined in terms of this pressure gradient. The hydrostatic pressure is included.

4.1.3.4.1.3 Rotating domains

In rotating domains transient simulations that include a buoyancy term, it is necessary to set the components of the gravity vector to be a function of the angle of rotation of the domain. The used set in this work is:

$g_x = 0$ [m/s^2] ,

$g_y = 0$ [m/s^2] ,

$g_z = -9.81$ [m/s^2] .

4.1.3.4.1.4 Multiphase flow

The density difference between air and a liquid mixture produces a buoyancy force in multiphase flows. The density of lighter fluid (air) is chosen to be the buoyancy reference density in the free surface flow model calculations; this gives constant pressure in the light phase and hydrostatic pressure in the heavier liquid mixture phase. Also, it simplifies the calculations of the pressure initial and pressure boundary conditions as well as the force in post-processing.

4.1.3.4.2 Laminar model

Laminar flow is governed by the unsteady Navier-Stokes equations. The laminar model is only appropriate if the flow is laminar. It can be applied at low Reynolds number flows with Re < 1000.

4.1.3.4.3 Isothermal model

This model requires a constant absolute temperature for the fluid. This can be used for the purpose of evaluating fluid properties that are temperature dependent. This model can be used to create an initial result file for a more complex model. The used temperature in this work is $\vartheta = 21$ °C.

4.1.3.4.4 Transport model

If the flow of a component like ethanol is modeled by using a transport equation, then it is transported with the fluid of glycerol and may diffuse through that. The time dependent equations of mass, momentum and energy conservation can be written as follows:

(1) *The continuity equation*:

$$\frac{\partial \rho}{\partial t} + \nabla \bullet (\rho \mathrm{U}) = 0. \tag{4-16}$$

(2) *The momentum equation*:

$$\frac{\partial \rho \mathrm{U}}{\partial t} + \nabla \bullet (\rho \mathrm{U} \otimes \mathrm{U}) = \nabla \bullet \left(-p + \eta \left(\nabla \mathrm{U} + (\nabla \mathrm{U})^{\mathrm{T}} \right) \right) + S_M . \tag{4-17}$$

(3) *The energy equation*:

$$\frac{\partial \rho h_{tot}}{\partial t} - \frac{\partial p}{\partial t} + \nabla \bullet (\rho \, \mathrm{U} \, h_{tot}) = \nabla \bullet (\lambda \nabla \mathrm{T}) + S_E . \tag{4-18}$$

(4) *The scalar transport equations*:

For a multicomponent fluid, transport equations are solved for velocity, pressure, temperature and other quantities of the fluid. These are described in the above equations (4-16 – 4-18). Additional equations must be solved to determine how the components of the fluid are transported within the fluid. The bulk motion of the fluid is modeled using single phase velocity-, pressure- and temperature fields. The influence of the multiple components

is found from the variation of different properties for the various components like variation in density which affects conservation of mass. Each component has its own Reynolds-averaged equation for conservation of mass, which can be expressed as:

$$\frac{\partial \tilde{\rho}_i}{\partial t} + \frac{\partial \left(\tilde{\rho}_i \tilde{U}_j\right)}{\partial x_j} = -\frac{\partial}{\partial x_j}\left(\rho_i \left(\tilde{U}_{ij} - \tilde{U}_j\right) - \overline{\rho_i'' \ U_j''}\right) + S_i \ . \tag{4-19}$$

Where: $\tilde{U}_j = \sum\left(\tilde{\rho}_i \tilde{U}_{ij}\right) / \overline{\rho}$.

The relative mass flux term $\rho_i\left(\tilde{U}_{ij} - \tilde{U}_j\right)$ accounts for differential motion of the individual components. This term is modeled to include effects of concentration gradients through the diffusion effect as in this equation:

$$\rho_i \left(\tilde{U}_{ij} - \tilde{U}_j\right) = -\frac{\rho_i D_i}{\overline{\rho}} \frac{\partial \tilde{\rho}_i}{\partial x_j} \ . \tag{4-20}$$

The definition of the mass fraction of component *i* is:

$$\tilde{Y}_i = \frac{\tilde{\rho}_i}{\overline{\rho}} \ . \tag{4-21}$$

Substituting equation (4-20) and (4-21) into (4-19) gives:

$$\frac{\partial \left(\overline{\rho} \tilde{Y}_i\right)}{\partial t} + \frac{\partial \left(\overline{\rho} \tilde{U}_j \tilde{Y}_i\right)}{\partial x_j} = \frac{\partial}{\partial x_j}\left(\rho_i D_i \frac{\partial \tilde{Y}_i}{\partial x_j}\right) - \frac{\partial}{\partial x_j}\left(\overline{\rho Y_i'' U_j''}\right) + S_i \ . \tag{4-22}$$

No chemical reaction is considered, and then the source term S_i can be neglected. For laminar flow, the turbulent scalar fluxes $\overline{\rho Y_i'' U_j''}$ are neglected. The mass fraction equation becomes [104]:

$$\frac{\partial \left(\overline{\rho} \tilde{Y}_i\right)}{\partial t} + \frac{\partial \left(\overline{\rho} \tilde{U}_j \tilde{Y}_i\right)}{\partial x_j} = \frac{\partial}{\partial x_j}\left(\rho_i D_i \frac{\partial \tilde{Y}_i}{\partial x_j}\right) \ . \tag{4-23}$$

This equation is used to calculate the composition of the fluid mixture.

4.1.3.4.5 Algebraic slip model

Algebraic slip mixture model (ASM), as with the Eulerian multiphase model is designed for use with two interpenetrating fluids and for liquid-liquid or gas-liquid mixture. A full set of Navier-Stokes equations is solved for the primary fluid (continuous phase). An algebraic equation for the slip velocity between the fluids is solved. The slip velocity is derived from the fluid properties and local flow conditions and is used to compute the velocity of the secondary phase (dispersed phase). The ASM model is not set up in the same way as other multiphase problems. It needs to define a variable composition mixture containing the fluids when setting the thermodynamic state of the mixture.

The continuous phase should be set to constraint. The remaining phases can be set to either algebraic slip or transport equation. Transport equations and algebraic slip components can be combined, meaning that a mixture of components may be present in the continuous phase. At least one component must be set to constraint. For the dispersed phases, the algebraic slip model is chosen. The algebraic slip option can be set to drag force balance or slip velocity. The drag force balance uses the closed relationship for the slip velocity, as will be shown in derivation of the algebraic slip equation:

(1) *Phase equations*:

Each phase has its own velocity field which can be calculated. The continuity equation for phase α is calculated from equation (4-7) and the momentum equation is equation (4-10).

(2) *Bulk equations*:

A bulk continuity equation is derived by summing equation (4-7) over all phases resulting in equation (4-8). And a bulk momentum equation by summing equation (4-8) over all phases gives equation (4-11).

(3) *Drift and slip relations*:

The slip velocity is the phase velocity relative to the continuous phase:

$$u_{S\alpha}^{i} = u_{\alpha}^{i} - u_{C}^{i}. \tag{4-24}$$

And the drift velocity is the phase velocity relative to the liquid mixture velocity in the bulk as:

$$u_{D\alpha}^{i} = u_{\alpha}^{i} - u_{m}^{i}. \tag{4-25}$$

The slip- and drift velocities are related by the following equation:

$$u_{D\alpha}^{i} = u_{S\alpha}^{i} - \sum_{\alpha} Y_{\alpha} u_{S\alpha}^{i}. \tag{4-26}$$

With these relationships, the phase continuity equation may be written in terms of mass fraction and drift velocity as:

$$\frac{\partial\left(\rho_{m} Y_{\alpha}\right)}{\partial t} + \frac{\partial}{\partial x^{i}}\left(\rho_{m} Y_{\alpha}\left(u_{m}^{i} + u_{D\alpha}^{i}\right)\right) = 0. \tag{4-27}$$

(4) *Derivation of the algebraic slip equation*:

The phase and bulk momentum equations are first transformed to nonconservative form by combining with the phase and bulk continuity equations. The phase momentum equation is:

$$\rho_{\alpha} r_{\alpha} \frac{\partial u_{\alpha}^{i}}{\partial t} + \rho_{\alpha} r_{\alpha} u_{\alpha}^{j} \frac{\partial u_{\alpha}^{i}}{\partial x^{j}} = -r_{\alpha} \frac{\partial p}{\partial x^{i}} + \frac{\partial\left(r_{\alpha} \tau_{\alpha}^{ji}\right)}{\partial x^{j}} + r_{\alpha} \rho_{\alpha} g^{i} + M_{\alpha}^{i}. \tag{4-10}$$

And the bulk momentum equation is:

$$\rho_{m} \frac{\partial u_{m}^{i}}{\partial t} + \rho_{m} u_{m}^{j} \frac{\partial u_{m}^{i}}{\partial x^{j}} = -\frac{\partial p}{\partial x^{i}} + \frac{\partial\left(\tau_{m}^{ji} + \tau_{D}^{ji}\right)}{\partial x^{j}} + \rho_{m} g^{i}. \tag{4-11}$$

Equation (4-10) and (4-11) are combined to eliminate the pressure gradient term, yielding:

$$
\begin{aligned}
M_\alpha^i = {} & r_\alpha \left(\rho_\alpha \frac{\partial u_{D\alpha}^i}{\partial t} + (\rho_\alpha - \rho_m) \frac{\partial u_m^i}{\partial t} \right) \\
& + r_\alpha \left(\rho_\alpha u_\alpha^j \frac{\partial u_\alpha^i}{\partial x^j} - \rho_m u_m^j \frac{\partial u_m^i}{\partial x^j} \right) \\
& - \frac{\partial \left(r_\alpha \tau_\alpha^{ji} \right)}{\partial x^j} + r_\alpha \frac{\partial \left(\tau_m^{ji} + \tau_D^{ji} \right)}{\partial x^j} \\
& - r_\alpha (\rho_\alpha - \rho_m) g^i \, .
\end{aligned}
\tag{4-28}
$$

Several assumptions are now made:

(1) The dispersed phase is assumed to immediately reach its final velocity, so the transient term on the drift velocity can be neglected.

(2) The approximation is made that:

$$
u_\alpha^j \frac{\partial u_\alpha^i}{\partial x^j} \approx u_m^j \frac{\partial u_m^i}{\partial x^j} \, .
$$

(3) The viscous stresses and apparent diffusion stresses are neglected.

With these approximations, the equation (4-28) simplifies to:

$$
M_\alpha^i = r_\alpha (\rho_\alpha - \rho_m) \left(\frac{\partial u_m^i}{\partial t} + u_m^j \frac{\partial u_m^i}{\partial x^j} - g^i \right). \tag{4-29}
$$

Also, it is assumed that the interphase momentum transfer is due only to drag and that the particles are spherical:

$$
M_\alpha^i = -\frac{3}{4} \frac{r_\alpha \rho_i}{d_P} C_D \left| u_{S\alpha} \right| u_{S\alpha}^i \, . \tag{4-30}
$$

This leads to the following closed relationship for the slip velocity:

$$
\left| u_{S\alpha} \right| u_{S\alpha}^i = -\frac{4}{3} \frac{d_P}{\rho_i C_D} (\rho_\alpha - \rho_m) \left(\frac{\partial u_m^i}{\partial t} + u_m^j \frac{\partial u_m^i}{\partial x^j} - g^i \right). \tag{4-31}
$$

Where the subscript *m* refers to bulk quantities, α refers to dispersed phase quantities and ρ_i refers to the density of component. The drag coefficient C_D is directly specified as a constant value of 0.47; the mean diameter d_p must be specified and is assumed to be a constant value of 0.0002 m [114 – 121]. Models for algebraic slip were introduced by Ishii [126]. Manninen and Taivassalo [127], provide a more general formulation. The effect of τ_D^{ji} in the bulk momentum equation is neglected in this work.

4.1.3.4.6 Modified algebraic slip model

The new developed modified algebraic slip model (MASM) is derived from the ASM but the diameter of the droplet d_p in Eq. 4-31 is a step function of time $d_p(t)$ [s. Chap. 5.3.5].

4.1.3.4.7 Constraint equation

If the flow of a component is modeled using a constraint equation, its mass fraction is calculated to ensure that all the component mass fractions sum to unity, i.e. the mass fraction of the component is set equal to the total mass fractions of the other components in the same fluid subtracted from unity. The CFX-10 solver solves $N_C - 1$ mass fraction equations (either transport equations or algebraic equations) for all except one of the components. The remaining component is known as the constraint component because its mass fraction is determined by the constraint equation:

$$\sum_{i=A,B,\ldots}^{N_C} Y_i = 1 \tag{4-32}$$

4.1.3.4.8 Sliding mesh model

The sliding mesh method is a new way of dealing with the impeller interaction. The main advantage of the sliding mesh method is that no experimentally obtained boundary conditions are needed, as the flow around the impeller blades is being calculated in detail. This allows modeling of impeller systems and reactors for which experimental data is difficult or impossible to obtain.

With the sliding mesh method the reactor is divided in two regions that are treated separately: the impeller region and the reactor region that includes the bulk of the liquid, the reactor wall and the reactor bottom, see Fig. 4.3. The grid in the impeller region rotates with the impeller. The grid in the reactor remains stationary. The two grids slide past each other at a cylindrical interface. In the reactor region the conservation equations for mass and momentum are solved. In the rotating impeller region a modified set of balance equations is solved.

Sliding mesh methods can be used to accurately predict the time dependent laminar flow pattern in stirred reactors, without the need for experimental data. A disadvantage is the long calculation time which is about an order of magnitude longer than with steady state calculations based on experimental impeller data. An important application for the sliding mesh method might be the development of new, optimized impeller designs for specific industrial applications. Other applications are the prediction of flow patterns with impellers for which no experimental data are available, the prediction of flow patterns in multiple impeller systems where there is significant interaction between the impellers and to predict time dependent flow patterns in systems where steady state assumptions are not justified.

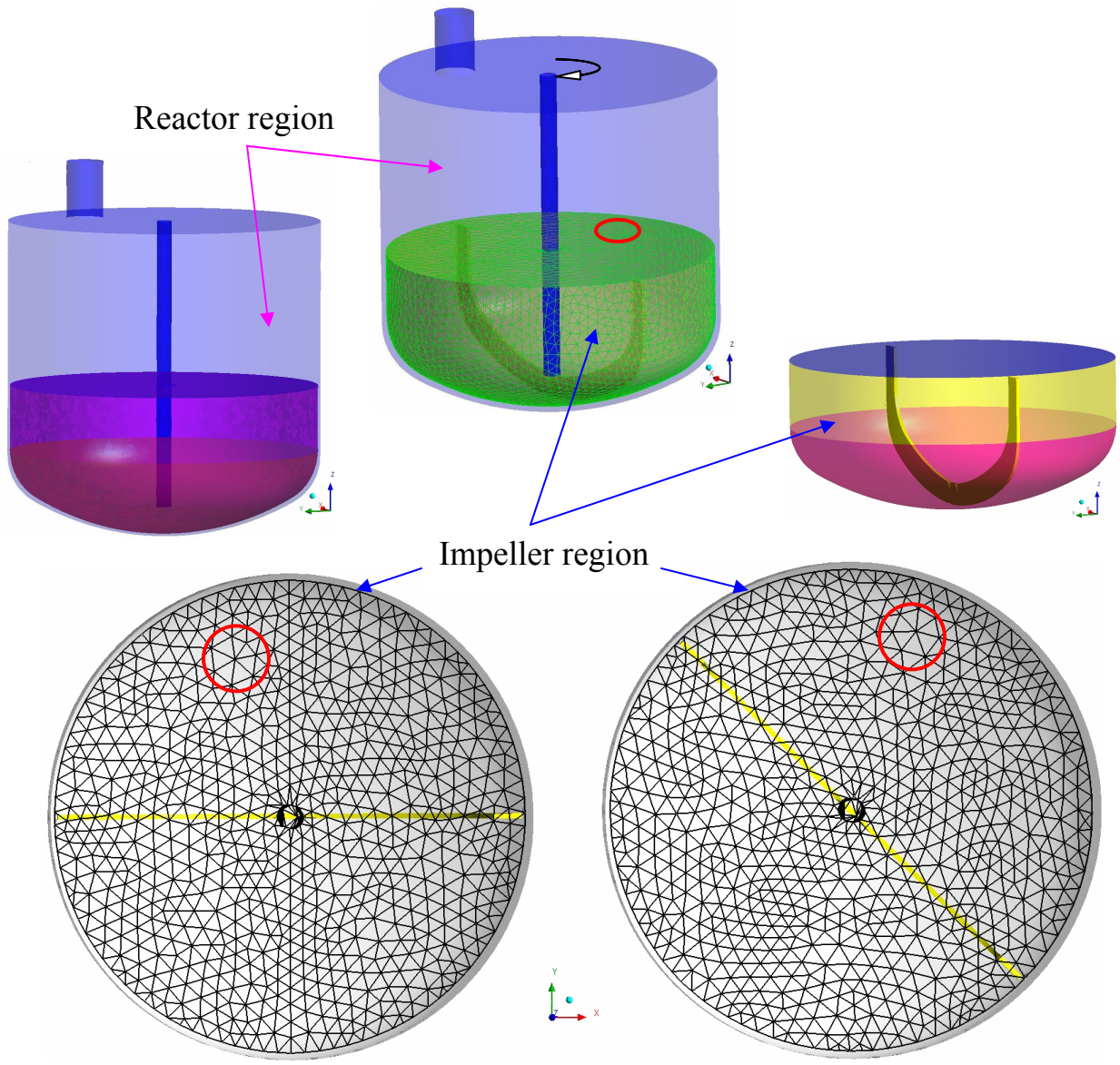

Figure 4.3: The reactor (stationary) and anchor impeller (rotating) regions and grid for the full geometry in the sliding mesh method at two different time steps. The grid in the impeller region moves with the impeller and slides past the stationary grid for the remaining part of the reactor.

The scheme in Fig. 4.4 shows the physical models and submodels are used in the simulations of liquids mixing procedure with CFX.

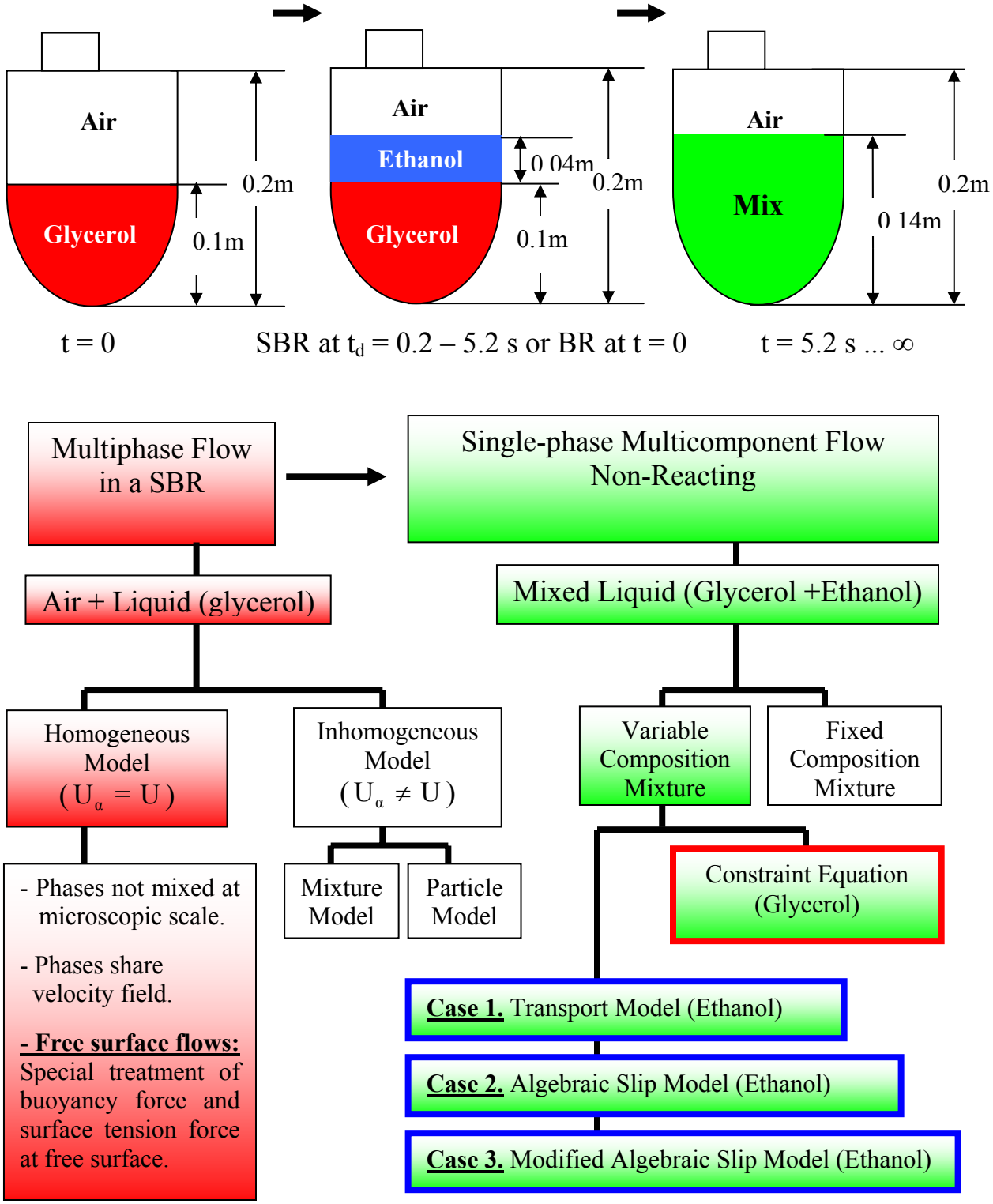

Figure 4.4: Homogeneous multicomponent free surface model with **Case 1.** Transport Model, **Case 2.** Algebraic Slip Model and **Case 3.** Modified Algebraic Slip Model in a SBR and a BR.

4.1.3.5 Domain conditions

4.1.3.5.1 General conditions

For the multiphase buoyancy model, the density of the light fluid (air) is used as the reference density. This simplifies the definition of pressure gradient, and hence the specification of pressure initial and boundary conditions in the hydrostatic limit:

$$\frac{\partial p}{\partial z} = -(\rho - \rho_{ref})g \,. \tag{4-33}$$

The domain of mixture with stirred vessel is rotating at a stirrer velocity of ω = 150 rpm around the z coordinate clockwise. The calculations reference pressure is p_{ref} = 1.01325 Pa. A rotating reference frame is used to perform the simulation [101].

4.1.3.5.2 Anchor- and shaft velocity

The anchor and shaft are rotating with the same velocity as the domain. Linear velocity of the anchor and shaft is:

$$u = \omega \pi d_v. \tag{4-34}$$

With ω = 150 1/min = 2.5 1/s and d_v = 0.2 m it is u = 1.57 m/s.

4.1.3.5.3 Fluids

Newtonian miscible liquids of ethanol and glycerol are used. The volumes of glycerol and ethanol are 2.45 L and 1.286 L respectively. The equivalent heights of glycerol and ethanol in the vessel are z = 0.1 m and 0.04 m respectively. The total liquid height is z = 0.14 m which corresponds to the total liquid volume of V = 3.736 L.

4.1.3.5.4 Semibatch reactor

4.1.3.5.4.1 Initial conditions

The initial conditions for the pressure field and volume fraction is done at t = 0 by using command expression language (CEL) to define the time step functions which describe the free surface shape between the air and the liquid phase. The following conditions and expressions are set in SBR:

(1) An initial volume fraction field where the volume fraction above the free surface is 1 for air and 0 for the glycerol and below the free surface is 0 for air and 1 for the glycerol. Initial height of glycerol in the vessel is 0.1 m. Then the initial volume fractions in step functions are:

$$\text{InitialVOFAir} = \text{step}((z - 0.1[\text{m}])/1[\text{m}]). \quad (4\text{-}35)$$

$$\text{InitialVOFglycerol} = 1 - \text{InitialVOFAir}. \quad (4\text{-}36)$$

Where InitialVOFAir is the initial volume fraction of air, and InitialVOFglycerol is the initial volume fraction of glycerol. The time step function for this case is shown in Fig. 4.5. The step function is 0 for negative value of this function, 1 for positive value and 0.5 for zero value. This value of this function must be dimensionless.

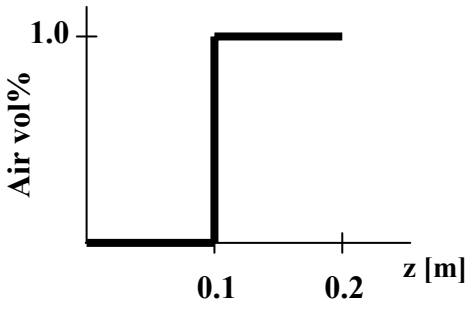

InitialVOFAir = step((z – 0.1[m])/1[m]).

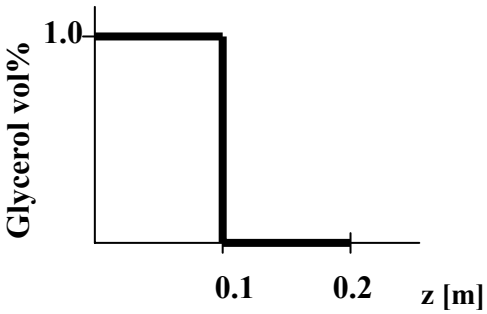

InitialVOFglycerol = 1 – InitialVOFAir.

Figure 4.5: Initial time step function of the air/glycerol volume fraction profiles at t = 0 in SBR.

(2) An initial pressure field for the domain where the pressure above the free surface is constant and the pressure below the free surface is a hydrostatic distribution. The time step function for this case is shown in Fig. 4.6.

$$\text{InitialP} = \rho_G \; g \; (H_l - z) \; \text{InitialVOFglycerol}. \qquad (4\text{-}37)$$

$$\text{InitialP} = 1262[\text{kg/m}^3] \; 9.81[\text{m/s}^2] \; (0.1[\text{m}] - z) \; \text{InitialVOFglycerol}.$$

Where InitialP is the initial pressure and ρ_G is the density of pure glycerol.

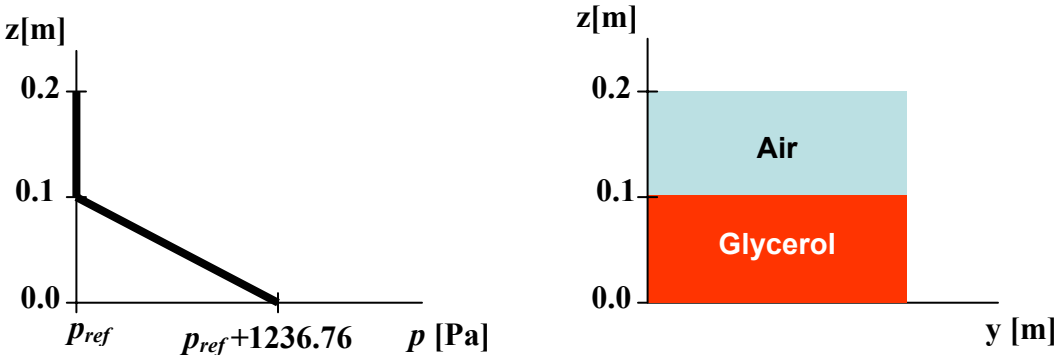

Figure 4.6: Initial time step function of the air/glycerol pressure profile at t = 0 in SBR.

4.1.3.5.4.2 Boundary conditions

4.1.3.5.4.2.1 Wall top

Using an opening boundary condition for the wall top of the domain helps constrain the flow and improve convergence. As the liquid mixture level increases, air tries to flow through the opening to maintain conservation of mass. The opening allows only the air to flow through but not the liquid mixture. This does not influence the flow or mixing process of the mixture phase, but changes the air flow above the liquid mixture phase. This is done using the following CEL time step functions:

(1) A volume fraction-specified for Opening boundary where the volume fraction above the free surface is 1 for air and 0 for liquid mixture of glycerol with ethanol and below the free surface is 0 for air and 1 for this liquid Mixture. Final height of the liquid mixture in the tank is 0.14 m. Then the Final volume fractions in step functions are:

$$\text{FinalVOFAir} = \text{step}((z - 0.14[\text{m}])/1[\text{m}]). \quad (4\text{-}38)$$

$$\text{FinalVOFMixture} = 1 - \text{FinalVOFAir}. \quad (4\text{-}39)$$

Where FinalVOFAir is the final volume fraction of air and FinalVOFMixture is the final volume fraction of the liquid mixture. The time step function for this case is shown in Fig. 4.7.

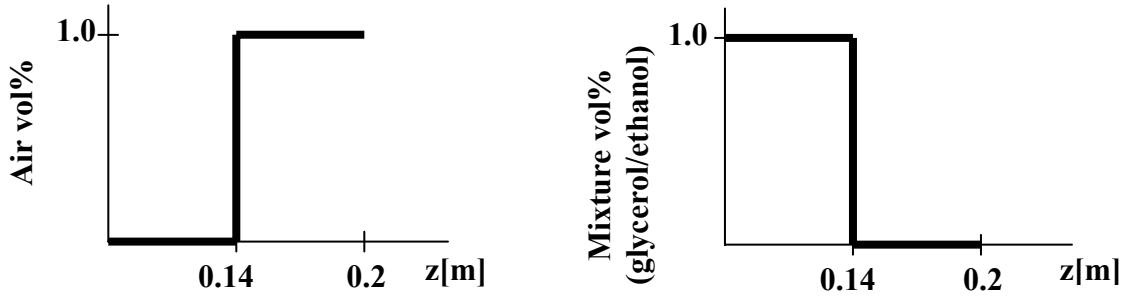

FinalVOFAir = step((Z – 0.14[m])/1[m]). **FinalVOFMixture = 1 – FinalVOFAir.**

Figure 4.7: Final time step function of the air/liquid mixture volume fraction profiles after t = 5.2 s in SBR at t_d = 5 s (from t_{di} = 0.2 s to t_{df} = 5.2 s).

2- A pressure-specified opening boundary where the pressure above the free surface is constant and the pressure below the free surface is a hydrostatic distribution [100].

$$\text{InitialP} = \rho_m \, g \, (H_l - z) \, \text{FinalVOFMixture}. \quad (4\text{-}40)$$

$$\text{FinalP} = 1108.43[\text{kg/m}^3] \, 9.81[\text{m/s}^2] \, (0.14[\text{m}] - z) \, \text{FinalVOFMixture}.$$

Where FinalP is the final absolute pressure and ρ_m is the density of the liquid mixture. This pressure is the momentum and mass static pressure. The time step function for this case is shown in Fig. 4.8.

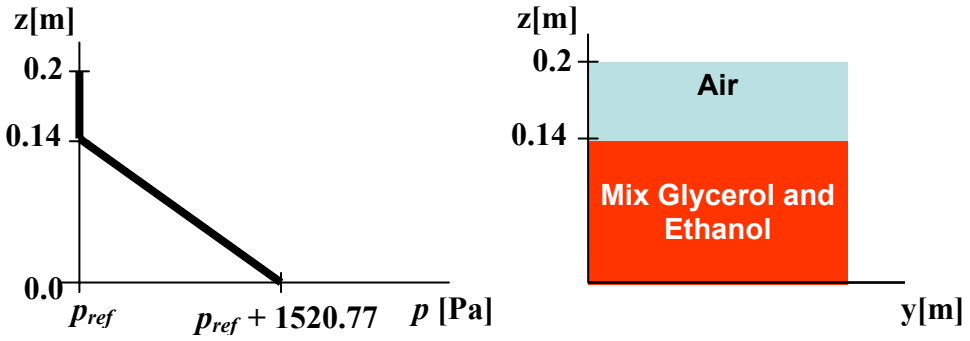

Figure 4.8: Final time step function of the air/liquid mixture pressure field after t = 5.2 s in SBR at t_d = 5 s (from t_{di} = 0.2 s to t_{df} = 5.2 s).

4.1.3.5.4.2.2 Bottom and cylindrical walls

The boundary conditions at the bottom and vessel walls are those derived assuming no-slip condition and counter rotating walls (stationary walls). No-slip means that the velocity of the fluid at the wall boundary is set to zero, so the boundary condition for the velocity becomes:

$$U_{Wall} = 0 \quad \text{at} \quad r = \frac{d_v}{2}. \qquad \Rightarrow \qquad u_x = u_y = u_z = 0$$

Where r is the vessel radius, d_v is the vessel diameter and $u_{x,y,z}$ is the velocity of the liquid in the coordinate directions x, y and z.

4.1.3.5.4.2.3 Shaft and anchor impeller

No-slip boundary conditions are used at the anchor impeller and the shaft.

$$\text{At} \quad r = 0 \qquad \Rightarrow \qquad u_x = u_y = 0 \qquad \Rightarrow \qquad \frac{\partial u}{\partial z} = 0$$

4.1.3.5.4.2.4 Inlet tube

In a SBR, simulations are accomplished at different ethanol feeding dosage times and different inlet tube diameters as following:

(1) For ethanol at dosage time t_d = 1s from t_{di} = 0.2 s to t_{df} = 1.2 s:

u_E = 0.64 m/s and $\dot{V}_E$ = 1.25 l/s for d_t = 5.0 cm

u_E = 2.90 m/s and $\dot{V}_E$ = 1.25 l/s for d_t = 2.3 cm

$$u_E = \frac{\dot{V}_E 4}{\pi d_t^2} \quad . \tag{4-41}$$

Where t_d is ethanol dosage time, t_{di} is the initial dosage time, t_{df} is the final dosing time, u_E is the feeding velocity, $\dot{V}_E$ is the volumetric flow rate and d_t is an inlet tube diameter. The time step function for d_t = 5.0 cm is shown in Fig. 4.9.

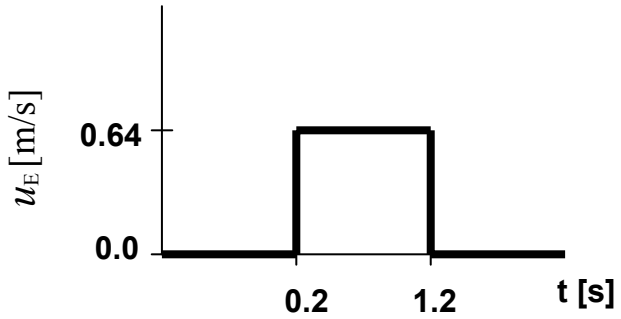

Figure 4.9: Time step function for ethanol inlet speed in a SBR with inlet tube diameter is 2.3 cm and dosing time is 1.0 s from 0.2 s to 1.2 s.

(2) For ethanol at dosage time t_d = 5s from t_{di} = 0.2 s to t_{df} = 5.2 s:

u_E = 0.128 m/s and $\dot{V}_E$ = 0.25 l/s for d_t = 5.0 cm

u_E = 0.578 m/s and $\dot{V}_E$ = 0.25 l/s for d_t = 2.3 cm

The inlet ethanol velocity and dosage time are defined and written according to CEL as the following time step functions for d_t = 2.3 cm:

f1 = step(t/1.0[sec] – t_{di}) 0.578 [m/sec]. (4-42)

f2= step(t/1.0[sec] – t_{df}) 0.578 [m/sec]. (4-43)

Inlet ethanol speed = f1 – f2. (4-44)

4.1.3.5.4.2.5 Periodic boundary

For periodic boundary condition: B1 = B2, where B is the transport property. As a result the mesh and boundary conditions are used in the simulations are shown in Figs. 4.10 and 4.11.

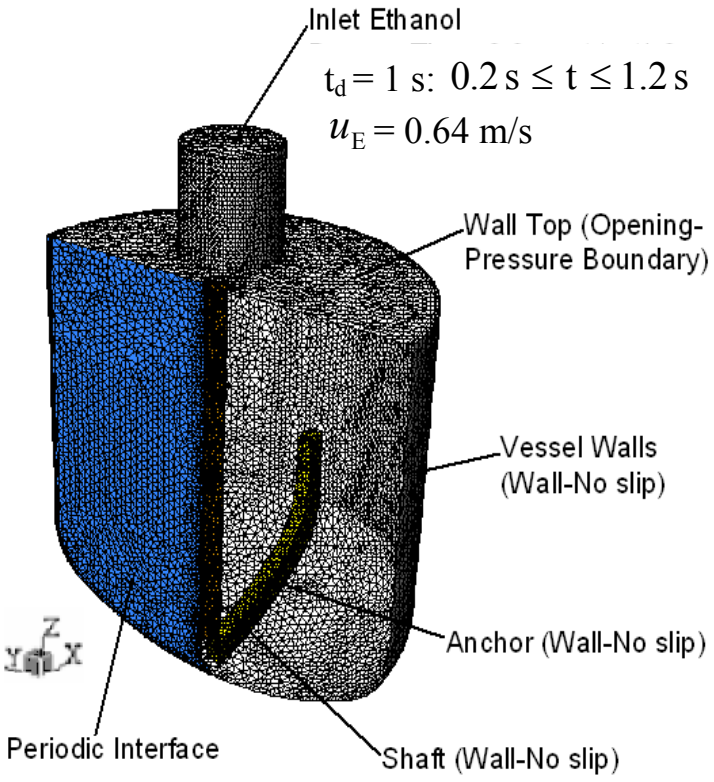

Figure 4.10: Meshing and boundaries for half geometry in SBR at t_d = 1 s, d_t = 5 cm.

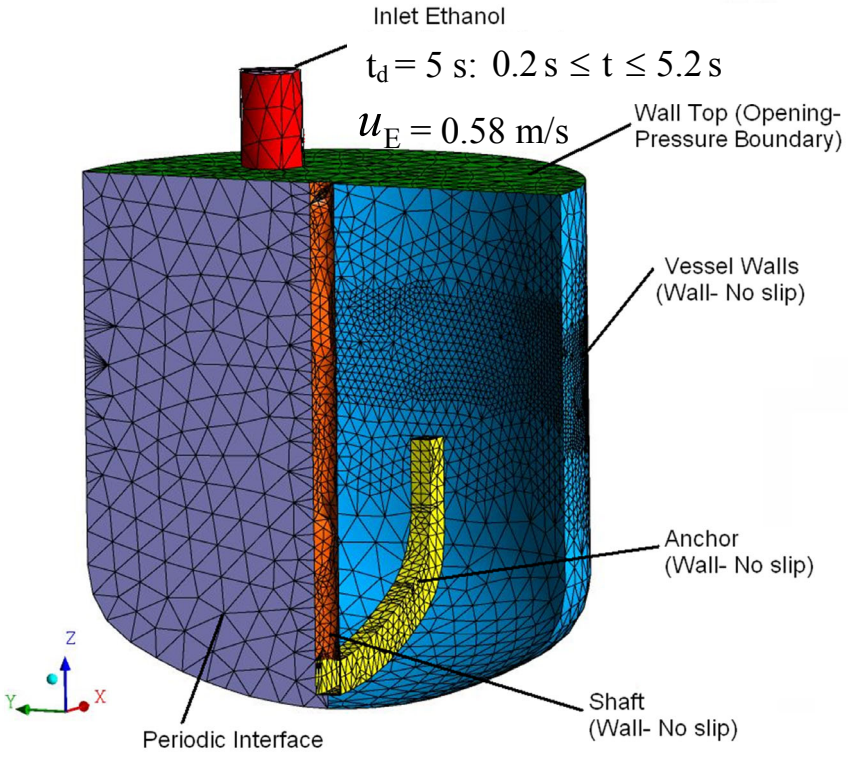

Figure 4.11: Meshing and boundaries for half geometry in SBR at $t_d = 5$ s, $d_t = 2.3$ cm.

4.1.3.5.5 Batch reactor

The same conditions as those are used in the SBR are used for the batch reactor (BR) except the following differences:

4.1.3.5.5.1 Initial conditions

The initial volume fractions of air/liquid mixture and the initial mass fractions of glycerol/ethanol in the liquid mixture are defined as following:

(1) The initial volume fraction field of air/liquid mixture at t = 0 are defined. The volume of glycerol fill the vessel to a height 0.1 m and the volume of ethanol fill the vessel for a height from 0.1 m to 0.14 m above glycerol forming a layer of thickness 0.04 m. The air phase is included in the simulation to study the deformation at the interface between the air and

the multicomponent liquid mixture phase. Air is set to be above the total liquid height of 0.14 m. CEL time step functions are set to define this situation:

InitAir = step((z−0.14[m])/1[m]). (4-45)

InitMix = 1−InletAir. (4-46)

Where InitAir is the initial volume fraction of the air phase and InitMix is the initial volume fraction of the liquid mixture phase. This condition is used for air/liquid mixture phases.

(2) The initial mass fractions of glycerol/ethanol in the liquid mixture are defined relative to their heights in the vessel. Two distinct layers are formed because of the density difference. These layers are defined in the program by using the following time step functions:

InGlycerol = step((0.1[m]−z)/1.0[m]). (4-47)

InEthanol = 1−InGlycerol. (4-48)

Where InGlycerol is the initial mass fraction of the glycerol and InEthanol is the initial mass fraction of the ethanol in the liquid mixture phase.

4.1.3.5.5.2 Boundary conditions

There is no inlet boundary condition. Opening boundary condition at a static pressure of 1.0 atm is used for the mass and momentum equation at the wall top.

4.1.4 CFX-solver manager

The CFX solver manager provides a graphical user interface to the CFX-solver in order to give information about the emerging solution, and to provide with an easy way to control the CFX-solver. It allows setting some, attributes for the CFD calculations and control the CFX-solver interactively as the solution develops.

The coupled solver approach is used in this work to solve the four linearised equations for momentum and mass conservation simultaneously. Lower number of iterations is required to get the convergence with this method. Resolution of the algebraic equations is carried out using high resolution advection and transient 2nd order backward Euler schemes. The maximum residuals for error calculation are 0.0001.

4.1.5 CFX-post

It is designed to allow easy visualisation and quantitative post-processing for the results of CFD simulations. The flow patterns of the liquid mixture with time can be predicted by drawing the vector plots of the mixture velocity. The contour plots are used to describe the dynamic viscosity with time. Different variables are calculated from CFD like ethanol concentration at different points in the tank. Animation also is used to show the real motion and flow of the liquid mixture stirred with the anchor impeller.

4.2 Simulation for full geometry in SBR and BR

These simulations are based on the sliding mesh model (transient stator rotor) which requires two domains with new interfaces between them for transferring the calculated variables.

4.2.1 Geometry building

The 3-D full geometry is designed using ICEM CFD 5.1 as mentioned before. Two separate assemblies are constructed, one is for the rotating part (anchor) and the second is for the stationary part (the rest parts of the vessel i.e. cylindrical walls, tank bottom, wall top and the inlet tube).

For the rotating part, the same anchor impeller as mentioned is used and new anchor interfaces are created to cover the domain of the anchor, these interfaces have the same shape as for the tank walls (bottom, cylindrical walls and top) which are described before. The available ICEM CFD tools of point, curve, surface, topology building, and e.g. transform are used to do this.

For the stationary part which includes all the boundaries that mentioned before except the anchor, also new interfaces were created same as those for the anchor with a very small distance from the anchor interfaces. The tank and anchor impeller assemblies are shown in Fig. 4.12.

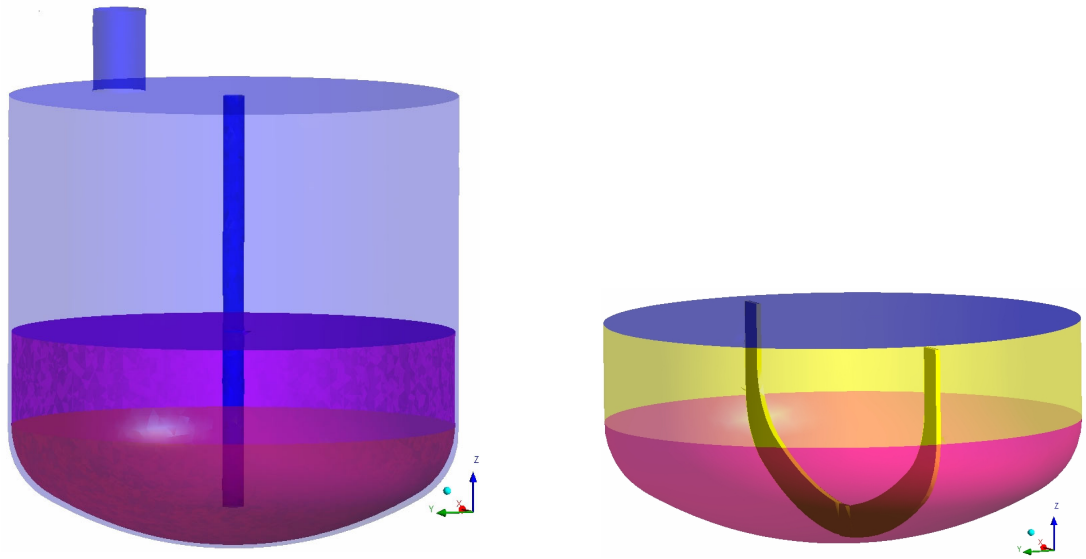

Figure 4.12: The reactor (stationary) left and anchor impeller (rotating) right regions for the full geometry.

4.2.2 Mesh generation

The unstructured tetrahedral cells are generated for both mentioned assemblies; the size of the cell is 0.007 m. Very small cell size is needed for this case to get good convergence and because of a very small clearance between the anchor and the walls of the tank to avoid the intersection between the two domains. Decreasing the cell size increases the number of the cells. The total number of tetrahedrons for the rotating assembly is 92,156 and the total number of tetrahedrons for the stationary assembly is 653,798. The total number of tetrahedrons is 745,954.

4.2.3 CFX-Pre

Two domains are created, one is the rotating part and the second is the stationary part. The rotating domain includes only the anchor impeller as a boundary, the domain motion is set to be rotating clockwise as in the experiment at angular velocity 150 rpm. The stationary domain includes the rest parts of the geometry like the inlet tube, vessel cylindrical and bottom walls, wall top and the shaft as shown in Fig. 4.12.The domain and fluid models are the same as those used in the half geometry modelling. Fig. 4.13 shows the full geometry in 3-D axis.

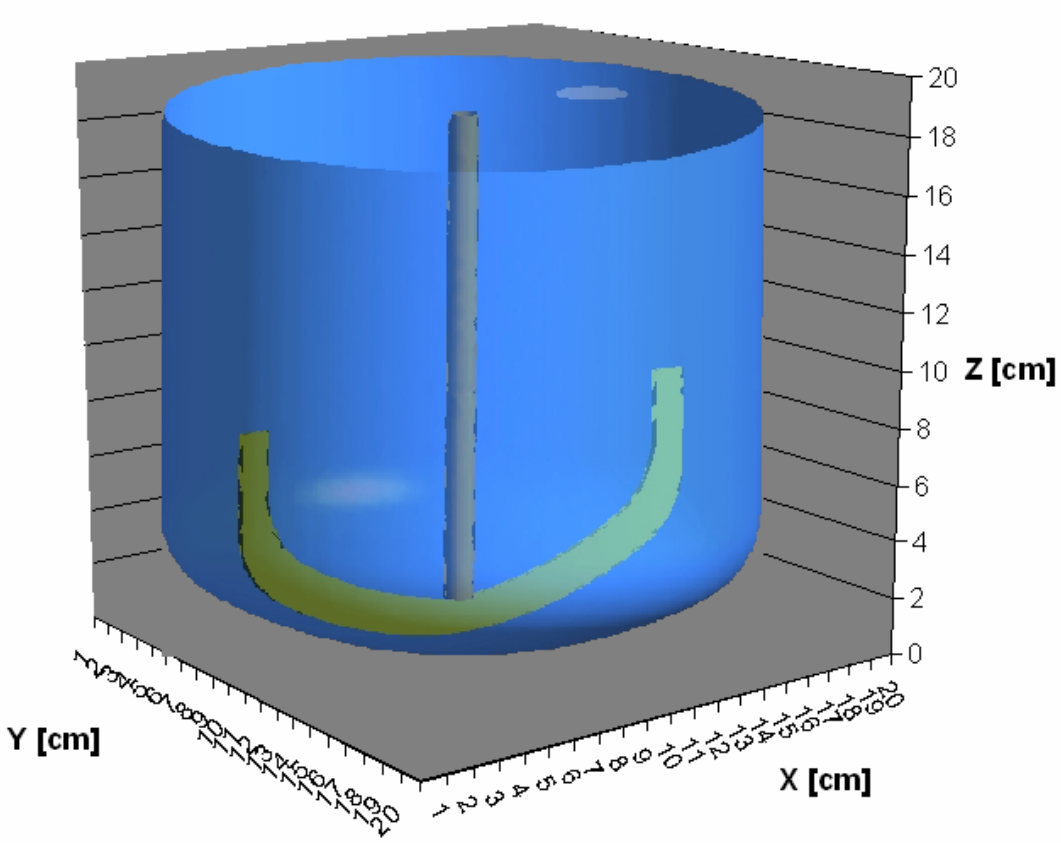

Figure 4.13: The full geometry in the 3-D coordinates.

To make connection between the two domains GGI (general grid interface) method is used. It is a physically based intersection algorithm to provide the complete freedom to change the grid topology and physical

distribution across the interfaces. This was done by creation three domain interfaces:

1- Wall top interface

2- Wall bottom interface

3- Cylindrical wall interface

Through these fluid-fluid interfaces all the calculated variables are transferred from the interface of the anchor to the corresponding interface of the tank i.e. from the top interface of the anchor to the top interface of the tank.

Transient rotor-stator model is a GGI frame change connection. It is used to calculate the velocity transfer from the rotating domain to the stationary domain. This model is important to account for transient interaction effects at a sliding (frame change) interface. It predicts the true transient interaction of the flow between the stator and rotor passage. The transient relative motion between the components on each side of the GGI connection is simulated. It accounts for all interaction effects between components that are in relative motion to each other. The interface position is updated each timestep, as the relative position of the grids on each side of the interface changes.

The initial and boundary conditions are the same as those for the half geometry. High resolution and second order Eulerian methods are used to control the solution for the equations of the used models and to get a good convergence with maximum residuals 0.001. The number of coefficient loops to get more precise results is 15.

5. RESULTS AND DISCUSSION

5.1 Experimental results

5.1.1 Mixture viscosities as a function of time and the determination of mixing times

5.1.1.1 Voltage / Viscosity calibration curves

The torque M of the shaft of the anchor impeller is determined when stirring pure glycerol in a BR at different temperatures between 10 °C and 50 °C. The viscosities η_G of glycerol at these temperatures are found in [47]. The torque M is measured as a voltage y_v and is shown in Tab. 5.1 for different temperatures.

Table 5.1: Viscosity and voltage values for pure glycerol at different temperatures.

Temperature ϑ [°C]	Voltage range y_v [mV]	Voltage net*) $y_{v,net}$ [mV]	Viscosity η_G [mPa s]
10	4996 – 5015	4851	3708
20	2435 – 2459	2293	1332
30	1452 – 1475	1309	564.5
40	1049 – 1056	899	274
50	841 – 848	691	139

*) $y_{v,net} = \tilde{y}_v - y_{v,0}$; $y_{v,0} = 154.1\,\text{mV}$.

At ϑ = 10 °C it is $\tilde{y}_v$ = (4996 + 5015) / 2 mV = 5005.5 mV.

The temperature dependence of y_v and η_G is shown in Figs. 5.1 and 5.2, respectively.

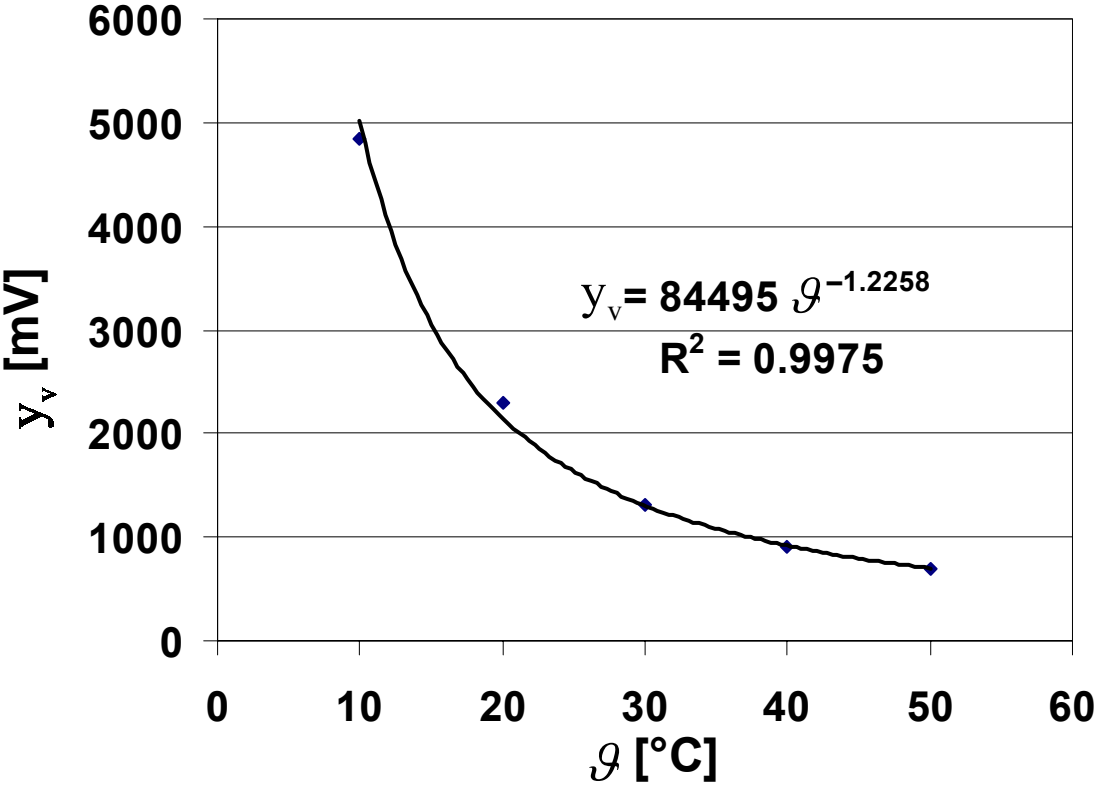

Figure 5.1: The measured y_v of pure glycerol as a function of temperature ϑ in a BR.

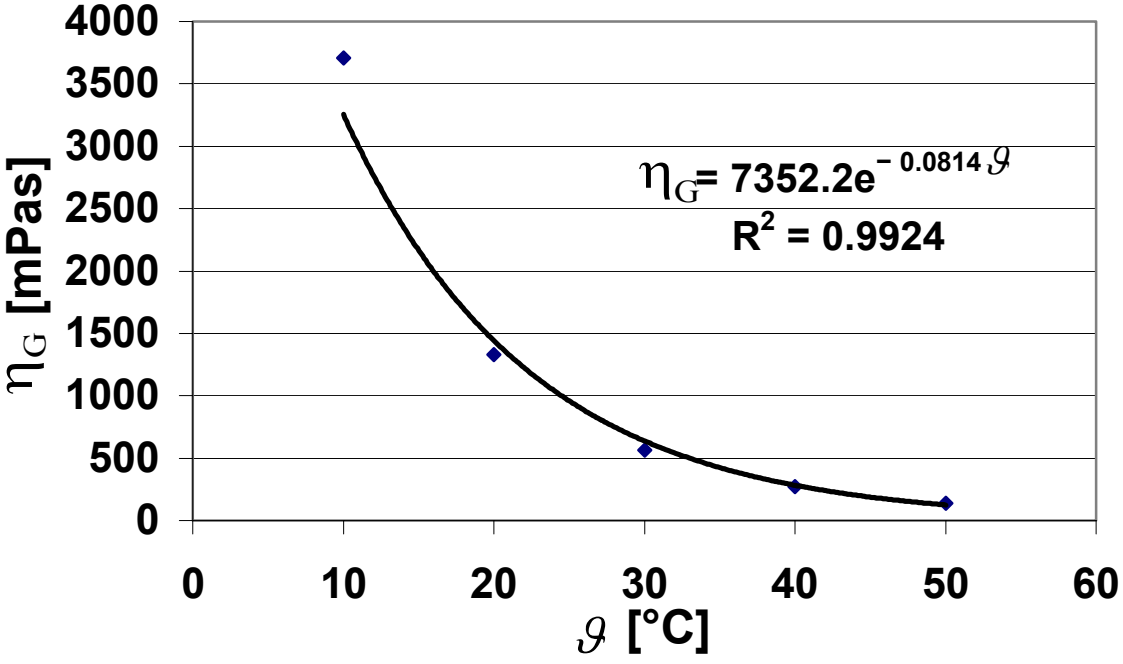

Figure 5.2: Viscosity η_G of pure glycerol as a function of temperature ϑ [47].

The relation between y_v and η_G is shown in Fig. 5.3. It shows a linear relationship with a root mean square $R^2 = 0.9973$.

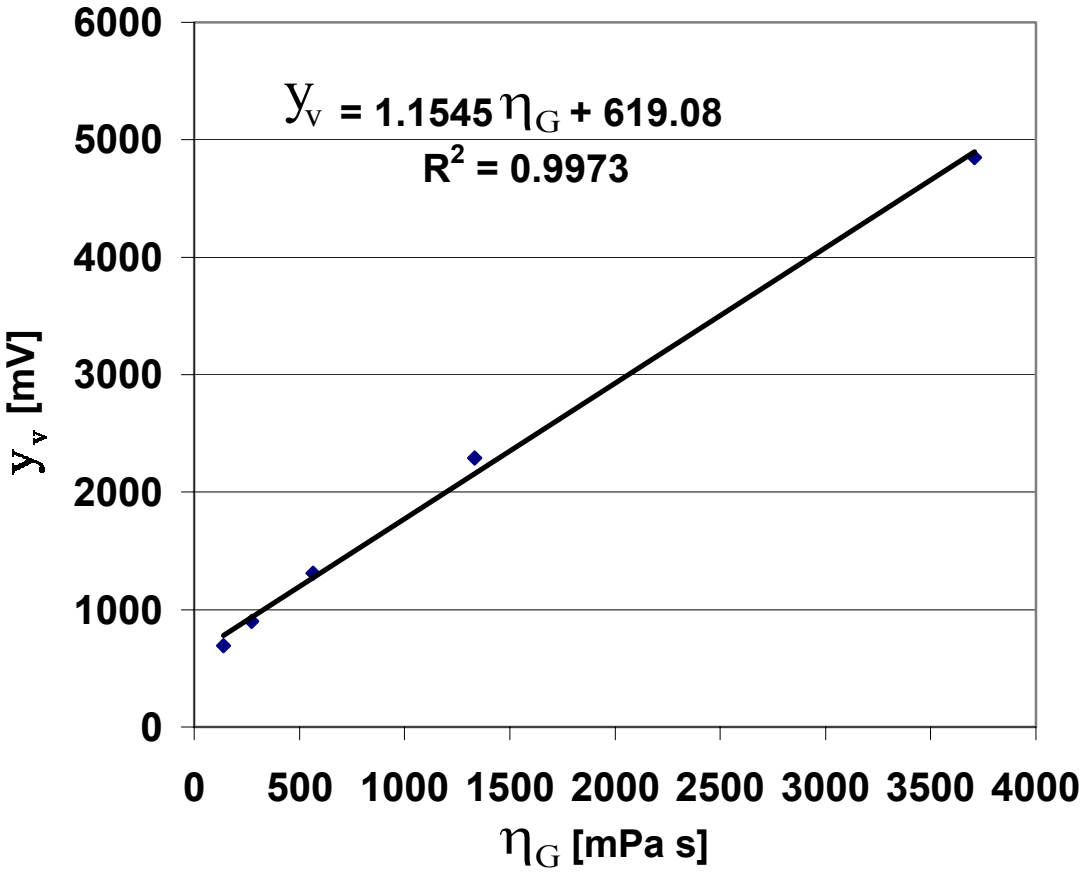

Figure 5.3: The calibration curve for pure glycerol.

From Fig. 5.3 it is possible to get any viscosity η_G value corresponding to any y_v value as a linear calibration curve which can be described by the following equation:

$$y_v = 1.1545\,\eta_G + 619.08. \qquad (5\text{-}1)$$

As an example for $y_v = 4851$ mV (s. Tab. 5.1) it follows from Eq. (5-1):

$$\eta_G = \frac{(y_v - 619.08)}{1.1545} \approx 3666\ \text{mPa s}.$$

5.1.1.2 Semibatch reactor

5.1.1.2.1 t_d = 5 s (26 vol% ethanol)

Two methods are used to determine the mixture viscosities $\eta_m(t)$ as a function of time and the mixing time t_m at ϑ = 21 °C, the torque method and the decolorisation method.

Torque method: The mixing behavior of ethanol and glycerol in a SBR with t_d = 5 s is characterized by measuring the transient mixture viscosity and mixing time with the torque method, also by visualizing the mixing behavior with a video camera. The mixture viscosity as a function of time is presented in Fig. 5.4. From this curve it can be seen the course of the mixing behavior. Also, it is possible to determine the viscosity of the ethanol/glycerol mixture at any time during the mixing process and to determine the mixing time which is required to get a constant viscosity of a homogeneous mixture.

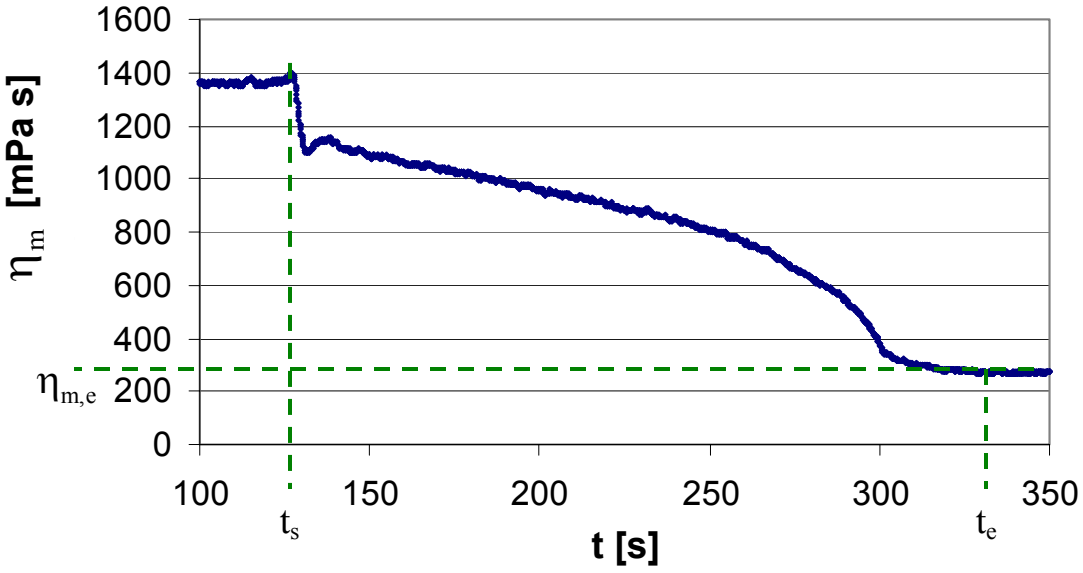

Figure 5.4: The measured mixture viscosity as a function of time for the determination of the mixing time of an ethanol/glycerol mixture in a SBR at t_d = 5 s (26 vol% ethanol).

Fig. 5.4 shows that the viscosity of pure glycerol before the addition of the second component ethanol has a constant value η_m = 1366 mPa s between $100\,s \leq t \leq 124\,s$. The dosage time is t_d = 5 s and the ethanol started from t_s = 124 s as a jet. The jet produce a local inlet pressure and cause a fast mixing, so that a viscosity decreases takes place through the period of the dosage time between $124\,s \leq t \leq 129\,s$ from η_m = 1366 mPa s up to η_m = 1110 mPa s. This sharp decreasing in the viscosity is due to the high pressure force and flow rate of the dosed ethanol. Between $129\,s \leq t \leq 280\,s$, the viscosity curve decreases slowly up to η_m = 600 mPa s caused by the mixing process.

Because of the density and viscosity difference, ethanol and glycerol form two layers. The upper layer of ethanol is the lighter one which has the low density and viscosity. The lower layer of glycerol is the heavier one which has the higher density and viscosity. After t = 280 s, the viscosity decreases again fast to reach the complete mixing at the time t_e = 332 s. The reason for this sharp decrease is the formation of a decreasing thickness layer of ethanol. The homogenization of the mixture takes place at t_e = 332 s with a final viscosity of η_m = 279 mPa s. Then the mixing time t_m is:

$$t_m = t_e - t_s = 332\,s - 124\,s = 208\,s. \quad (5\text{-}2)$$

Decolorisation method: Mixing time is determined when the yellow color of the liquid mixture disappeared and becomes colorless, that means all the iodine solution in glycerol has completely reacted with the stoichiometric amount of the sodium thiosulfate solution in the ethanol, if a complete homogeneous mixing is obtained. This mixing behavior as a function of time is determined with a video camera. Figs. 5.5-a and 5.5-b show this

behavior and it is possible to get the required mixing time if the liquid mixture of ethanol and glycerol becomes colorless and homogeneous. During the dosage of ethanol, part of the dosed ethanol is moved toward the impeller and dispersed in glycerol from the circumference which has the highest velocity towards to the shaft. After the dosage, the remaining part of ethanol forms a thin layer of a lower viscosity and density liquid. This layer is dispersed from the top end of the impeller toward to the shaft forming a symmetrical vortex around the shaft. This vortex becomes larger with time until a complete mixing is obtained. The mixing time from the decolorisation method is found to be $t_m = 206$ s which is very close to that obtained from the torque method $t_m = 208$ s.

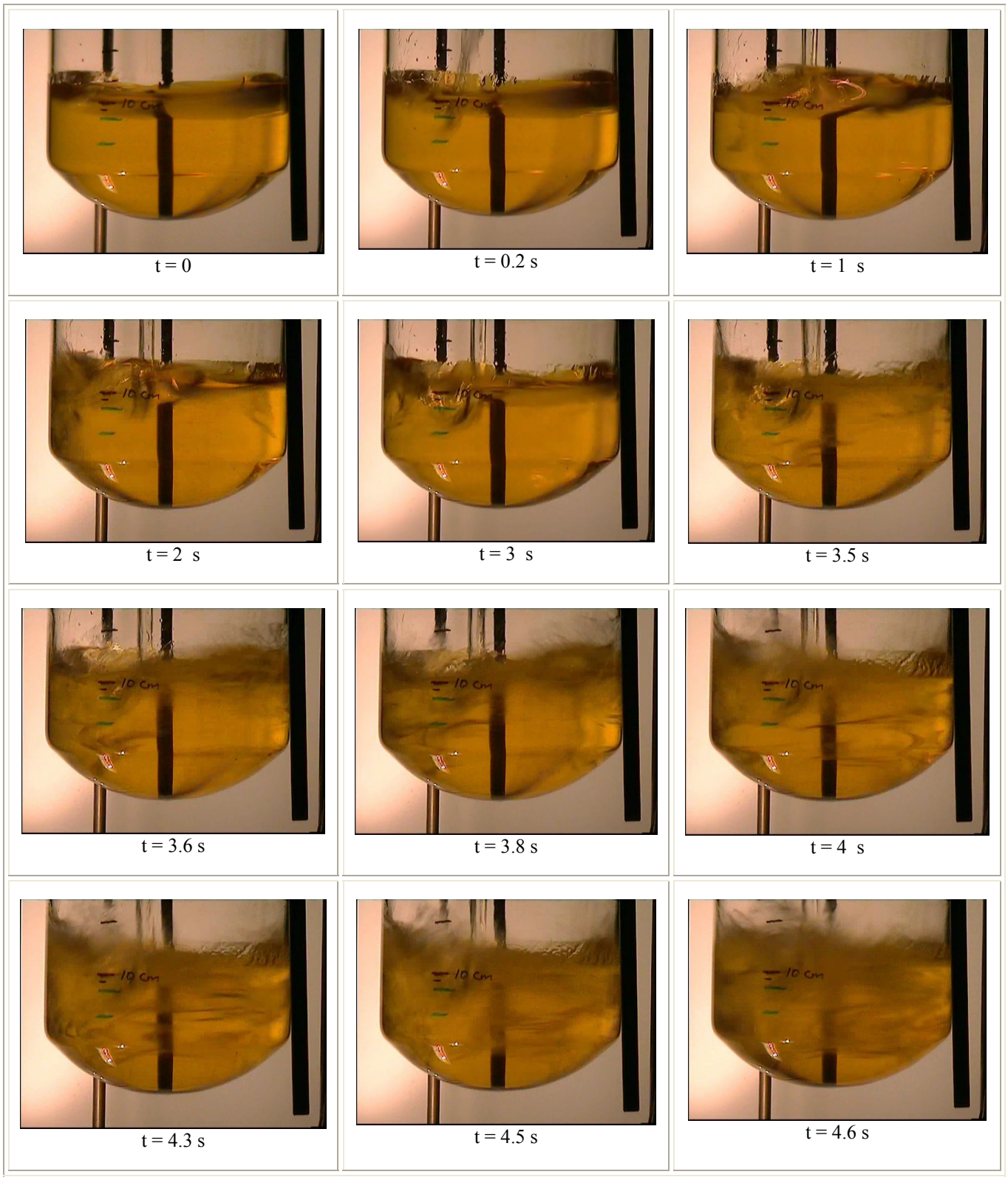

Figure 5.5-a: The dynamic mixing behavior of glycerol/ethanol in a SBR at t_d = 5 s (26 vol% ethanol) at different times t = 0 – 4.6 s, visualized by the decolorisation method.

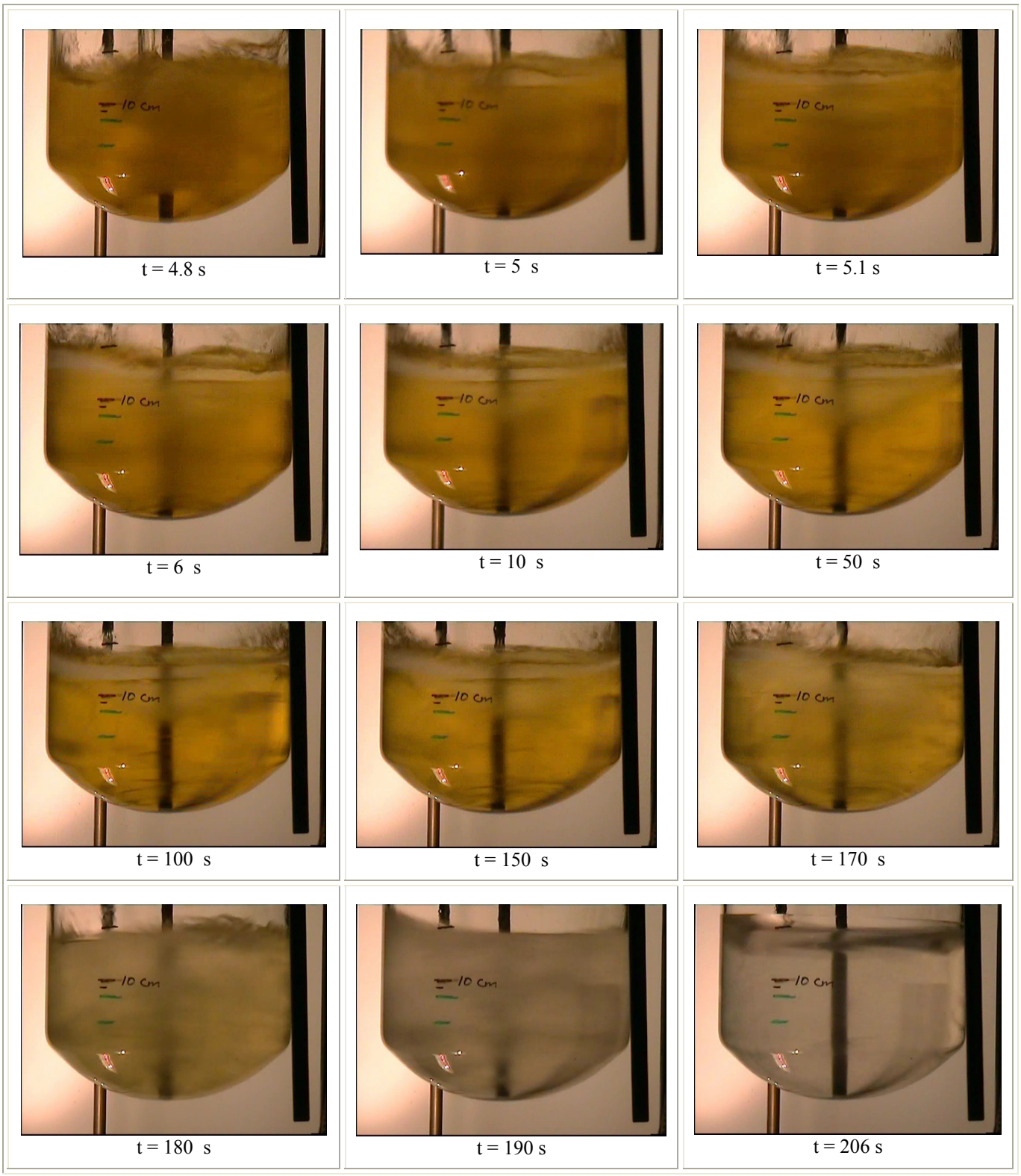

Figure 5.5-b: The dynamic mixing behavior of glycerol/ethanol in a SBR at t_d = 5 s (26 vol% ethanol) at different times t = 4.8 s – 206 s, visualized by the decolorisation method the decolorisation begins at t = 180 s.

5.1.1.2.2 t_d = 5 s (33 vol% ethanol)

The torque method is used to determine the mixture viscosity η_m as a function of time and mixing time at ϑ = 21 °C. This SBR with t_d = 5 s (33 vol% ethanol) is the same procedure to that mentioned in the previous section 5.1.1.2.1 with t_d = 5 s (26 vol% ethanol). The trend of the viscosity curve of time is shown in Fig. 5.6.

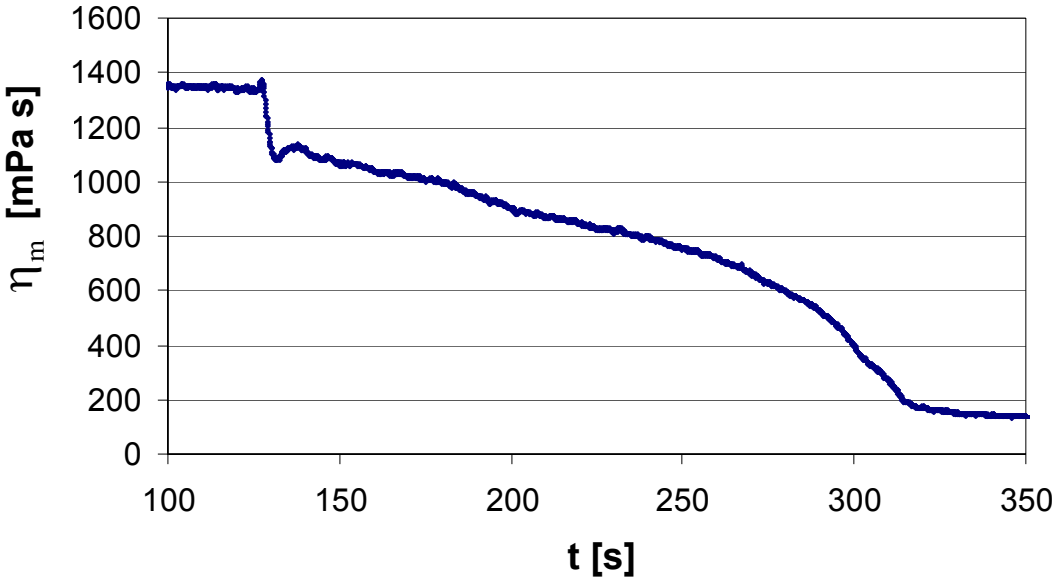

Figure 5.6: The measured mixture viscosity as a function of time for the determination of the mixing time of ethanol/glycerol mixture in a SBR at t_d = 5 s (33 vol% ethanol).

Fig. 5.6 shows that, the viscosity of pure glycerol before the addition of the second component ethanol has a constant value η_m = 1361 mPa s between 100 s ≤ t ≤ 128 s. The dosage time for ethanol started from t_s = 128 s as a jet, due to the developed jet with high inlet pressure through the inlet tube of 2.3 cm diameter, a fast mixing and viscosity decrease takes place in the period of the dosage time between 128 s ≤ t ≤ 133 s from η_m = 1361 mPa s up to η_m = 1093 mPa s. This sharp decreasing in the

viscosity is due to the high pressure force and flow rate of the dosed ethanol. Between 133 s ≤ t ≤ 310 s, the viscosity curve decreases slowly and the viscosity values decreases from η_m = 1093 mPa s at t = 133 s up to η_m = 716 mPa s at t = 260 s due to the disappearance of the inlet pressure force and the appearance of the buoyancy force effect which depends on the density difference between ethanol and glycerol.

Because of the density and viscosity difference, two layers of ethanol and glycerol are formed. The upper layer of ethanol is the lighter one which has the low density and viscosity. The lower layer of glycerol is the heavier one which has the higher density and viscosity. After t = 260 s, again the viscosity reduction increased strongly and fast to reach the final and the complete mixing, this is may be due to the gradual formation of the liquid mixture of ethanol/glycerol which has almost physical properties for the density and viscosity are close to the small layer which is found at t = 260 s. The homogenization of the mixture took place after t_e = 355 s and the final viscosity of this mixture is η_m = 134 mPa s. Then the mixing time t_m is:

$t_m = t_e - t_s$ = 355 s – 133 s = 222 s.

5.1.1.2.3 t_d = 10 s (33 vol% ethanol)

The torque method is used to determine the mixture viscosities η_m as a function of time and mixing time at ϑ = 21 °C. This SBR with t_d = 10 s is the same procedure to that mentioned in the previous sections 5.1.1.2.1 with t_d = 5 s (26 vol% ethanol) and 5.1.1.2.2 t_d = 5 s (33 vol% ethanol). The profile for the viscosity of the liquid mixture as a function of time is shown in Fig. 5.7.

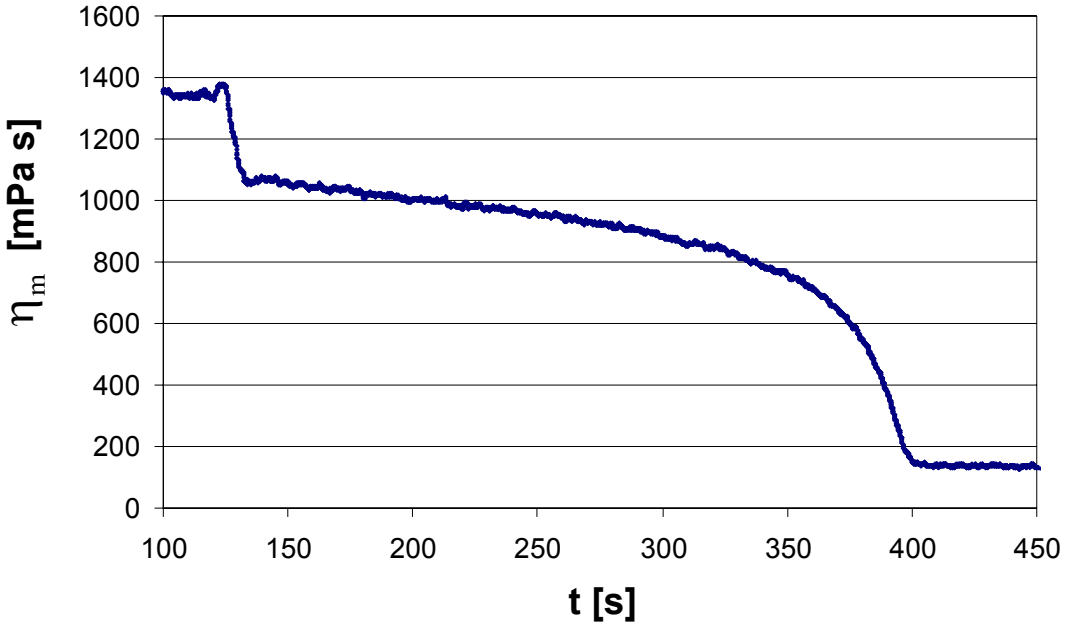

Figure 5.7: The measured mixture viscosity as a function of time for the determination of the mixing time of ethanol/glycerol mixture in a SBR at t_d = 10 s (33 vol% ethanol).

Fig. 5.7 shows that, the viscosity of pure glycerol before the addition of the second component ethanol has a constant value η_m = 1362 mPa s between 100 s ≤ t ≤ 120 s. The dosage time for ethanol started from t_s = 120 s as a jet, due to the developed jet with high inlet pressure through the inlet tube of 2.3 cm diameter, a fast mixing and viscosity reduction take place in the period of the dosage time between 120 s ≤ t ≤ 130 s from η_m = 1362 mPa s up to η_m = 1020 mPa s. This sharp decreasing in the viscosity is due to the high pressure force and flow rate of the added ethanol. Between 130 s ≤ t ≤ 350 s, the viscosity curve decreases slowly and the viscosity values decreases from η_m = 1020 mPa s at t = 130 s up to η_m = 815 mPa s at t = 350 s due to the disappearance of the inlet pressure force and the appearance of the buoyancy force effect which depends on the density difference between ethanol and glycerol.

Because of the density and viscosity difference, two layers of ethanol and glycerol are formed. The upper layer of ethanol is the lighter one which has the low density and viscosity. The lower layer of glycerol is the heavier one which has the higher density and viscosity. After t = 350 s, again the viscosity reduction increased strongly and fast to reach the final and the complete mixing at the time t_e = 402 s, this is due to a slow formation of the liquid mixture of ethanol/glycerol which has almost physical properties for the density and viscosity are close to the small layer which is found at t = 350 s. The homogenization of the mixture takes place at t_e = 402 s with a final viscosity mixture η_m = 130 mPa s. Then the mixing time t_m is:

$t_m = t_e - t_s = 402\ s - 120\ s = 282\ s.$

When comparing Fig. 5.6 with Fig. 5.7, it is clear that for t_d = 5 s (33 vol% ethanol) the flow rate of the added ethanol is higher from t_d = 10 s, the reduction in the viscosity in the period of dosing is the same because approximately the same quantity of ethanol is added for both dosage times. In the slow viscosity reduction period, the viscosity reduction for t_d = 5 s (33 vol% ethanol) is higher from t_d = 10 s, this is due to the higher inlet flow rate and pressure forces which force ethanol to distribute in glycerol and this forces reduce the effect of buoyancy forces and density differences. This also reduces the effect of drag forces and makes the mixing faster. As a result, as the dosing time decreases from t_d = 10 s to t_d = 5 s, the flow rate of the inlet flow increases from 0.129 L/s to 0.251 L/s, respectively. Also, the mixing time to get a homogeneous mixture decreases from t_m = 282 s to t_m = 222 s.

5.1.1.3 Batch reactor

5.1.1.3.1 H_l = 0.14 m (33 vol% ethanol)

Two methods are used to determine the mixture viscosities η_m as a function of time and the mixing time t_m at ϑ = 21 °C, the torque method and the decolorisation method.

Torque method: In a batch mixing process glycerol with iodine solution forms a yellow lower heavier layer at a height of H_G = 0.1 m and an ethanol layer with sodium thiosulfate solution at a height of H_E = 0.04 m above glycerol. The upper transparent lighter layer has a volume fraction of ethanol (33 vol% ethanol). Both layers are initially at t = 0 are stationary at a total liquid height H_l = 0.14 m , when the mixing started, ethanol started to diffuse in glycerol but very slowly due to the very large differences of density and viscosity and the very low kinetic energy of ethanol flow to glycerol. The velocity of the anchor impeller will transfer from the higher sublayers of ethanol with a large velocity that are close to the end of the anchor to the lower sublayers of ethanol with a lower velocity. The interface between the two liquid phases has a high surface tension, this needs a high force to destroy it, and to increase the dispersion and diffusion of ethanol in glycerol, and this requires very a long time of mixing to reach to this point.

This behavior is illustrated in Fig. 5.8 which represents the transient viscosity as a function of time. When the mixing started, the mixture viscosity is η_m = 1047 mPa s at t = 0, a very slow decrease for the viscosity due to the slow diffusion of ethanol in glycerol because of the low slip velocity of ethanol up to t = 270 s. After t > 270 s a faster mixing occurred because the interface between ethanol and glycerol is destroyed and then

ethanol dispersed in glycerol much easier leading to a homogeneous mixture with viscosity η_m = 110 mPa s at t_m = 342 s.

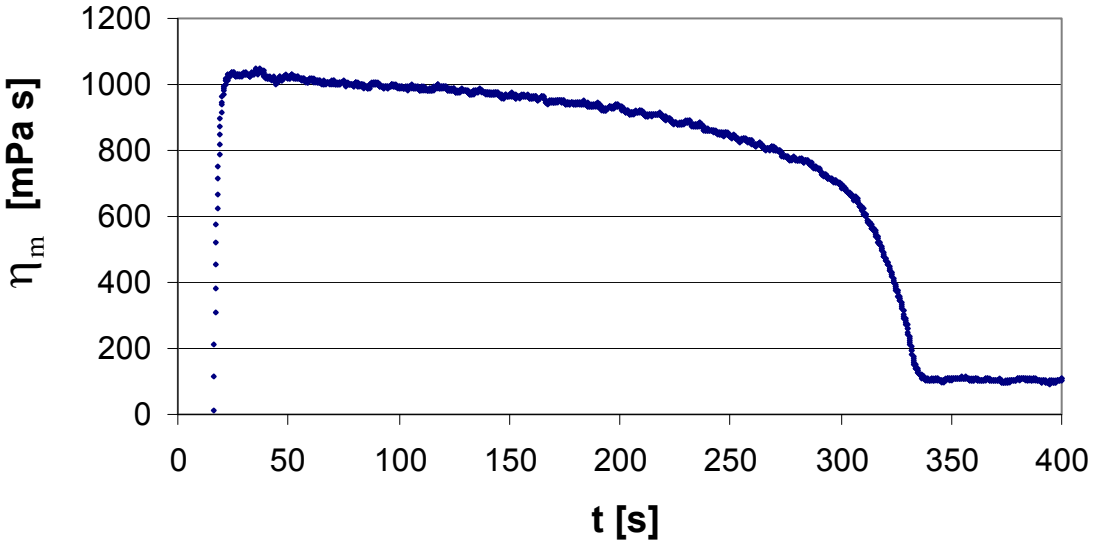

Figure 5.8: The measured mixture viscosity as a function of time for the determination of the mixing time of ethanol/glycerol mixture in a BR with H_l = 0.14 m.

Decolorisation method: The dynamic mixing behavior is visualized by a video camera as can be shown in Figs. 5.9-a and 5.9-b as a function of time. Initially at t = 0, the two distinct liquid phases are distinguished as described in the previous section. When the anchor stirer starts with a constant speed at ω = 150 rpm, the ethanol at the interface with glycerol starts to disperse from the top ends of the vertical blade which have the highest shearing forces to push ethanol in glycerol forming a vortex symmetrically to the shaft at the interface between the two liquid phases which increases with mixing time i.e. becomes wider and longer. Large numbers of filaments are formed and spread from the shaft of the stirrer towards the vessel wall. This elongated filaments or ethanol droplets are transformed into a set of ellipsoidal or more complex structures [55]. As the velocity or the impeller

shear forces transfer to the top surface of ethanol layer, oscillations are formed at the top surface of the light layer during the mixing process. After 4 minutes, the colourless lighter layer (ethanol) split and a faster mixing occurs with the yellow heavier layer (glycerol) to get one colourless homogeneous liquid phase (s. Fig. 5.9-b, t = 312 s). The mixing time from the decolorisation method is found to be t_m = 340 s which is very close to that obtained from the torque method t_m = 342 s.

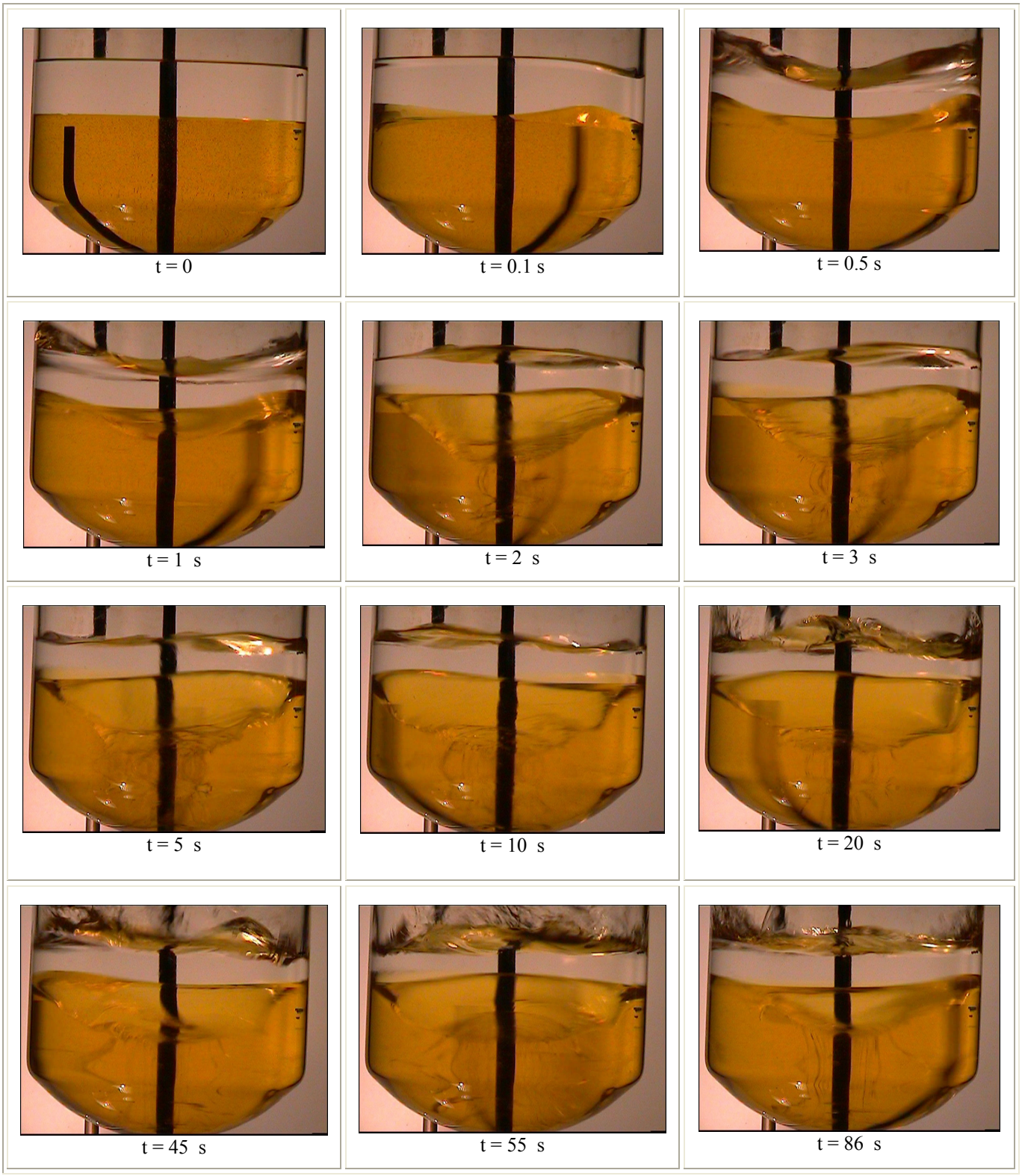

Figure 5.9-a: The dynamic mixing behavior (pan cake effect) of glycerol/ethanol in a BR with H_l = 0.14 m (33 vol% ethanol) at different times t = 0 – 86 s, visualized by the decolorisation method.

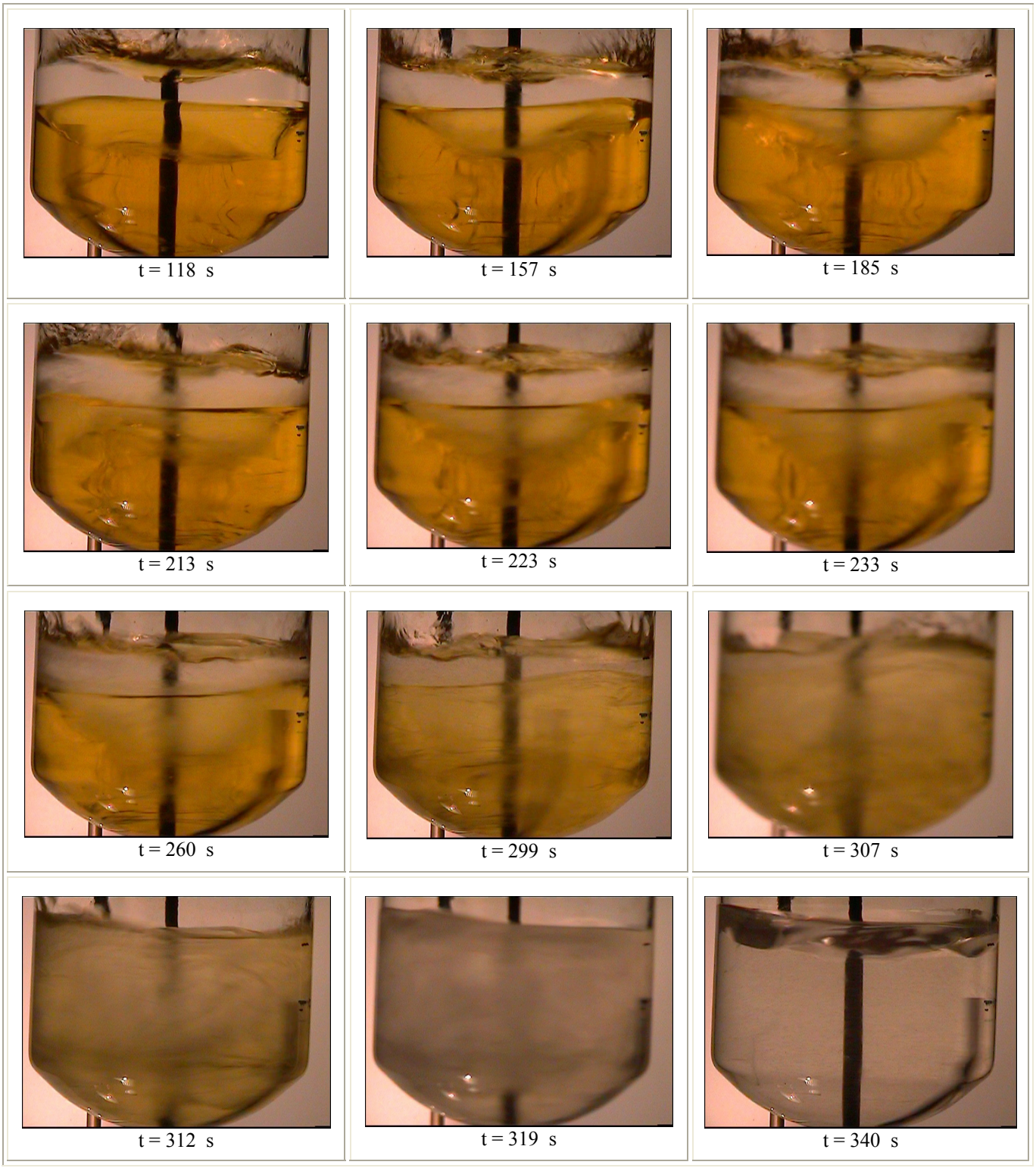

Figure 5.9-b: The dynamic mixing behavior (pan cake effect) of glycerol/ethanol in a BR with H_l = 0.14 m (33 vol% ethanol) at different times t = 118 s – 340 s, visualized by the decolorisation method, the decolorisation begins at t = 312 s.

5.1.1.3.2 H_l = 0.09 m (33 vol% ethanol)

Two methods are used to determine the mixture viscosities η_m as a function of time and the mixing time t_m at ϑ = 21 °C, the torque method and the decolorisation method.

Torque method: The same volume fractions of ethanol and glycerol (33 vol% ethanol) are used in this experiment with H_l = 0.09 m as well as in the previous part H_l = 0.14 m. Ethanol and glycerol volume fractions are 0.33 and 0.67, respectively. The transient mixture dynamic viscosity is shown in Fig. 5.10; the unsteady and unstable mixing performance is due to the turbulent flow in the BR because the total liquid height is at the top end for the vertical arm of the anchor. That means all the liquid moves with the same anchor speed and this causes the mixing process of ethanol/glycerol faster. The mixing time in the case of torque method is t_m = 20 s.

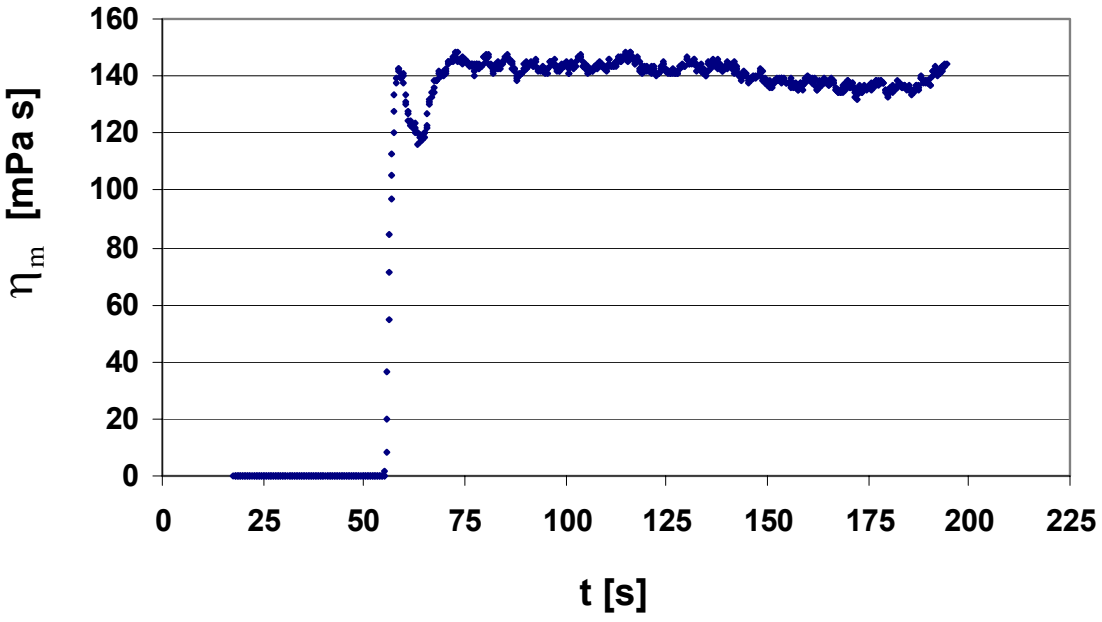

Figure 5.10: The measured mixture viscosity as a function of time for the determination of the mixing time of ethanol/glycerol mixture in a BR with H_l = 0.09 m.

Decolorisation method: Here it can be seen (s. Figs. 5.11-a and 5.11-b) that the mixing behaviour is completely different from the mixing when the total liquid height is 0.14 m for the same volume fractions of the two layers of ethanol and glycerol. This happens because the shear force of the anchor impeller (which ends here with the upper ethanol level) due to its rotational speed ω = 150 rpm has a dominant effect on the mixing behavior. This force destroyed the interface between the two liquids and leads to an effective distributing of the two liquids in each other, so that one homogeneous transparent liquid phase occurs in a very short time. The mixing time from the decolorisation method is t_m = 17 s.

Viscosity and density differences in this case do not remarkably increase the mixing time, because all liquids are in the region where both shear stresses and turbulence intensities are high [55]. This implies that a deformation of the interface is not the limiting factor in this mixing process. This is confirmed by visualization photographs in Figs. 5.11-a and 5.11-b, which shows that the deformation is very fast. Also, when all the liquid is transported to the stirrer, the homogenization time depends on the rate of distribution of ethanol [68].

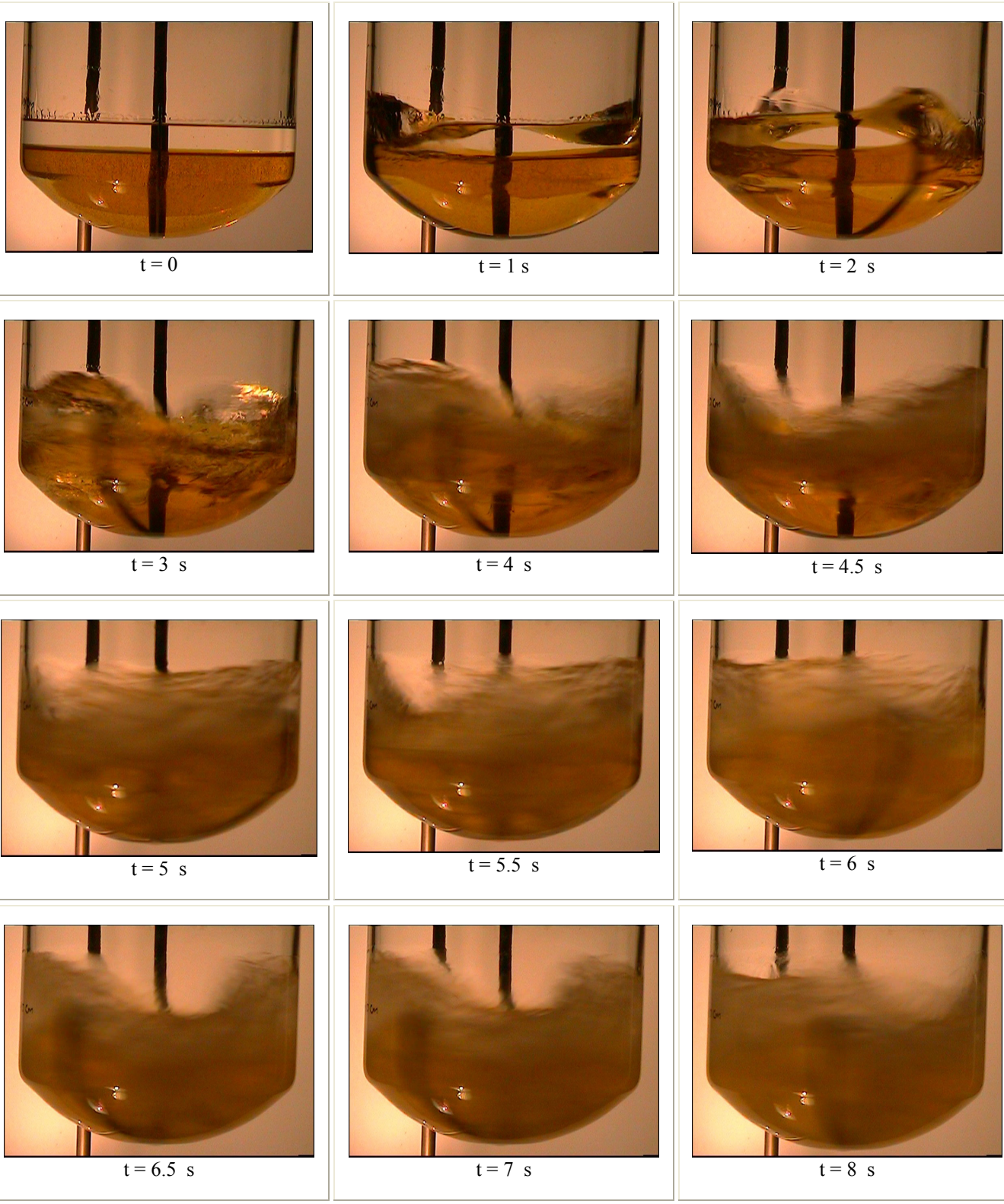

Figure 5.11-a: The dynamic mixing behavior of glycerol/ethanol in a BR with H_l = 0.09 m (33 vol% ethanol) at different times t = 0 – 8 s, visualized by the decolorisation method.

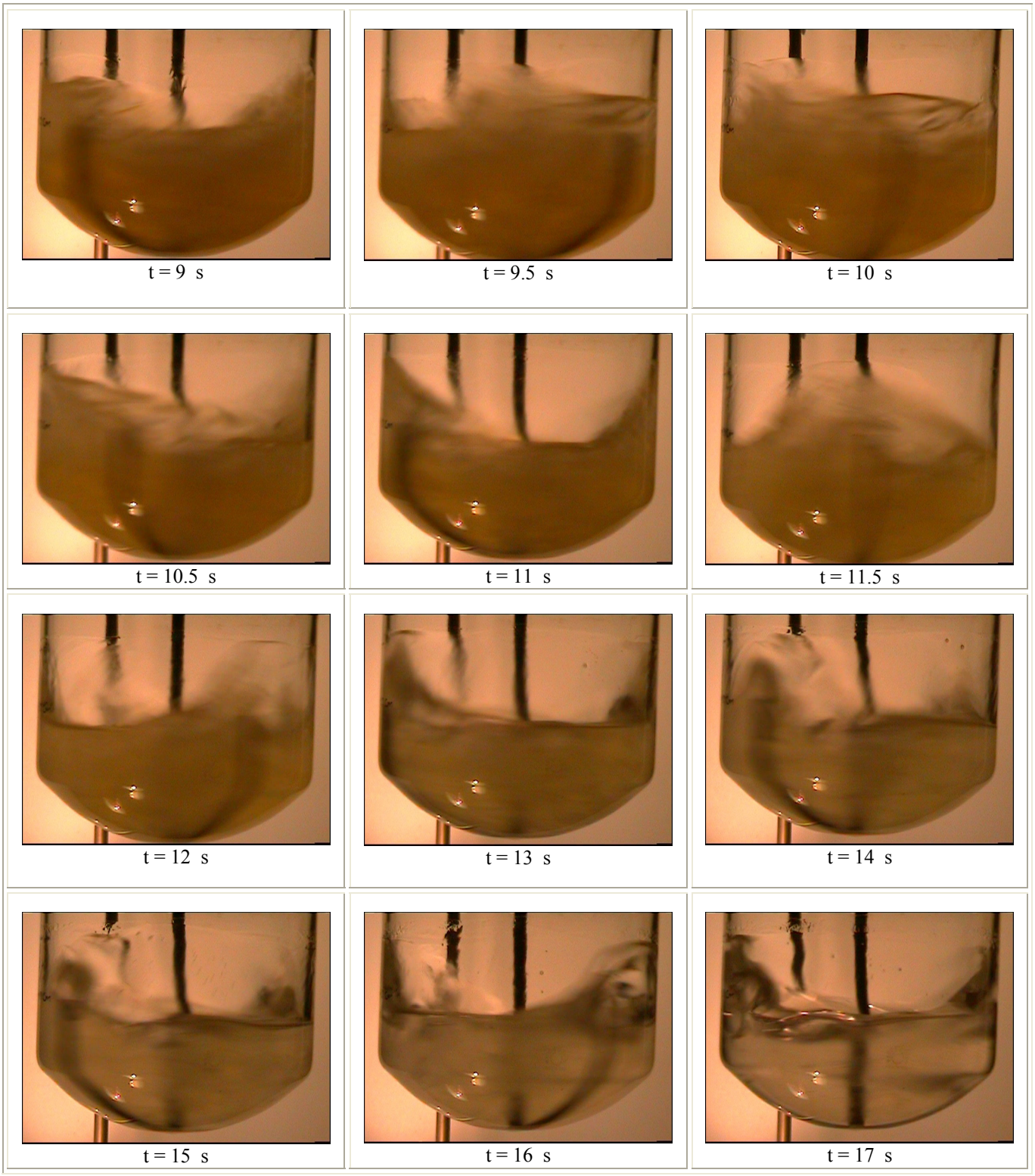

Figure 5.11-b: The dynamic mixing behavior of glycerol/ethanol in a BR with H_l = 0.09 m (33 vol% ethanol) at different times t = 9 s – 17 s, visualized by the decolorisation method, the decolorisation begins at t = 15 s.

5.1.2 Visualization of the dynamic behavior of pure glycerol in a BR

The dynamic behavior of the pure glycerol in a BR with anchor impeller is visualized with a digital video camera. Different pictures are taken every 0.2 s. From Fig. 5.12 it can be recognized that a vortex is formed outside of the shaft (in the center) and becomes larger with increasing time.

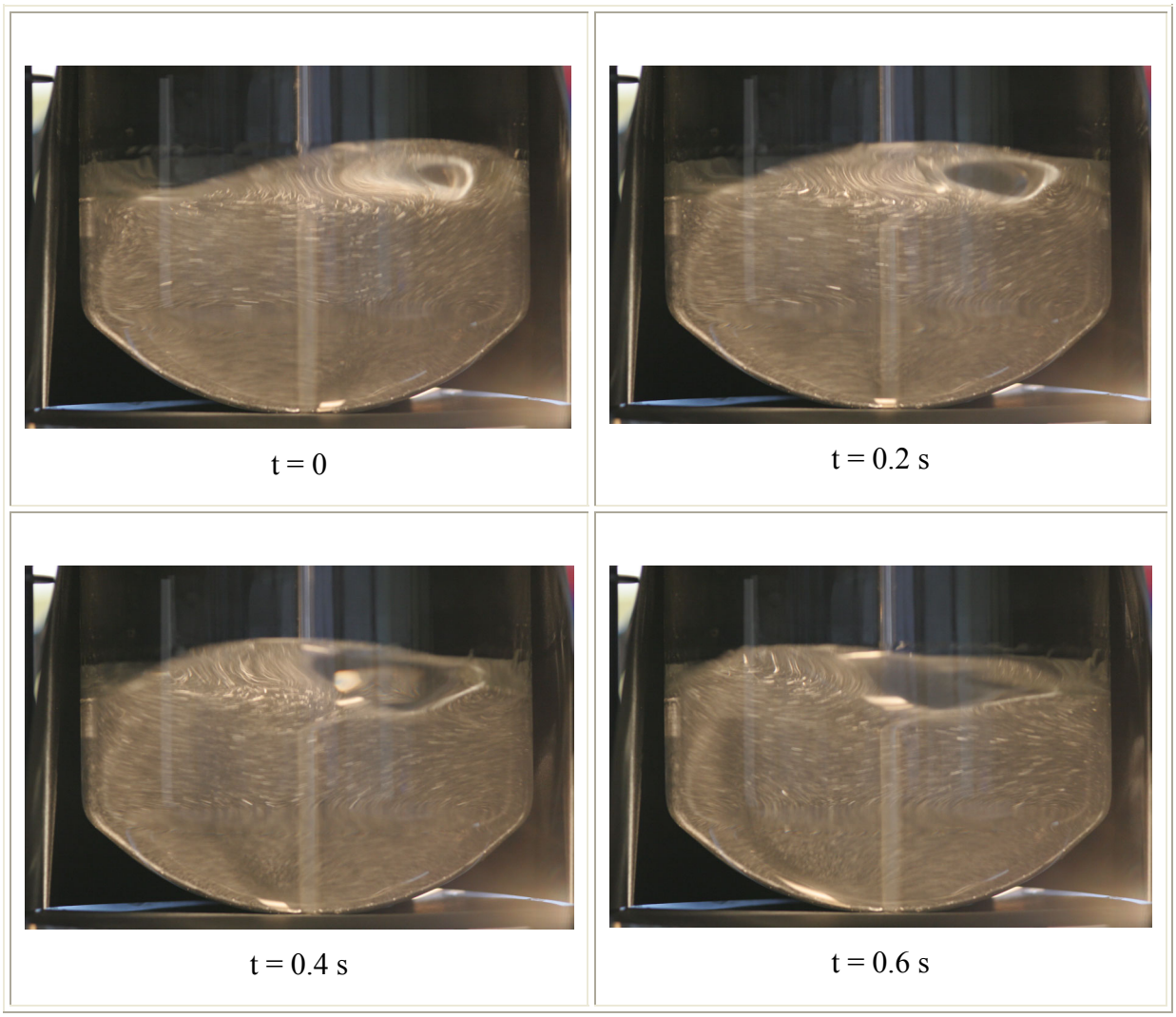

Figure 5.12: Visualization of the dynamic behavior of pure glycerol in a BR with anchor impeller at t = 0, 0.2, 0.4 and 0.6 s.

The surface of glycerol is nearly plane outside of the vortex, caused by the relatively large viscosity η_G of glycerol.

The bottom of the vessel is curved, so that the distance between the blades and the vessel is very small to allow the blades of the anchor impeller to work as a scraper for the viscous glycerol. The direction of anchor rotation is clock wise. The primary flow (Fig. 5.13) in the glycerol is tangential which can be seen from the top view; it is created by the rotation of the horizontal blade. From the front view, the secondary flow (axial and radial) can be recognized (Fig. 5.13). The flow of the glycerol from the tip of the anchor blade at point 1 is directed to the liquid in the vicinity to point 2, then to the vessel wall at point 3 forming a vortex between the points 1, 2 and 3. A second vortex is formed between the points 4, 5 and 6 with an opposite rotation direction.

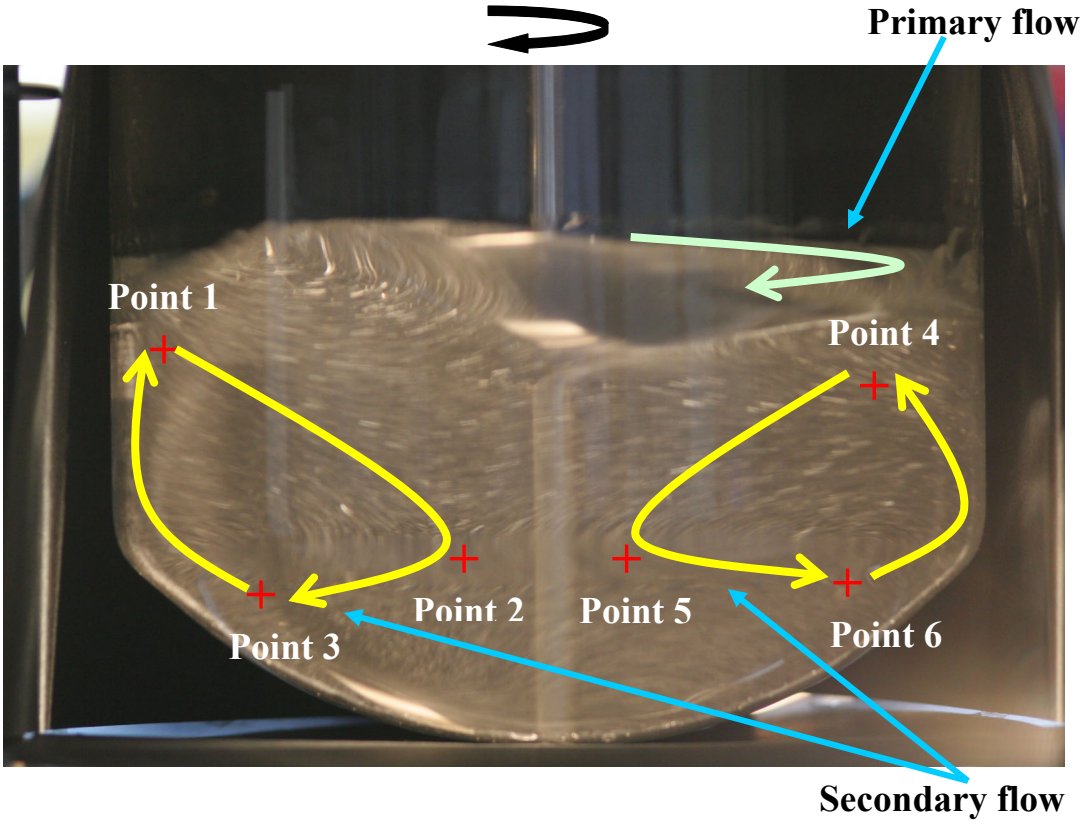

Figure 5.13: The formation of a primary- and secondary flow in pure glycerol in a stirred BR.

5.2 Important quantities influencing the mixing behavior predicted by CFD Simulation

The following simulations are done in half geometry by using transport model (s. Chap. 4.1.3.4.4) and viscosity model (s. Eq. 4-2) for ideal mixture to reduce the required time for numerical solution (CPU time t_{CPU}). The aim of these simulations is to study the effect of the grid size and cells number on CPU time, and to determine the best mixing requirements such as dosage time, inlet tube diameter, anchor velocity and the width of the impeller in the case of SBR, in addition to the effect of different mixture ratios of glycerol to ethanol in the case of BR. The calculated results are analyzed and discussed in detail (s. Chap. 5.2.1 – 5.3).

5.2.1 Semibatch reactor

5.2.1.1 The effect of mesh refinement and cells number

The grid is generated by using ICEM CFD program. Unstructured tetrahedral cells are adapted because this type of grid is suitable for complex geometries which need fine mesh. Different grids in the range between 16,000 – 600,000 tetrahedron cells are used to test their effects on the CPU time and the calculated mixing time t_m, viscosity- and velocity fields in SBR at t_d = 1 s. The grids, the cell size and CPU time in each case are shown in Figs. 5.14 – 5.19. Mesh refinement, e.g. from 5 mm to 2.5 mm cell size, at the interface between the air and the liquid mixture phases is very important to give a sharp distinction between the two phases. Also, the deformation of the liquid mixture at the interface is studied and can be visualized in CFX-post.

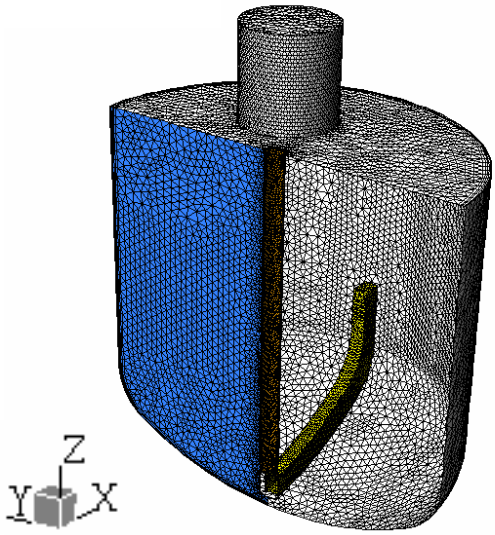

Figure 5.14: The half geometry in the 3-D coordinates with number of cells of 622,994 tetrahedrons, cell size of 1 mm and t_{CPU} = 20 d.

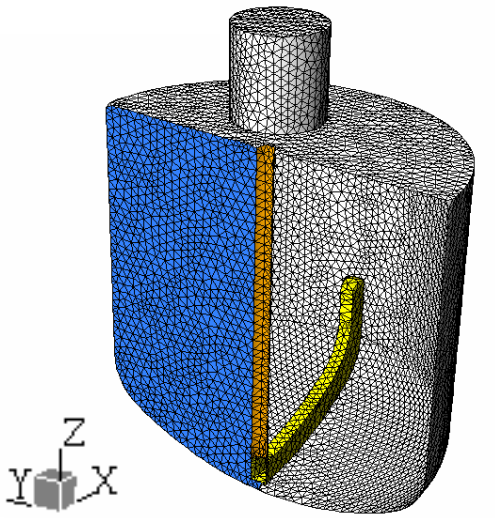

Figure 5.15: The half geometry in the 3-D coordinates with number of cells of 326,768 tetrahedrons, cell size of 5 mm and t_{CPU} = 10 d.

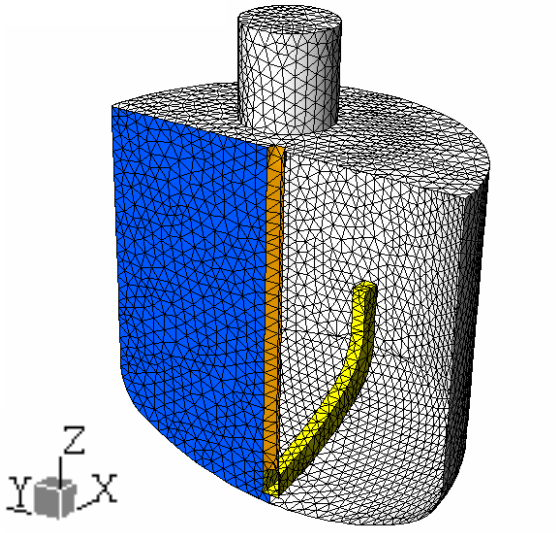

Figure 5.16: The half geometry in the 3-D coordinates with number of cells of 119,327 tetrahedrons, cell size of 7 mm and t_{CPU} = 5 d.

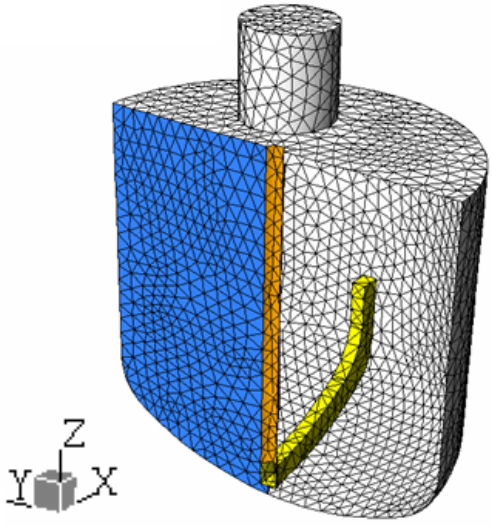

Figure 5.17: The half geometry in the 3-D coordinates with number of cells of 58,127 tetrahedrons, cell size of 9 mm and t_{CPU} = 3 d.

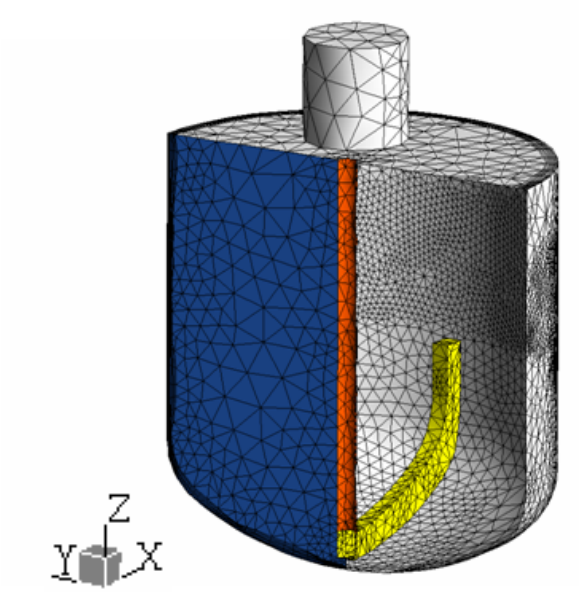

Figure 5.18: The half geometry in the 3-D coordinates with number of cells of 26,000 tetrahedrons, cell size of 15 mm with double refinements at the interface and t_{CPU} = 2 d.

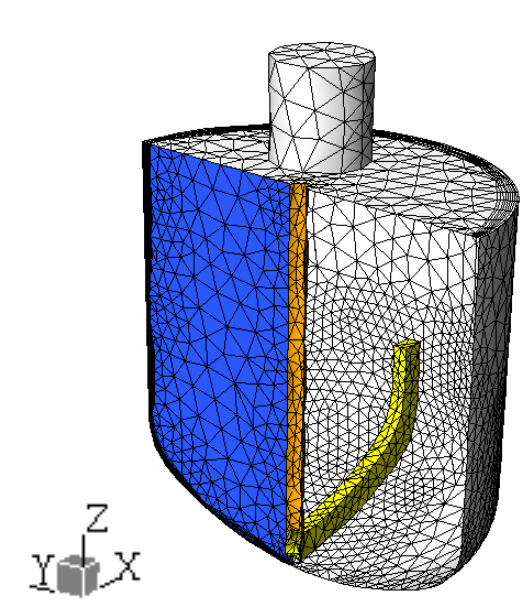

Figure 5.19: The half geometry in the 3-D coordinates with number of cells of 15,828 tetrahedrons, cell size of 17 mm with refinements at the bottom and t_{CPU} =1 d.

The effect of the cells number on the viscosity- and velocity fields for the liquid mixture of ethanol and glycerol is studied in a SBR at anchor velocity of 150 rpm, inlet tube diameter of 5 cm, inlet ethanol velocity of 0.64 m/s and dosage time of 1 s. It is found that as the cell size increases from 1 mm in case of about 600,000 cells to 17 mm in case of about 16,000 cells, the required time for the numerical solution decreases from t_{CPU} = 20 d to t_{CPU} = 1 d as shown in Fig. 5.20.

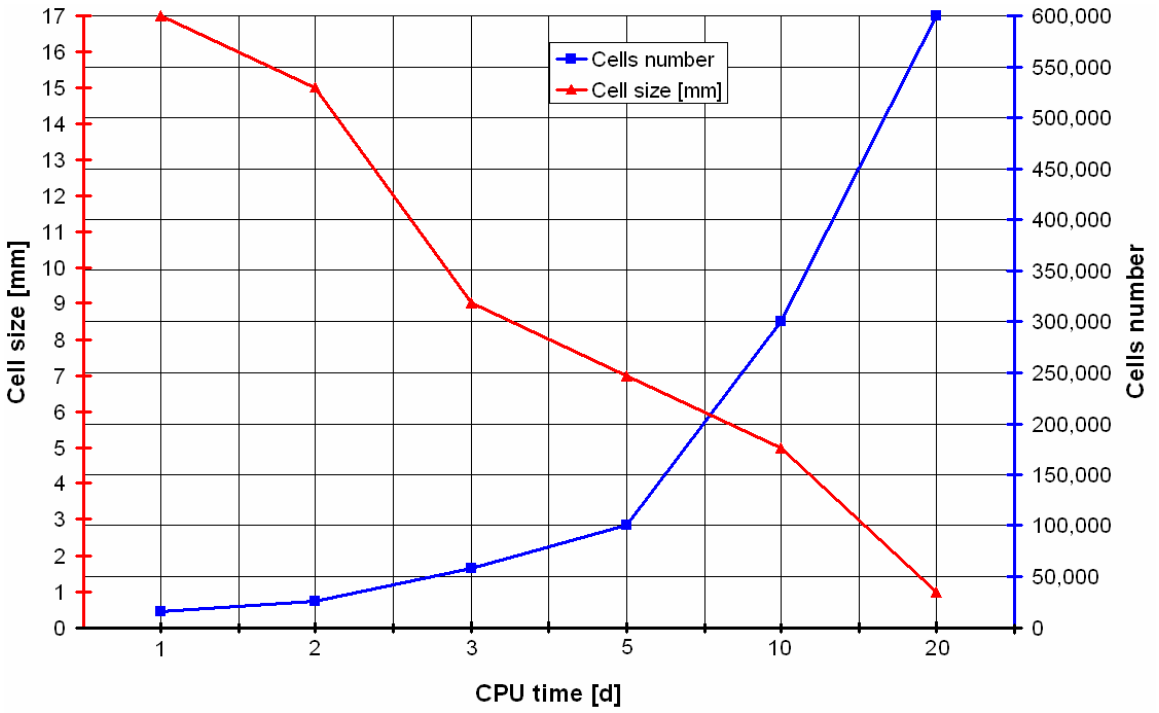

Figure 5.20: The effect of cells number and mesh size on the time requirements of numerical solution (CPU).

The flow- and viscosity fields for cells number of 26,000 and 600,000 tetrahedrons are shown in Fig. 5.21. For 600,000 tetrahedron cells, a sharper and more distinct interface between the liquid mixture and air is obtained. For both cells number the velocity fields are similar. In both cases the radial and axial secondary flows are produced by the anchor impeller before and during the dosage of ethanol, and new circulations near the maximum curvature of the blade of the impeller are formed after the dosage. The dosed ethanol flows towards to the impeller from the circumference forming eddies or vortices in the vicinity between the impeller and the shaft. The liquid mixture volume fraction field (contour surface plot), the dynamic viscosity field (contour lines) and velocity field (vectors) are shown in Fig. 5.21 during the dosage period from t = 0.2 s to 1.2 s. After t = 1.2 s the liquid mixture reaches a constant dynamic viscosity and a homogeneous mixture

(the liquid has a completely green colour) in case of 600,000 tetrahedron cells at t_m = 8 s faster than in the case of 26,000 cells at t_m = 13 s.

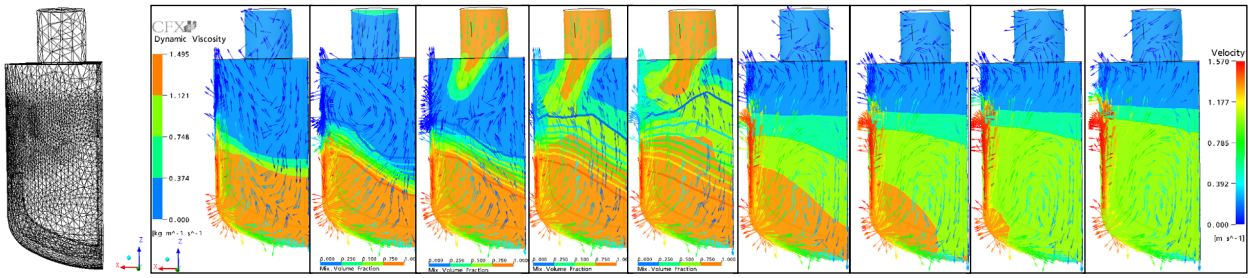

(a) 26,000 tetrahedrons cells

t = 0.1 s 0.2 s 0.3 s 0.7 s 1.2 s 5.0 s 8.0 s 10 s 20 s

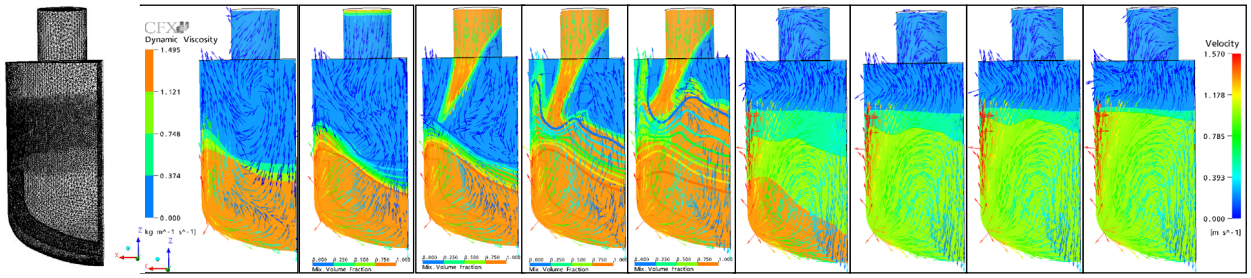

(b) 600,000 tetrahedrons cells

Figure 5.21: Effect of cells number on the mixture viscosity- and mixture velocity fields on xz-plane at y = 0.03 m for t_d = 1 s in SBR for (a) 26,000 and (b) 600,000 tetrahedrons

The calculated mixture dynamic viscosities η_m and mixture velocities u_m as a function of time t for cells number 26,000 and 600,000 tetrahedrons can also be shown in Fig. 5.22. Initially at t = 0 pure glycerol is stirred for 0.2 s, its viscosity remains constant at 1.495 Pa s. From the beginning of the dosage at t = 0.2 s ethanol is added, then the viscosity of the mixture η_m decreases sharply to reach the minimum of 0.81 Pa s and 0.91 Pa s for 600,000 and 26,000 tetrahedron cells, respectively at t = 1.2 s (the end of the dosage). This decrease of η_m is caused by the high initial momentum of the ethanol jet which enhance the mixing process. After the dosage, the

viscosity η_m increase gradually because the shear forces of the rotating anchor impeller dominate in the mixing and the buoyancy effect rise part of ethanol to the surface of the liquid mixture. A complete mixing is obtained when a constant mixture viscosity of $\eta_m = 0.980$ Pa s and $\eta_m = 1.067$ Pa s at $t_m = 8$ s and 13 s for 600,000 and 26,000 tetrahedron cells, respectively are found. The velocity u_m increases when the viscosity η_m decreases. Small differences in the calculated velocities and viscosities for both cell numbers is concluded, while the $t_{CPU} = 20$ d for 600,000 cells and $t_{CPU} = 2$ d for 26,000 cells. Therefore it is used the 26,000 cells for all calculations.

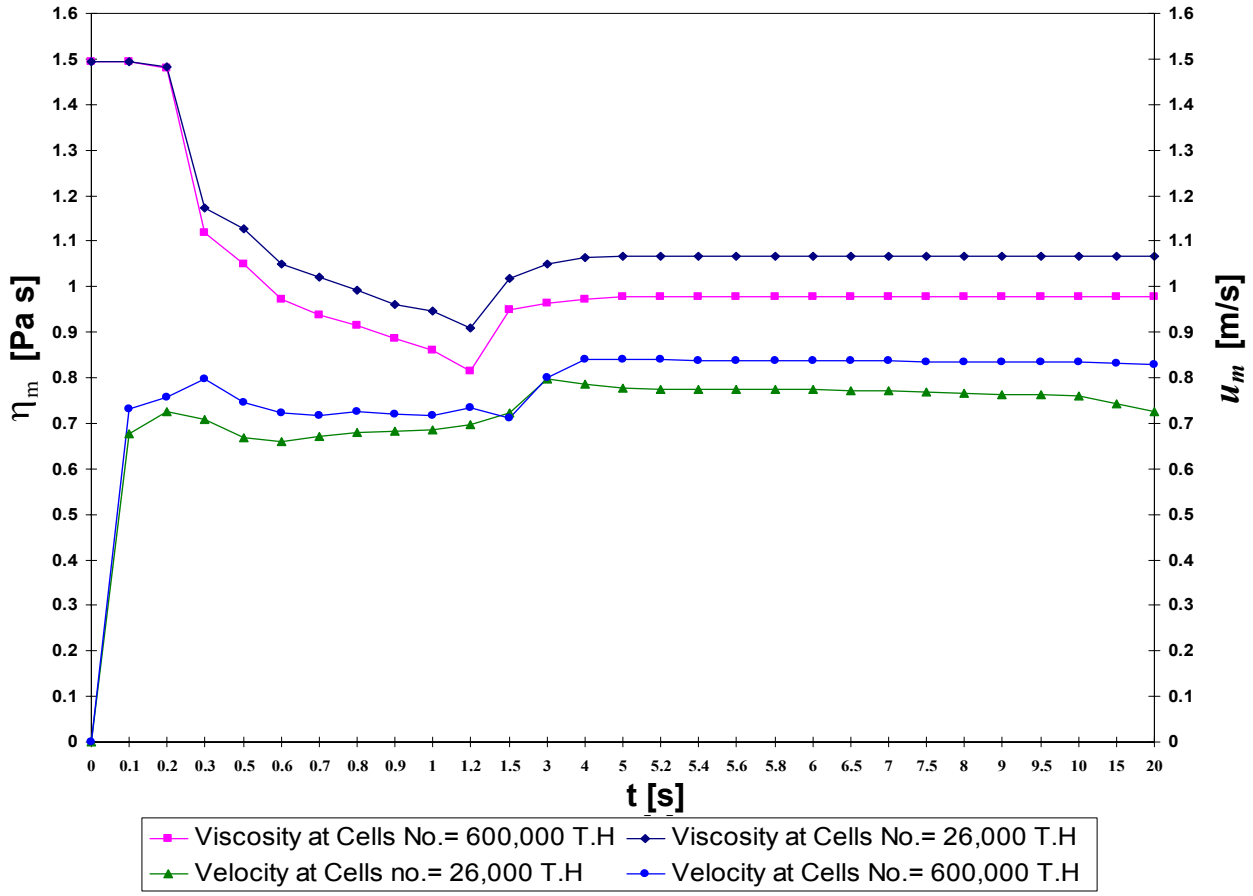

Figure 5.22: Flow velocity and mixture viscosity as a function of time on xz-plane at y = 0.03 m for 600,000 and 26,000 tetrahedron cells number (T.H).

5.2.1.1.1 Flow field pattern for 26,000 cells

For calculation the following results, the grid of 26,000 tetrahedron cells are used including a refinement above the top end of the impeller to get more precise calculations at the interface between the air and the liquid mixture are shown in Fig. 5.23.

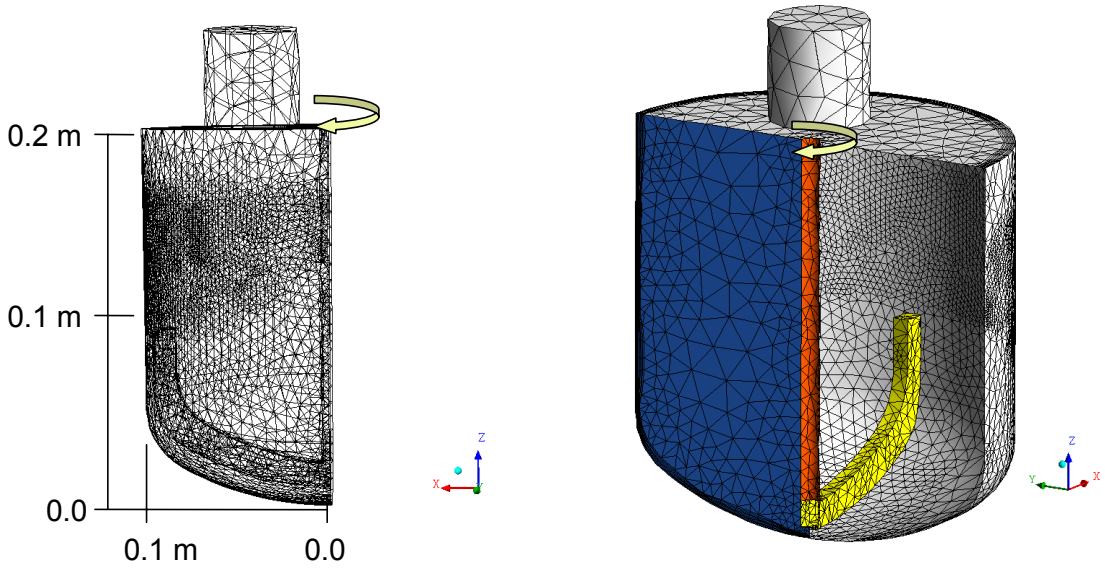

Figure 5.23: Grid of 26,000 tetrahedron cells including a refinement at the interface of air and liquid mixture, side view (left) and front view (right)**.**

The dynamic viscosity field is used to predict the interface between air and glycerol at t = 0 as shown in Fig. 5.24. The SBR at t_d = 1 s ($0.2\,s \le t_d \le 1.2\,s$) contains at t = 0 pure glycerol with height until 0.1m. The hydrostatic pressure-, viscosity- and flow velocity axial profiles at t = 0 are shown in Fig. 5.25. According to the initial boundary condition for the hydrostatic pressure field, the maximum absolute pressure of p_{abs} = 900 Pa which is calculated by CFD ($p_{tot} = p_{abs} + p_{ref}$ = 102,225 Pa where p_{ref} = 101,325 Pa) is found near the bottom of the vessel and it decreases to p_{abs} = 0 (where p_{tot} = 101,325 Pa) for z > 0.1 m. The flow velocity is u_m = 0 because the impeller is stationary at t = 0. A constant viscosity η_m = 1.495 Pa s for

pure glycerol exists between $0 \leq z \leq 0.1\,\text{m}$. The decrease of the viscosity profile at z = 0.1 m is not vertical because the space resolution at the interface is limited.

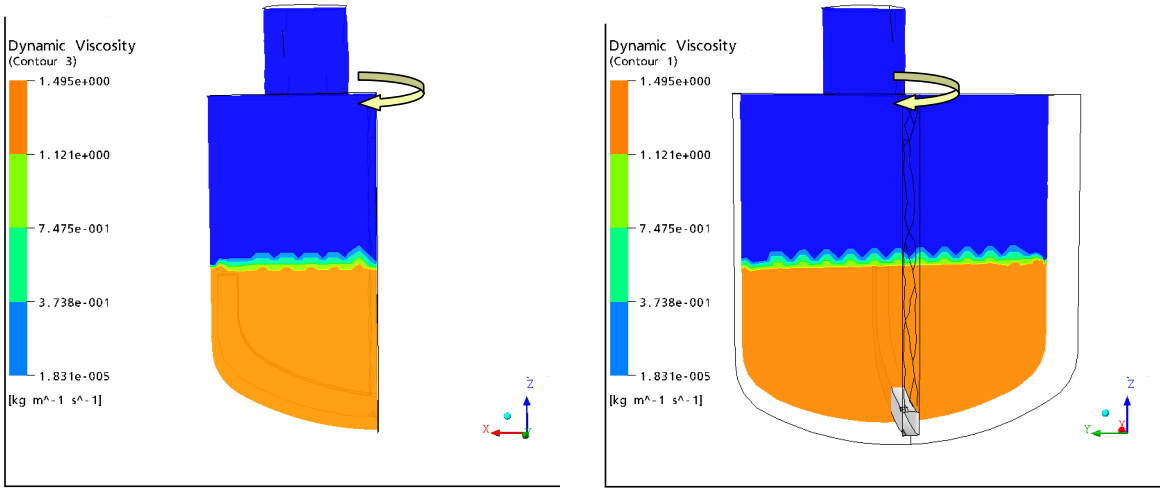

Side View **Front View**

Figure 5.24: Viscosity field (vertical contour planes side and front view) for 26,000 tetrahedrons cells at t = 0 in a SBR at t_d = 1 s.

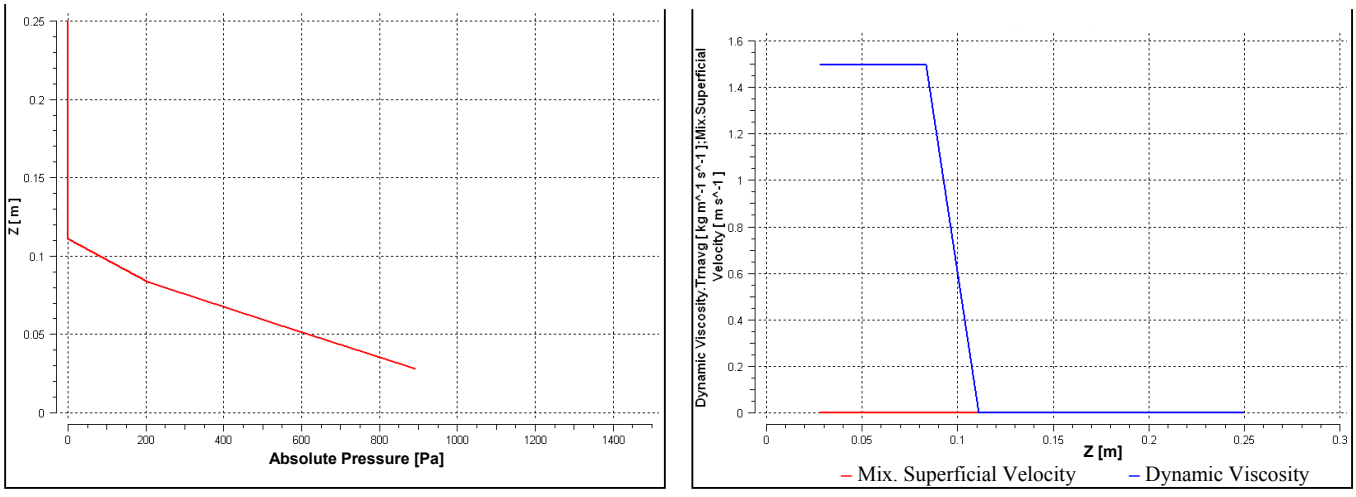

Figure 5.25: Diagrams for hydrostatic pressure p_{abs} (left), velocity and viscosity (right) as a function of z for 26,000 cells at t = 0 s in SBR at t_d = 1 s.

For t = 0.1 s the viscosity field is shown in Fig. 5.26-(A) indicates the convex shape of the air/glycerol interface when the anchor rotates clock wise at ω = 150 rpm. The velocity field in Fig. 5.26-(B) shows the mainly axial flow of glycerol up towards the tip of the impeller which has the maximum flow velocity (red colour). The axial pressure profile in Fig. 5.26-(C) is similar to that in Fig. 5.25-(left) as described before but the ambient pressure value is found for z > 0.08 m because of the existence of the convex shape at the interface due to the movement of the impeller. The axial velocity profile of the glycerol has a constant value of 0.2 m/s between $0 \le z \le 0.05$ m and decreases for z > 0.05 m, caused by a decrease of the liquid velocity for z > 0.05 m with increasing the height z above the impeller blade. A second reason is that the vortex formation and the space resolution at the interface are limited. The viscosity of glycerol remains constant up to z = 0.06 m. The decrease of the viscosity profile at z = 0.08 m is not vertical because the space resolution at the interface is limited as shown in Fig. 5.26-(D).

For t = 0.7 s, the dosed ethanol between $0.2\,\text{s} \le t_d \le 1.2\,\text{s}$, flows towards to the impeller near the cylindrical wall of the vessel. A small mass of ethanol is mixed with the bulk liquid, whereas a larger mass rise to the surface of the liquid mixture. The viscosities η_m are small in the upper part and large in the lower part of the vessel (s. Fig. 5.27-(A)). The air above glycerol is replaced by the dosed ethanol which forms a layer with a height of H_E = 0.04 m. A secondary flow velocity field is formed mainly axial towards to the tip of the impeller. No circulations between shaft and impeller at this time are formed (s. Fig. 5.27-(B)). The axial hydrostatic pressure p_{abs} = 1200 Pa which is calculated by CFD ($p_{tot} = p_{abs} + p_{ref}$ = 102,525 Pa where p_{ref} = 101,325 Pa) is a maximum near the bottom (z = 0.03 m) of the vessel. It decreases gradually to reach the ambient pressure p_{ref} near the

interface at z = 0.14 m between the air and liquid mixture as shown in Fig.5.27-(C). The pressure near the bottom of the vessel increases from p_{abs} = 770 Pa at t = 0.1 s to p_{abs} = 1200 Pa at t = 0.7 s.

The axial viscosity profile $\eta_m(z)$ is constant up to z = 0.06 m then it decreases gradually until z = 0.15 m where a high mass fraction of ethanol (low viscosity) is present. Higher axial velocities of the liquid mixture at t = 0.7 s are found compared with that at t = 0.1 s caused by the additional momentum of the dosed ethanol. The axial velocity profile reaches a minimum at a height of z = 0.15 m where the flow field of the anchor impeller dominates and end the influence of the incoming ethanol flow still very small. With increasing the height for z > 0.15 m the influence of inlet flow increases until z = 0.25 m, there the flow field of incoming ethanol dominates (s. Fig 5.27-(D)).

The mixing of ethanol with glycerol at t = 5 s from the tip of the impeller towards to the shaft leading to concave shape of the interface between ethanol and the liquid mixture, and then ethanol flows to the cylindrical wall of the vessel. Above the tip of the impeller, the velocities of the liquid decrease to reach the minimum at the interface between the liquid mixture and air which has no concave shape (s. Fig. 5.28-(A)).

It is observed from the viscosity fields at t = 10 s in Fig 5.29-(A) that the maximum viscosities of the liquid mixtures are found near the corner of the vessel at the bottom. This is caused by only a weak mixing in this zone. A homogeneous and a constant mixture viscosity are obtained at $t_m \approx 15$ s as shown in Fig. 5.30-(A). A concave interface with the air is formed at t = 20 s as shown in Fig. 5.31-(A). Secondary flow with a circulation in the direction of the anchor movement (behind the impeller) is formed. The minimum velocities are found near the shaft, whereas the maximum velocities are

found near the cylindrical wall of the vessel see Fig 5.28-(B). Similar velocity fields are obtained for t = 10 s, t = 15 s and t = 20 s as shown in Figs. 5.29-(B), 5.30-(B) and 5.31-B, respectively.

The axial hydrostatic pressure profiles at t = 5, 10, 15 and 20 s (after the dosed ethanol) shows that the maximum pressure of p_{abs} = 1300 Pa is found near the bottom of the vessel, and then it decreases linearly to reach the ambient pressure p_{ref} at the interface with air at z = 0.16 m (s. Figs. 5.28-(C), 5.29-(C), 5.30-(C) and 5.31-(C) for t = 5, 10, 15 and 20 s, respectively).

The axial velocities increase from the bottom of the vessel to reach the maximum near the tip of the impeller and the interface between the liquid mixture and air. For z > 0.15 m there is a decrease of the axial velocities caused by the absence of the impeller effect. The axial mixture viscosity profiles decrease to reach the minimum at the interface with air (s. Figs. 5.28-(D), 5.29-(D), 5.30-(D) and 5.31-(D) for t = 5, 10, 15 and 20 s, respectively). The axial velocities of the liquid mixture decrease with time until a complete mixing with constant mixture viscosity is obtained.

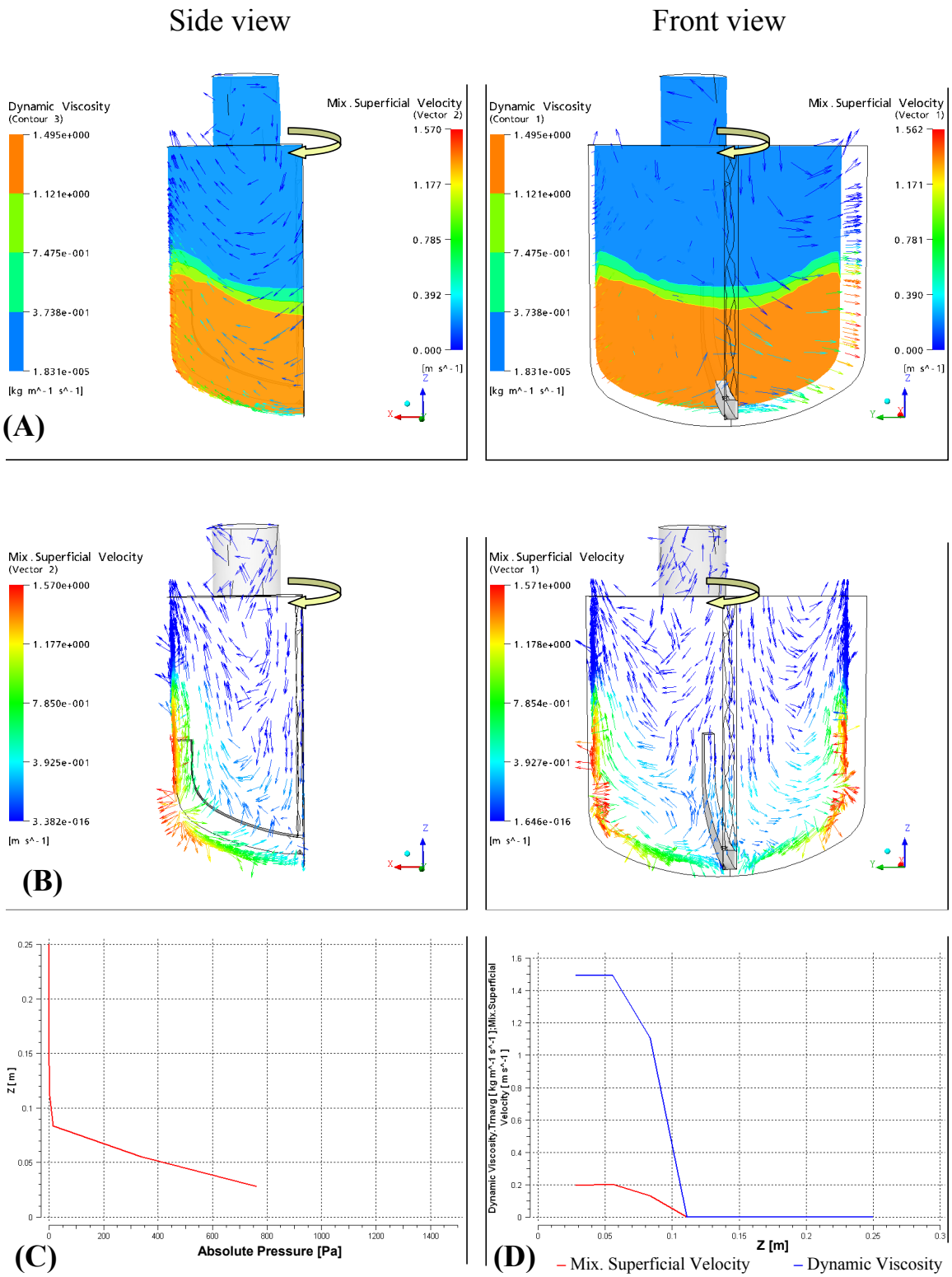

Figure 5.26: Fields of mixture viscosity (A), flow velocity (B) (side view (left) and front view (right)) and hydrostatic pressure profile (C), axial flow velocity and viscosity profiles (D) for 26,000 tetrahedron cells at t = 0.1 s in a SBR at t_d = 1 s.

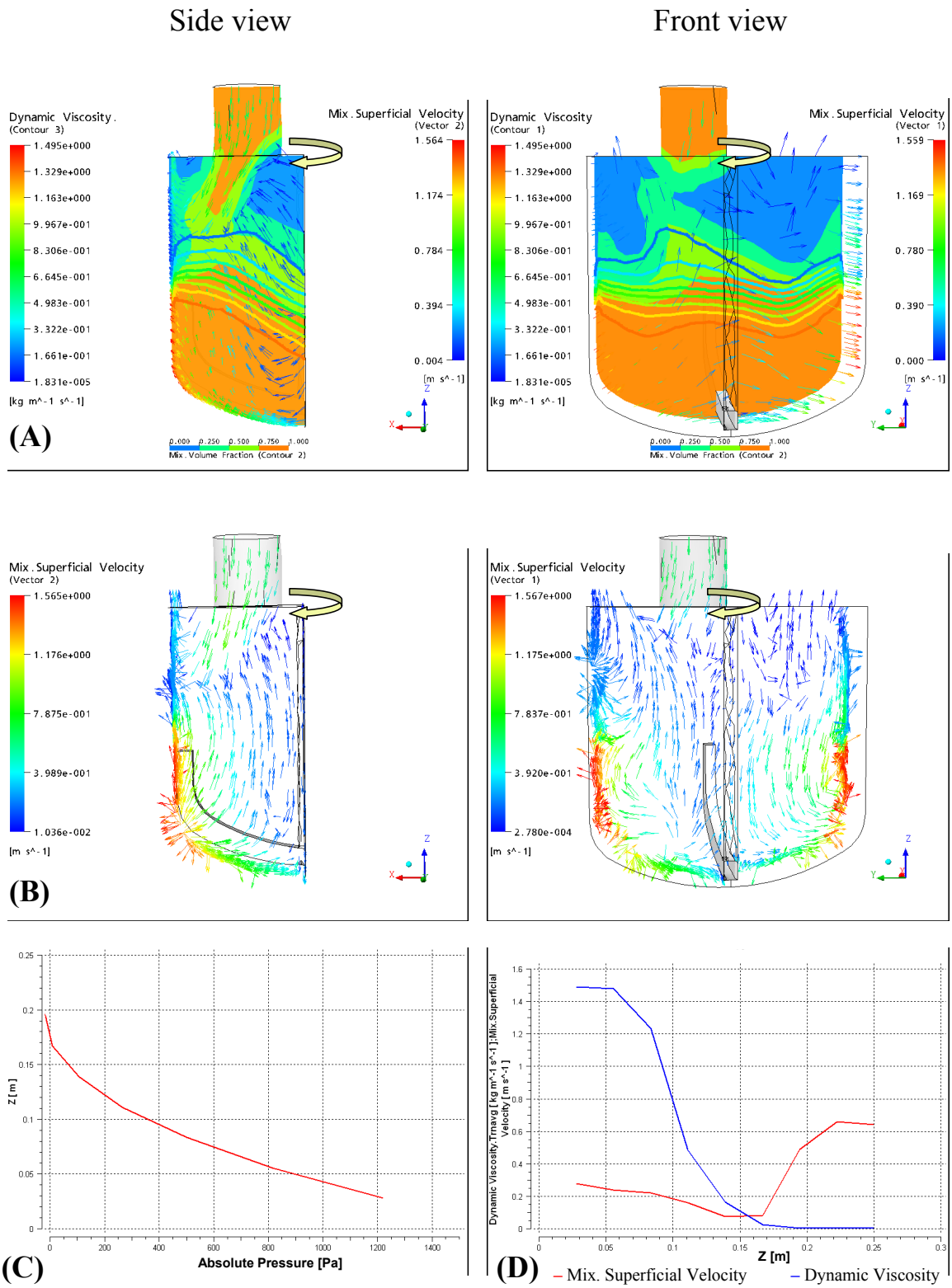

Figure 5.27: Fields of mixture viscosity (A), flow velocity (B) (side view (left) and front view (right)) and hydrostatic pressure profile (C), axial flow velocity and viscosity profiles (D) for 26,000 tetrahedron cells at t = 0.7 s in a SBR at t_d = 1 s.

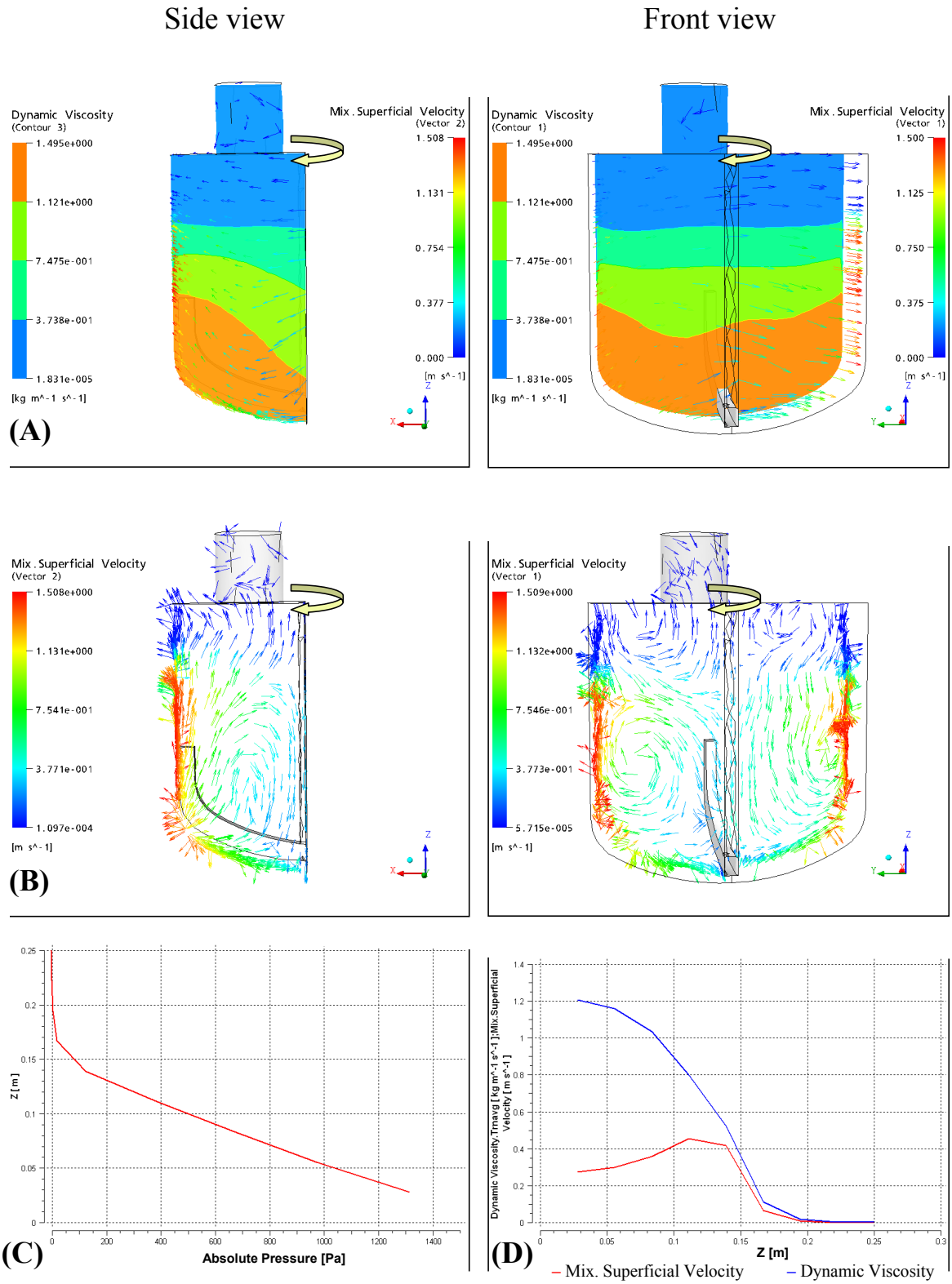

Figure 5.28: Fields of mixture viscosity (A), flow velocity (B) (side view (left) and front view (right)) and hydrostatic pressure profile (C), axial flow velocity and viscosity profiles (D) for 26,000 tetrahedron cells at t = 5 s in a SBR at t_d = 1 s.

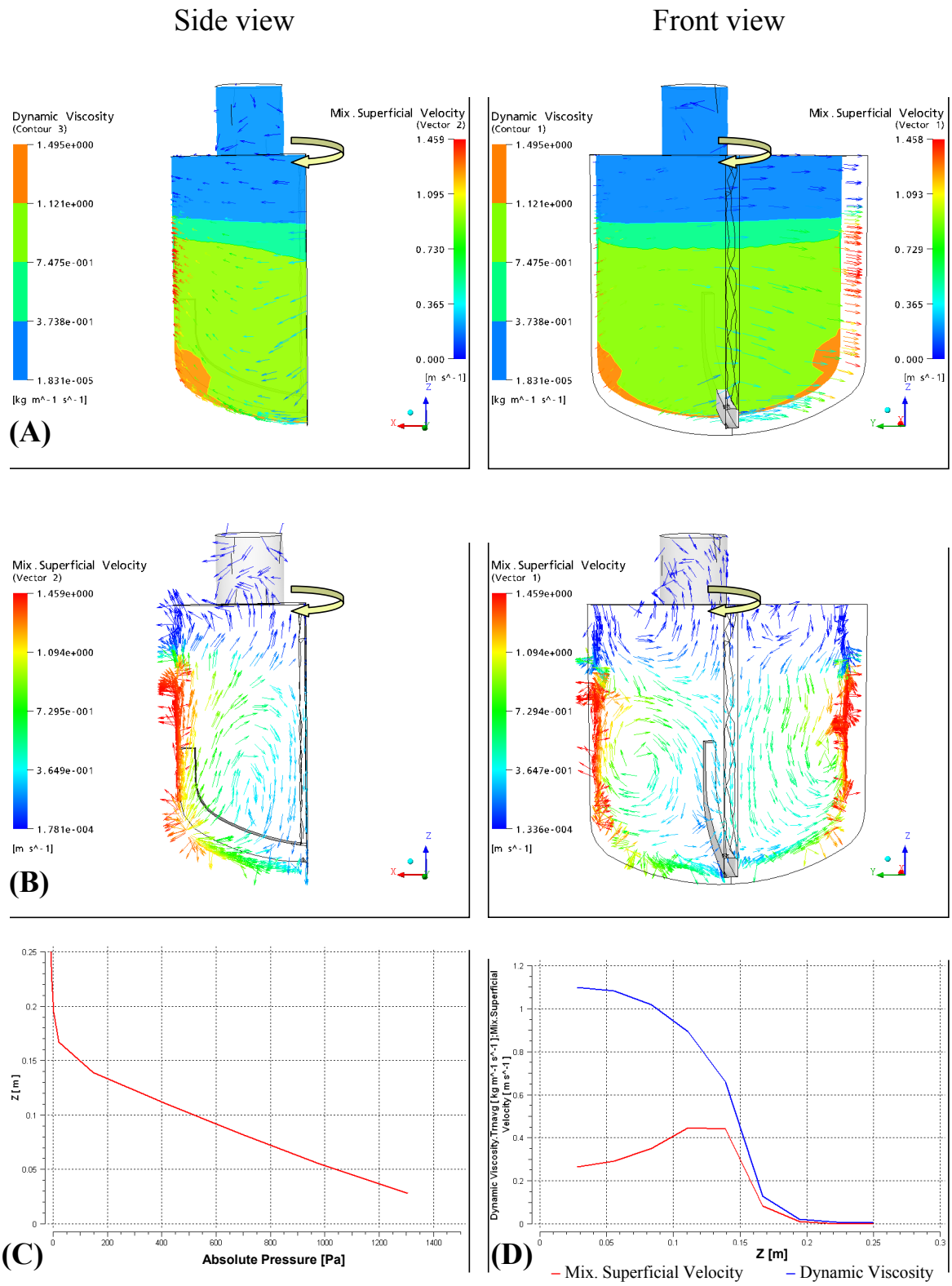

Figure 5.29: Fields of mixture viscosity (A), flow velocity (B) (side view (left) and front view (right)) and hydrostatic pressure profile (C), axial flow velocity and viscosity profiles (D) for 26,000 tetrahedron cells at t = 10 s in a SBR at t_d = 1 s.

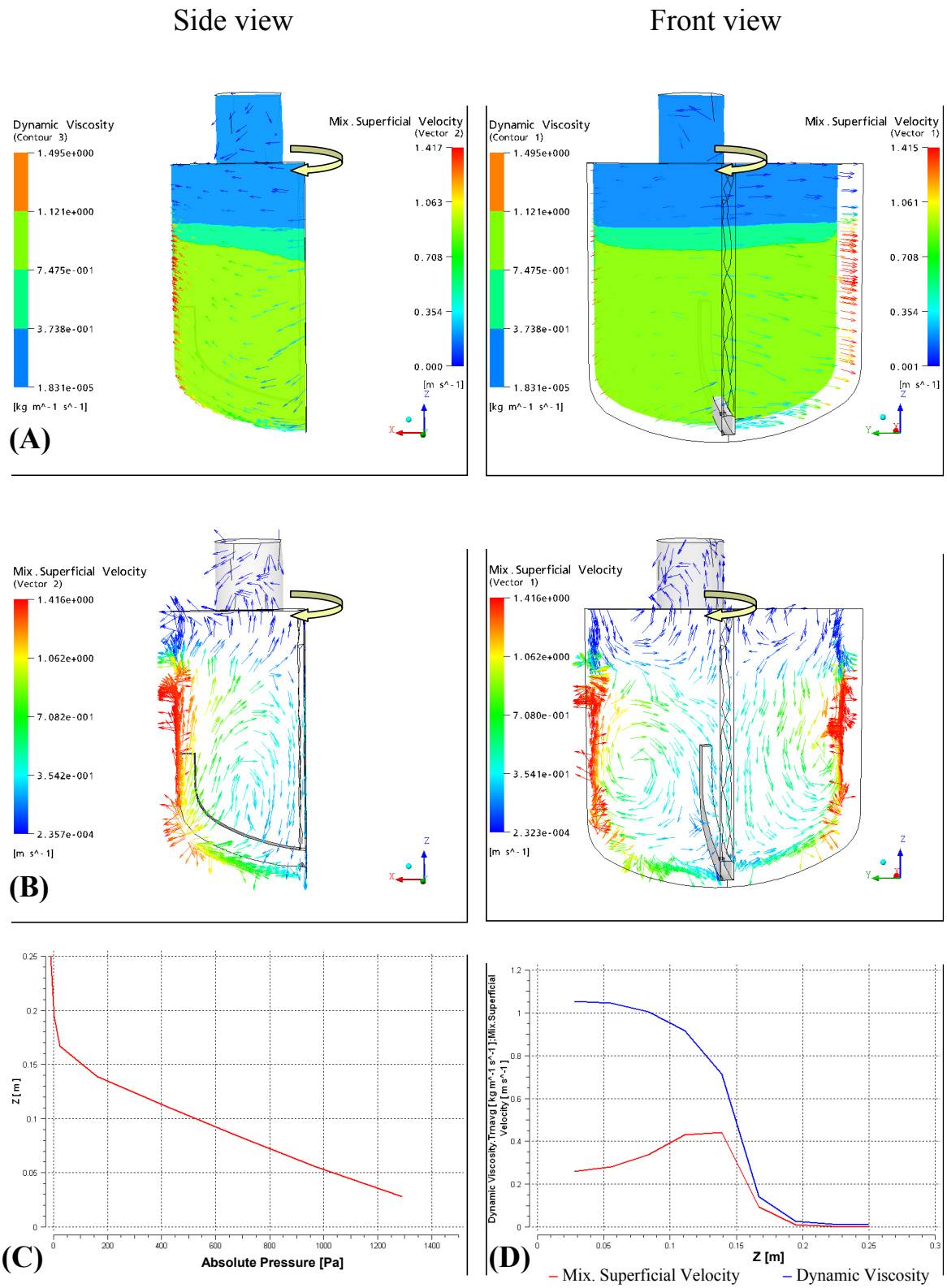

Figure 5.30: Fields of mixture viscosity (A), flow velocity (B) (side view (left) and front view (right)) and hydrostatic pressure profile (C), axial flow velocity and viscosity profiles (D) for 26,000 tetrahedron cells at t = 15 s in a SBR at t_d = 1 s.

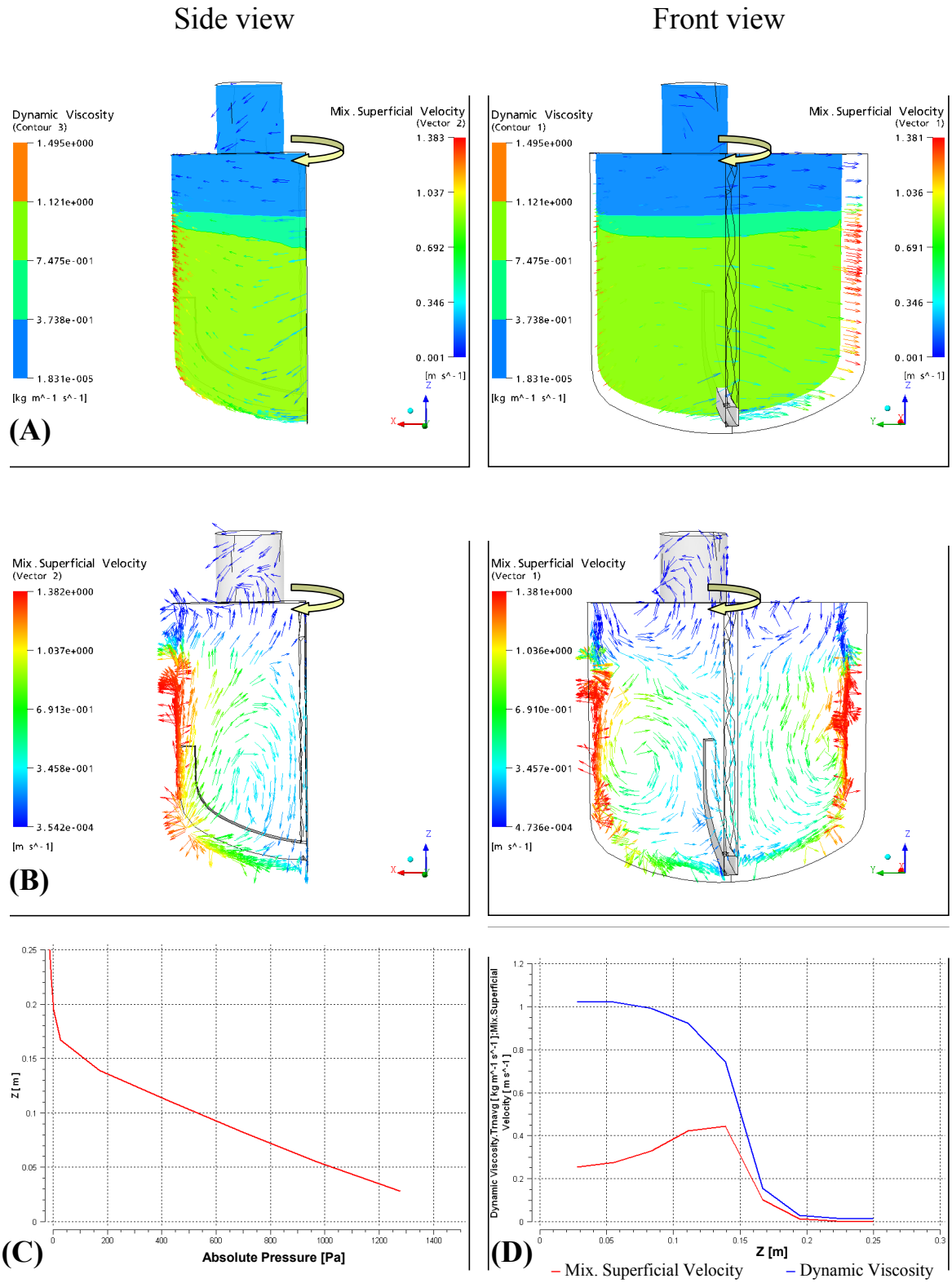

Figure 5.31: Fields of mixture viscosity (A), flow velocity (B) (side view (left) and front view (right)) and hydrostatic pressure profile (C), axial flow velocity and viscosity profiles (D) for 26,000 tetrahedron cells at t = 20 s in a SBR at t_d = 1 s.

5.2.1.2 The effect of dosage time

Different dosage times of ethanol t_d = 1 s and t_d = 5 s are used in the CFD simulations for inlet tube diameters of d_t = 2.3 cm and d_t = 5 cm. The fields of flow velocity, viscosity and volume fraction of the liquid mixture are studied at ω = 150 rpm. The time dependent velocity- and viscosity fields are calculated.

5.2.1.2.1 Inlet tube diameter of 5 cm

The velocities of the dosed ethanol are u_E = 0.64 m/s and u_E = 0.128 m/s for t_d = 1 s (from 0.2 s to 1.2 s) and t_d = 5 s (from 0.2 - 5.2 s), respectively. The same mass of the dosed ethanol is used. For t_d = 1 s the fields of flow velocity, viscosity and volume fraction of the liquid mixture as a function of time in Fig. 5.32-a are presented as described in Fig. 5.21-a for 26,000 tetrahedron cells. When the dosage time increases to t_d = 5 s the inlet volumetric flow rate of ethanol decreases from 1.25 L/s to 0.25 L/s. The dosed ethanol will flow slowly near the wall of the inlet tube and the cylindrical wall of the vessel to form a layer above glycerol. A very small mass of ethanol is mixed with glycerol during the dosage which causes longer mixing time as shown in Fig. 5.32-b.

For dosage time of t_d = 1 s the viscosity profile decreases sharply and continuously up to the end of the dosage at t = 1.2 s. The reason of this decrease is the high flow velocity, pressure force and volume of the dosed ethanol which increase the flow velocity of the liquid mixture to 0.8 m/s and accelerate the mixing process. For t > 1.2 s, ethanol is redistributed completely in glycerol only under the effect of anchor rotation from the top end of the impeller towards the shaft and towards the cylindrical wall as

shown in Fig. 5.32, causing the viscosity of the liquid mixture increases to reach the constant mixture viscosity of 1.067 Pa s at t_m = 13 s (s. Fig. 5.33).

For t_d = 5 s the viscosity profile decreases slowly (s. Figs. 5.32 and 5.33) as a function of time t until the mixture is homogenized and a constant mixture viscosity of η_m = 1.126 Pa s is obtained at t_m = 20 s. As the flow velocity of inlet ethanol increases from 0.128 m/s at t_d = 5 s to 0.64 m/s at t_d = 1 s, the final constant mixture viscosity decreases from η_m = 1.126 Pa s to η_m = 1.067 Pa s, because the high velocity of the inlet jet stream of ethanol leads to a nearly complete mixing of the ethanol with glycerol (η_m is smaller) whereas the slow feed stream caused only a weak mixing and most of the dosed ethanol rises up to the interface between air and liquid at which the velocity is approximately zero (η_m is larger).

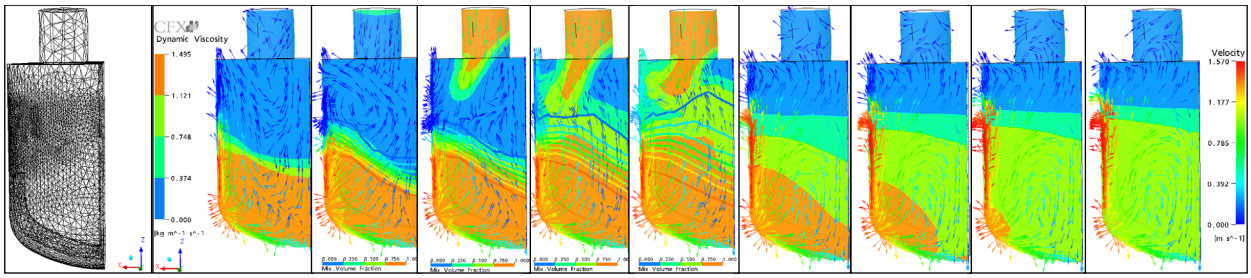

(a) t_d = 1 s t = 0.1 s 0.2 s 0.3 s 0.7 s 1.2 s 5.0 s 8.0 s 10 s 20 s

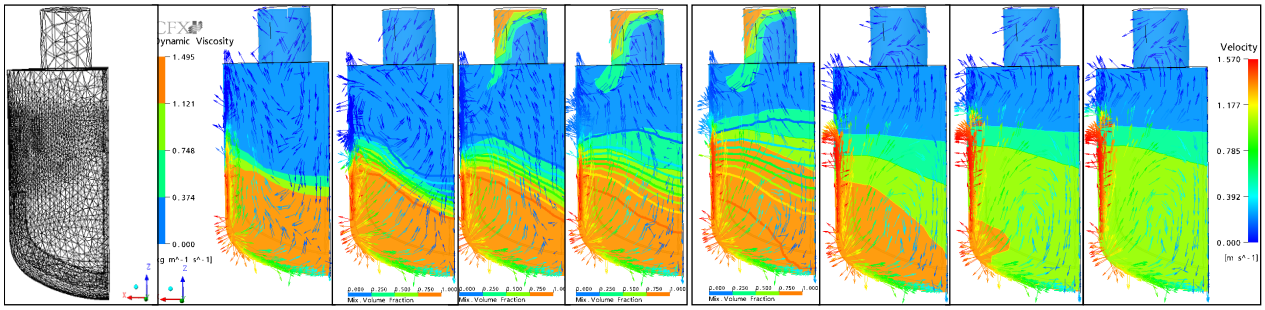

(b) t_d = 5 s t = 0.1 s 0.2 s 0.7 s 3.0 s 5.2 s 10 s 18 s 20 s

Figure 5.32: Mixture viscosity-, flow velocity- and volume fraction fields on xz-plane at y = 0.03 m for (a) t_d = 1 s and (b) t_d = 5 s for d_t = 5 cm in a SBR.

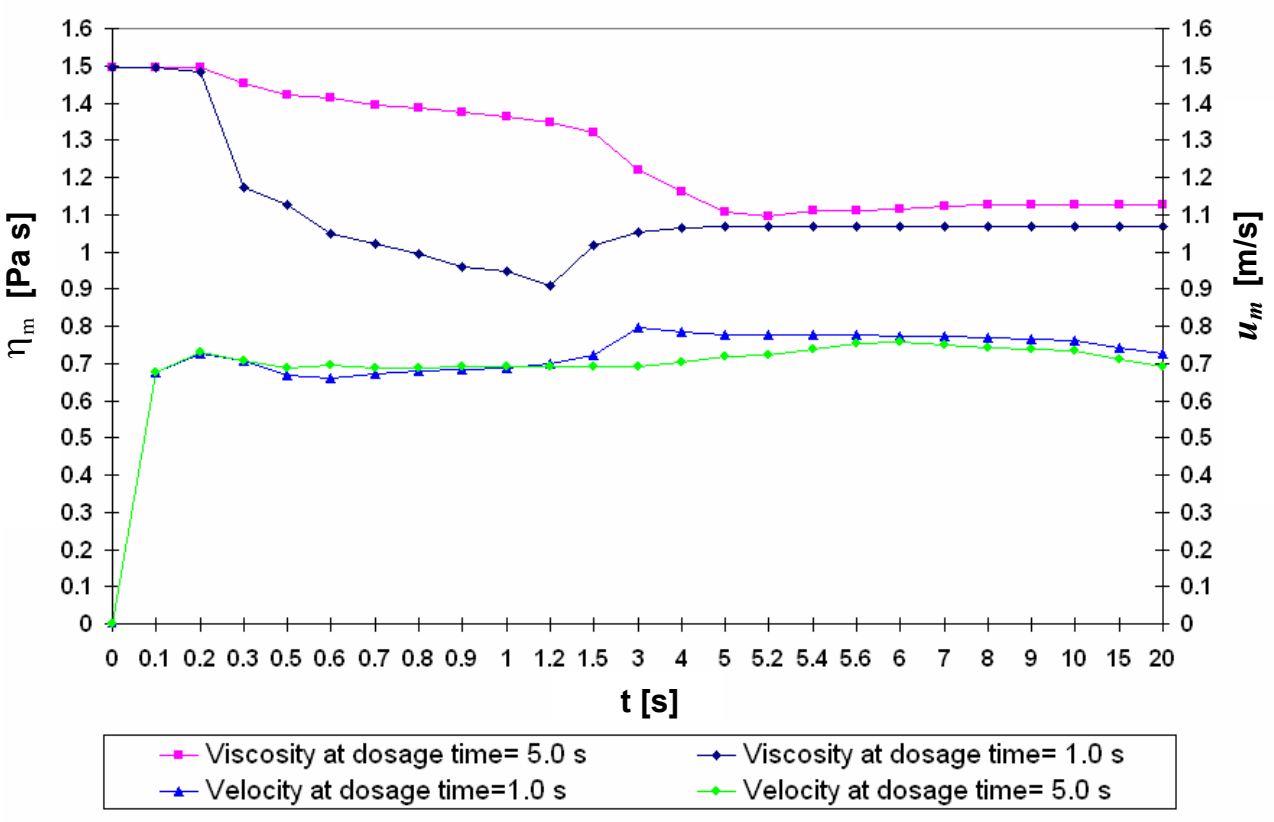

Figure 5.33: Flow velocity and mixture viscosity as a function of time on xz-plane at y = 0.03 m for t_d = 1 s and t_d = 5 s at ω = 150 rpm and ethanol flow velocity at the inlet is 0.64 m/s and 0.128 m/s, respectively for d_t = 5 cm in a SBR.

5.2.1.2.2 Inlet tube diameter of 2.3 cm

When ethanol is dosed at t_d = 1 s, the high inlet flow velocity of 2.9 m/s causes a high pressure force on the glycerol liquid surface and push ethanol to a deep location near the bottom in the vessel and then it is intensively mixed with glycerol to get a fast distribution of the ethanol. For this, a homogeneous mixture is obtained at t_m = 7 s without formation of any dead zone with a weak mixing. Also the free interface shape is more concave than that for t_d = 5 s as can be seen from the viscosity-, velocity- and volume fraction fields of the liquid mixture from Fig. 5.34-a.

For t_d = 5 s (s. Fig. 5.34-b) the lower inlet flow velocity of 0.58 m/s of ethanol or its low flow rate of 0.25 L/s caused the down flow of ethanol to reach slowly to the glycerol interface. Because of its lower density ethanol formed a layer above the glycerol. The mixing process is slow while the anchor shifts the liquid from the cylindrical wall of the vessel to the inner region. A homogeneous mixture is obtained at t_m = 27.5 s. A dead zone with weak mixing at the corner of the vessel is formed. Fig. 5.34 shows that there is a small change of the viscosity field during the dosage of ethanol between $0.2\,\text{s} \le t_d \le 5.2\,\text{s}$. This proves that most of the dosed ethanol rises up to the interface between air and liquid.

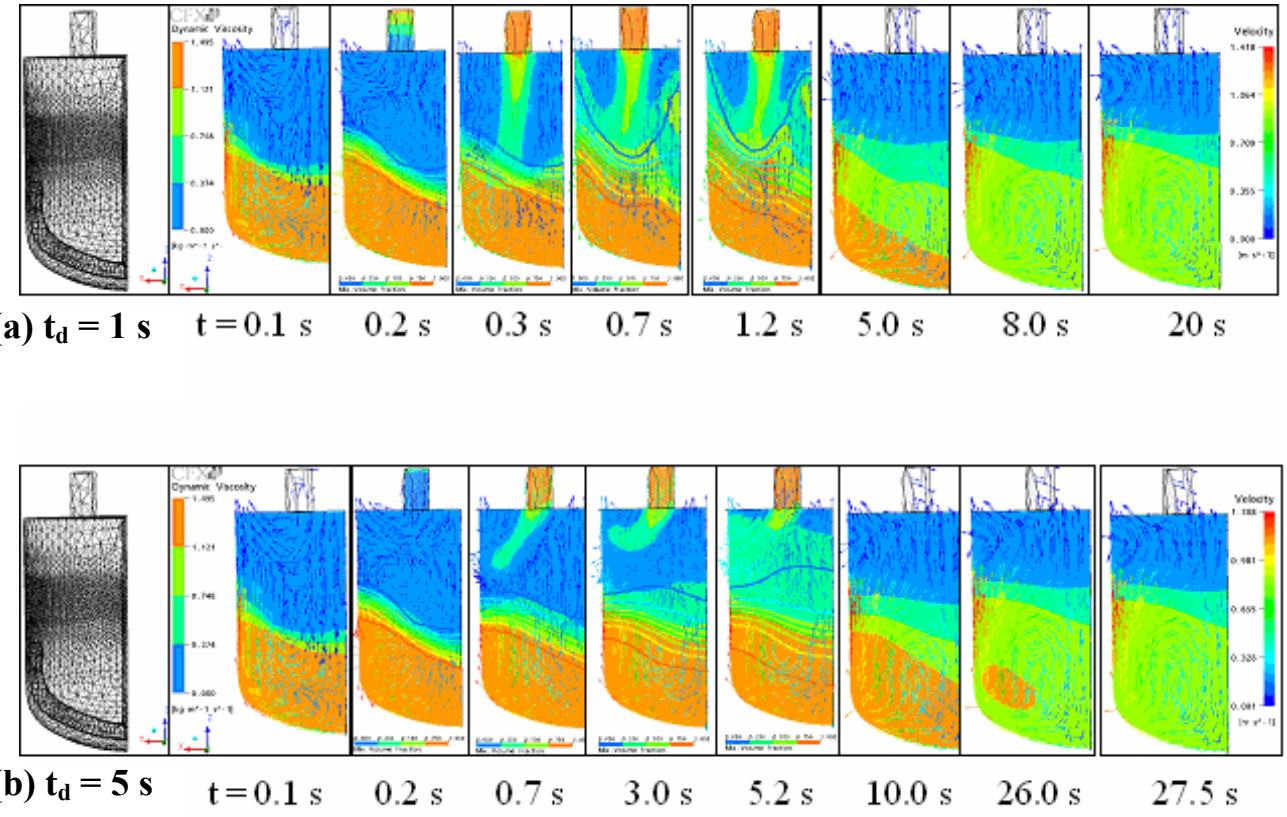

Figure 5.34: Mixture viscosity-, flow velocity- and volume fraction fields on xz-plane at y = 0.03 m for (a) t_d = 1 s and (b) t_d = 5 s for d_t = 2.3 cm in a SBR.

Fig. 5.35 shows the viscosity and velocity courses as a function of time for dosage times 1 s and 5 s. The high velocity of the inlet jet stream of

ethanol at t_d = 1 s leads to a nearly complete mixing of the ethanol with glycerol (η_m is smaller), whereas the slow inlet stream of ethanol at t_d = 5 s causes only a weak mixing and most of the dosed ethanol rises up to the interface between air and liquid at which the velocity is approximately zero (η_m is larger). A slow and small decrease of the mixture viscosity is found for t_d = 5 s between $0.2\,s \le t_d \le 5.2\,s$ due to a low mixing process, whereas a fast and great decrease of the mixture viscosity is found for t_d = 1 s between $0.2\,s \le t_d \le 1.2\,s$ due to an intensive mixing process.

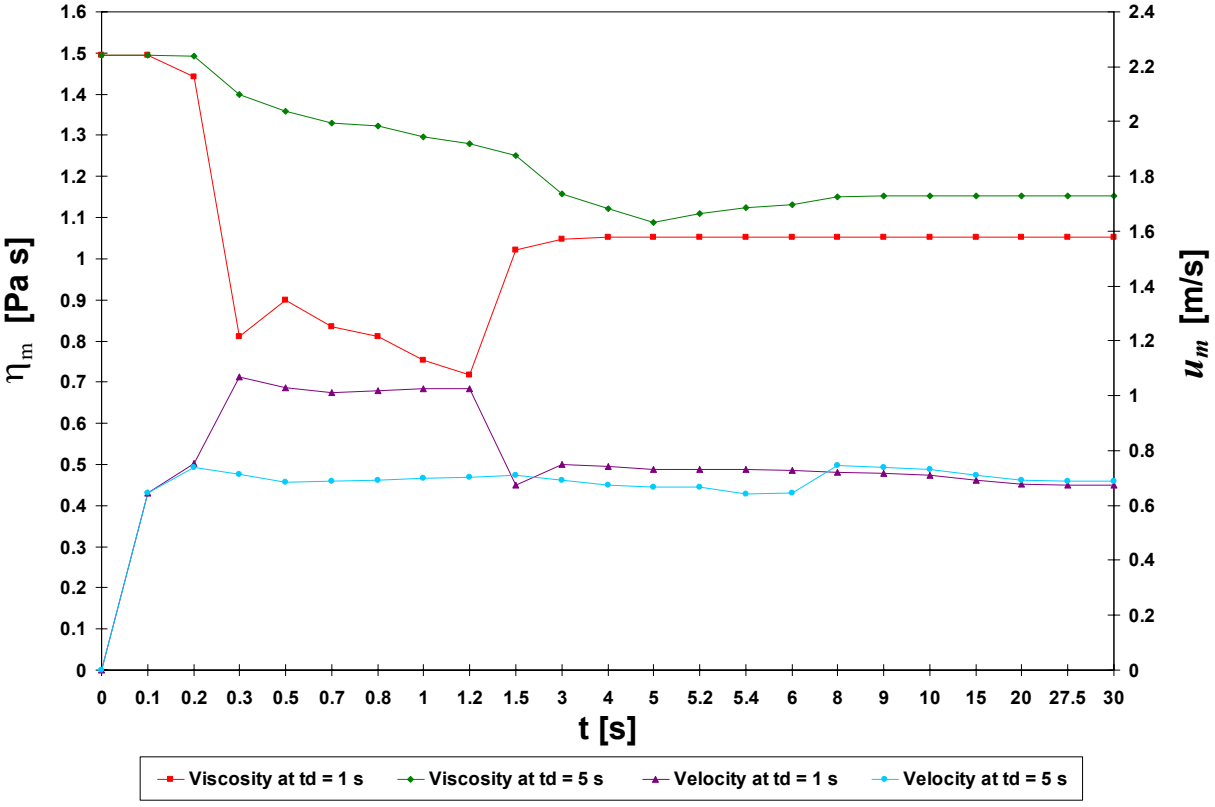

Figure 5.35: Flow velocity and mixture viscosity as a function of time on xz-plane at y = 0.03 m for t_d = 1 s and t_d = 5 s at ω = 150 rpm and ethanol velocity at the inlet is 2.89 m/s and 0.58 m/s, respectively for d_t = 2.3 cm in a SBR.

5.2.1.3 The effect of inlet tube diameter

Different inlet tube diameters of d_t = 2.3 cm and d_t = 5 cm are used in the CFD simulations for dosage times of ethanol t_d = 1 s and t_d = 5 s. The fields

of flow velocity, viscosity and volume fraction of the liquid mixture as a function of time are studied at ω = 150 rpm. The time dependent mixture velocities u_m and mixture viscosities η_m are calculated.

5.2.1.3.1 Dosage time t_d = 1 s

The velocities of the dosed ethanol are u_E = 0.64 m/s and u_E = 2.9 m/s for d_t = 5 cm and d_t = 2.3 cm, respectively. In both cases the same mass of the dosed ethanol is used. Initially glycerol is stirred until t = 0.2 s with a constant viscosity of η_G = 1.495 Pa s (Figs. 5.36 and 5.37). For d_t = 2.3 cm when ethanol is dosed between $0.2\,s \le t_d \le 1.2\,s$, the viscosity η_m decreases much more than η_m for d_t = 5 cm (Fig. 5.37). This is due to the high velocity of the dosed ethanol of u_E = 2.9 m/s at d_t = 2.3 cm which causes a high pressure force on the bulk liquid and leads to a faster mixing with glycerol. A second reason is the dosed ethanol may reaches the bottom of the vessel because the inlet ethanol jet has higher velocity than the bulk and it is normal to the glycerol interface in the middle of the vessel as can be shown from mixture flow velocity-, viscosity- and volume fraction fields in Fig. 5.36. The high inlet ethanol velocity leads to an increase in the bulk velocity from u_m = 0.7 m/s to the maximum u_m = 1.03 m/s which causes the sharp decrease in the viscosity η_m during the dosage (Fig. 5.37). The higher velocity of inlet ethanol stream gives the bulk liquid higher kinetic energy to accelerate the mixing process with glycerol.

For d_t = 5 cm the dosed ethanol stream between $0.2\,s \le t_d \le 1.2\,s$ does not fill the whole space of the inlet tube and flows therefore to the cylindrical wall of the vessel because the velocity of the bulk liquid in this case is higher than that for the dosed ethanol (Fig. 5.36-a). After the end of the

dosage time the viscosity η_m increases again because the velocity u_m has no significant change so that the distribution of ethanol is limited (Fig. 5.37). The liquid mixture flows from the tip of the impeller to the centre of the vessel and then to the cylindrical wall under the influence of the flow field of the anchor impeller. A Secondary flow in addition to a circulation formation between the shaft and the impeller for both tube diameters can be recognized from t = 5 s to t = 20 s (Fig. 5.36).

The final mixture viscosities for d_t = 2.3 cm and d_t = 5 cm are η_m = 1.05 Pa s at t_m = 7 s and η_m = 1.067 Pa s at t_m = 13 s, respectively. For that as the inlet tube diameter increases, the inlet ethanol velocity decreases and a slower mixing occurs.

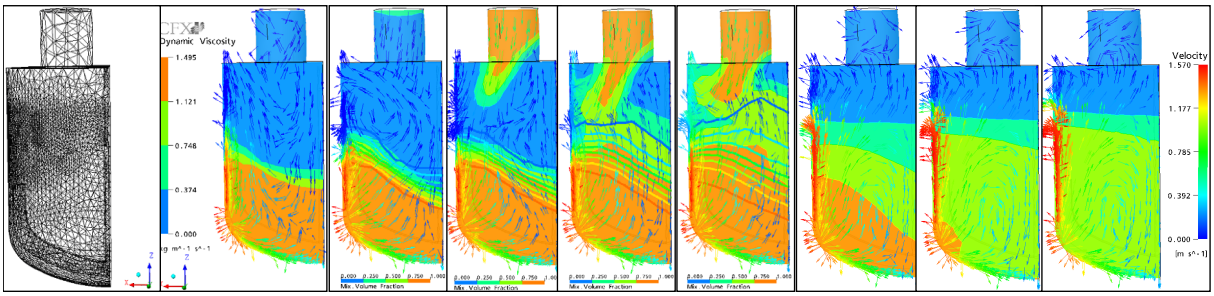

(a) d_t = 5 cm t = 0.1s 0.2 s 0.3 s 0.7 s 1.2 s 5 s 10s 20s

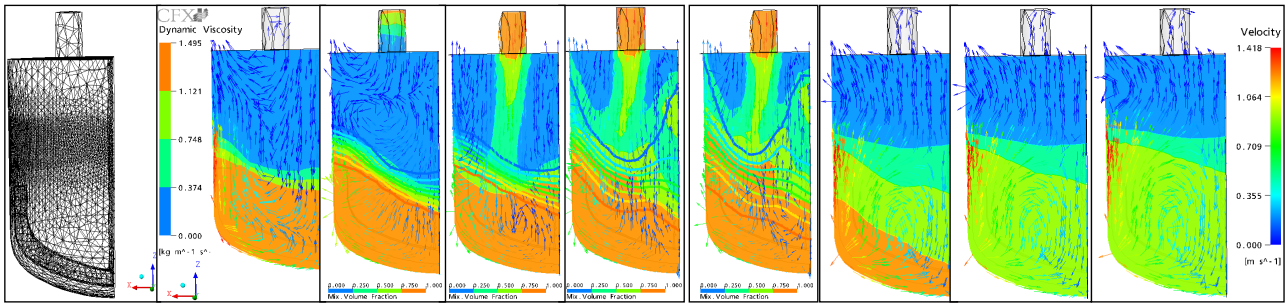

(b) d_t = 2.3 cm t = 0.1 s 0.2 s 0.3 s 0.7 s 1.2 s 5.0 s 8.0 s 20 s

Figure 5.36: Mixture viscosity, flow velocity and volume fraction fields on xz-plane at y = 0.03 m for (a) d_t = 5 cm and (b) d_t = 2.3 cm for t_d = 1 s in a SBR.

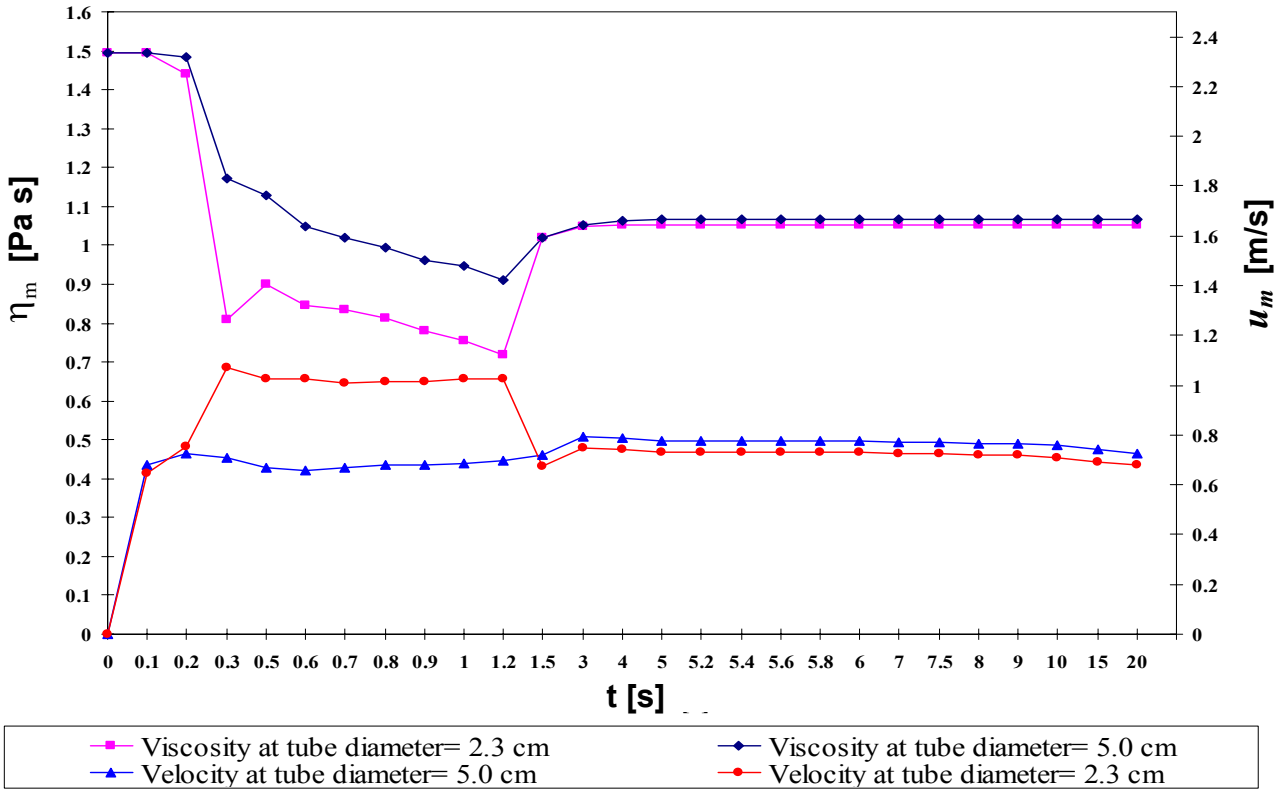

Figure 5.37: Flow velocity and mixture viscosity as a function of time on xz-plane at y = 0.03 m for d_t = 5 cm and d_t = 2.3 cm at ω = 150 rpm and ethanol velocity at the inlet is 0.64 m/s and 2.89 m/s, respectively for t_d = 1 s in a SBR.

5.2.1.3.2 Dosage time t_d = 5 s

The velocities of the dosed ethanol are u_E = 0.59 m/s and u_E = 0.128 m/s for d_t = 2.3 cm and d_t = 5 cm, respectively. As in the case of t_d = 1 s the inlet velocity of ethanol is higher for the smaller tube but still lower than the bulk velocity of the liquid mixture. The inlet flow stream will be shifted to the cylindrical wall by the impeller and then mixed with glycerol from the circumference to the shaft of the vessel as can be seen from the viscosity fields η_m in Figs. 5.32-b and 5.34-b leading to an circulation between the shaft and impeller as can be seen from the flow velocity fields for t > 5.2 s. A dead zone with a higher viscosity i.e. less mixing is found near the curved

corner of the impeller at t = 26 s (s. Fig. 5.34-b). This behavior may be due to the lower inlet velocity of ethanol than that of the bulk liquid. The buoyant forces rise up ethanol (lower density) to the liquid interface. A longer mixing time of t_m = 27.5 s is required to get a complete mixing compared with d_t = 5 cm (s. Figs. 5.33 and 5.35).

For d_t = 5 cm the inlet flow velocity of ethanol is three times lower from that of d_t = 2.3 cm. As in the cases before the inlet flow goes to the wall of the vessel slowly and the mixing takes place between the shaft and the impeller. The most of ethanol is mixed near the cylindrical wall with the bulk glycerol, because the velocity at the cylindrical wall is higher than that near the shaft, so that ethanol will be mixed faster with glycerol. A homogeneous mixture is obtained in a shorter mixing time of t_m = 20 s compared with that for d_t = 2.3 cm. When a small mass of ethanol flows towards to the shaft and a large mass of ethanol is mixed near the cylindrical wall, and then a small layer of ethanol will be formed above the bulk liquid mixture. Therefore a homogeneous mixture will be obtained in shorter mixing time t_m (s. Fig. 5.32-b). It is noticed that the weak mixing zone in this case is at t = 18 s near the corner of the vessel at the bottom. The axial velocities are low above the tip of the anchor impeller and below the anchor blades near the bottom of the vessel. This distribution of the axial velocity leads to a circulation between the shaft and the impeller as can be seen from the velocity field in Fig. 5.32-b for t > 5.2 s.

5.2.1.4 The effect of anchor velocity

Radial and axial flow velocity fields as a function of time are calculated by CFD simulations in a SBR with d_t = 5 cm for different anchor velocities from ω = 25 rpm to ω = 400 rpm and dosage times t_d = 1 s and t_d = 5 s. The ethanol concentrations at four different positions in the vessel are calculated as a function of time. The final mixture viscosity η_m (t_m) is calculated as a function of the anchor velocity.

5.2.1.4.1 Dosage time t_d =1 s

When the anchor velocity increases from ω = 25 rpm to ω = 400 rpm (s. Fig. 5.38), the shear forces and the mixture flow velocity u_m become higher above the impeller and near the shaft. Then a larger mass of the dosed ethanol flows towards to the impeller leading to a faster mixing as can also be seen from the mixture viscosity field. A secondary flow not yet with circulation between the shaft and impeller is obtained at ω = 25 rpm, because the axial flow velocity is not large enough to push the ethanol layer towards the bulk liquid, therefore a larger mass fraction of unmixed ethanol exists and leads to a small viscosity decrease to the mixture viscosity at t = 20 s. Further increasing the anchor velocity gives higher axial velocity which leads now to a circulation between the shaft and impeller. Indeed the circulation accelerates the mixing of ethanol with glycerol and decreases also the mass fraction of the unmixed ethanol. For that a final mixture viscosity is obtained with smaller mixing time when increasing the anchor velocity. The radial centrifugal forces rise up the liquid mixture near the cylindrical wall leading to a concave interface with the air as shown in Fig. 5.38.

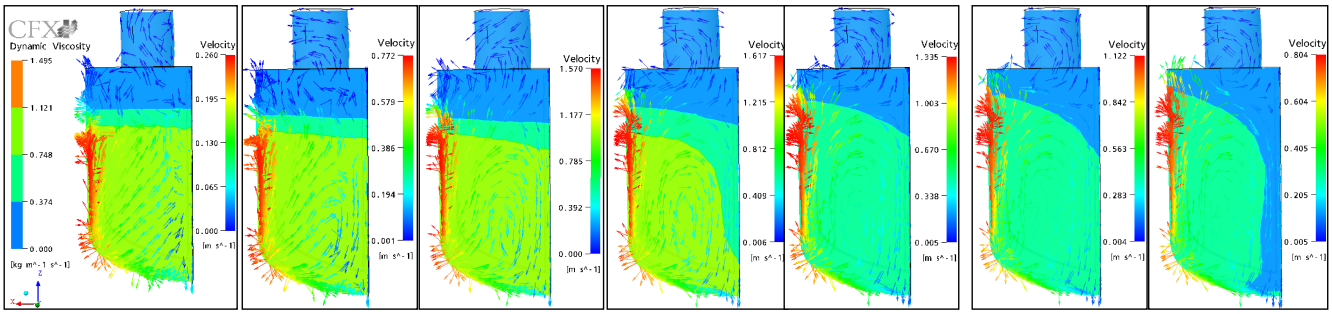

Figure 5.38: Mixture viscosity- and flow velocity fields for different anchor velocities ω on xz-plane at y = 0.03 m for t_d = 1 s and d_t = 5 cm at t = 20 s in a SBR.

The radial flow velocity fields in y directions at t = 20 s for ω = 25, 75, 150, 250 and 300 rpm are shown in Figs. 5.39-a and b, 5.41-a and b, 5.43-a and b, 5.45-a and b and 5.47-a and b, respectively. In the case of ω = 25 rpm, no secondary flow is found.

The radial flow velocity field at z = 0.0738 m shows the primary tangentional flow which is created by the horizontal blade of the impeller. The maximum flow velocity is found between the tip of impeller and the cylindrical wall. A vortex movement along with the anchor blade is formed at the tip of the impeller (Fig. 5.39-b (J)).

Ethanol concentration at four different points near the shaft and the cylindrical wall as a function of time is shown in Fig. 5.40. The mixing time at which all the points have the same concentration of ethanol is t_m = 17 s. The ethanol concentration at z = 0.125 m near the cylindrical wall is lower than that near the shaft because there exist high shear forces. The mixing of ethanol with glycerol accelerates near the tip of the impeller. Similar flow velocity fields for ω = 75 rpm but higher axial, radial and tangential velocities are obtained (Figs. 5.41-a, 5.41-b) leading to a mixing time of t_m = 15 s (Fig. 5.42).

As the velocity of the anchor impeller increases to ω = 150, 250 and 300 rpm, then the axial and radial velocities increase. The circulation starts to appear at ω = 150 rpm between the impeller and the shaft and it becomes larger when the velocity increases. Similar flow velocity field can be seen in Figs. 5.43-a and b, 5.45-a and b and 5.47-a and b for ω = 150, 250 and 300 rpm, respectively. As in the cases before secondary flow is caused by the motion of the liquid mixture from the high velocity near the impeller to the lower velocity near the shaft leading to a circulation between the impeller and the shaft. The distribution of ethanol is controlled by the secondary flow in the axial direction.

The upward radial and axial velocities are very high at y = 0.018 m behind and close to the impeller, the downward axial velocity near the shaft is low and can be seen in Figs. 5.43-a (A), 5.45-a (A) and 5.47-a (A). For y = 0.027 m and y = 0.03 m the radial flow velocity decreases and the axial flow velocity and circulation dominate (Figs. 5.43-a (B and C), 5.45-a (B and C) and 5.47-a (B and C)). For y = 0.05 m a complete axial circulation loop is found in the middle between the impeller and shaft (Figs. 5.43-a (D), 5.45-a (D) and 5.47-a (D)). In front of the impeller from y = - 0.018 m to y = - 0.03 m the downward axial flow velocity dominates and a small circulation can be seen above the impeller (Figs. 5.43-a and b (F, G and H), 5.45-a and b (F, G and H) and 5.47-a and b (F, G and H)).

When the anchor velocity increases the radial trailing vortex near the anchor tip becomes larger at z = 0.074 m leading to a higher distribution of ethanol in the bulk liquid (Figs. 5.43-b (J and K), 5.45-b (J and K) and 5.47-b (J and K)). It can be concluded that the impeller velocity has a greater effect on the secondary axial flow than on the primary tangentional flow.

The mixing times for ω = 150 rpm, 250 rpm and 300 rpm are t_m = 13 s, 7 s and 5 s, respectively as can be seen from ethanol concentration as a function of time in Figs. 5.44, 5.46 and 5.48. As the anchor velocity increases the mixing time decreases.

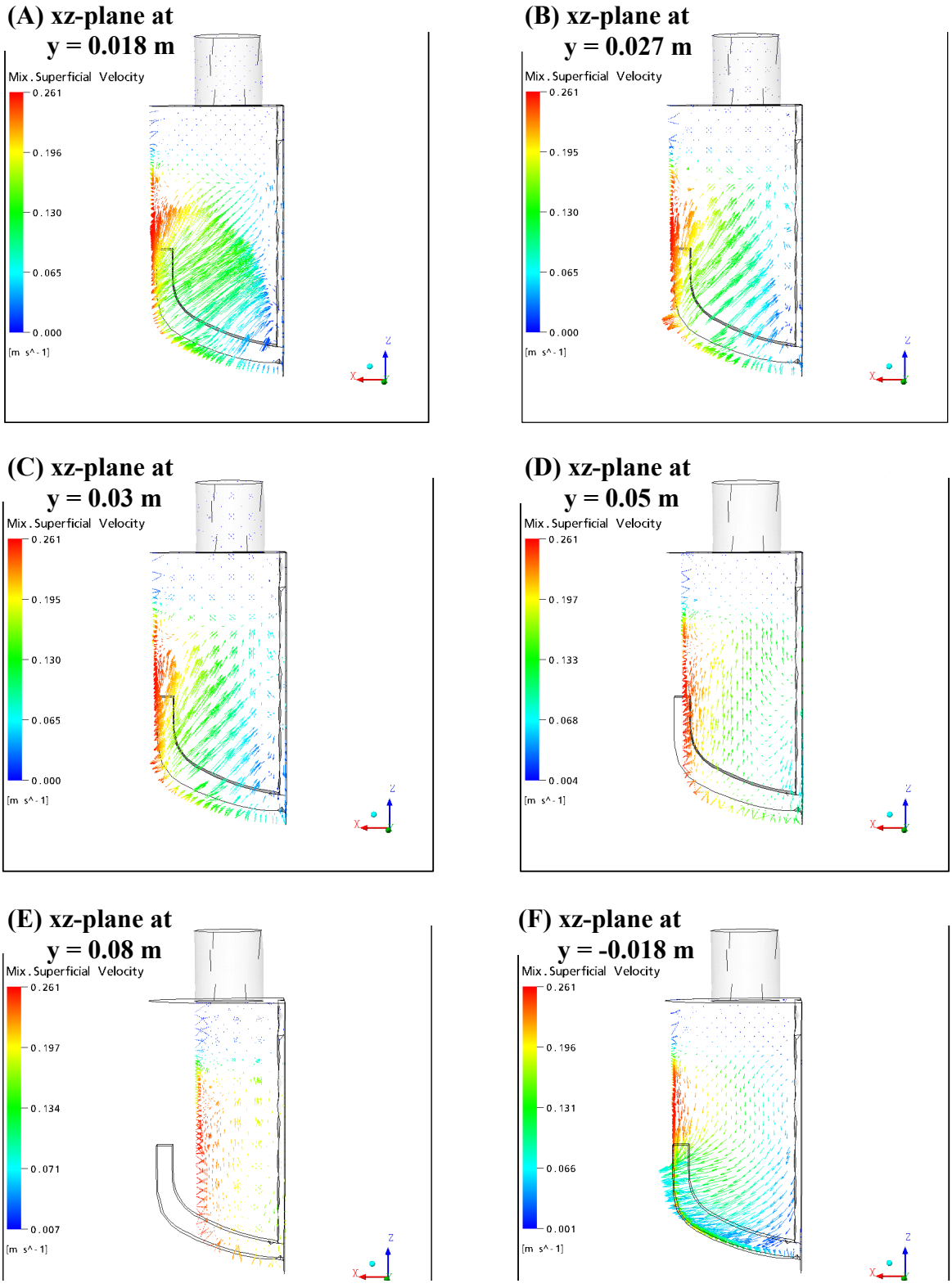

Figure 5.39-a: The calculated radial flow velocity field for different xz-planes in y-direction showing a secondary flow of an ethanol/glycerol mixture at ω = 25 rpm, t = 20 s and t_d = 1 s in a SBR.

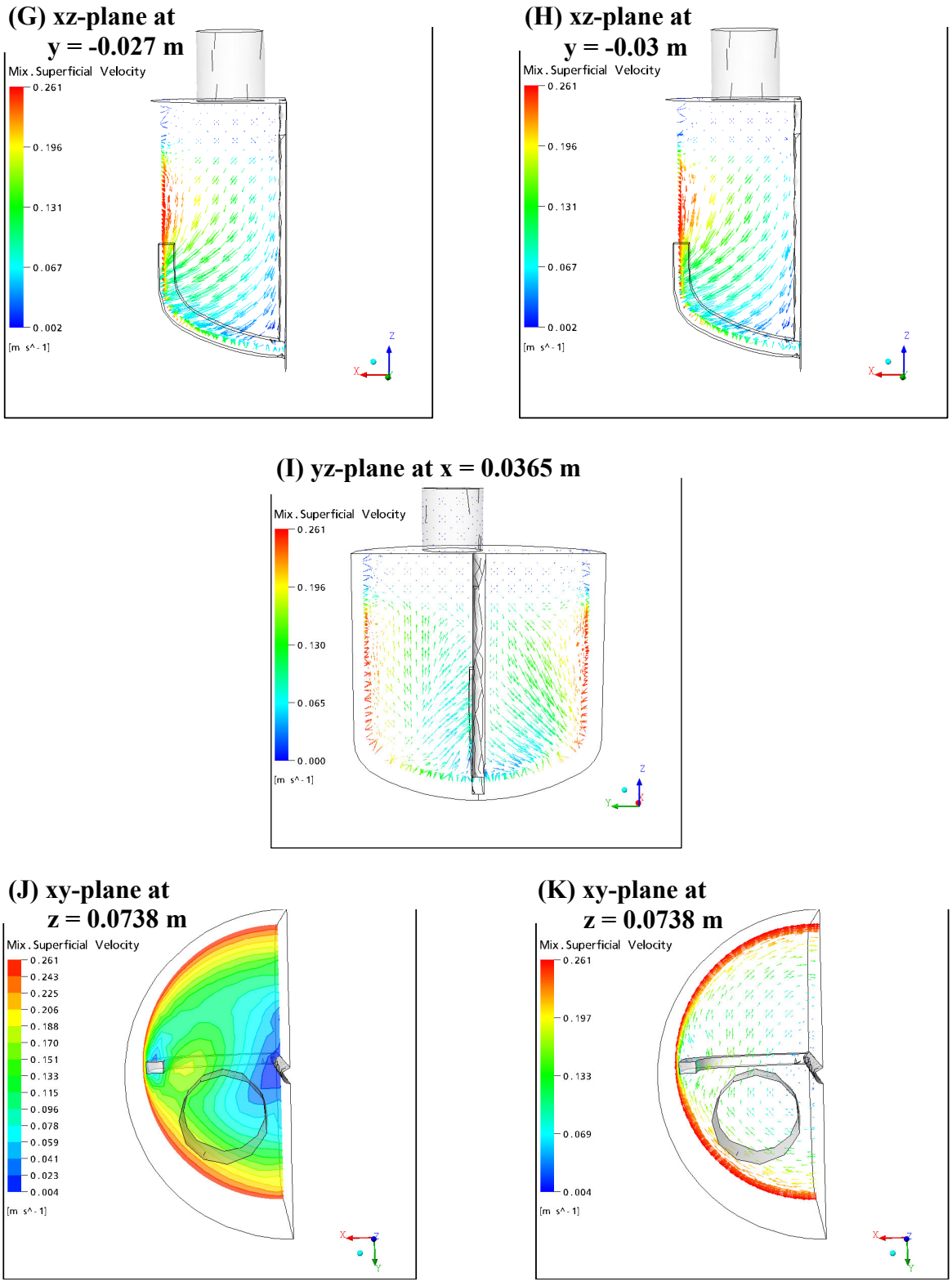

Figure 5.39-b: The calculated radial flow velocity field for different x,y,z-planes in x,y,z-directions showing a secondary flow of an ethanol/glycerol mixture at ω = 25 rpm, t = 20 s and t_d = 1 s in a SBR.

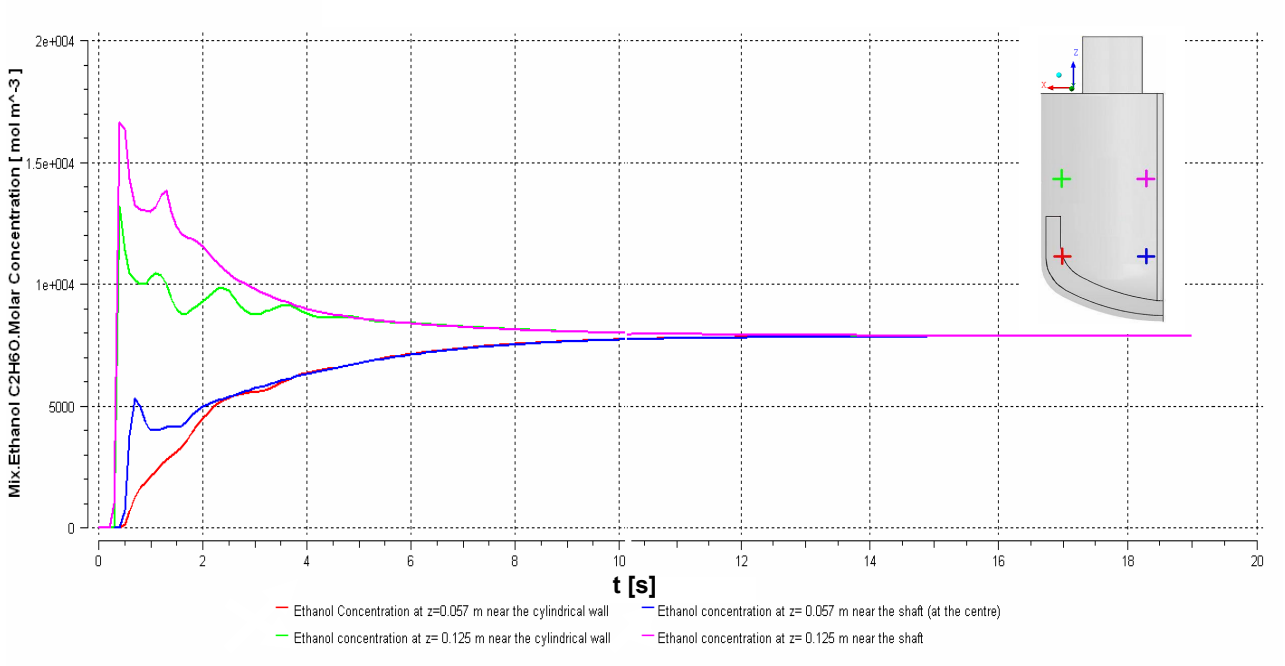

Figure 5.40: Ethanol concentration as a function of time at ω = 25 rpm at four different positions in a SBR at t_d = 1 s.

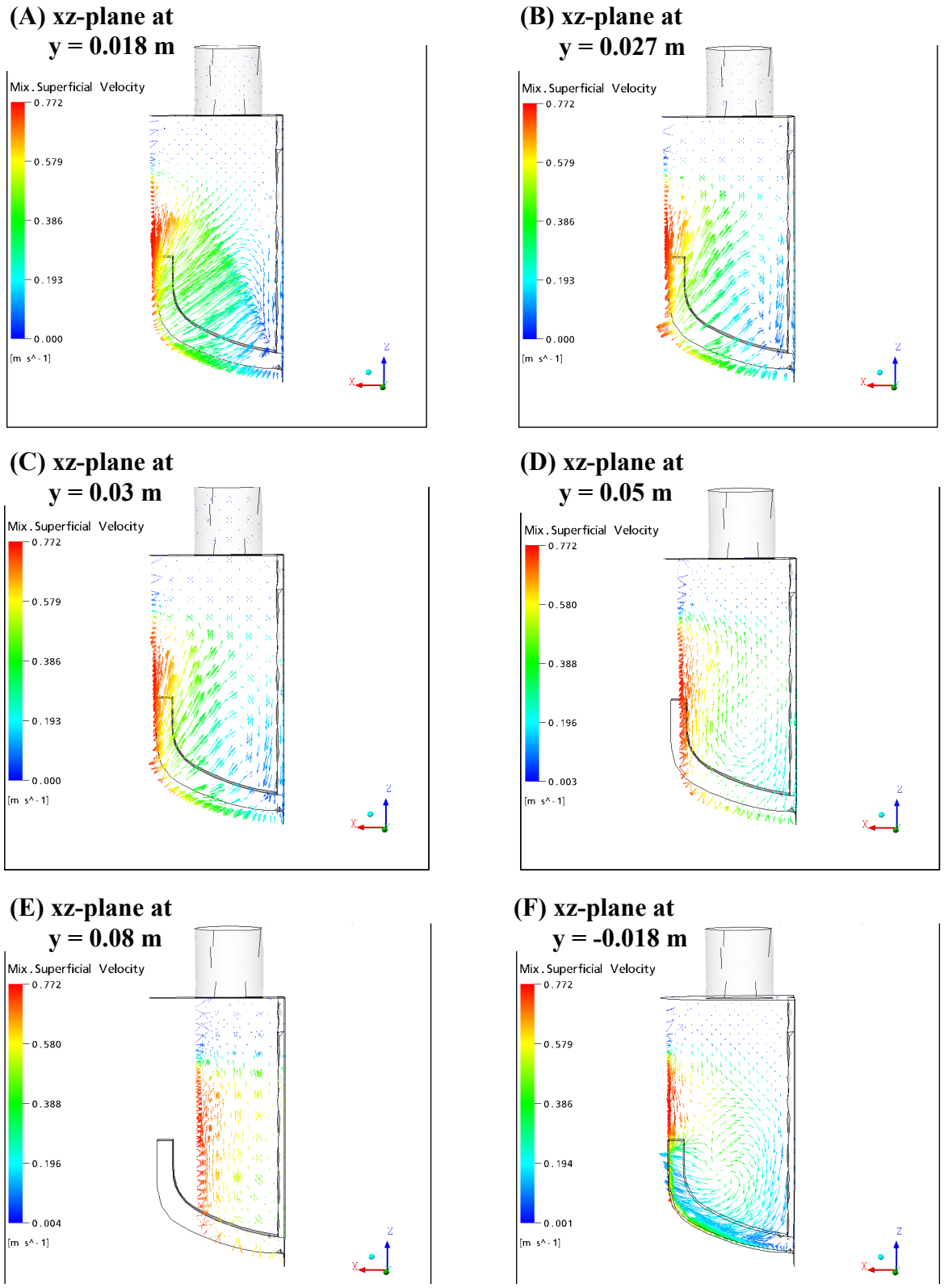

Figure 5.41-a: The calculated radial flow velocity field for different xz-planes in y-direction showing a secondary flow of an ethanol/glycerol mixture at ω = 75 rpm, t = 20 s and t_d = 1 s in a SBR.

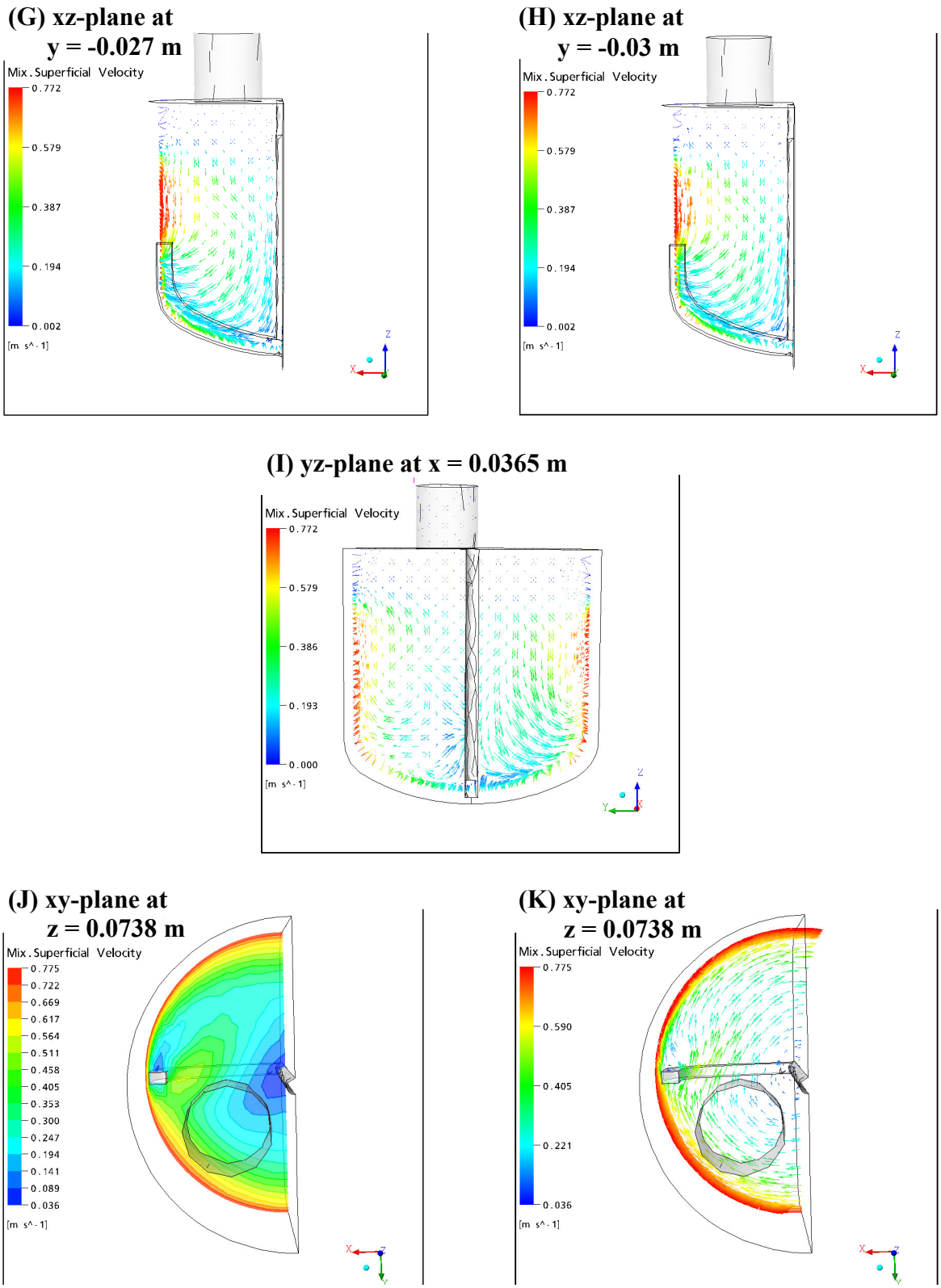

Figure 5.41-b: The calculated radial flow velocity field for different x,y,z-planes in x,y,z-directions showing a secondary flow of an ethanol/glycerol mixture at ω = 75 rpm, t = 20 s and t_d = 1 s in a SBR.

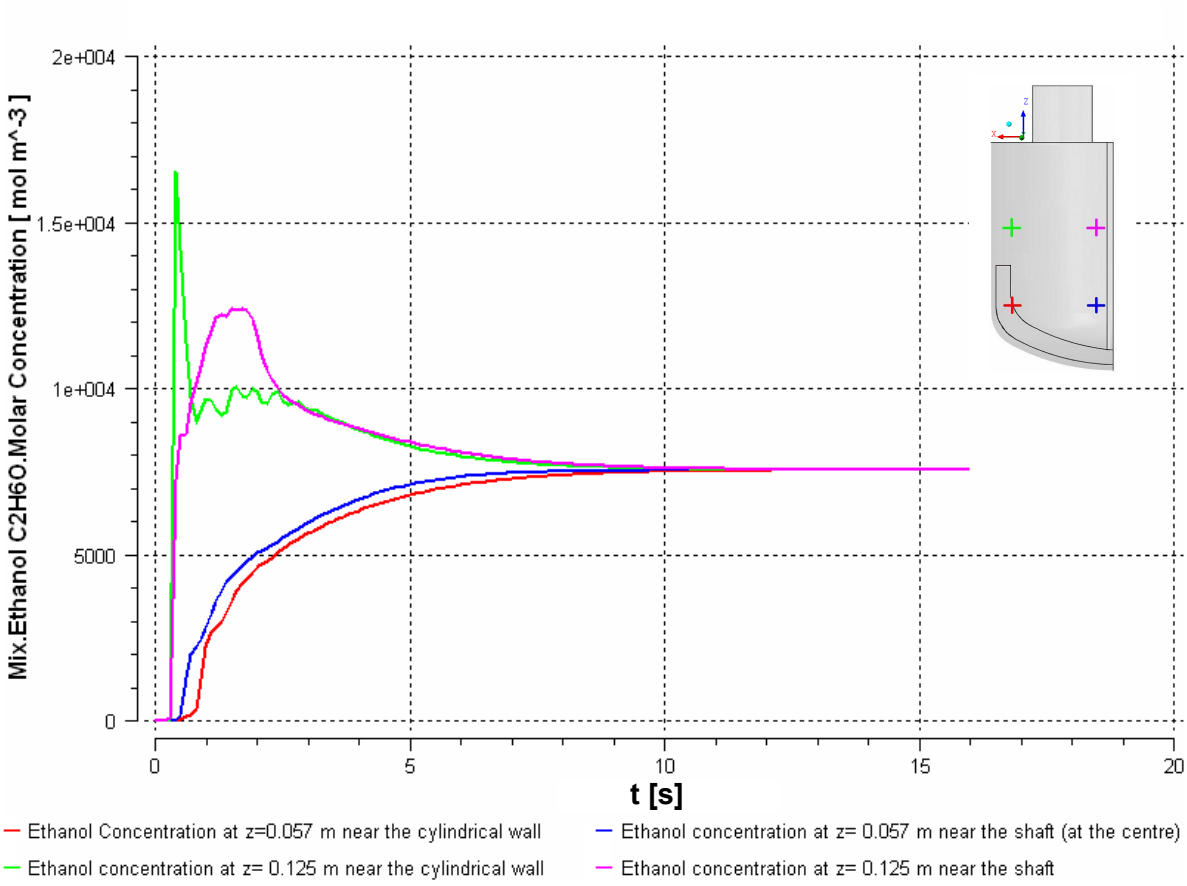

Figure 5.42: Ethanol concentration as a function of time for ω = 75 rpm at four different positions in a SBR at t_d = 1 s.

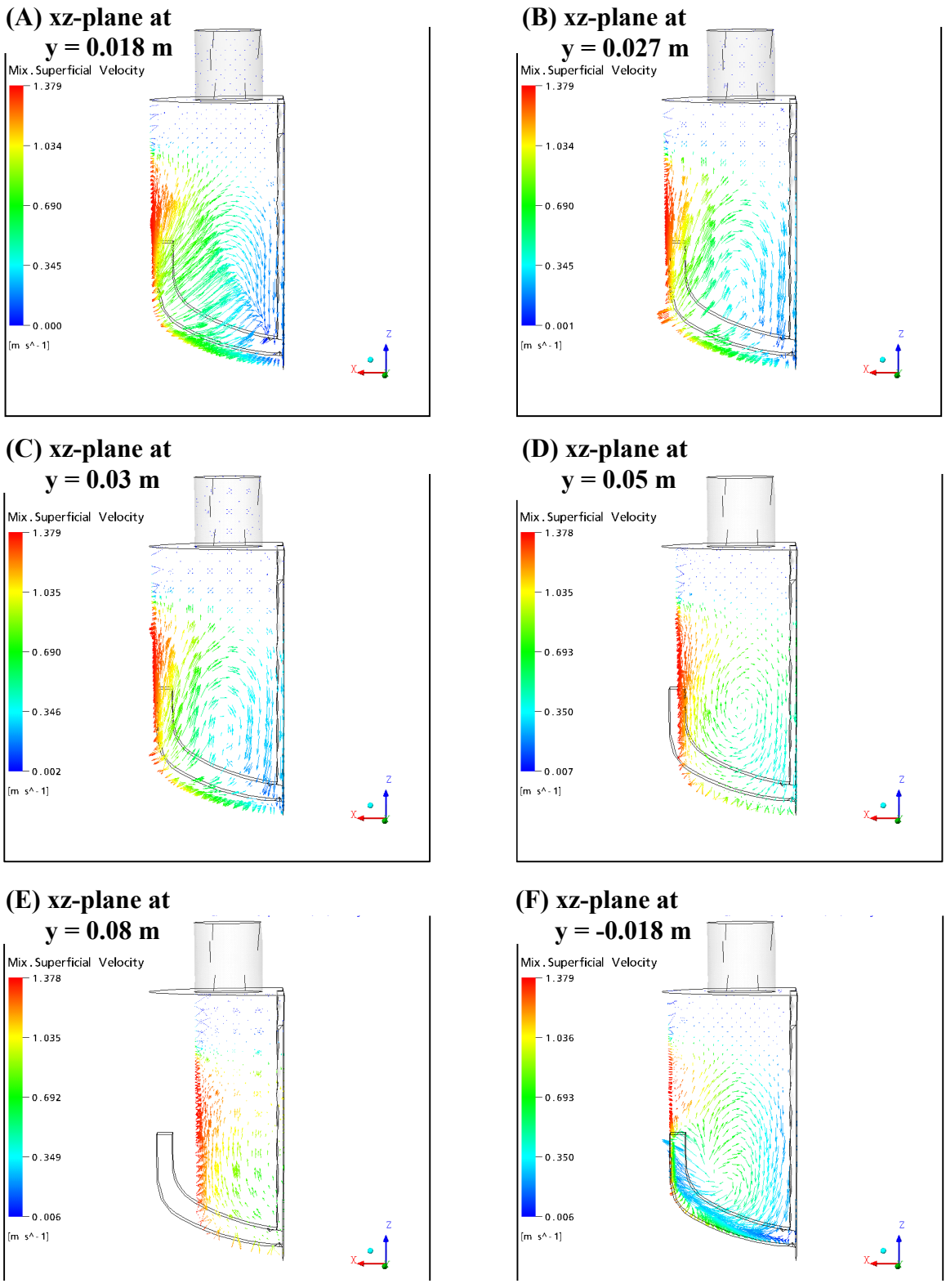

Figure 5.43-a: The calculated radial flow velocity field for different xz-planes in y-direction showing a secondary flow of an ethanol/glycerol mixture at ω = 150 rpm, t = 20 s and t_d = 1 s in a SBR.

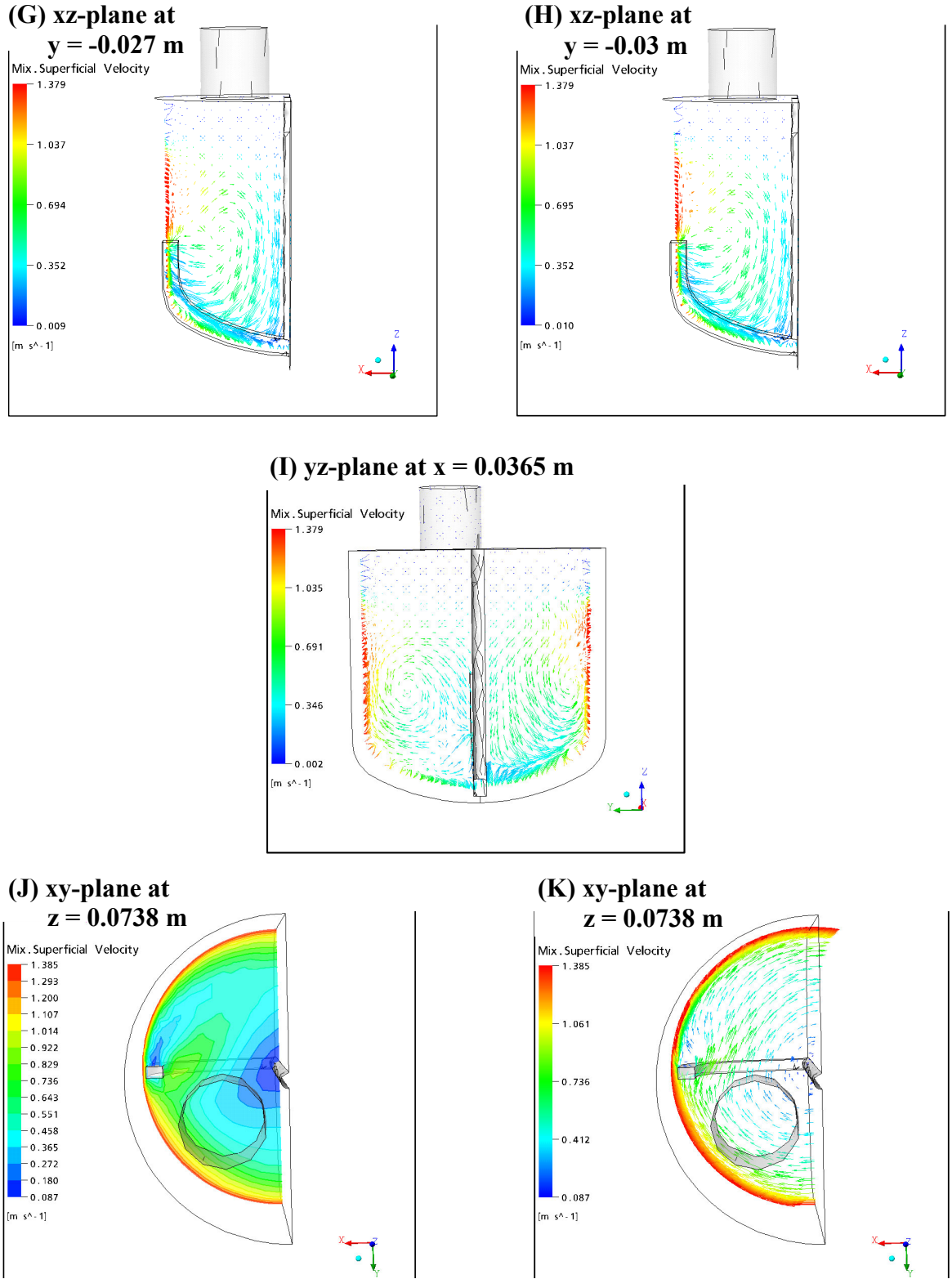

Figure 5.43-b: The calculated radial flow velocity field for different x,y,z-planes in x,y,z-directions showing a secondary flow of an ethanol/glycerol mixture at ω = 150 rpm, t = 20 s and t_d = 1 s in a SBR.

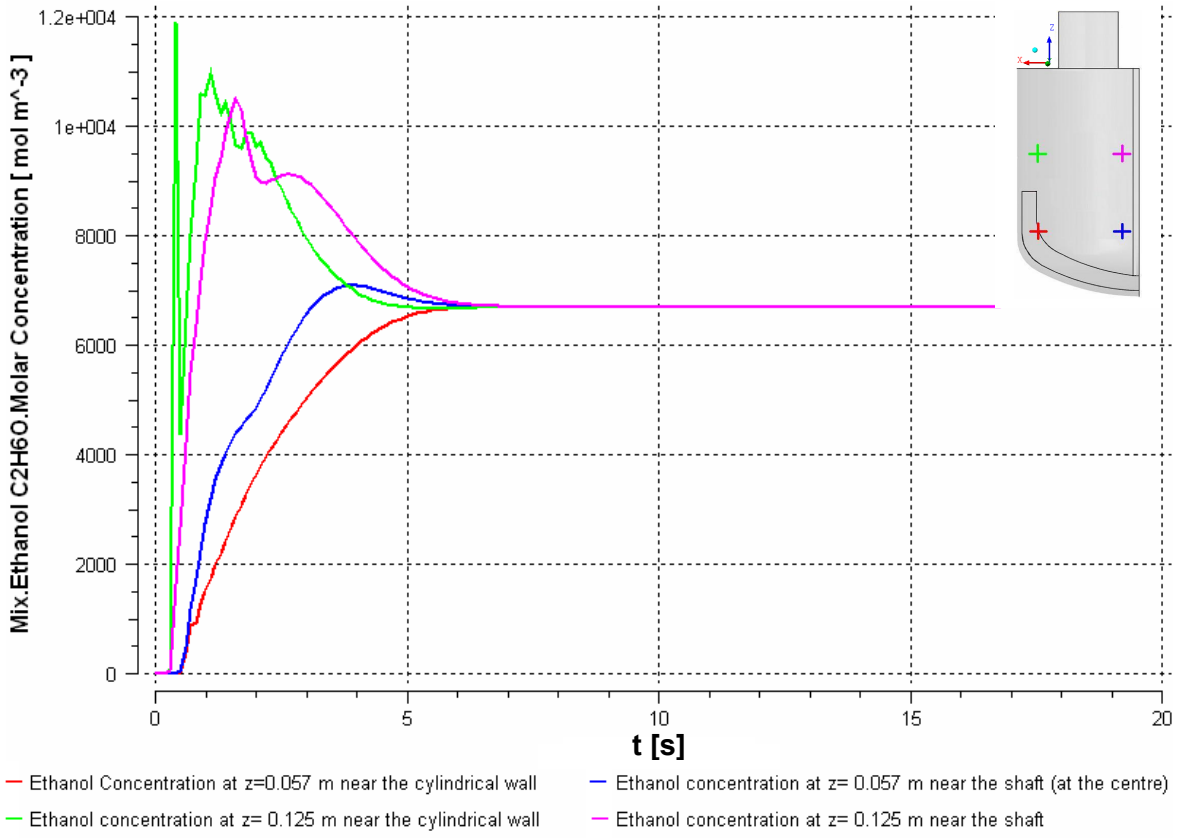

Figure 5.44: Ethanol concentration as a function of time for ω = 150 rpm at four different positions in a SBR at t_d = 1 s.

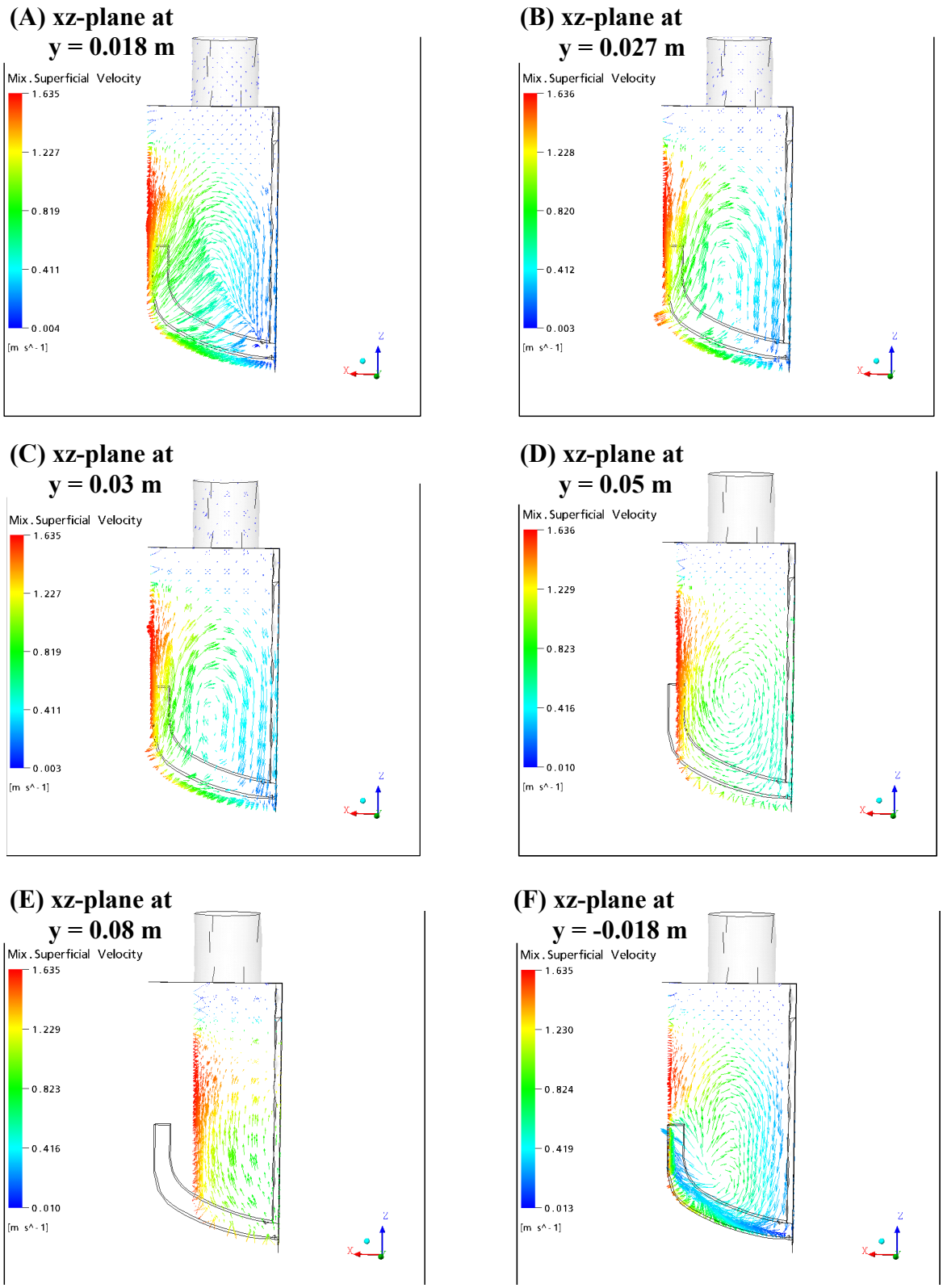

Figure 5.45-a: The calculated radial flow velocity field for different xz-planes in y-direction showing a secondary flow of an ethanol/glycerol mixture at ω = 250 rpm, t = 20 s and t_d = 1 s in a SBR.

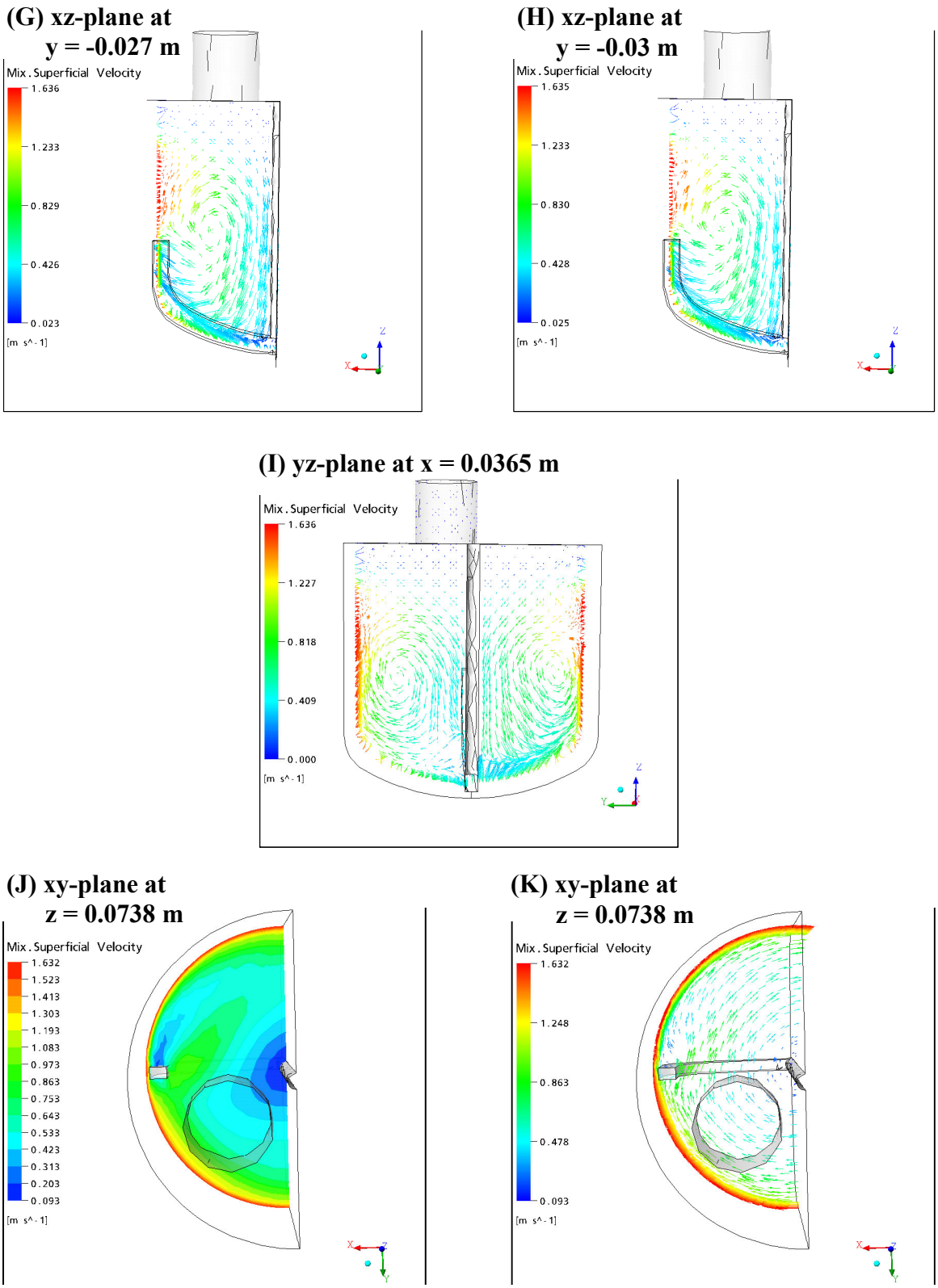

Figure 5.45-b: The calculated radial flow velocity field for different x,y,z-planes in x,y,z-directions showing a secondary flow of an ethanol/glycerol mixture at ω = 250 rpm, t = 20 s and t_d = 1 s in a SBR.

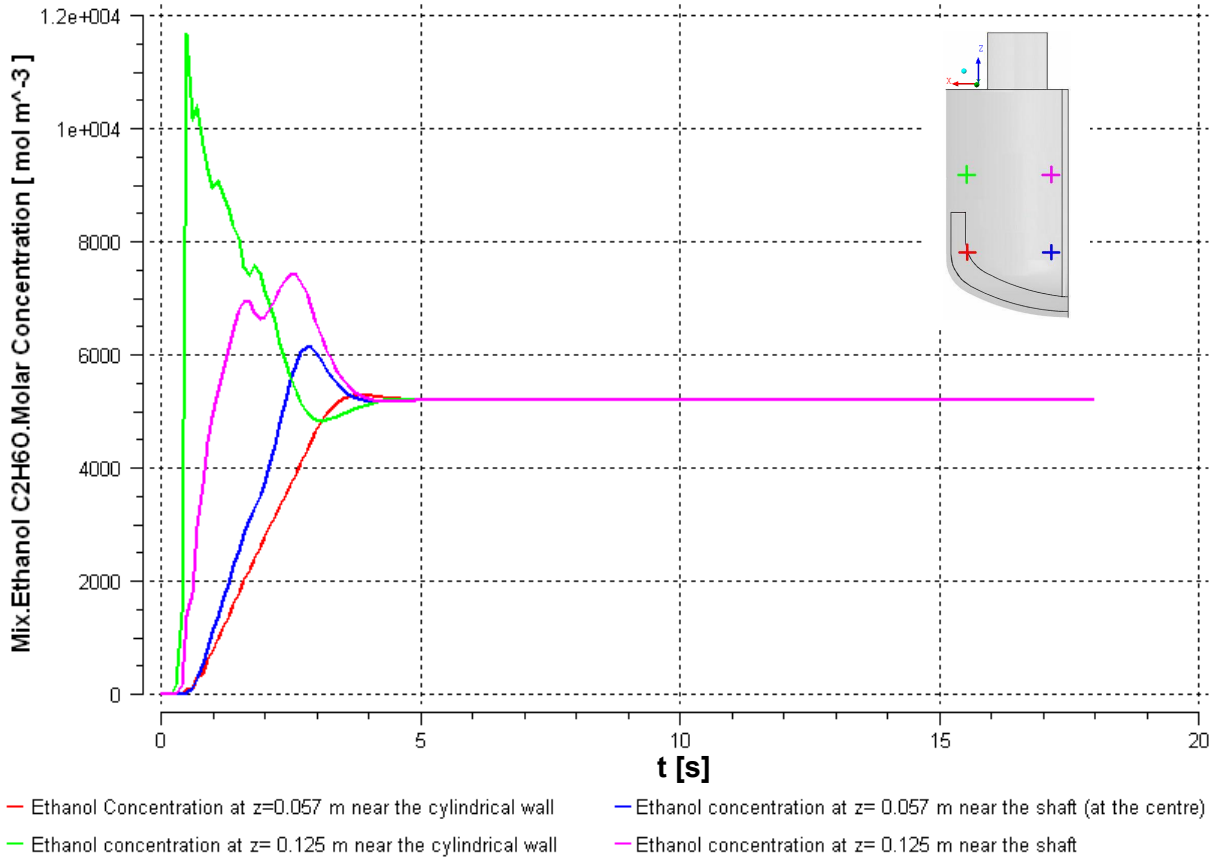

Figure 5.46: Ethanol concentration as a function of time for ω = 250 rpm at four different positions in a SBR at t_d = 1 s.

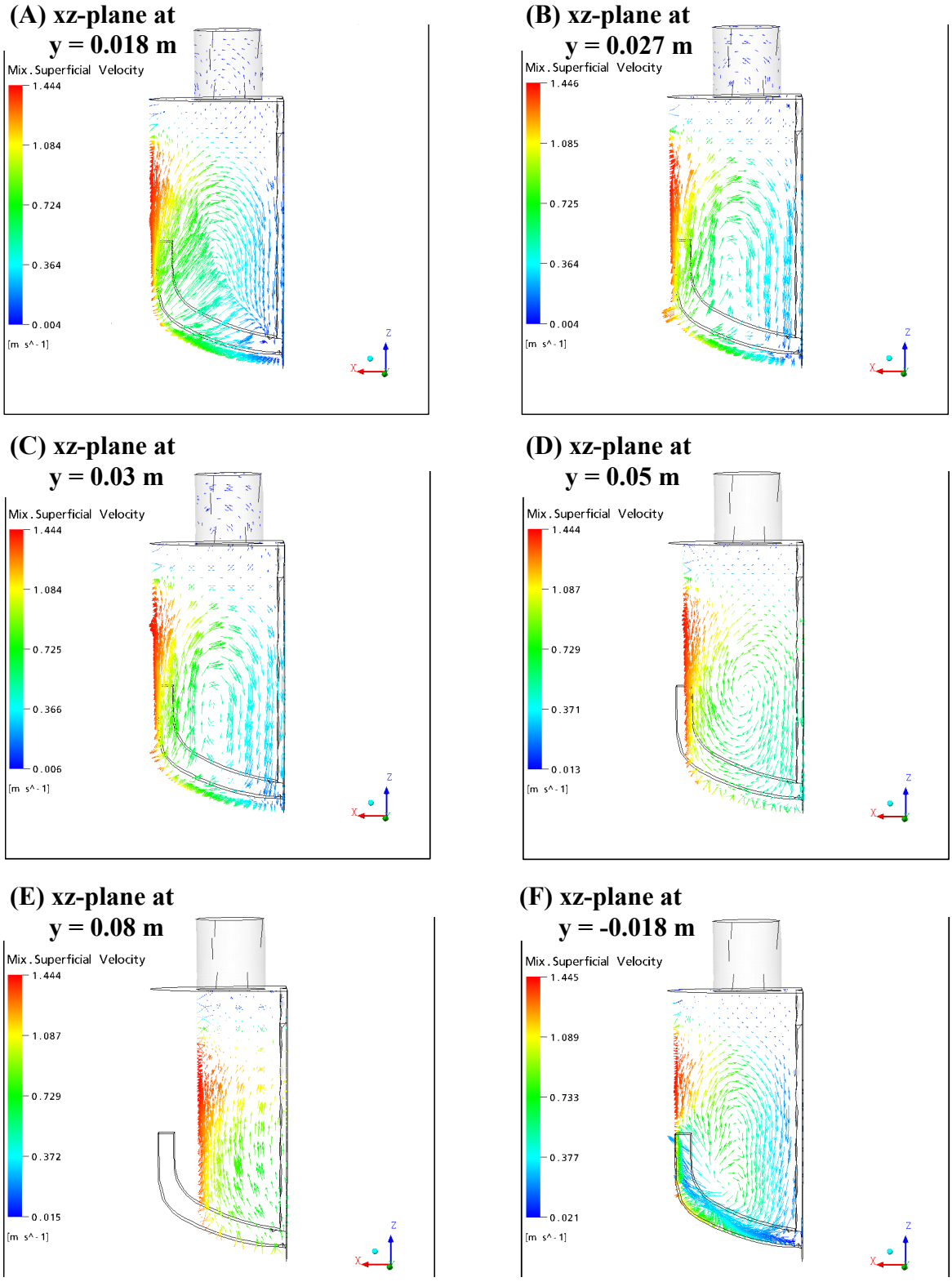

Figure 5.47-a: The calculated radial flow velocity field for different xz-planes in y-direction showing a secondary flow of an ethanol/glycerol mixture at ω = 300 rpm, t = 20 s and t_d = 1 s in a SBR.

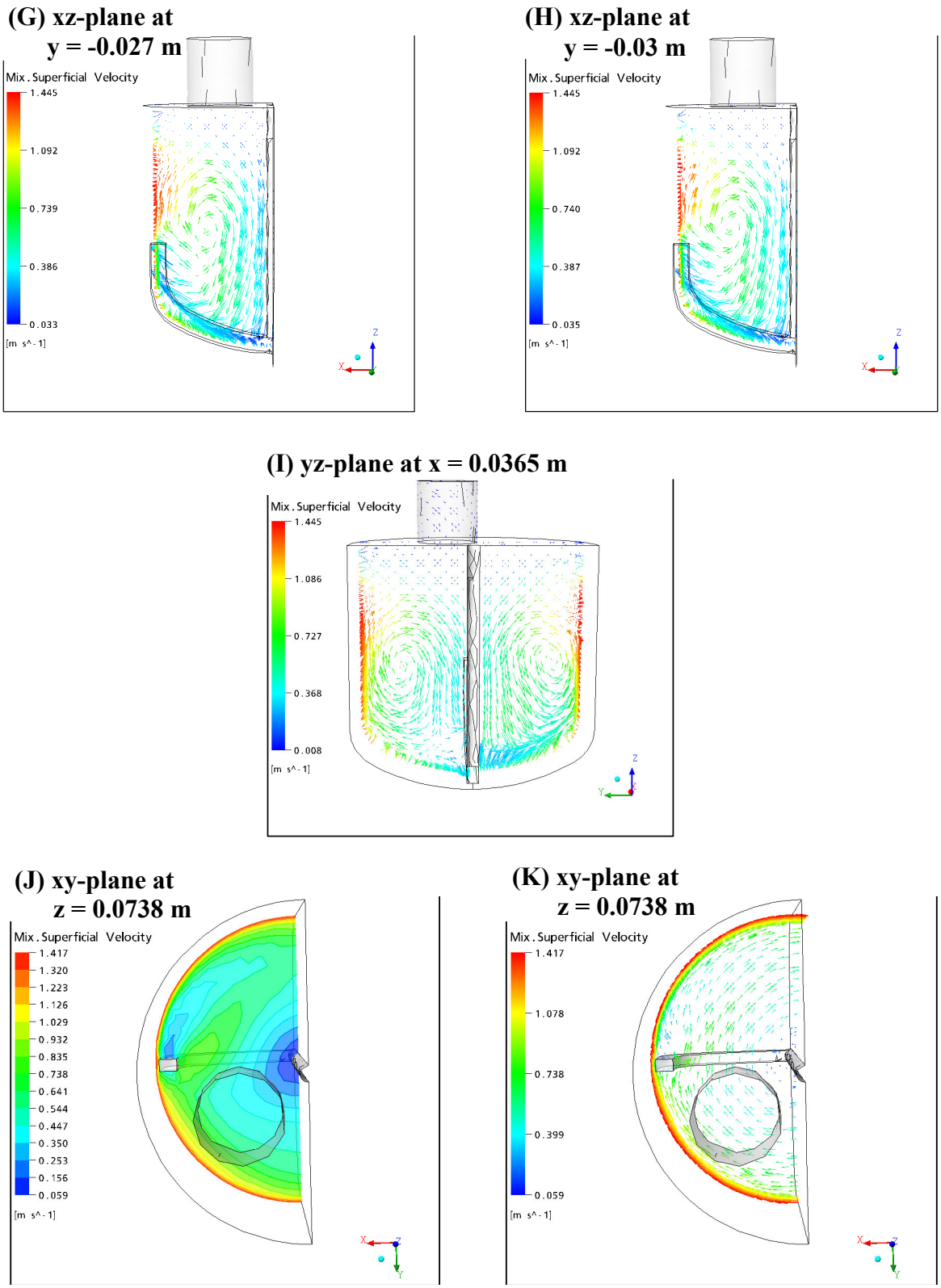

Figure 5.47-b: The calculated radial flow velocity field for different x,y,z-planes in x,y,z-directions showing a secondary flow of an ethanol/glycerol mixture at ω = 300 rpm, t = 20 s and t_d = 1s in a SBR.

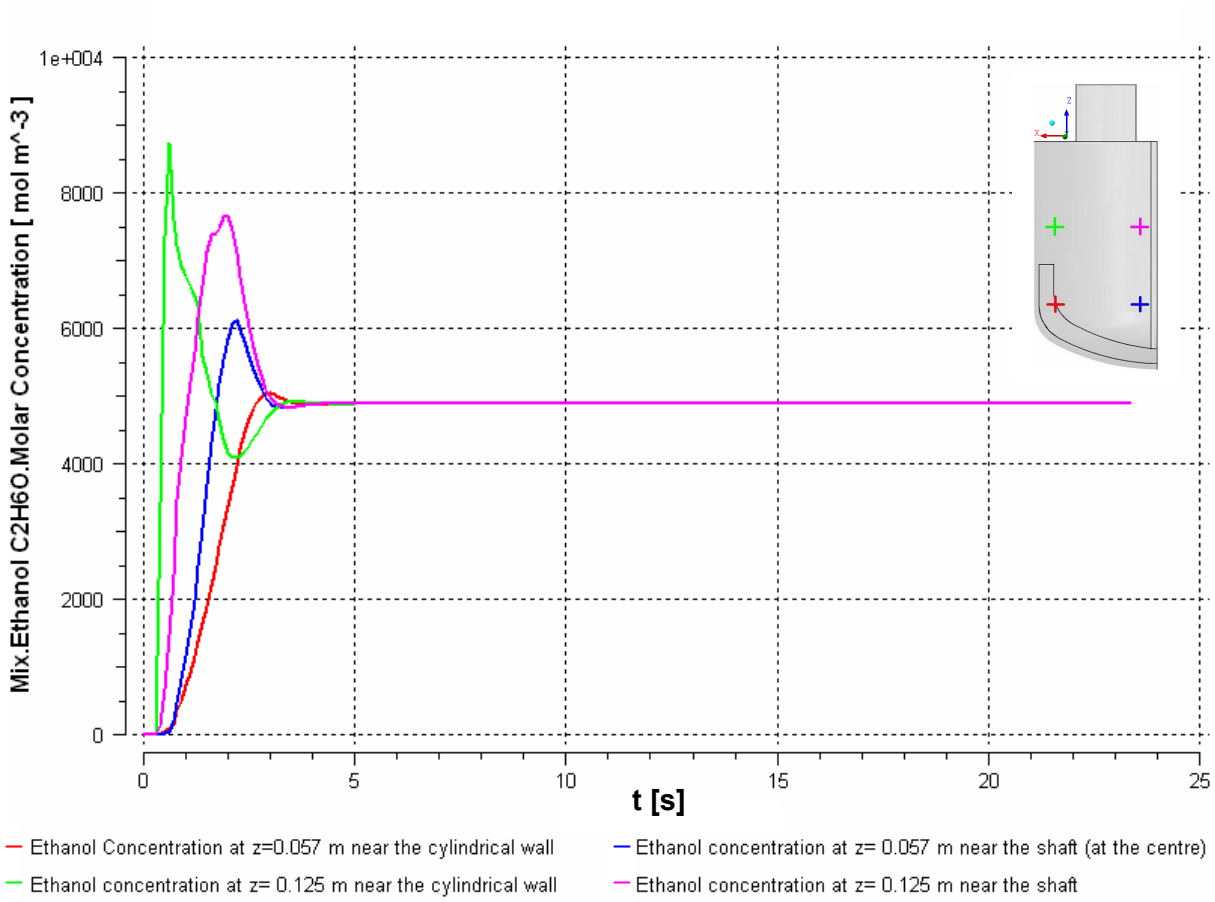

Figure 5.48: Ethanol concentration as a function of time for ω = 300 rpm at four different positions in a SBR at t_d = 1 s.

5.2.1.4.2 Dosage time t_d = 5 s

Secondary flow similar to the cases before can be seen from the axial flow velocity field in the radial y coordinate for ω = 150 rpm and t_m = 20 s in Figs. 5.49- a and b. The axial downward flow and circulation are found a little bit above the tip of the impeller leading to a small circulation loop between the impeller and shaft at the same height of the impeller tip. A complete circulation always is found behind the impeller at y = 0.05 m (Fig. 5.49-a-(A), (B), (C) and (D)). Figs. 5.49-c and d show the radial velocity fields in z coordinate at t_m = 20 s. The flow field is approximately tangential near the horizontal blade of the impeller at z = 0.024 m (Fig. 5.49-a-(A)). A vortex is formed towards to the inside of the vertical blade of the impeller at z = 0.0575 m –in the middle between the horizontal blade and the tip of the impeller–, this vortex accelerates the distribution of ethanol in the bulk (Fig. 5.49-c-(M)). At the tip of the vertical blade at z = 0.086 m, the vortex spread around the impeller tip and enhance the mixing process (Fig. 5.49-c-(N)). Above the tip of the impeller a tangential flow velocity is obtained at z = 0.0983 m and z = 0.123 m (Fig. 5.49-c-(O) and (P), respectively). The radial velocity decreases above the impeller, the minimum velocity is found at the interface between the liquid mixture and air (Figs. 5.49-c-(P) and (Q) and 5.49-d).

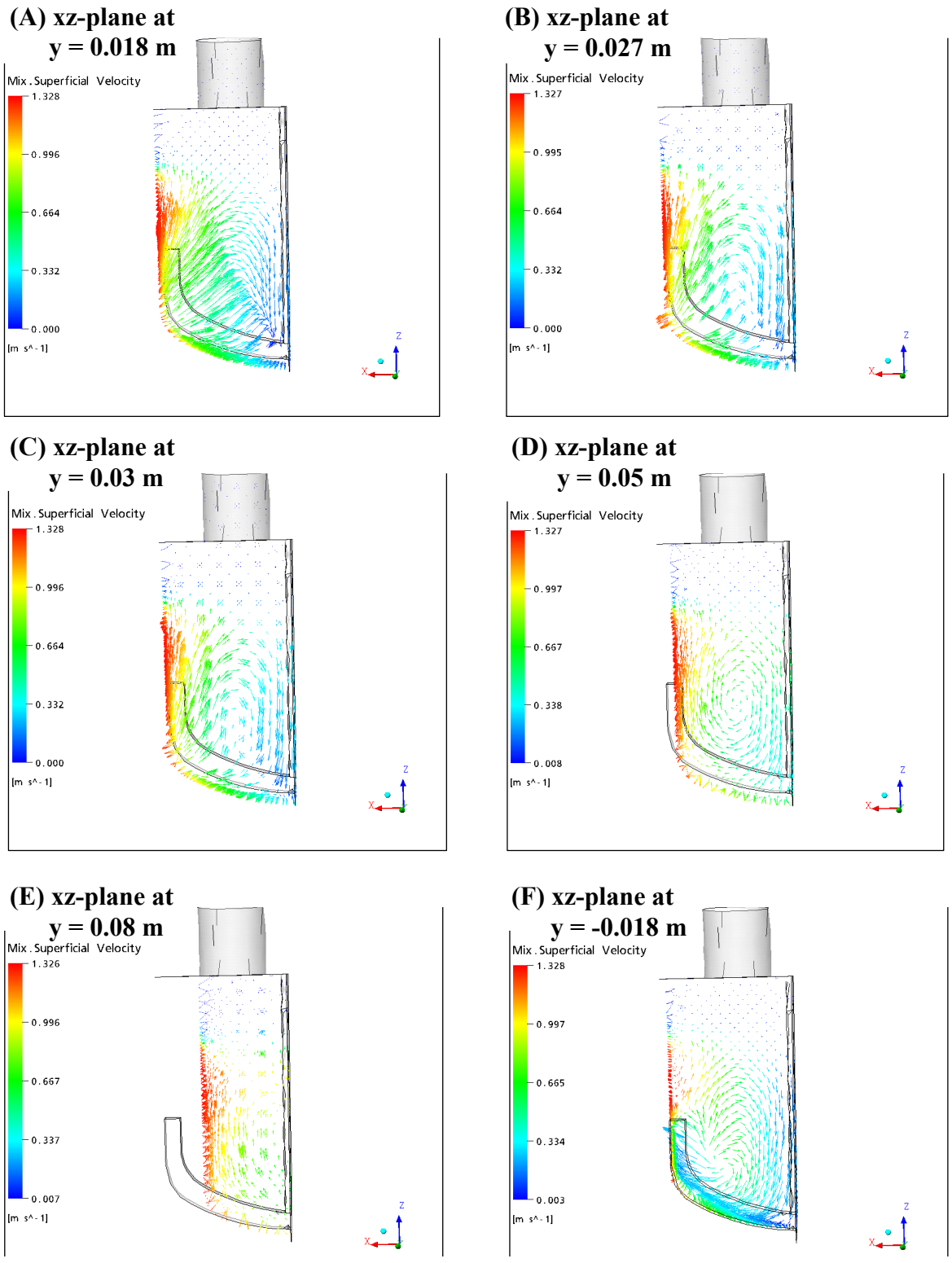

Figure 5.49-a: The calculated radial flow velocity field for different xz-planes in y-direction showing a secondary flow of an ethanol/glycerol mixture at ω = 150 rpm, t = 20 s and t_d = 5 s in a SBR.

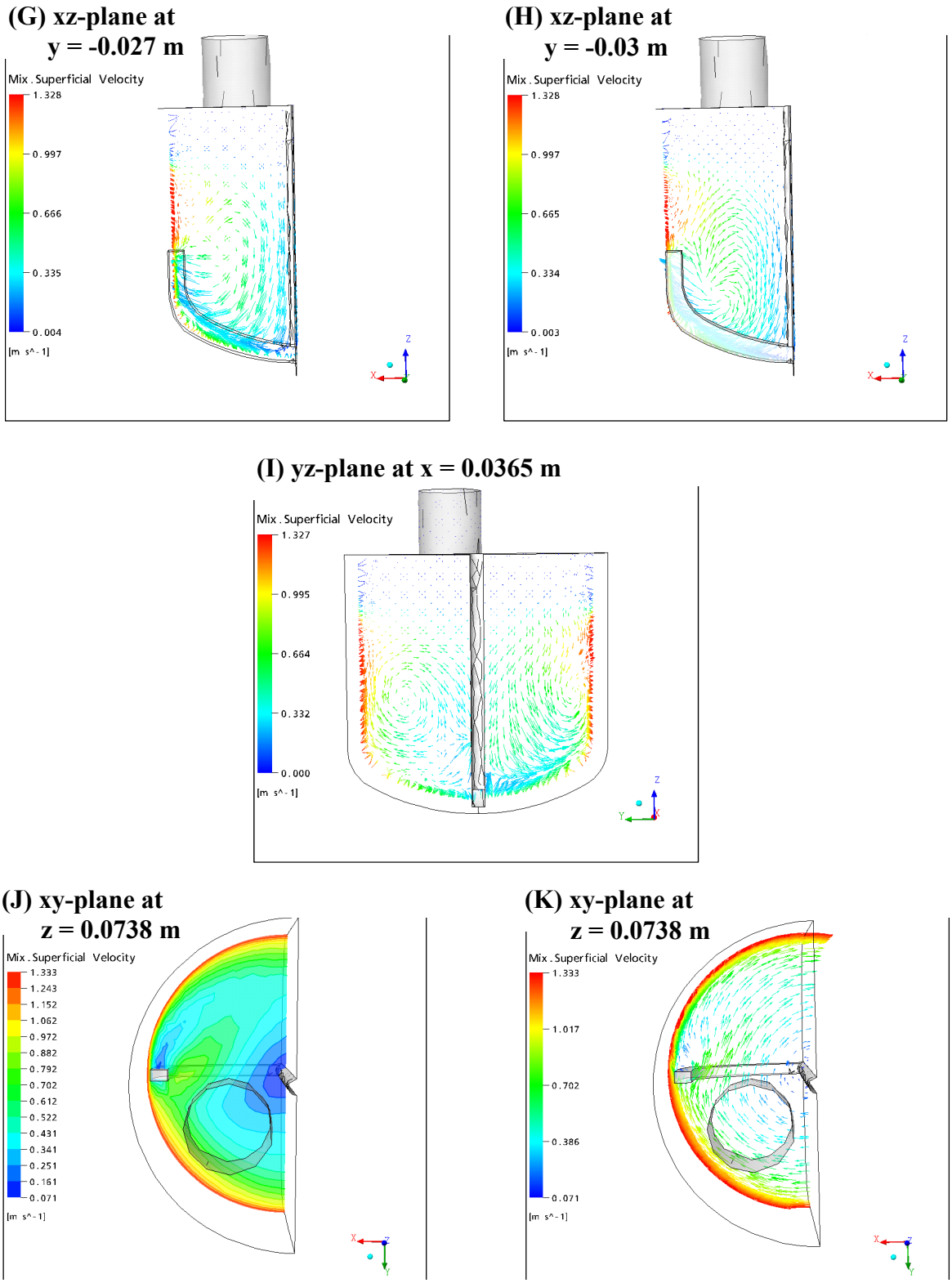

Figure 5.49-b: The calculated radial flow velocity field for different x,y,z-planes in x,y,z-directions showing a secondary flow of an ethanol/glycerol mixture at ω = 150 rpm, t = 20 s and t_d = 5 s in a SBR.

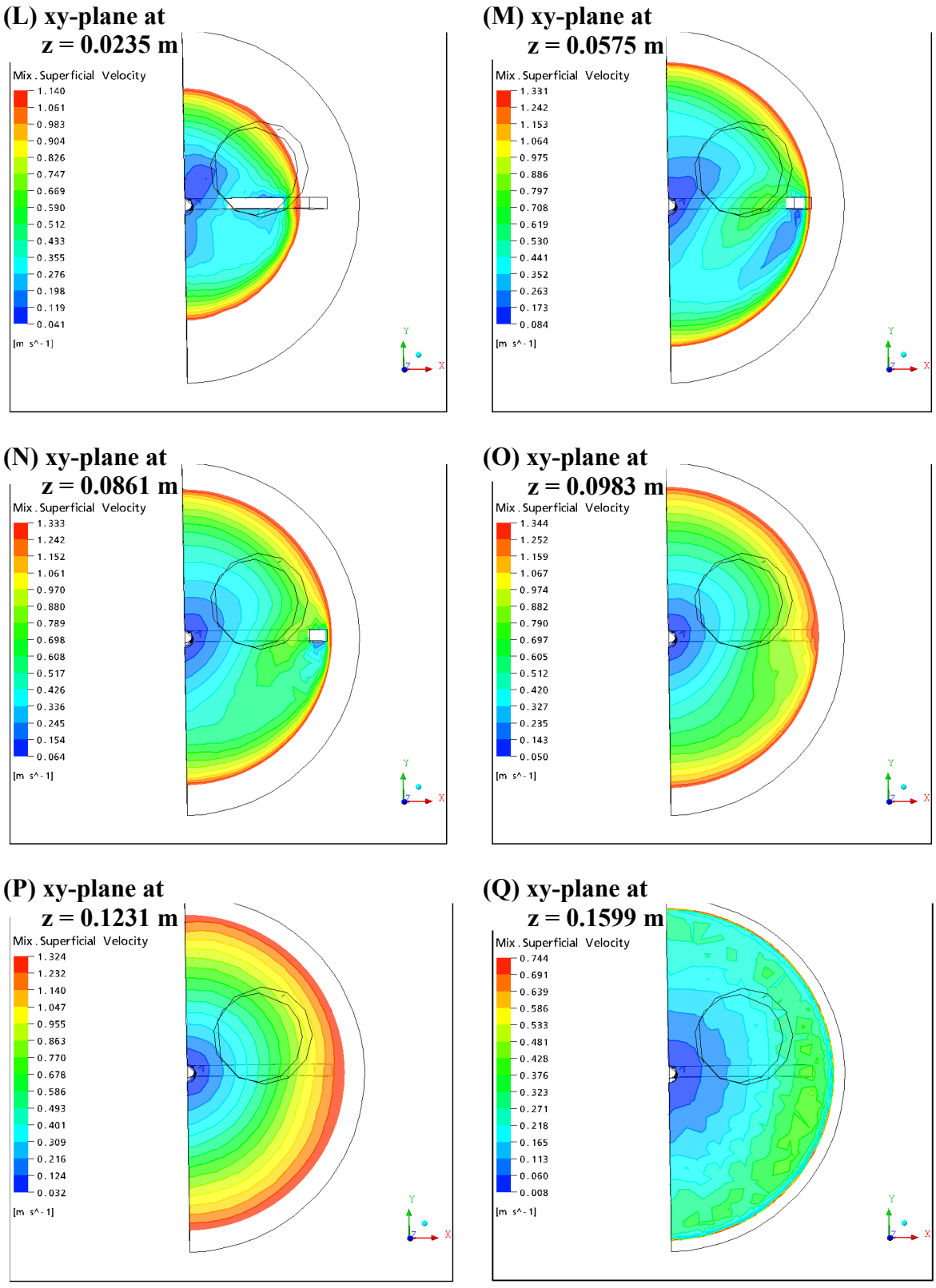

Figure 5.49-c: The calculated radial flow velocity field for different xy-planes in z-direction of an ethanol/glycerol mixture at ω = 150 rpm, t = 20 s and t_d = 5 s in a SBR.

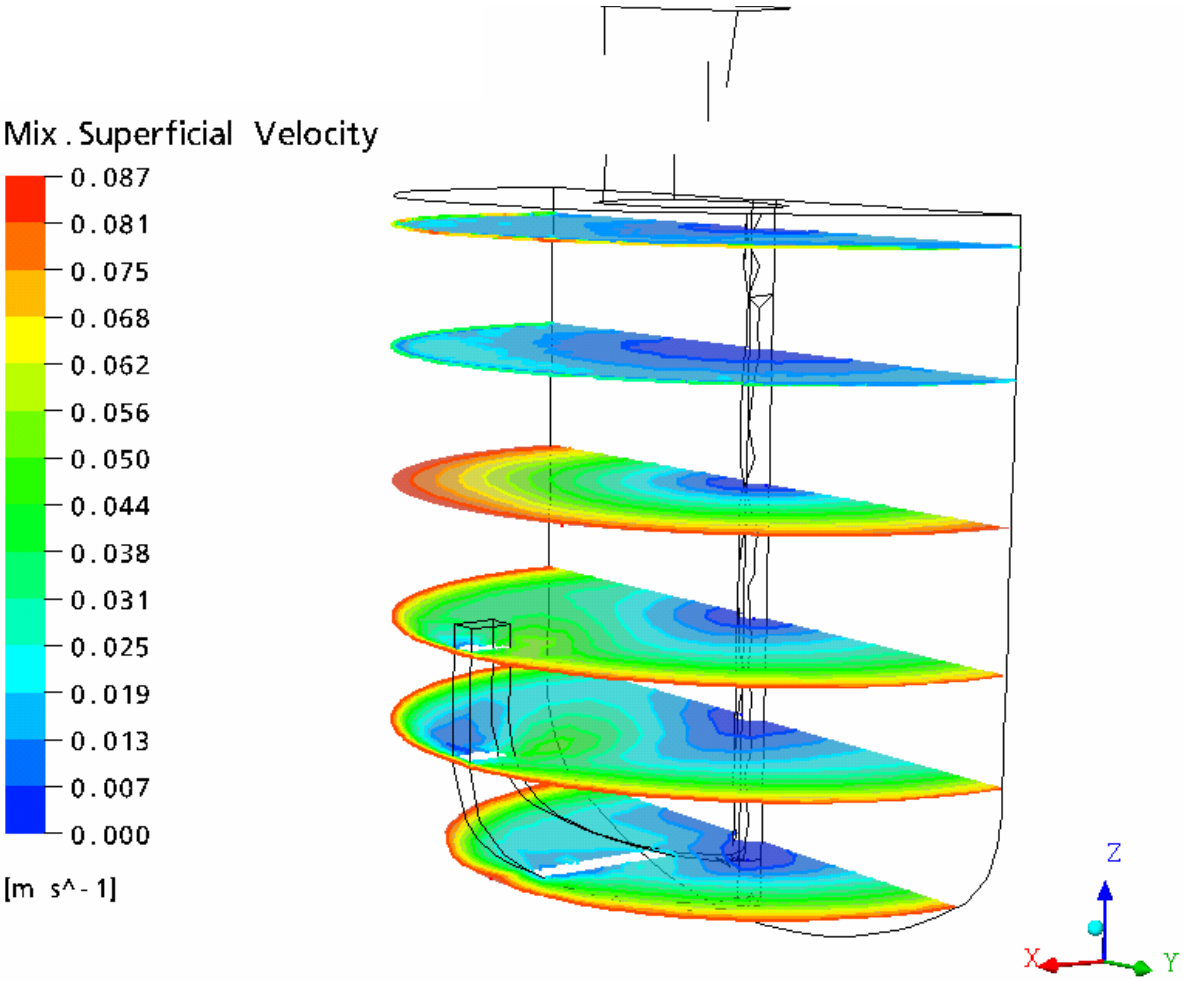

Figure 5.49-d: The calculated radial flow velocity fields of an ethanol/glycerol mixture for different xy-planes in z-direction at ω = 150 rpm, t = 20 s and t_d = 5 s in a SBR.

For t_d = 5 s when the anchor velocity increases, the final mixture viscosity increases up to ω = 250 rpm, because the mass fraction of the unmixed ethanol decreases (Fig. 5.50). A small decreasing of the mixture viscosity is found between ω = 250 rpm and ω = 350 rpm because it may be exist a small mass of the low velocity dosed ethanol at the liquid interface near the cylindrical wall. The high anchor velocity rise the level of the bulk liquid near the cylindrical wall. A constant final mixture viscosity η_m is found after ω = 350 rpm.

For t_d = 1 s the final mixture viscosity is directly proportional to the anchor velocity up to ω = 350 rpm then it becomes constant, because all the dosed mass of ethanol is completely mixed with glycerol (Fig. 5.50).

The final mixture viscosity at t_d = 1 s is lower than that for t_d = 5 s up to ω = 250 rpm because the velocity of the dosed ethanol at t_d = 1 s is higher. Similar final mixture viscosity for both dosages is found at ω = 300 rpm. Above ω = 300 rpm it is surprising that the final mixture viscosity at t_d = 1 s is higher than that at t_d = 5 s, because the high anchor velocity produces high upward shear forces which collides with the high inlet ethanol velocity stream in case of t_d = 1 s, and resists ethanol to be mixed completely with glycerol leading to a higher final mixture viscosity.

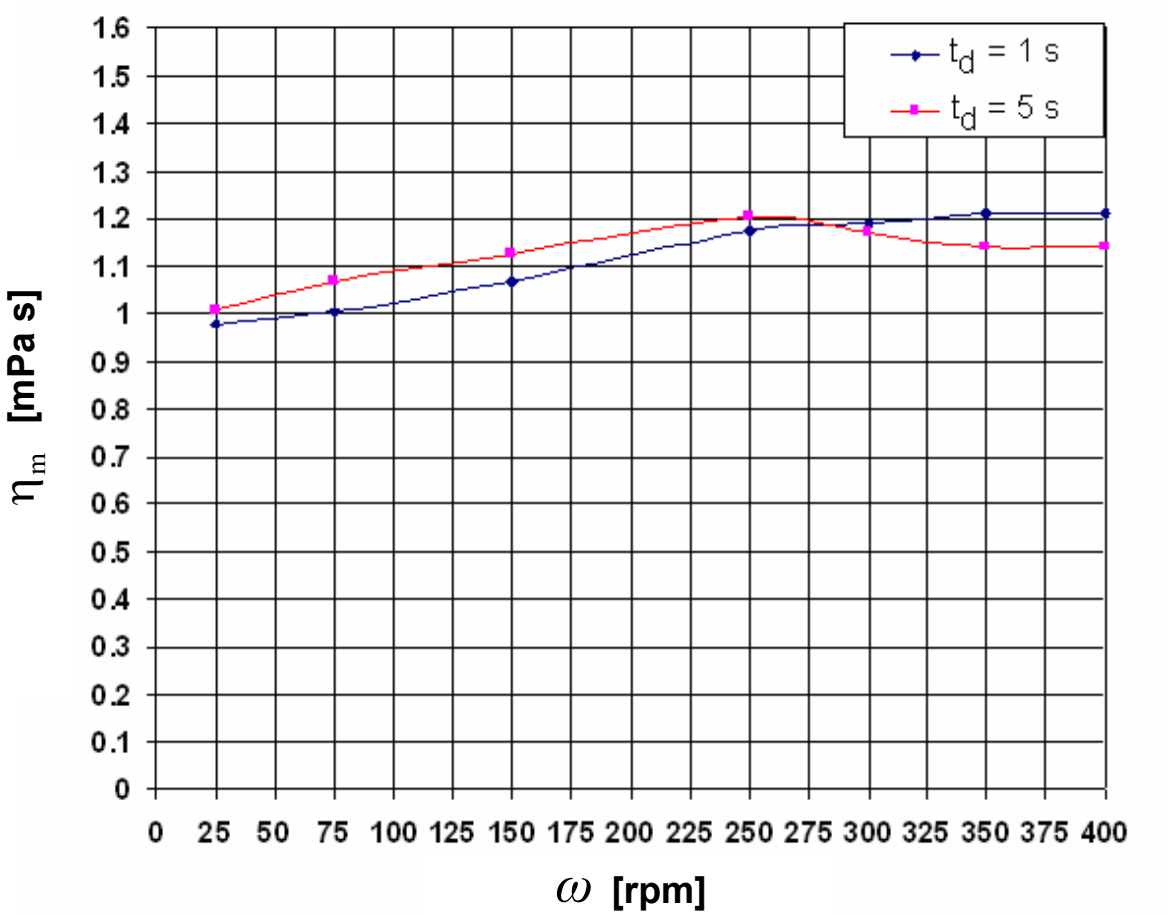

Figure 5.50: Final mixture viscosity as a function of anchor velocity in a SBR with d_t = 5 cm and 26,000 tetrahedrons cells for t_d = 1 and t_d = 5 s at t = 20 s.

5.2.1.5 The effect of anchor dimensions

The mixing time and the flow velocity-, mixture viscosity- and volume fraction fields as a function of time are studied in a SBR at t_d = 5 s between $0.2\,s \le t_d \le 5.2\,s$, d_t = 5 cm and ω = 150 rpm for two types of anchors with two different horizontal blade widths. The two anchor impellers with horizontal blade widths of w_h = 0.015 and 0.012 m for wide and thin horizontal blades, respectively are shown in Fig. 5.51.

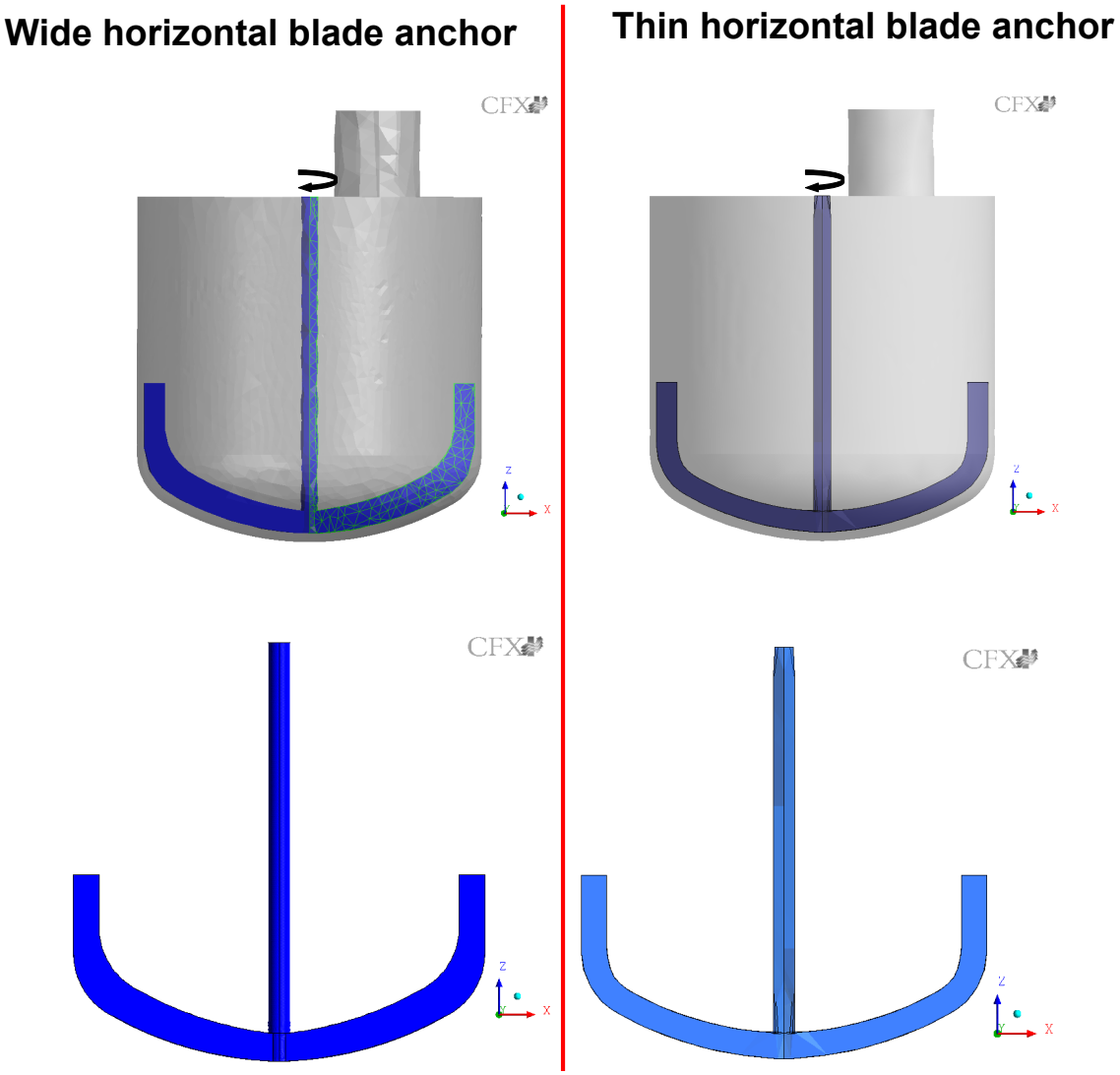

Figure 5.51: Anchor impellers with horizontal blade widths of w_h = 0.015 m (left) and w_h = 0.012 m (right).

Before the dosage of ethanol similar fields of mixture viscosity and flow velocity are obtained for both impellers but higher radial velocity is found near the corner of the wide blade impeller (Fig. 5.52-a). A faster mixing of ethanol with glycerol in the case of a wide blade impeller is obtained as it can be seen from the velocity field of left column (e.g. in Fig. 5.52-b) in comparison to the clear smaller velocities in the case of the thin horizontal blade anchor (right column in Fig. 5.52-b). The faster mixing is caused by the high axial velocities and circulation which lead to a decrease of the mixture viscosity near the bottom of the vessel as can be seen from the contour lines of constant mixture viscosity at t = 5.2 s in Fig. 5.52-b. A larger mass of ethanol flows towards the shaft will be mixed with glycerol leading to a clear lower mixture viscosity with a sharp convex shape for wide horizontal blade anchor at t = 10 s (left column in Fig. 5.52-b) than in the case of thin horizontal blade anchor at t = 10 (right column in Fig. 5.52-b).

Ethanol is continuously transported by the impeller towards the shaft and mixed with glycerol leading to a sharper convex shape in case of the blade width of w_h = 0.015 m (left column in Fig. 5.52-c) compared to that of w_h = 0.012 m (right column in Fig. 5.52-c) which can be seen from the viscosity field between $11\,s \le t \le 13\,s$. Then ethanol is mixed with glycerol from the shaft towards the cylindrical wall leading to a small zone with high mixture viscosity near the corner of the vessel (left column in Fig. 5.52-d). A faster mixing occurs in the case of the wide blade anchor compared with the thin blade anchor (right column in Fig. 5.52-d) in which the mixing is still from the impeller towards the shaft as can be seen from the viscosity field between $15\,s \le t \le 18\,s$.

It is found that the mixing times for blade widths of w_h = 0.015 m and w_h = 0.012 m are t_m = 19 s and t_m = 28 s as can be seen in Figs. 5.52-e and 5.52-f, respectively. When the width of the anchor impeller blade increases the required mixing time to get a constant homogenous mixture viscosity decreases.

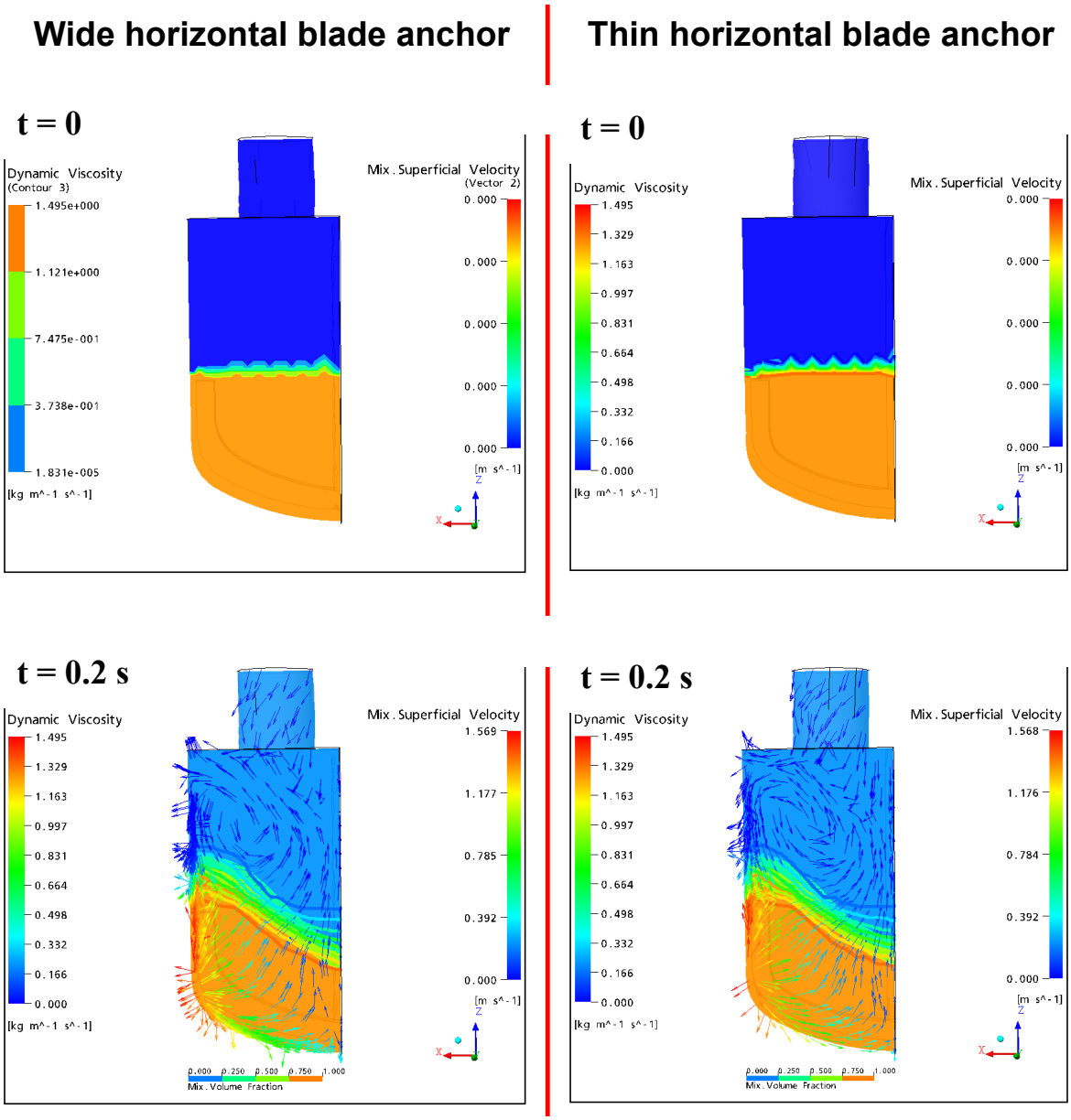

Figure 5.52-a: Mixture viscosity-, flow velocity- and volume fraction fields for horizontal blade widths of w_h = 0.015 m (left) and w_h = 0.012 m (right) for ω = 150 rpm in a SBR with t_d = 5 s at t = 0 and 0.2 s.

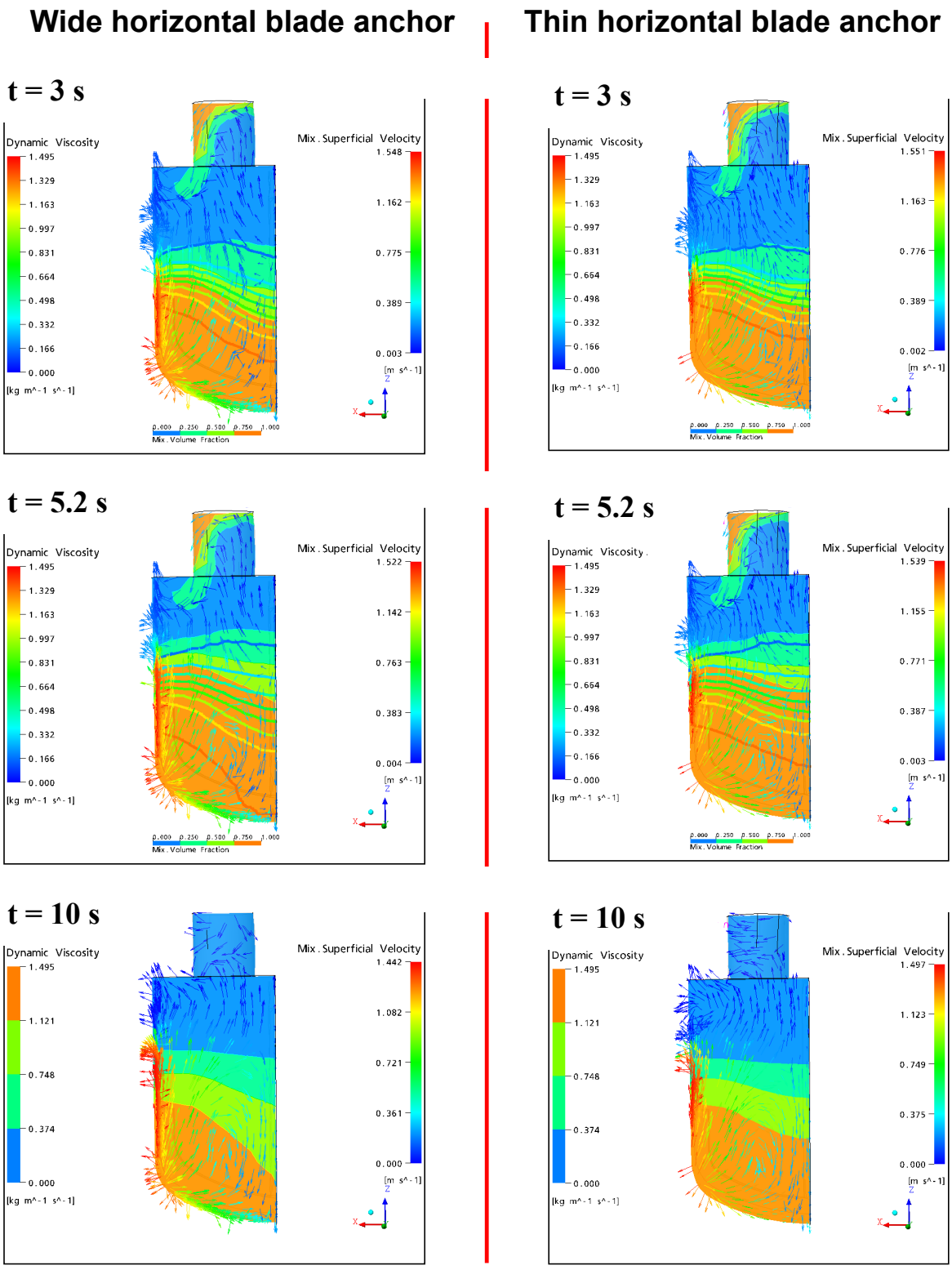

Figure 5.52-b: Mixture viscosity-, flow velocity- and volume fraction fields for horizontal blade widths of w_h = 0.015 m (left) and w_h = 0.012 m (right) for ω = 150 rpm in a SBR with t_d = 5 s at t = 3 s, 5.2 s and 10 s.

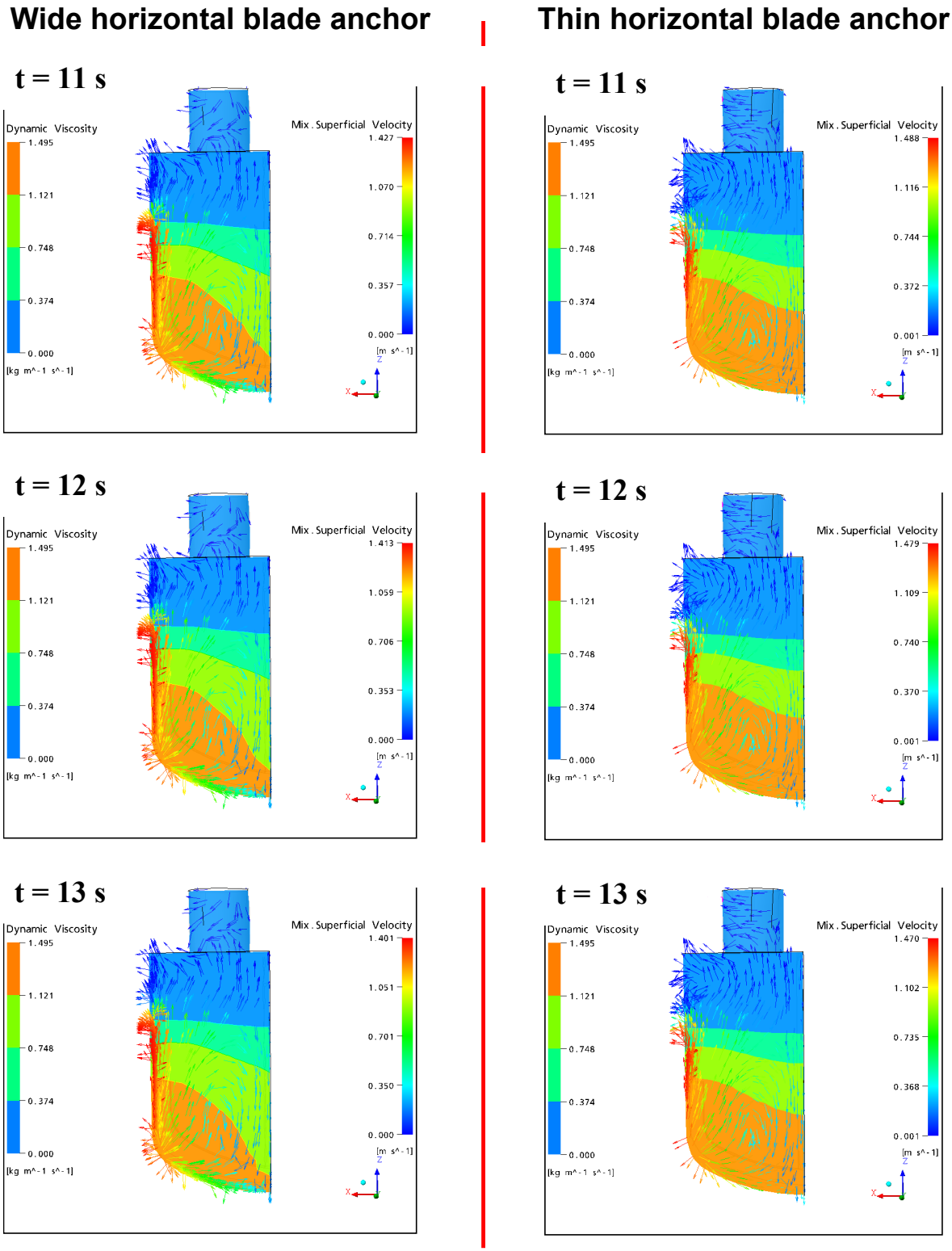

Figure 5.52-c: Mixture viscosity-, flow velocity- and volume fraction fields for horizontal blade widths of w_h = 0.015 m (left) and w_h = 0.012 m (right) for ω = 150 rpm in a SBR with t_d = 5 s at t = 11 s, 12 s and 13 s.

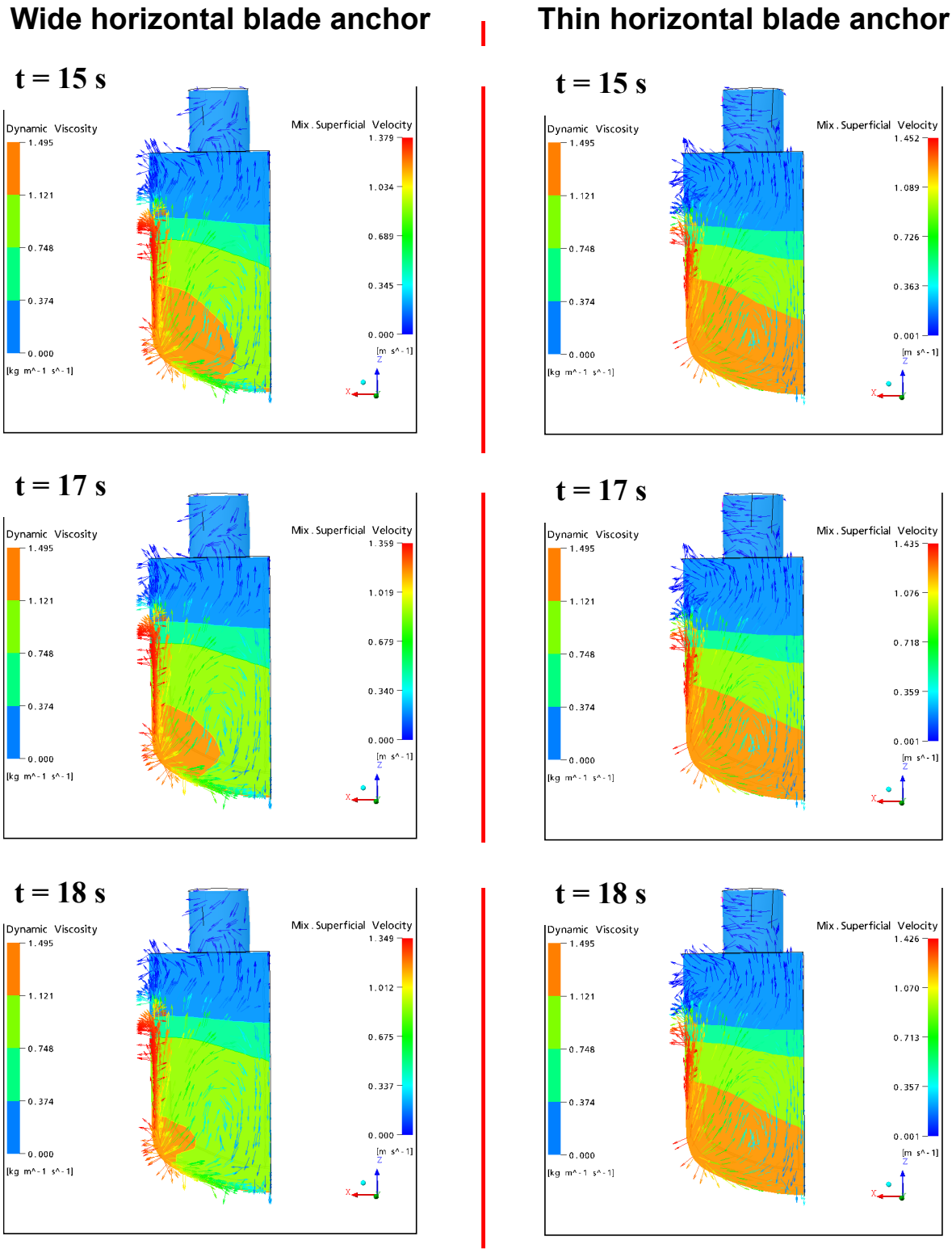

Figure 5.52-d: Mixture viscosity-, flow velocity- and volume fraction fields for horizontal blade widths of w_h = 0.015 m (left) and w_h = 0.012 m (right) for ω = 150 rpm in a SBR with t_d = 5 s at t = 15 s, 17 s and 18 s.

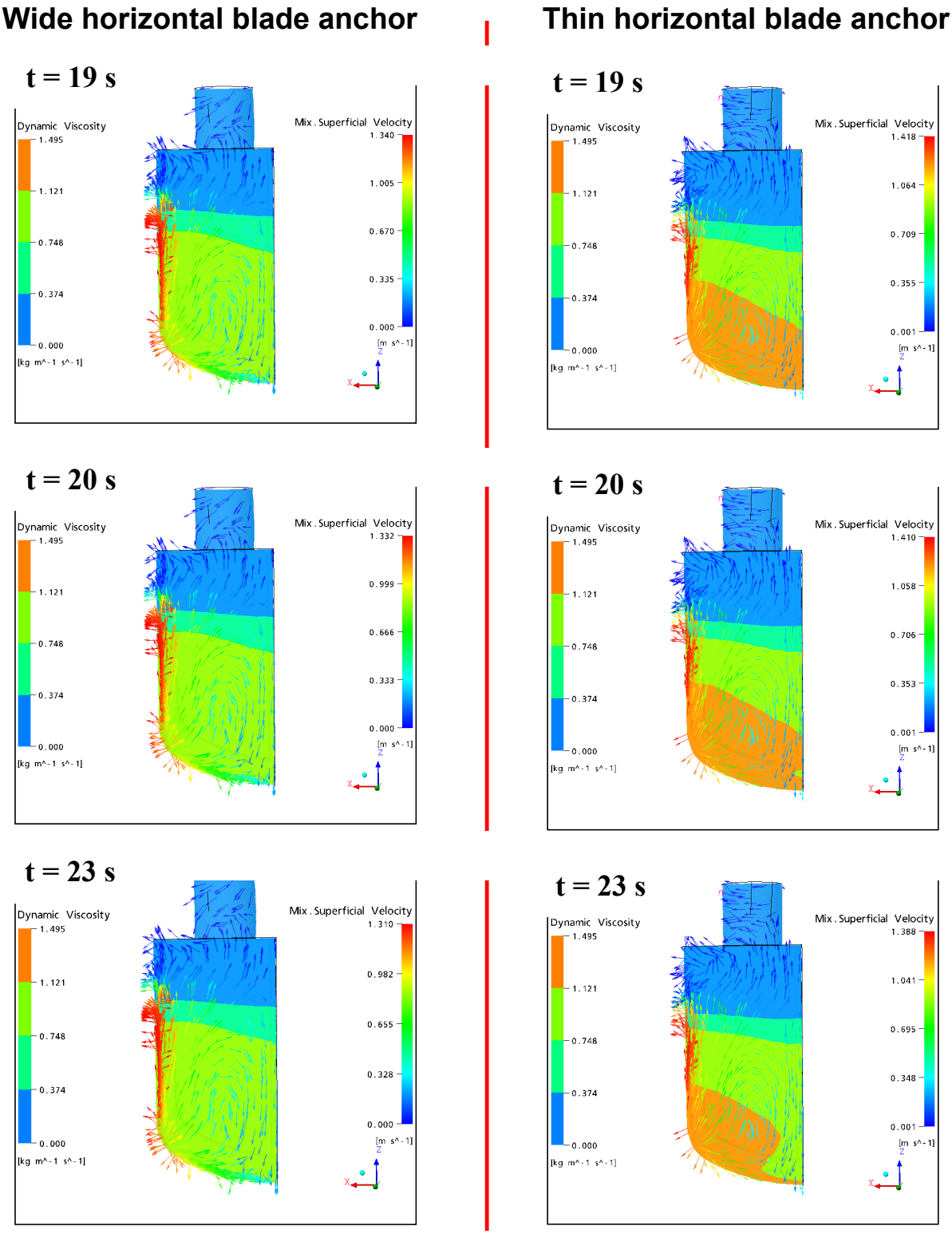

Figure 5.52-e: Mixture viscosity-, flow velocity- and volume fraction fields for horizontal blade widths of w_h = 0.015 m (left) and w_h = 0.012 m (right) for ω = 150 rpm in a SBR with t_d = 5 s at t = 19 s, 20 s and 23 s.

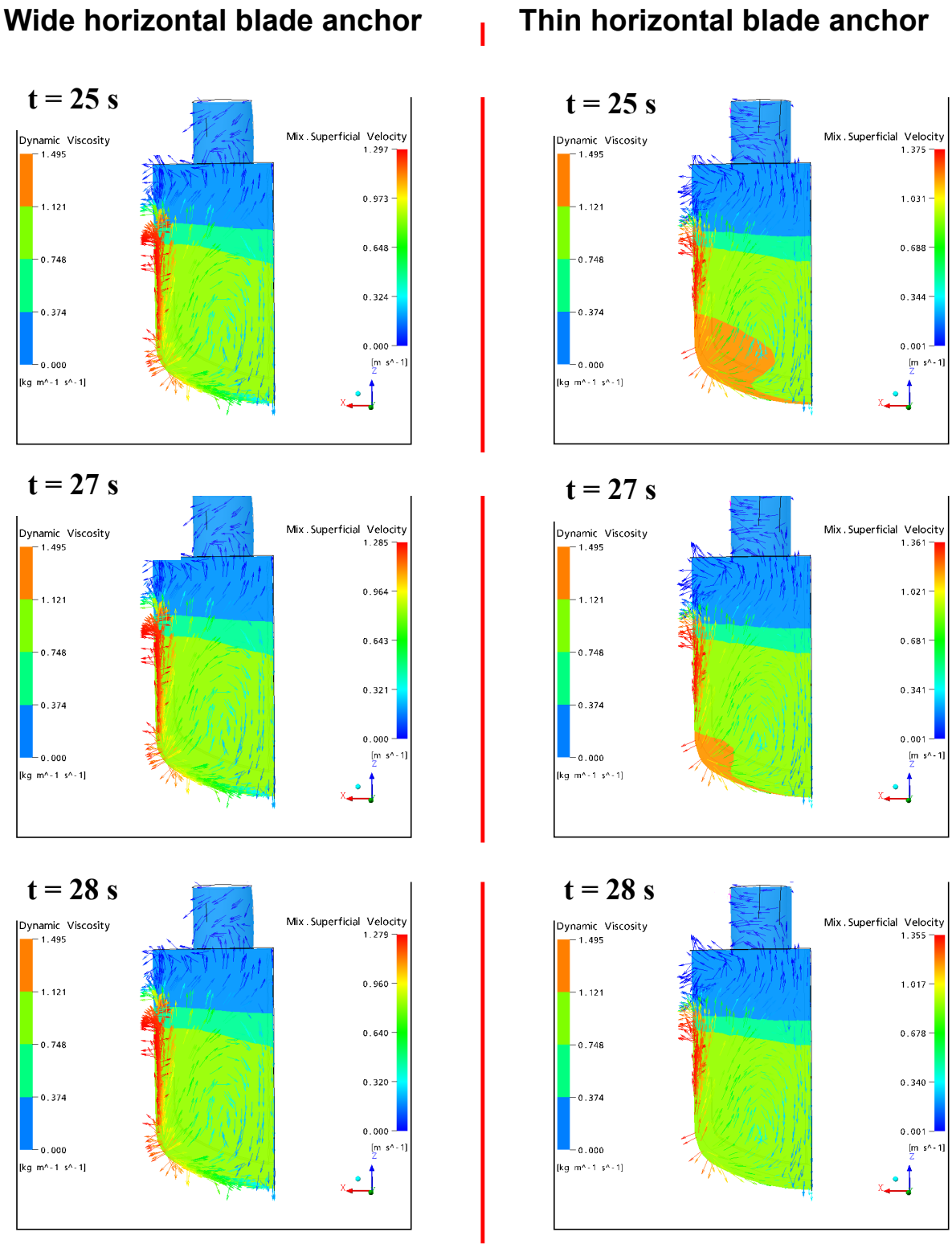

Figure 5.52-f: Mixture viscosity-, flow velocity- and volume fraction fields for horizontal blade widths of w_h = 0.015 m (left) and w_h = 0.012 m (right) for ω = 150 rpm in a SBR with t_d = 5 s at t = 25 s, 27 s and 28 s.

5.2.2 Batch reactor

5.2.2.1 The effect of different mixture ratios of glycerol to ethanol

Mixtures of different volume fraction of ethanol and glycerol are used i.e. 100 % glycerol (H_G = 0.14 m), 100 % ethanol (H_E = 0.14 m), a mixture of 67 % glycerol (H_G = 0.1 m from the bottom) and 33 % ethanol (H_E = 0.04 m above the glycerol) and a mixture of 16 % glycerol (H_G = 0.04 m from the bottom) and 84 % ethanol (H_E = 0.1 m above the glycerol).

From the calculated 3D-flow velocity field axial and radial (horizontal in x-direction) velocity components as a function of x, y, z-directions in the BR at ω = 150 rpm are determined.

5.2.2.1.1 Glycerol (H_G = 0.1 m) and ethanol (H_E = 0.04 m)

The final mixture viscosity η_m = 1.07 Pa s of this liquid mixture is determined as described in the case of SBR (s. Chap. 5.2.1.1). Similar to the case of SBR a secondary flow can also be observed (Fig. 5.53). The highest axial flow velocities are found at the tip of the impeller and near the cylindrical wall of the vessel. The axial flow is caused by the vertical part of the blade of the impeller, whereas the radial flow is caused by the horizontal part of the blade of the impeller. An axial circulation is found behind the anchor impeller at a distance of $d_v/2$ from the shaft. The smallest flow velocities are found near the shaft.

The axial velocities u_{ax} as a function of x at t = 10 s are shown in Fig. 5.54-(a). The negative flow velocities mean a downward flow and the positive flow velocities are upward flow. It can be recognized that the downward axial velocity reach the maximum at x ≈ 0.01 m. The sharp decrease of the downward velocity u_{ax} and of the upward u_{ax} for $x \geq 0.03$ m

is caused by a circulation flow formed between $0.03\,\text{m} \le x \le 0.06\,\text{m}$. The downward $u_{ax} \approx -0.1$ m/s at x = 0.03 m and the upward $u_{ax} \approx 0.1$ m/s at x = 0.06 m have a similar absolute value. The centre of the circulation is found at x = 0.045 m and corresponds to the flex point F of the velocity profile in Fig. 5.54-(a). At the flex point F it is found the dead zone where is $u_{ax} \approx 0$. The maximum of u_{ax} is found at x = 0.078 m in the middle of the vertical part of the impeller at which high shear forces exist.

The maximum of u_{ax} curve is shifted in the y-direction to y = 0.04 m due to the position of the anchor impeller which has a relative large distance from the y-axis (Fig. 5.54-(b)). This means that in the y-direction the upward u_{ax} increase at a larger y-value then the x-value. A small circulation flow is calculated between $0.07\,\text{m} \le y \le 0.09\,\text{m}$ and it has the flex point F of the velocity profile at the centre of the circulation at y = 0.076 m where is $u_{ax} \approx 0$. The upward u_{ax} reaches a maximum at y = 0.09 m and decreases to $u_{ax} \approx 0$ near the cylindrical wall at y = 0.1 m similar as in the x-direction. The axial velocity u_{ax} increases in the z-direction from the bottom of the vessel up to z = 0.07 m near the tip of the impeller to a maximum (Fig. 5.54-(c)). Then u_{ax} decreases for z > 0.07 m above the impeller up to a minimum u_{ax} is reached at z = 0.17 m. In this height the flow velocity is zero at the interface between the liquid mixture and air. The sharp decrease of u_{ax} is caused by an increasing vertical distance from the horizontal part of the impeller, where the flow velocities decrease fastly to the neglecting velocity at the interface between liquid and air.

The radial velocity profile in x coordinates in Fig. 5.54-(d) shows an increase of the magnitude of the radial velocity between the shaft and x = 0.06 m where the circulation exists. A small radial vortex exists between x = 0.075 m and x = 0.085 m because of the symmetric velocities around

x = 0.08 m. The maximum radial velocity is found near the cylindrical wall. The radial velocity increases from the shaft up to y = 0.06 m and then it decreases towards to the cylindrical wall (Fig. 5.54-(e)). The radial velocity decreases from the bottom of the vessel up to z = 0.085 m near the impeller tip and then increases up to z = 0.14 m (Fig. 5.54-(f)) near the interface of the liquid mixture with air (the axial circulation zone). The velocities decrease again above the interface.

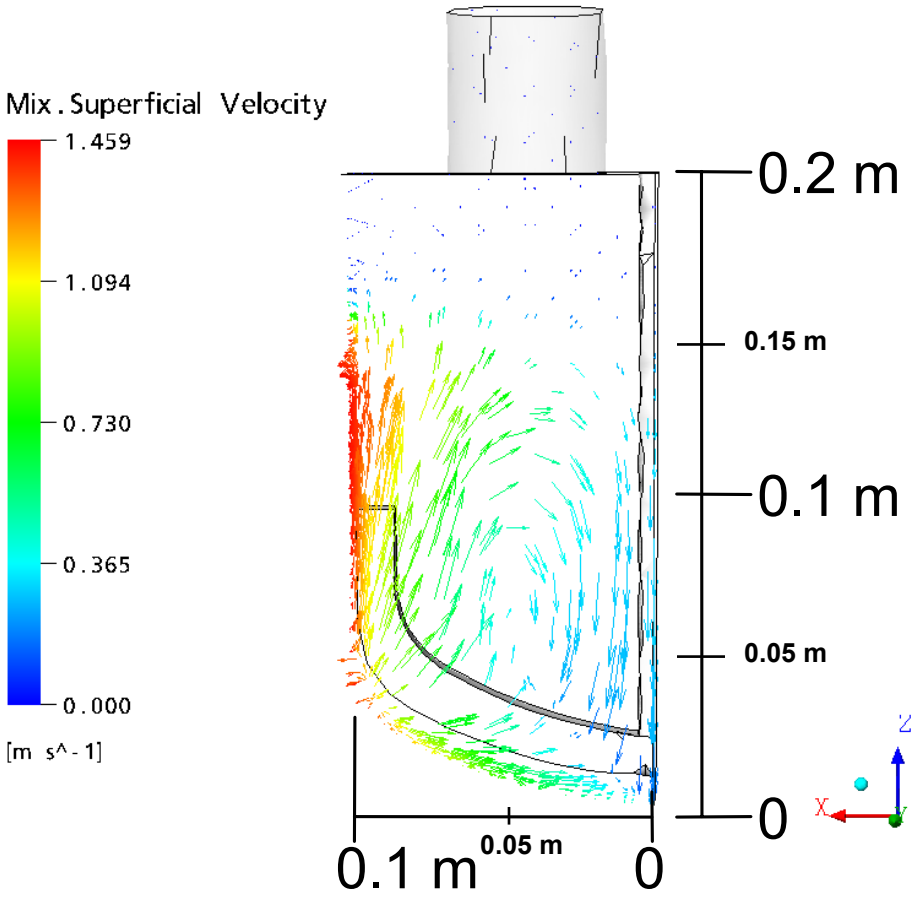

Figure 5.53: Calculated flow velocity field at t = 10 s for a mixture of glycerol (H_G = 0.1 m) and ethanol (H_E = 0.04 m) in a BR.

Axial velocities

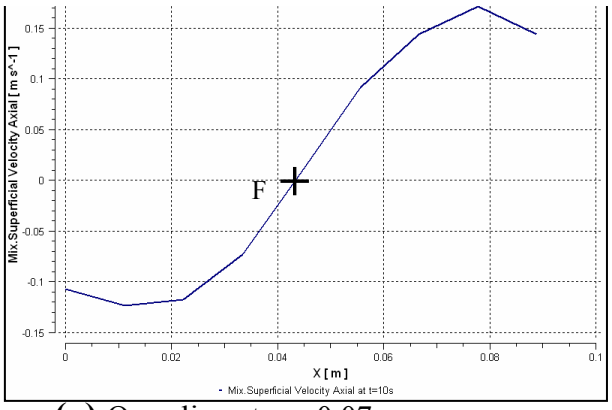

(a) On x-line at z = 0.07 m.

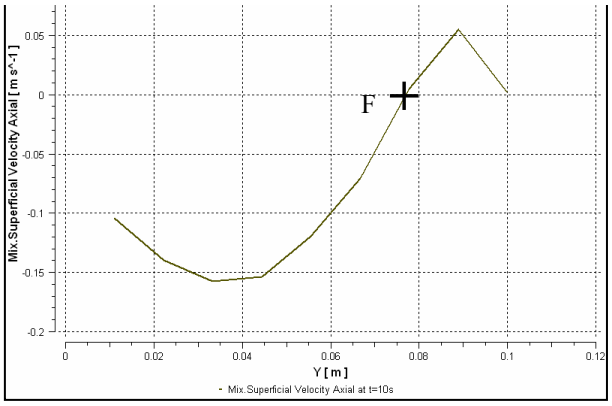

(b) On y-line at z = 0.07 m.

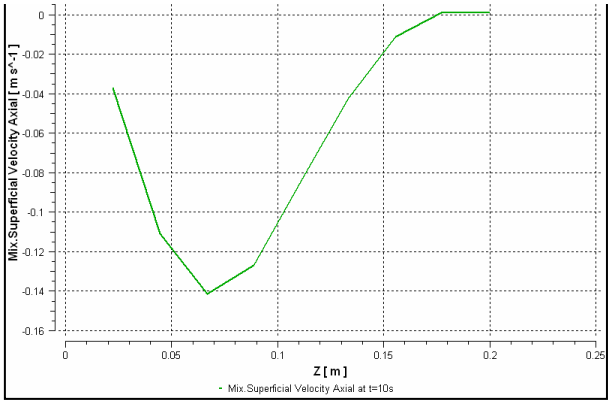

(c) On z-line at y = 0.05 m.

Radial velocities

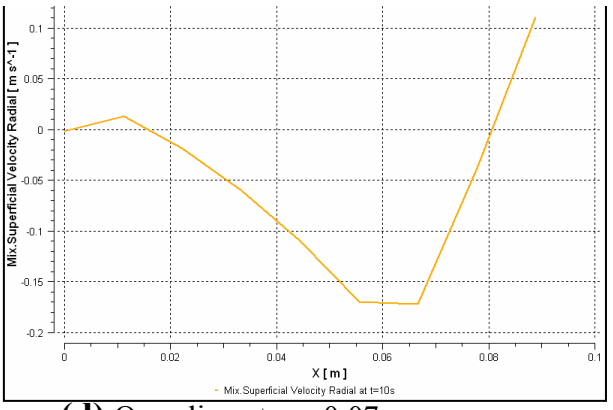

(d) On x-line at z = 0.07 m.

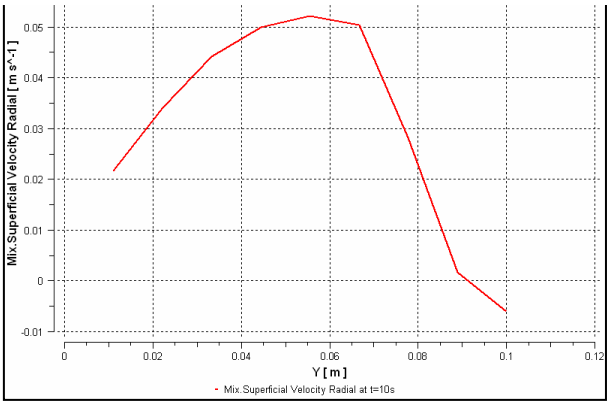

(e) On y-line at z = 0.07 m.

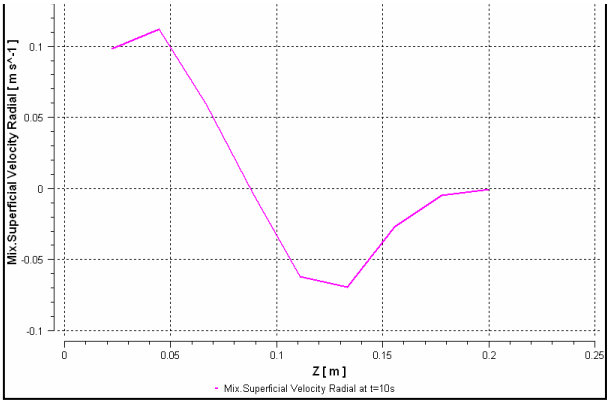

(f) On z-line at y = 0.05 m.

Figure 5.54: Mixture velocity profiles axial (left) and radial (right) in x,y,z coordinates at t = 10 s for a mixture of glycerol (H_G = 0.1 m) and ethanol (H_E = 0.04 m) in a BR.

5.2.2.1.2 Glycerol (H_G = 0.04 m) and ethanol (H_E = 0.1 m)

The final viscosity of this liquid mixture is 0.36 Pa s. Secondary flow field mainly axial can be seen in Fig. 5.55 near the cylindrical wall of the vessel and the vertical blade of the impeller. A wider and shorter circulation compared to that obtained in the previous case in Fig. 5.53 is found near the vertical blade of the anchor impeller.

The axial velocities as a function of x, y, z at t = 10 s are shown in Fig. 5.56-(left). Similar axial velocity profiles to that for the case before in Fig. 5.54-(a), (b) and (c) are found. The axial velocities as a function of x in Fig. 5.56-(a) are lower than that in Fig. 5.54-(a), especially near the shaft between $0 < x < 0.03$ m. The axial velocities as a function of y in Fig. 5.56-(b) are nearly similar to that in Fig. 5.54-(b), but the axial velocities near the shaft between $0 < y < 0.06$ m have lower values. The axial velocities as a function of z in Fig. 5.56-(c) are higher than that in Fig. 5.54-(c) because the liquid mixture here has a lower viscosity by a factor of 3.

The radial velocities as a function of x between $0.03 \text{ m} < x < 0.07$ m in Fig. 5.56-(d) are lower than that in Fig. 5.54-(d) caused by the existed circulation between the shaft and the impeller there. The radial velocities as a function of y in Fig. 5.56-(e) are higher than that in Fig. 5.54-(e), whereas the radial velocities as a function of z in Fig. 5.56-(f) are lower than that in Fig. 5.54-(f).

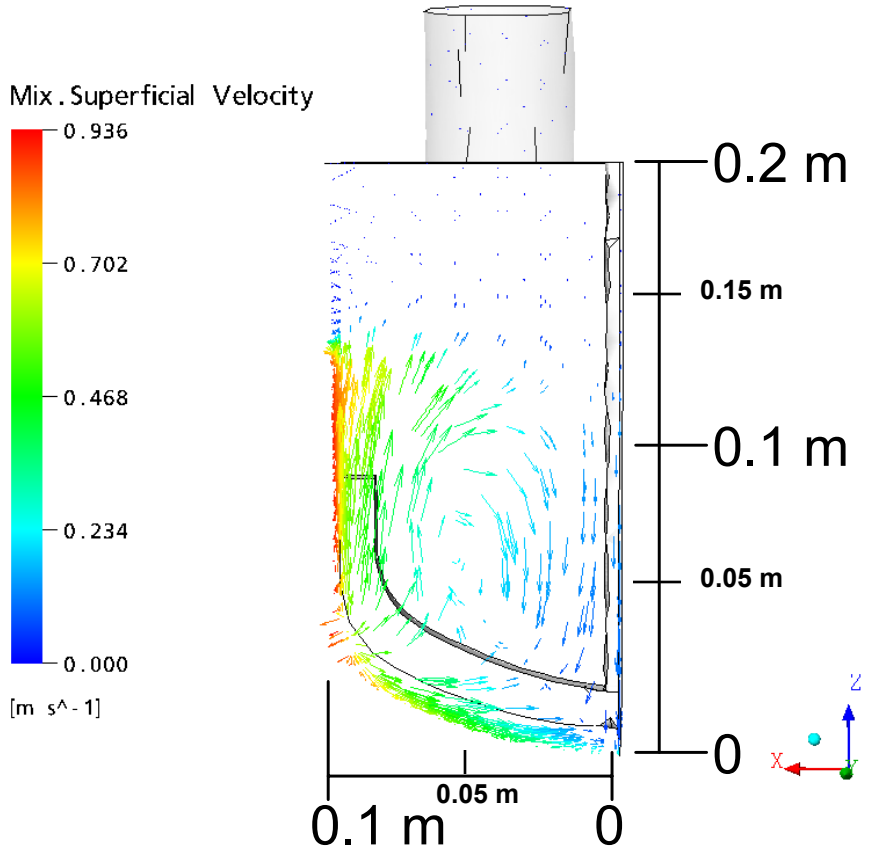

Figure 5.55: Calculated flow velocity field at t = 10 s for the mixture of glycerol (H_G = 0.04 m) and ethanol (H_E = 0.1 m) in a BR.

Axial velocities

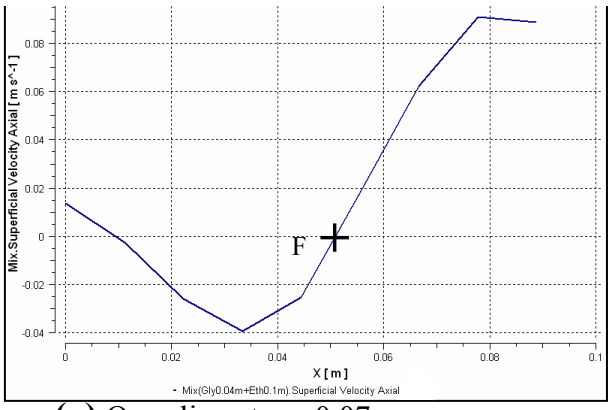

(a) On x-line at z = 0.07 m.

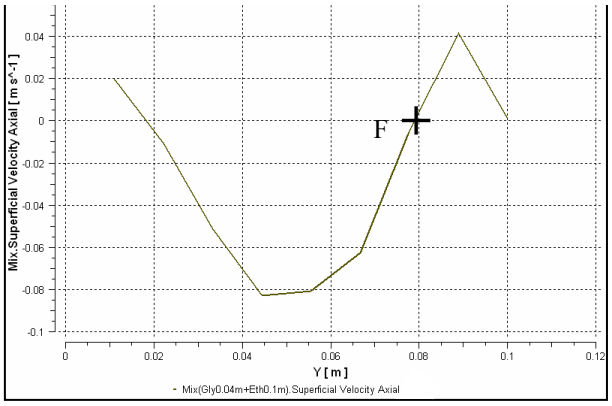

(b) On y-line at z = 0.07 m.

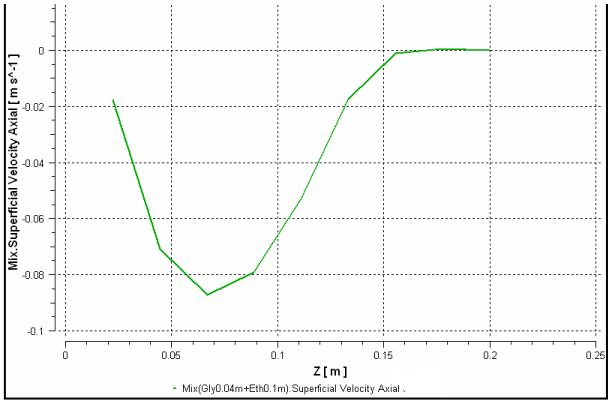

(c) On z-line at y = 0.05 m.

Radial velocities

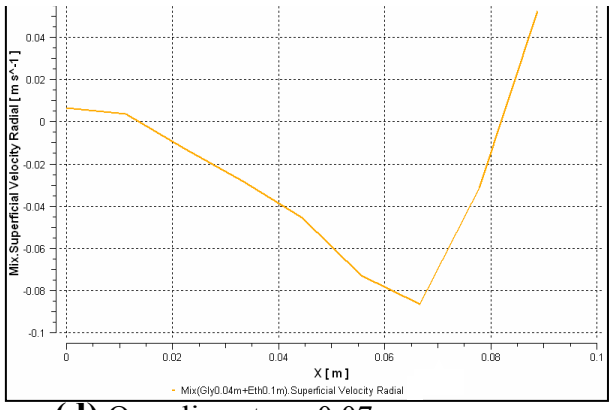

(d) On x-line at z = 0.07 m.

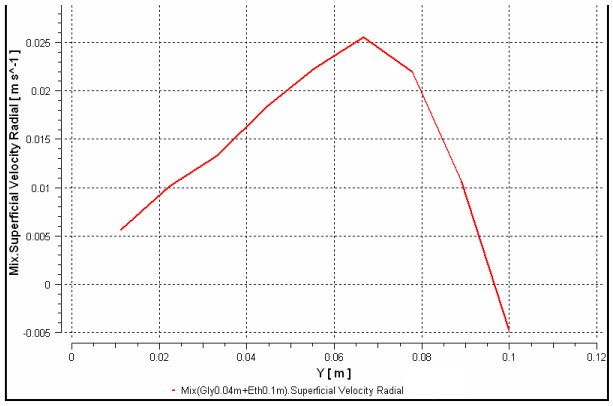

(e) On y-line at z = 0.07 m.

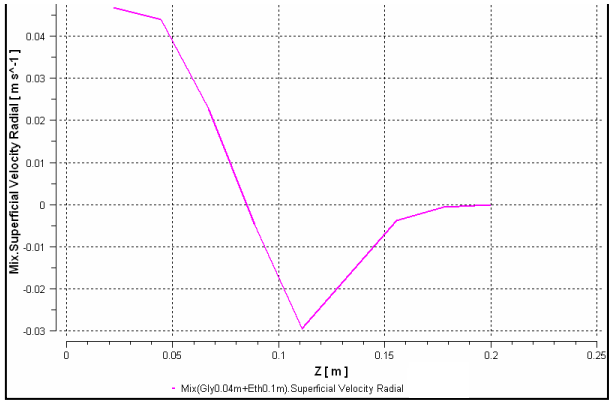

(f) On z-line at y = 0.05 m.

Figure 5.56: Mixture velocity profiles axial (left) and radial (right) in x,y,z coordinates at t = 10 s for a mixture of glycerol (H_G = 0.04 m) and ethanol (H_E = 0.1 m) in a BR.

5.2.2.1.3 Pure glycerol

A secondary flow with axial circulation near the horizontal blade of the anchor impeller can be seen in Fig. 5.57. Similar velocity flow field to that for the case of the liquid mixture with a viscosity of 1.067 Pa s in Fig. 5.53 is obtained. The axial and radial velocity profiles for pure glycerol with a viscosity of 1.495 Pa s as a function of x, y, z in Fig. 5.58 are similar to that for the mixture viscosity of 1.067 Pa s in Fig. 5.54 because the both cases have high viscosities. The axial and radial velocities as a function of x, y, z in Fig. 5.58 can be described similar to that in Chap. 5.2.2.1.1. The high radial flow velocities near the tip of the anchor impeller transported the axial circulation towards the horizontal blade of the impeller.

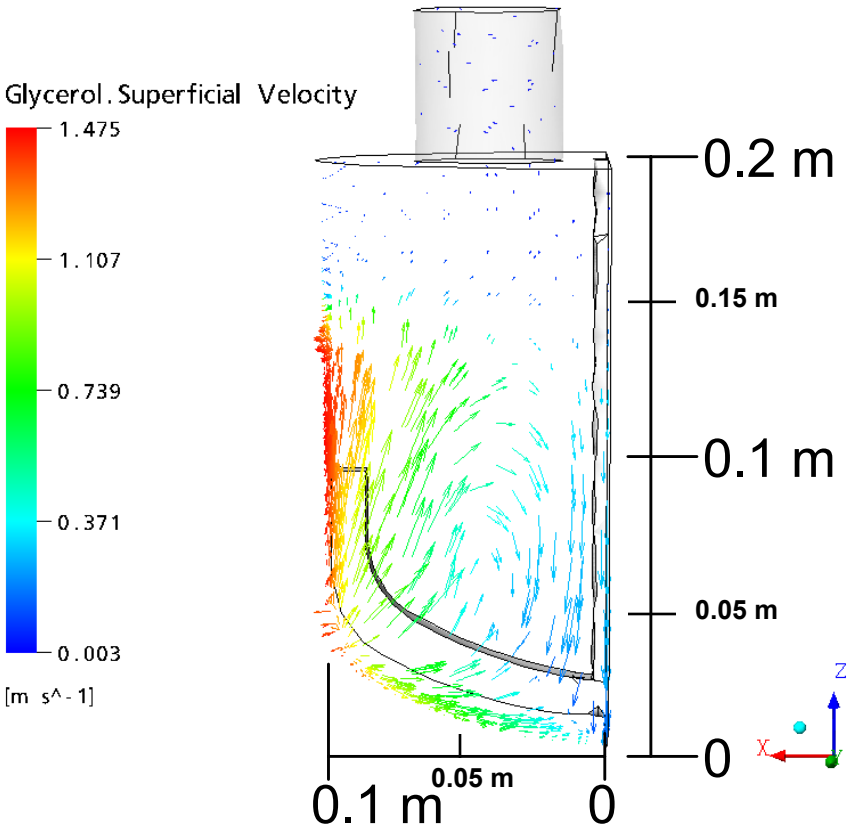

Figure 5.57: Calculated flow velocity field at t = 10 s for pure glycerol in a BR.

Axial velocities

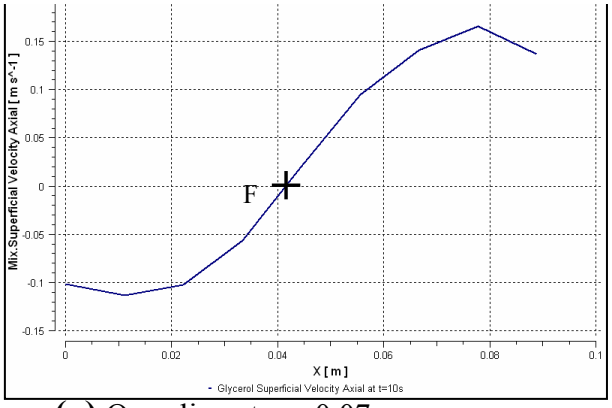

(a) On x-line at z = 0.07 m.

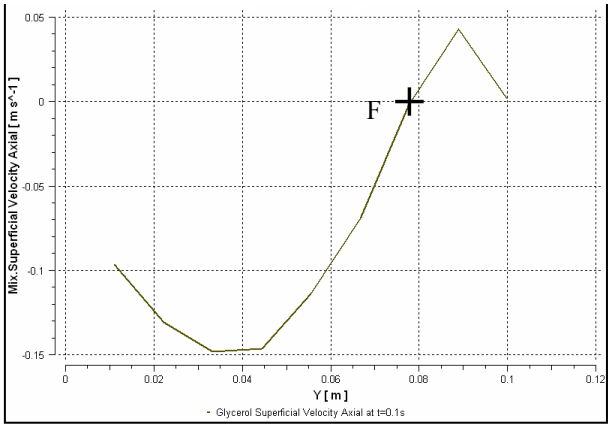

(b) On y-line at z = 0.07 m.

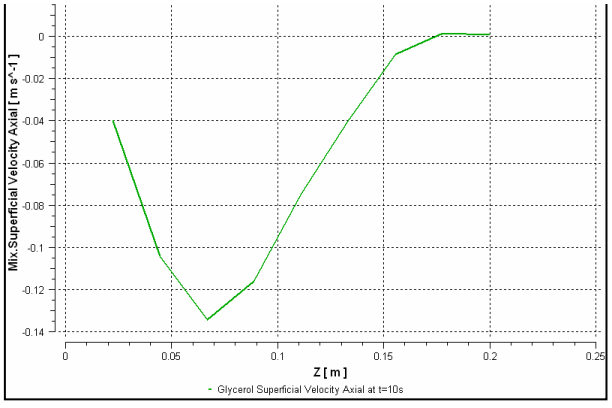

(c) On z-line at y = 0.05 m.

Radial velocities

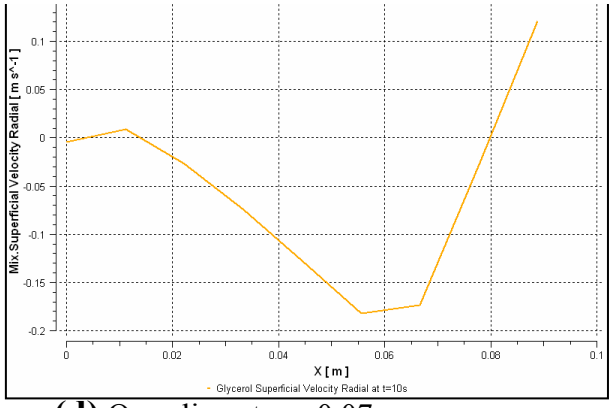

(d) On x-line at z = 0.07 m.

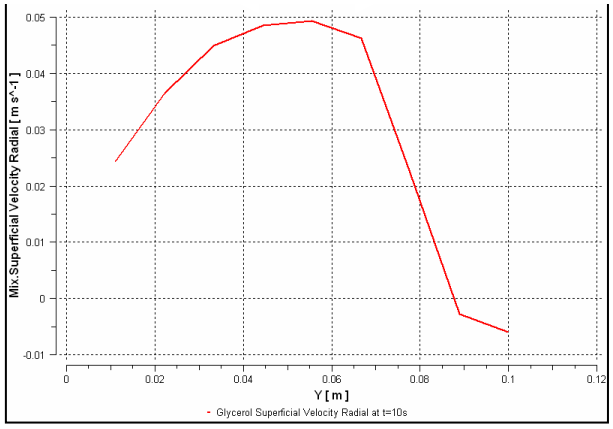

(e) On y-line at z = 0.07 m.

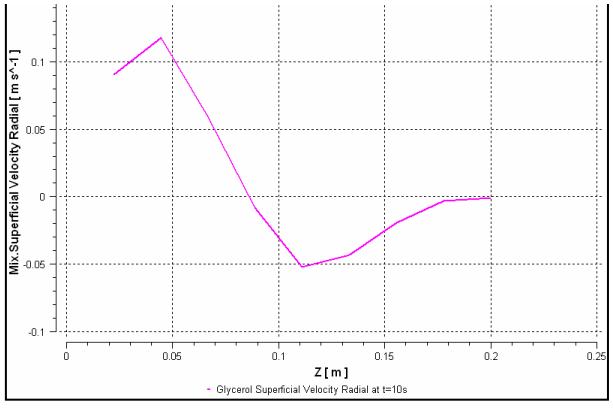

(f) On z-line at y = 0.05 m.

Figure 5.58: Mixture velocity profiles axial (left) and radial (right) in x,y,z coordinates at t = 10 s for pure glycerol (H_G = 0.14 m) in a BR.

5.2.2.1.4 Pure ethanol

Ethanol has a low viscosity of 0.00012 Pa s. The secondary flow velocity field is mainly axial as can be seen in Fig. 5.59 at t = 10 s. No axial circulation between the impeller and the shaft is obtained because ethanol has a low viscosity and low axial and radial velocities compared to that in the previous cases which have higher viscosities and velocities (Figs. 5.53, 5.55 and 5.57).

The axial and radial velocity profiles in as a function of x, y, z at t = 10 s for pure ethanol are shown in Fig. 5.60. These velocity profiles are similar to the axial and radial velocity profiles for the higher liquid mixture viscosities in Figs. 5.54, 5.56 and 5.58 with small differences. Because the low viscosity and density of ethanol causes a turbulent flow between the shaft and impeller which leading to a higher variation of the axial and radial velocities in this region compared with that in the cases before. The axial velocities in x coordinate are high near the cylindrical wall of the vessel upward and at x = 0.025 m downward as can be seen in Fig. 5.60-(a). The axial velocities in y coordinate are high at x = 0.025 m upward and at x = 0.065 m downward (Fig. 5.60-(b)). The axial velocity profile in z coordinate is similar to the cases before e.g. pure glycerol (Fig. 5.58-(c)) but lower velocities are found near the shaft and the cylindrical wall as can be seen in Fig. 5.60-(c).

The radial velocity profiles in x and y coordinates are similar to the cases before e.g. pure glycerol (Fig. 5.58-(d) and (e)) near the shaft and the cylindrical wall but a large variation of the radial velocities for pure ethanol are found between $0.02\,\text{m} \le x \le 0.08\,\text{m}$ and $0.02\,\text{m} \le y \le 0.08\,\text{m}$ as can be seen in Figs. 5.60-(d) and (e). The radial velocity is the highest near the horizontal blade of the impeller at z = 0.025 m downward and near the

impeller tip at z = 0.08 m as can be seen in Figs. 5.59 and 5.60-(f). A high variation of the radial velocities are found between z = 0.08 m and z = 0.15 m due to the high fluctuations at the interface between the pure ethanol and air.

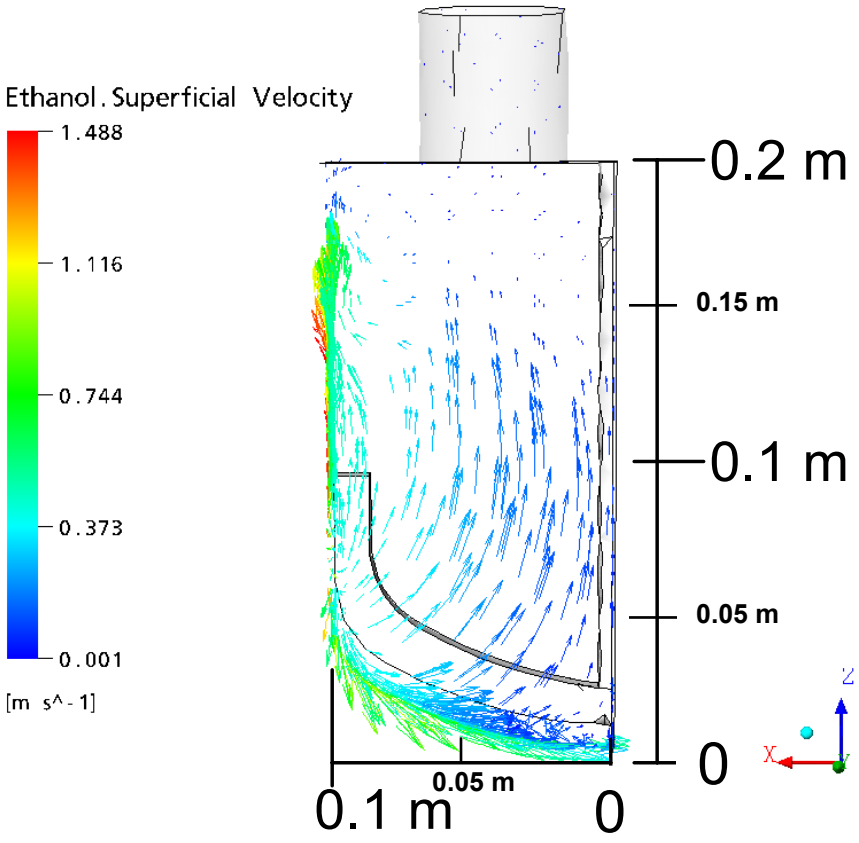

Figure 5.59: Calculated flow velocity field at t = 10 s for pure ethanol in a BR.

Axial velocities

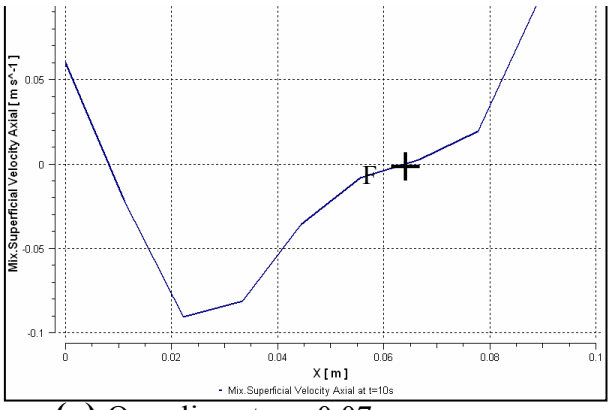

(a) On x-line at z = 0.07 m.

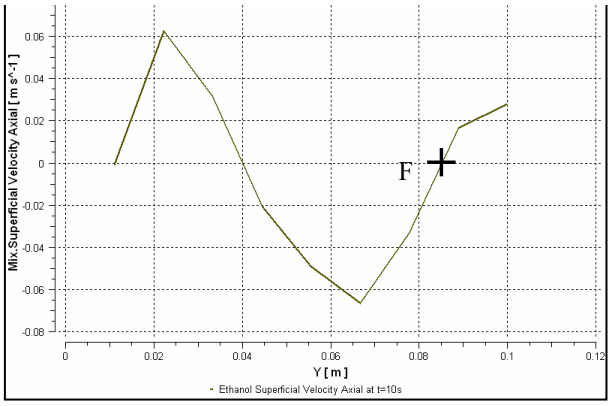

(b) On y-line at z = 0.07 m.

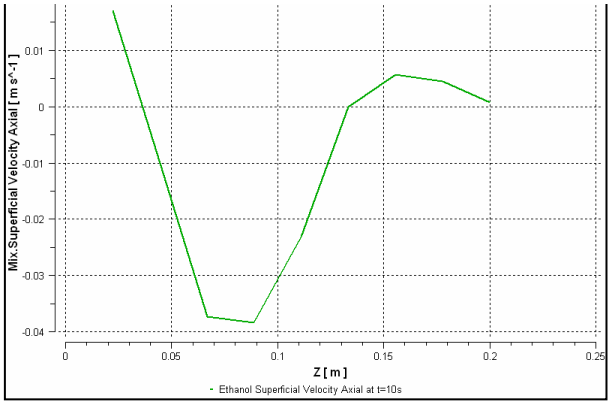

(c) On z-line at y = 0.05 m.

Radial velocities

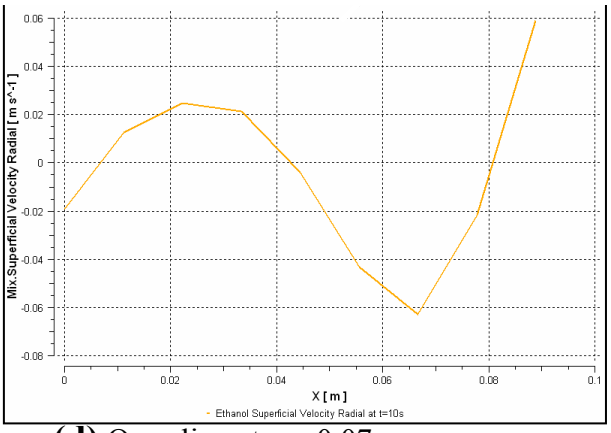

(d) On x-line at z = 0.07 m.

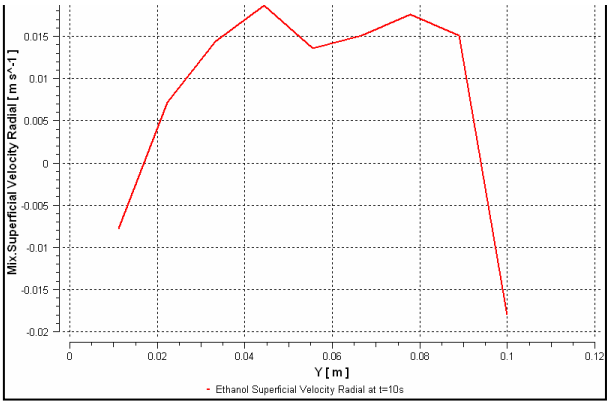

(e) On y-line at z = 0.07 m.

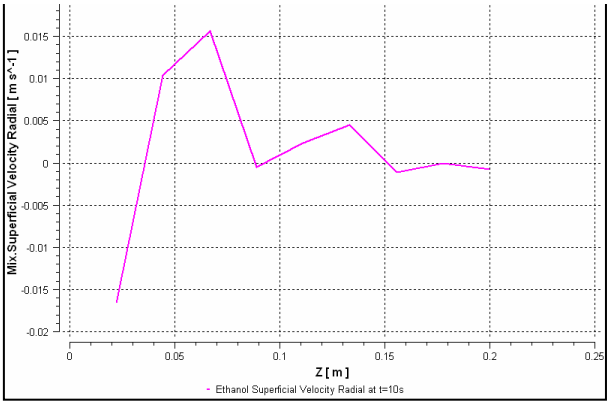

(f) On z-line at y = 0.05 m.

Figure 5.60: Mixture velocity profiles axial (left) and radial (right) in x,y,z coordinates at t = 10 s for pure ethanol in a BR.

5.3 CFD simulations predicting the mixture viscosities as a function of time and the mixing times in SBR and BR

The simulations are carried out in a full 3D-geometry at ϑ = 21 °C and ω = 150 rpm similar to that used in the experiment. These simulations are done by using the sliding mesh method, homogeneous laminar buoyant flow model for air/liquid, standard free surface flow model, algebraic slip mixture model for ethanol/glycerol and non ideal binary mixture viscosity model. The following experiments are used for validation of the CFD simulations.

5.3.1 SBR at t_d = 5 s (26 vol% ethanol)

A good agreement between the calculated and measured dynamic viscosity $\eta_m(t)$ of the ethanol/glycerol liquid mixture as a function of time is shown in Fig. 5.61. At t = 0 only glycerol exists in the vessel where the maximum viscosity is η_G = 1361.88 mPa s. During the dosage time of ethanol between $0.2\,s \le t_d \le 5.2\,s$, a sharp decrease of glycerol viscosity to 1142 mPa s occurs. This means an initial fast mixing of a part of the dosed ethanol is observed because the dosed ethanol flow to the stirrer region near the cylindrical wall where high shear forces exist leading to a break up into ethanol droplets with a constant diameter d_p = 0.2 mm (s. Fig. 5.62) [55]. The high flow rate of the dosed ethanol gives the bulk liquid additional kinetic energy to exceed the buoyancy forces. After the dosage the remaining part of the dosed ethanol rises up to the liquid interface forming a thin layer of ethanol above the bulk liquid which has higher viscosity and density. This small layer can re-enter the bulk glycerol by vortices or by diffusion [55], then a slow deformation and dispersion of ethanol droplets

[98] occurs leading to a slow decrease of the mixture viscosity to $\eta_m = 669.5$ mPa s at t = 150 s.

For t > 150 s a fast mixing again is observed due to the absence of the buoyancy forces and destroying the rest layer of ethanol at the interface. The remaining ethanol is rapidly transported into the bulk glycerol leading to a fast deformation of the interface [55] and dispersion until a homogeneous liquid mixture with viscosity of $\eta_m = 279$ mPa s at $t_m = 208$ s is obtained.

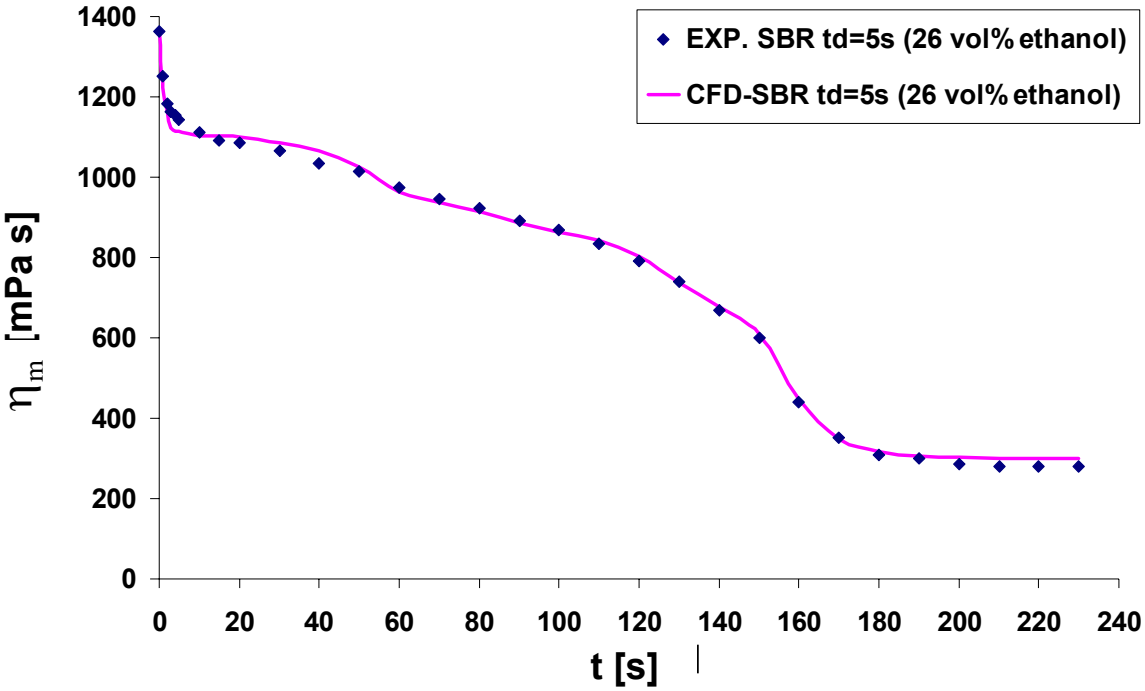

Figure 5.61: The dynamic viscosity of an ethanol/glycerol mixture as a function of time in a SBR at $t_d = 5$ s (26 vol% ethanol), experimentally and by using CFD simulation.

The ethanol droplet diameters as a function of time for a SBR can be seen in Fig. 5.62. It is shown that a large and slow break up of the droplet diameter d_p is found for $t \leq 50$ s. A small and fast decrease of the droplet diameter is obtained for $50\,s \leq t \leq 160\,s$ until a complete mixing occurs at t = 180 s with a final mean droplet diameter $d_p \approx 10^{-7}$ m (s. Chap. 5.3.5.1). For $d_p < 10^{-7}$ m, there is no more influence of d_p on η_m. The droplets of the

dosed ethanol may pass through several main zones: The stirrer region; the free surface, the bottom of the vessel and the bulk. In each zone there is a chance that the ethanol droplets will be divided into smaller droplets or mixed into the bulk liquid. In addition, in each zone the droplets have a chance to move to another zone [55].

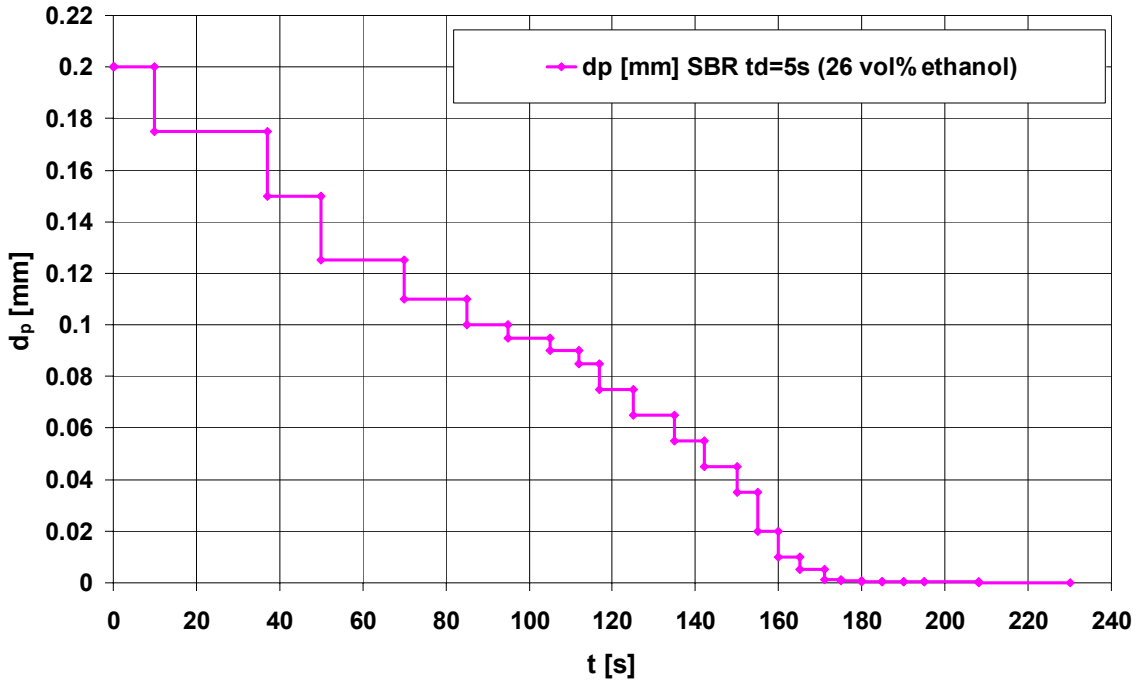

Figure 5.62: Calculated ethanol droplet diameter as a function of time (s. Chap. 5.3.5.1) in a SBR at t_d = 5 s (26 vol% ethanol) by using CFD simulation.

From Figs. 5.61 and 5.62 the dynamic viscosity of ethanol and glycerol mixture as a function of ethanol droplet diameter can be shown in Fig. 5.63. It is concluded that when the droplet diameter of ethanol decreases, the mixture viscosity decreases and so the flow velocity of the liquid mixture increases. This means when the droplet diameter of ethanol d_p decreases (η_m decreases also), then the polynomial equation for a calculated Reynolds number $Re_m(d_p)$ (s. Eq. 2-6) increases (Fig. 5.64-a). The Reynolds number $Re_m(t)$ of the liquid mixture as a function of time increases (Fig. 5.64-b)

because the mixture viscosity $\eta_m(t)$ decreases and the velocity of the liquid mixture u_m increases.

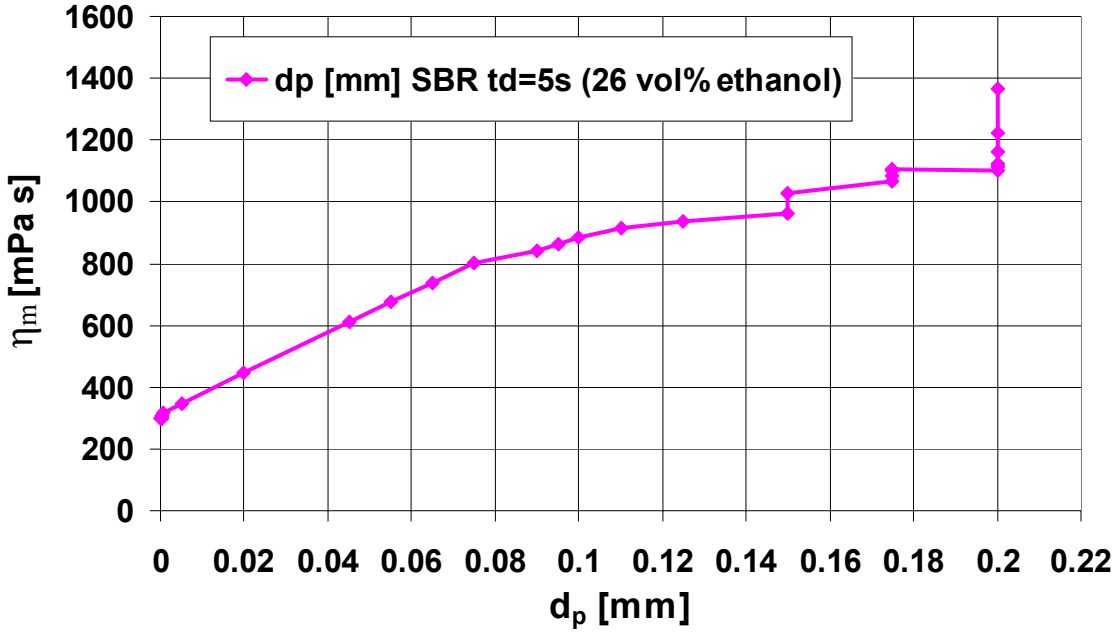

Figure 5.63: The dynamic viscosity of an ethanol/glycerol mixture as a function of ethanol droplet diameter in a SBR at t_d = 5 s (26 vol% ethanol) by using CFD simulation.

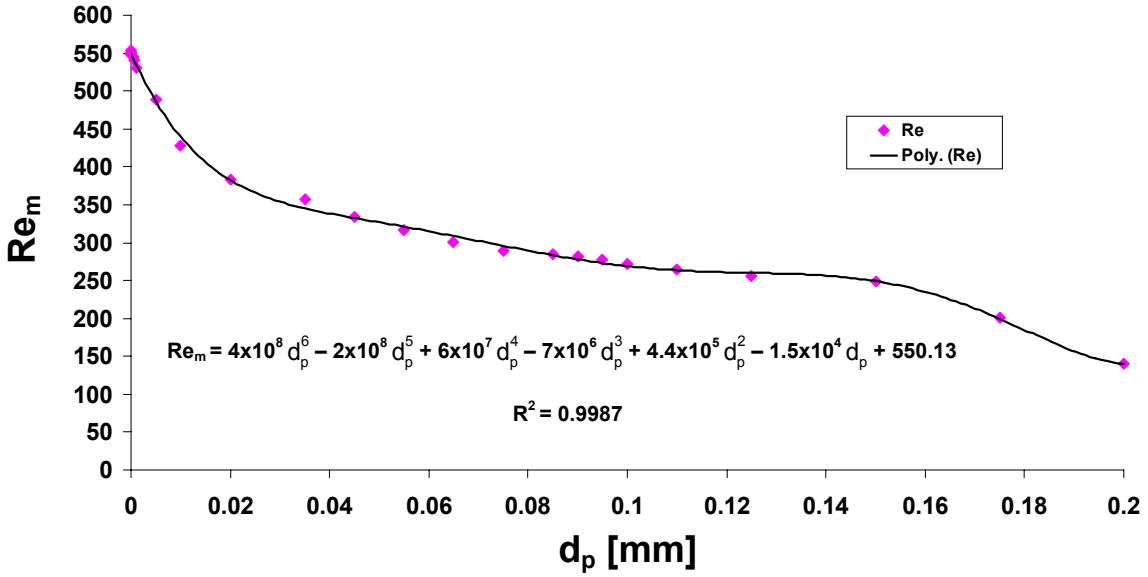

Figure 5.64-a: Reynolds number Re_m as a function (polynomial) of ethanol droplet diameter d_p in a SBR at t_d = 5 s (26 vol% ethanol) with ω = 150 rpm by using CFD simulation.

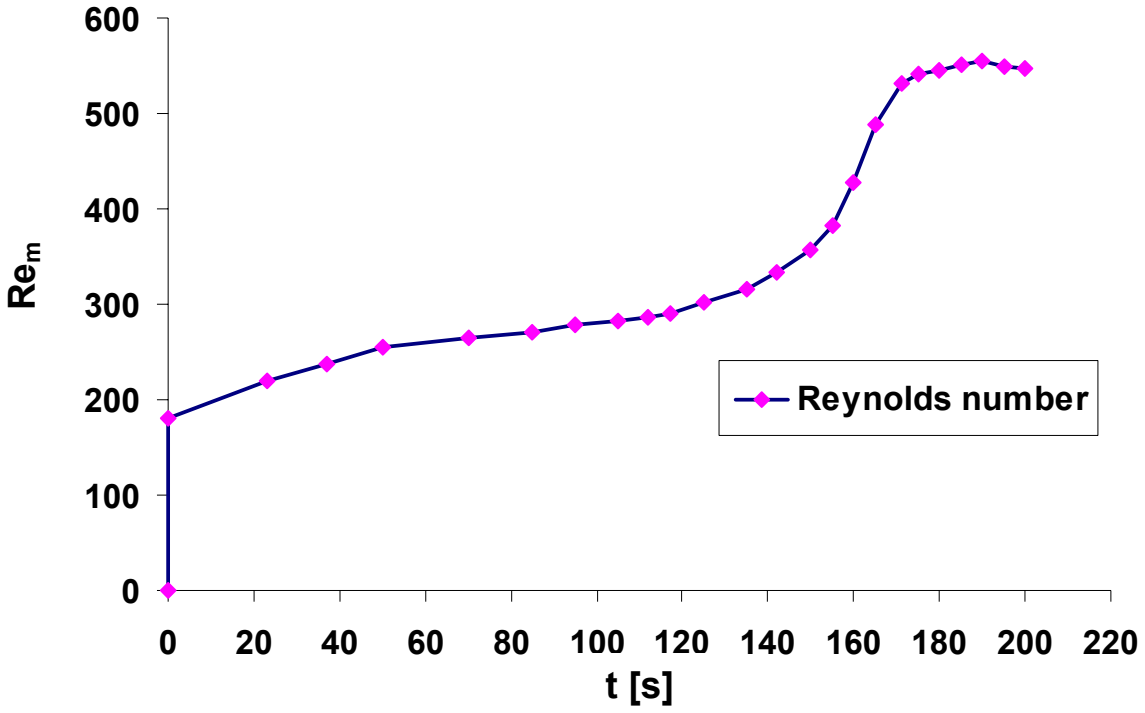

Figure 5.64-b: Calculated Reynolds number Re_m as a function of time in a SBR at t_d = 5 s (26 vol% ethanol) with ω = 150 rpm by using CFD simulation.

To calculate the mixing time t_m, ethanol mass fractions at different positions in the vessel near the impeller, in the middle between the impeller and the shaft (mixing is caused by the diffusion between ethanol and glycerol) and near the shaft (mixing is caused essentially by the gravity) are calculated as a function of time (Fig. 5.65). Initially at t = 0 there is no ethanol in the vessel. During the dosage of ethanol high ethanol mass fractions are found at the points P_3, P_4 and P_5 above the anchor impeller because a layer of ethanol is formed above the bulk mixture due to the buoyancy forces. After the dosage for t > 0.2 s, ethanol mass fractions at the points P_3, P_4, P_5, P_8 and P_9 decrease as a function of time because the dispersion and distribution of ethanol in glycerol increase. Low ethanol mass fractions are found at the points P_1, P_2, P_6 and P_7 which are below the tip of

the anchor impeller, and then for t > 0.2 s ethanol mass fractions increase because ethanol is transported into the bulk mixture. The mixing time t_m and a homogeneous mixture are obtained when all the points have the same constant mass fraction of ethanol at t_m = 205 s. It is concluded from Fig. 5.65 that the mixing is faster at the tip of the anchor impeller where the maximum shear forces and maximum flow velocity appear then at the intermediate region between the shaft and impeller and last near the shaft where the lowest velocity occurs. The calculated distribution of ethanol mass fractions (Fig. 5.65) between all these points can explain the mixing behavior and flow velocity field of ethanol in glycerol as a function of time.

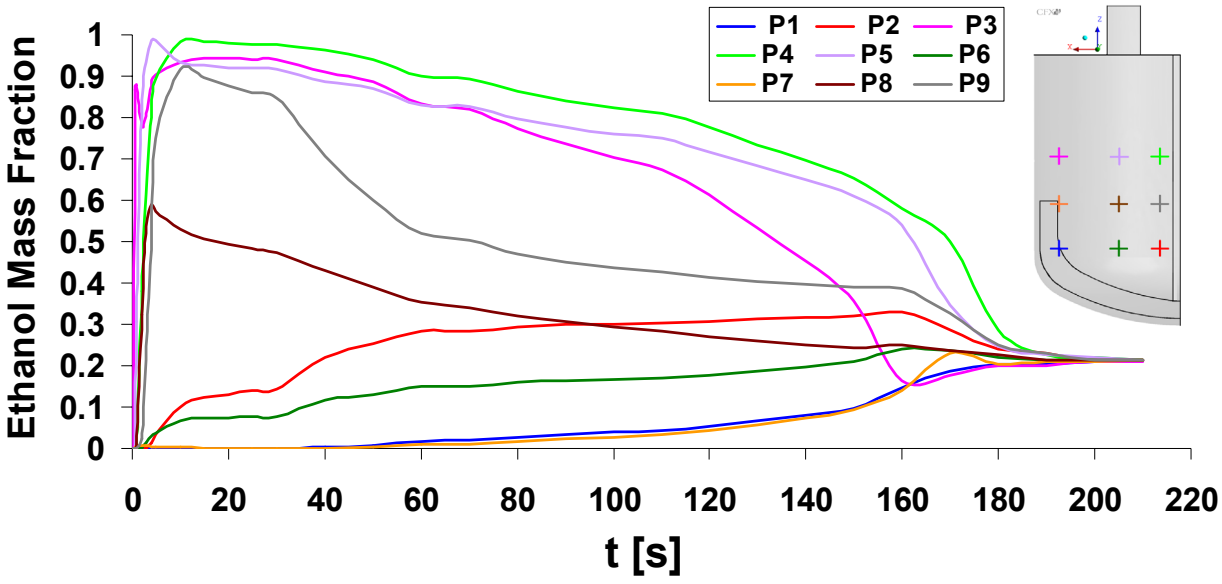

Figure 5.65: Ethanol mass fraction as a function of time, calculated by using CFD simulation at nine different positions in the SBR at t_d = 5 s (26 vol% ethanol).

The calculated dynamic mixing behaviors of ethanol with glycerol are visualized as it is shown in Fig. 5.66. Initially at t = 0 only pure glycerol exists in the vessel while the anchor stirrer do not rotate. During the dosage of ethanol between $0.2\,\text{s} \leq t_d \leq 5.2\,\text{s}$ a part of the dosed ethanol is transported

to the stirrer region and transported into the bulk mixture from the cylindrical wall of the vessel towards to the shaft as can be seen in Fig. 5.66 at t = 2 s. Then the ethanol input distributes over the bulk liquid as shown at t = 5 s (fast mixing during the dosage time period). After the dosage, the buoyant effect appears because the shear forces of the stirrer can not exceed the buoyant forces which are caused by the density difference between ethanol and glycerol. Then the remaining part of the dosed ethanol rises up to the interface of the bulk mixture, and re-disperse from the tip of the anchor impeller towards to the shaft and then towards to the cylindrical wall of the vessel leading to a circulation behind the anchor as can be shown at t = 100 s in agreement with the experiment.

The droplets of ethanol break up until all the dosed ethanol is completely mixed with glycerol to get a homogeneous mixture with constant values of viscosity, ethanol mass fraction and ethanol droplet diameter. The calculated mixing time is t_m = 205 s. The calculation and the visualisation of the mixing behavior in a SBR at t_d = 5 s (26 vol% ethanol) are in a good agreement.

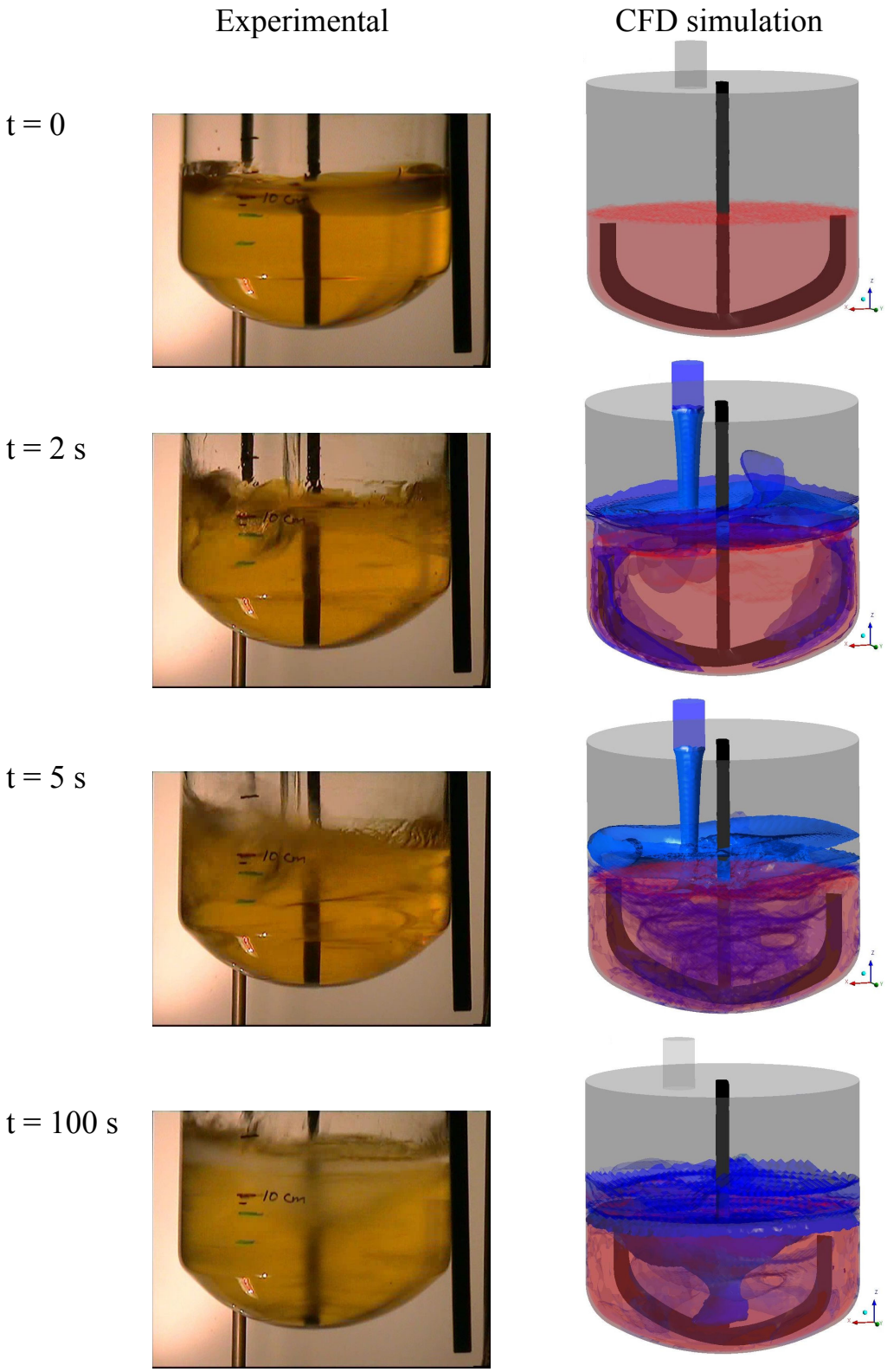

Figure 5.66: The dynamic mixing behavior of an ethanol/glycerol mixture in a SBR at t_d = 5 s and ω = 150 rpm, shown by video visualization (left) and CFD simulation (right) using an isosurface of ethanol mass fractions at different time between $0 \leq t \leq 100$ s.

The density field ρ_m (x,z) of ethanol and glycerol mixture during the dosage in a SBR at t = 2 s is shown in Fig. 5.67. The low density ethanol rises up to the bulk liquid interface. Therefore the higher mixture density is found near the bottom of the vessel whereas the lower mixture density is found near the liquid interface. A symmetrical vortex around the shaft is observed. The dynamic mixing behavior from the calculated density field is in a good agreement with the experiments which visualize the mixing behaviour of the dosed ethanol towards to the impeller with the bulk glycerol at t = 2 s (Fig. 5.67).

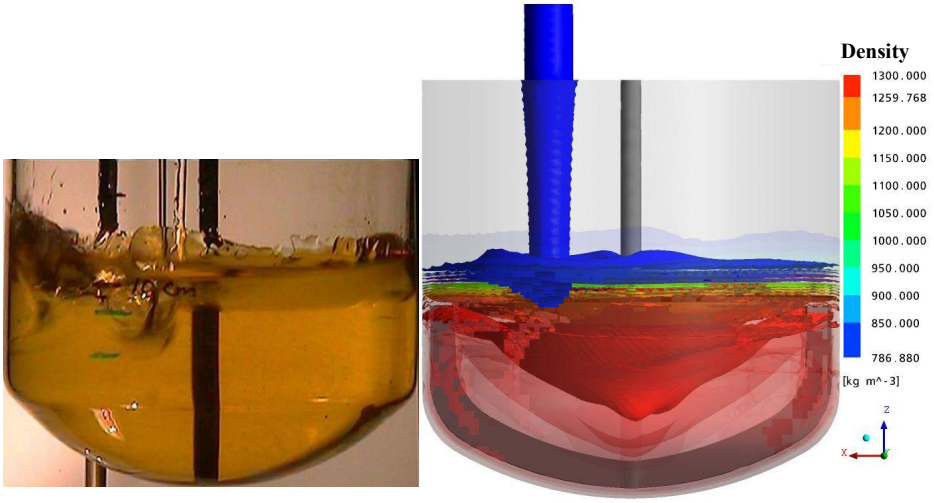

Figure 5.67: The density field of an ethanol/glycerol in a SBR for t_d = 5 s and ω = 150 rpm, by video visualization (left) and CFD simulation (right) using isosurfaces of the mixture density ρ_m, at t = 2 s.

5.3.2 SBR at t_d = 5 s (33 % ethanol)

A good agreement between the calculated and measured dynamic viscosity of the ethanol/glycerol mixture as a function of time can be shown in Fig. 5.68. Similar behavior to the case at t_d = 5 s (26 vol% ethanol) in Fig. 5.61 is obtained with a sharper decrease of the mixture viscosity during the dosage of ethanol because a larger volume of ethanol is mixed with glycerol

leading to a lower final mixture viscosity of η_m = 138 mPa s. The mixture viscosity decreases slowly between $5.2\,s \le t \le 140\,s$ because the buoyant forces which rise ethanol up to the liquid interface due to its lower density are higher than the shear forces which are caused by the impeller. Therefore the break up into ethanol droplets will be small between $5.2\,s \le t \le 140\,s$. A fast mixing and a sharp decrease of the mixture viscosity η_m occurs between $140\,s \le t \le 200\,s$ until a complete mixing and a constant mixture viscosity of η_m = 138 mPa s at t_m = 222 s are obtained.

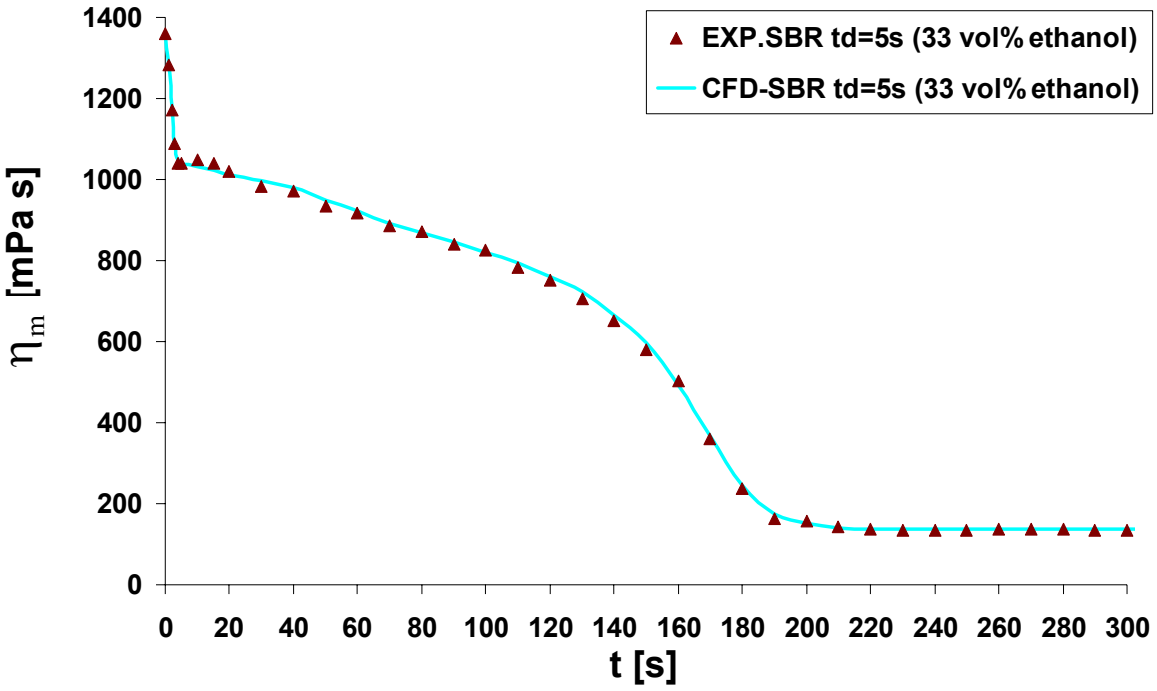

Figure 5.68: Mixture viscosity of an ethanol/glycerol as a function of time in a SBR at t_d = 5 s (33 vol% ethanol), experimentally and by using CFD simulation.

To get a good agreement between experimental values and CFD calculations it is assumed that the ethanol droplet diameter as a function of time is given as shown in Fig. 5.69. A large scale and slow break up of the ethanol droplet is found for t < 70 s. A small decrease of the ethanol droplet diameter occurs between $70\,s \le t \le 180\,s$ until a complete mixing is obtained

when ethanol droplet diameter and the final mixture viscosity of η_m = 138 mPa s remain constant at t_m = 220 s. A longer mixing time is obtained compared with that at t_d = 5 s (26 vol% ethanol) because a larger mass of ethanol is mixed with glycerol and a higher layer of ethanol above the bulk mixture is formed.

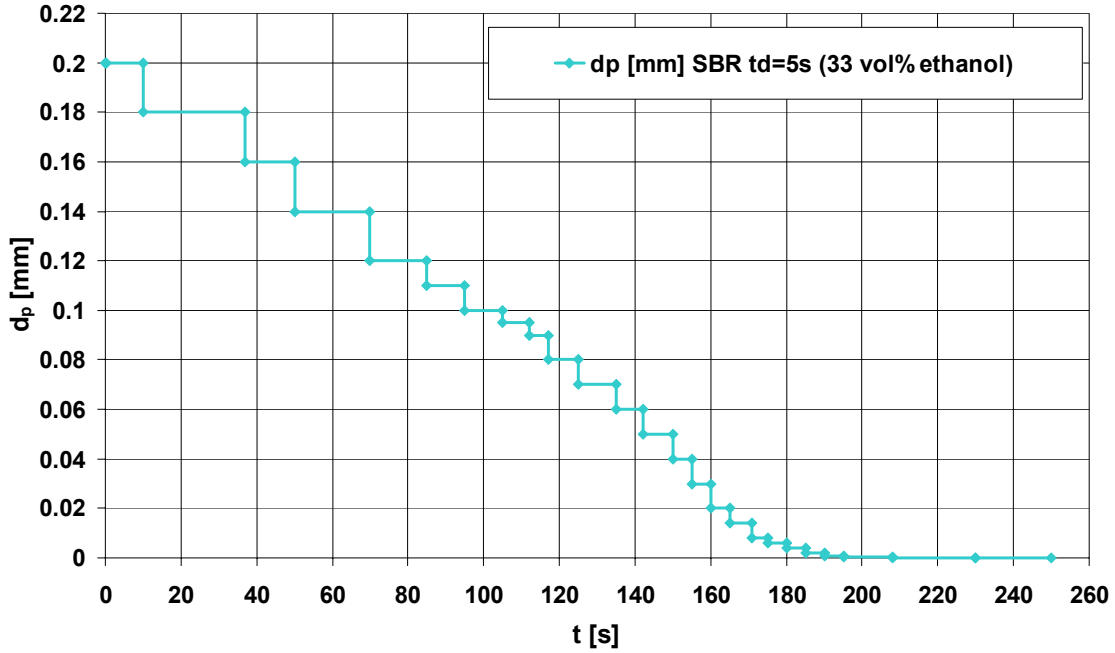

Figure 5.69: Calculated ethanol droplet diameter as a function of time (s. Chap. 5.3.5.2) in a SBR at t_d = 5 s (33 vol% ethanol) by using CFD simulation.

From Figs. 5.68 and 5.69 the mixture viscosity of ethanol and glycerol as a function of ethanol droplet diameter can be shown in Fig. 5.70. It is concluded that when the droplet diameter of ethanol decreases, the mixture viscosity decreases. A slower decrease of the mixture viscosity at t_d = 5 s (33 vol% ethanol) compared to that at t_d = 5 s (26 vol% ethanol) in Fig. 5.62 is obtained because the lower inlet flow velocity of ethanol leads to a small mass of ethanol can be mixed with glycerol and a higher layer of ethanol above glycerol is formed.

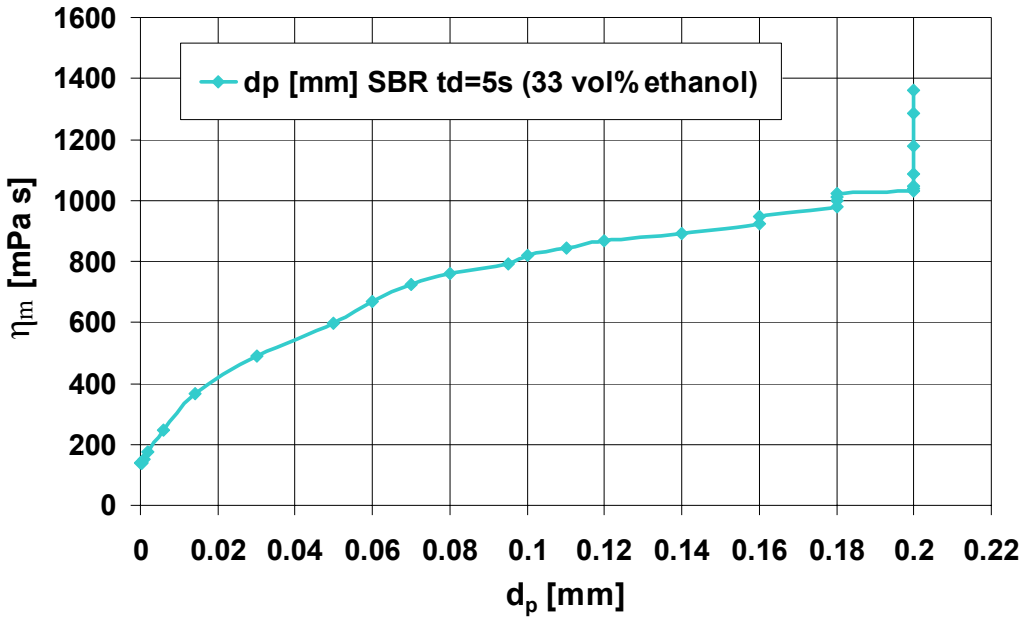

Figure 5.70: The dynamic viscosity of ethanol/glycerol mixture as a function of ethanol droplet diameter in a SBR at t_d = 5 s (33 vol% ethanol) by using CFD simulation.

The mixture viscosity $\eta_m(t)$ as a function of time for a SBR with t_d = 5 s (26 vol% ethanol) and t_d = 5 s (33 vol% ethanol) at ϑ = 21 °C and ω = 150 rpm which are determined from the experiments and CFD simulations can be shown in Fig. 5.71. It is found that when the volume fraction of the dosed ethanol increases from 26 vol% to 33 vol%, the mixing time increases from t_m = 205 s to t_m = 220 s and the final mixture viscosity decreases from η_m = 300 mPa s to η_m = 180 mPa s. The existence of a larger volume fraction (33 vol%) of ethanol above the tip of anchor impeller needs a longer time to transfer the ethanol layer at the interface to the bulk liquid. Therefore a longer mixing time is necessary for 33 vol% ethanol than that for 26 vol% ethanol. This means that larger volume fraction (33 vol%) of dosed ethanol leads to a lower final mixture viscosity.

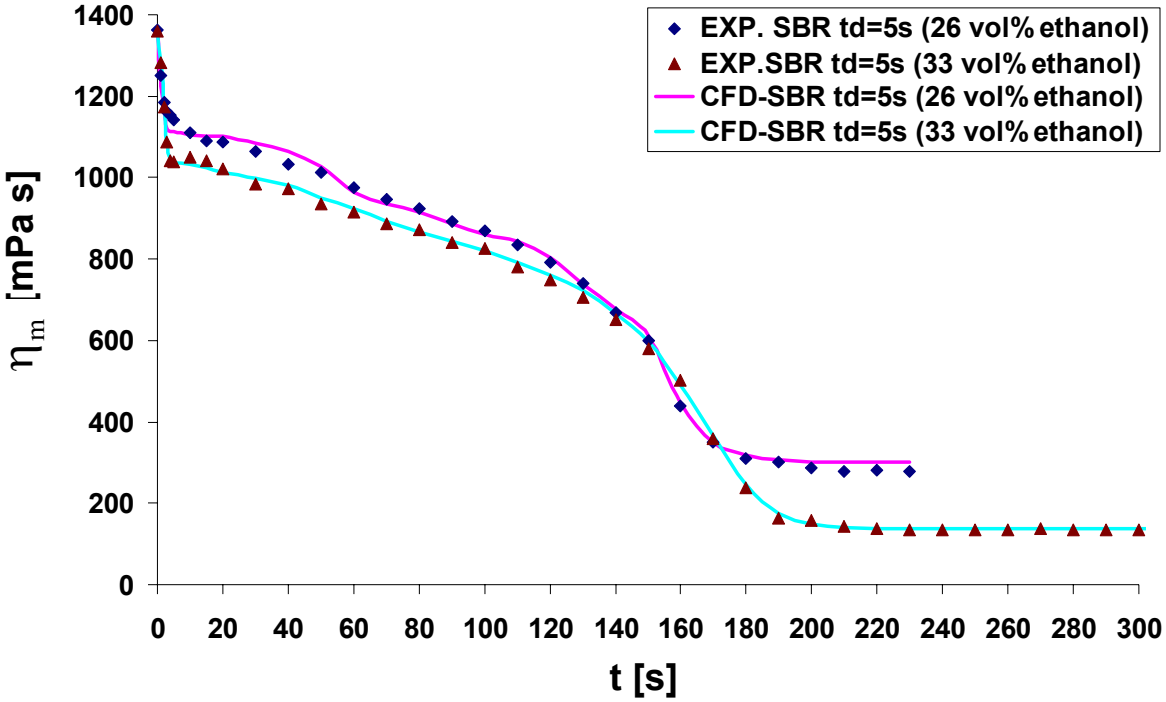

Figure 5.71: The mixture viscosity as a function of time for ethanol/glycerol in a SBR for t_d = 5 s (26 vol% ethanol) and t_d = 5 s (33 vol% ethanol) at ϑ = 21 °C and ω = 150 rpm, determined experimentally and by using CFD simulation.

5.3.3 SBR at t_d = 10 s (33 % ethanol)

A good agreement between the calculated and measured dynamic viscosity of the ethanol/glycerol mixture as a function of time at t_d = 10 s can be seen in Fig. 5.72. A fast decrease of the mixture viscosity similar to the case at t_d = 5 s (33 vol% ethanol) during the dosage of ethanol between $0.2\,\text{s} \le t_d \le 10.2\,\text{s}$ is obtained. A slower decrease of the mixture viscosity compared to that in the cases at t_d = 5 s is obtained during the dosage of ethanol between $10.2\,\text{s} \le t \le 210\,\text{s}$. Because the velocity of the dosed ethanol here is lower than that at t_d = 5 s (33 vol% ethanol), then a slower and a smaller break up into ethanol droplets occurs. A small mass of ethanol reaches to the bottom of the vessel and the larger mass of ethanol rise to the

interface of the bulk mixture. Therefore a higher layer of ethanol above the bulk mixture is formed compared with that at t_d = 5 s (33 vol% ethanol).

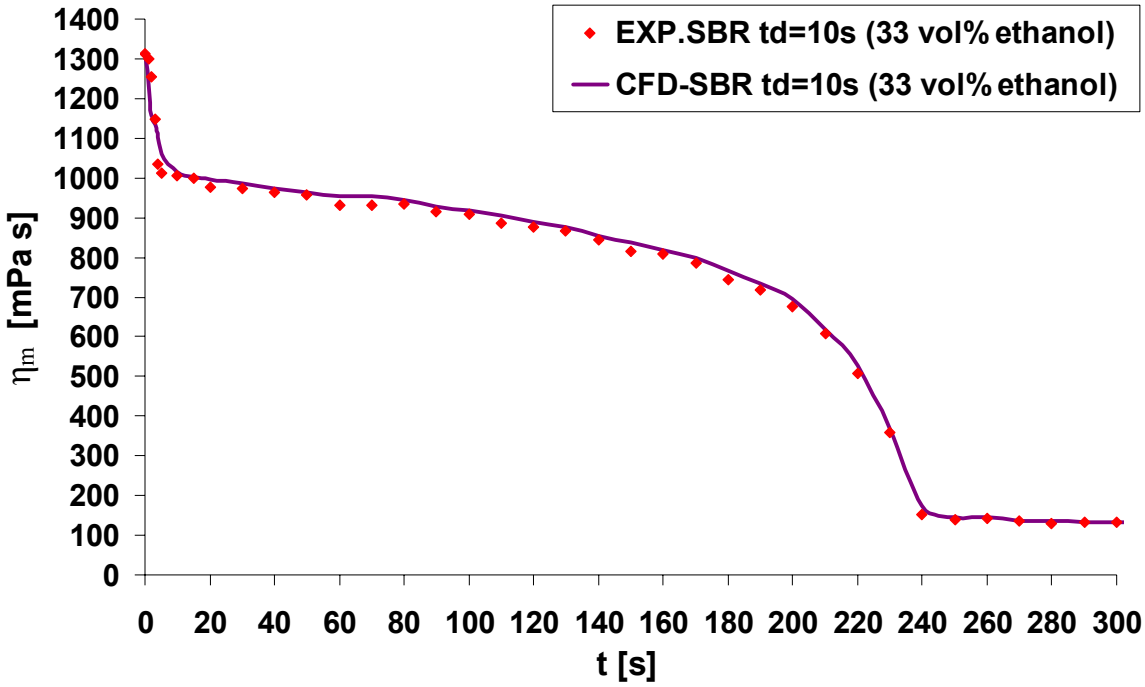

Figure 5.72: Mixture viscosity of ethanol/glycerol as a function of time in SBR at t_d = 10 s (33 vol% ethanol), experimentally and by using CFD simulation.

The time dependent ethanol droplet diameter at t_d = 10 s (Fig. 5.73) shows a slow break up of the ethanol droplet for t < 158 s. A fast decrease of the ethanol droplet diameter occurs between $158\,s \leq t \leq 220\,s$ until a complete mixing is obtained at t_m = 280 s and η_m = 137 mPa s (s. Fig. 5.72) where no further decrease of ethanol droplet diameter occurs. The final mixture viscosity in this case is similar to that at t_d = 5 s (33 vol% ethanol) where η_m = 138 mPa s (s. Fig. 5.68) because similar volume fractions of ethanol and glycerol are used, but a longer mixing time t_m = 280 s is found in the case of t_d = 10 s (33 vol% ethanol) compared to that at t_d = 5 s (33 vol% ethanol) where t_m = 220 s because of the faster inlet flow for t_d = 5 s.

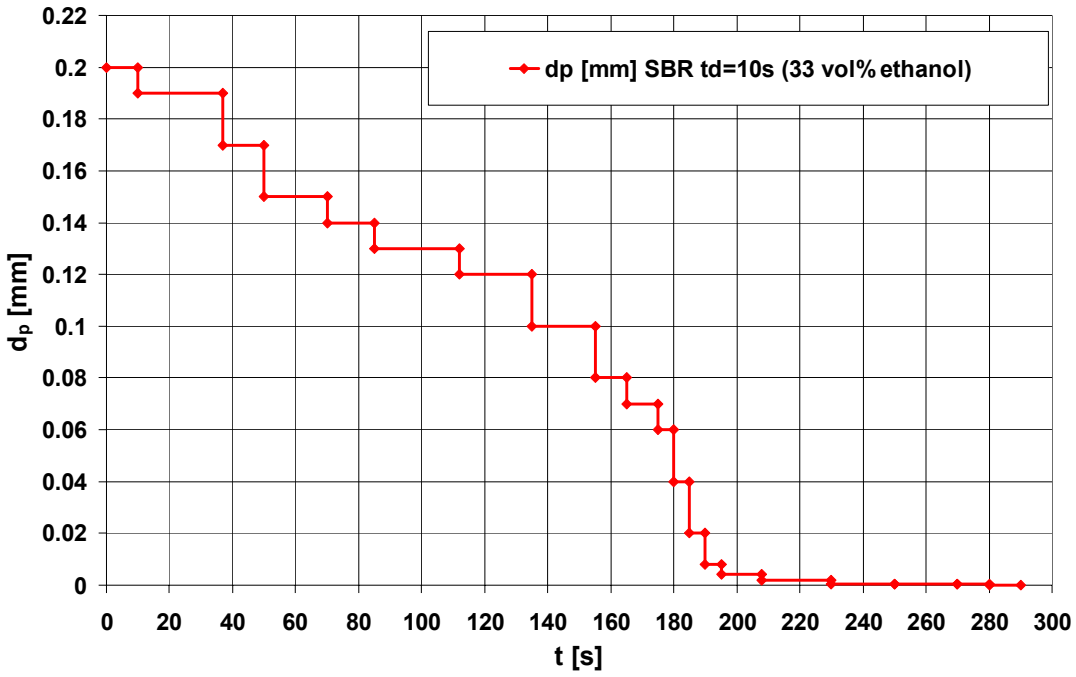

Figure 5.73: Calculated ethanol droplet diameter as a function of time (s. Chap. 5.3.5.3) in a SBR at t_d = 10 s (33 vol% ethanol) by using CFD simulation.

From Figs. 5.72 and 5.73 the mixture viscosity of ethanol and glycerol as a function of ethanol droplet diameter can be shown in Fig. 5.74. It is found that when the droplet diameter of ethanol decreases between $0.01\,\text{mm} \leq d_p \leq 0.2\,\text{mm}$, the mixture viscosity decreases slowly from η_m = 1000 mPa s to η_m = 700 mPa s. For d_p < 0.01 mm a fast decrease of the mixture viscosity occurs. A slower decrease of the mixture viscosity between $0.01\,\text{mm} \leq d_p \leq 0.2\,\text{mm}$ at t_d = 10 s (33 vol% ethanol) compared to that at t_d = 5 s (33 vol% ethanol) in Fig. 5.70 is obtained because the lower inlet flow velocity of ethanol leads to a small mass of ethanol can be mixed with glycerol and a higher layer of ethanol above glycerol is formed.

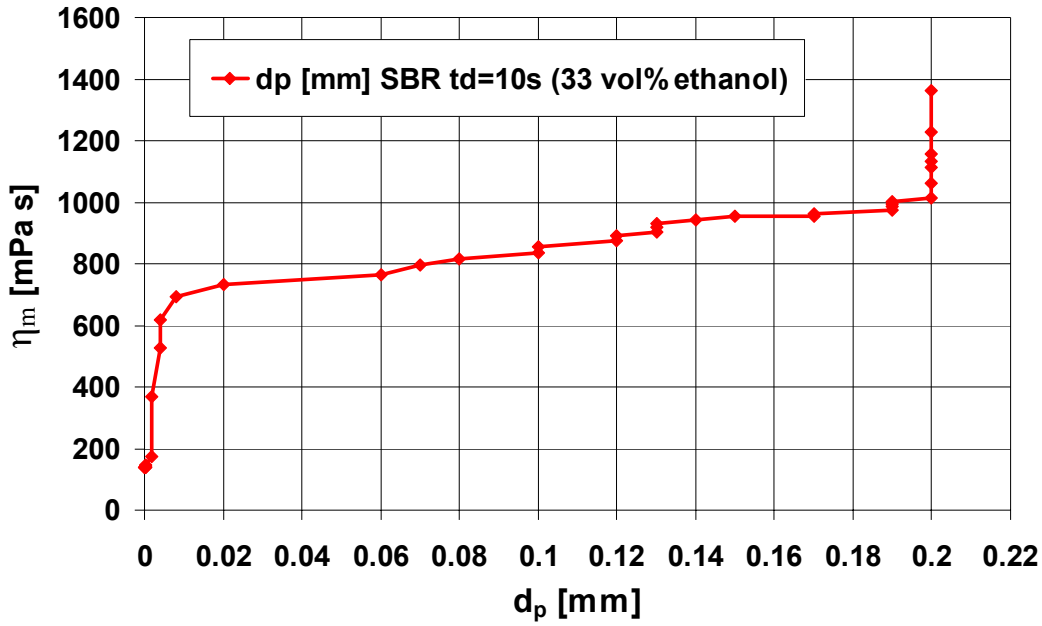

Figure 5.74: The dynamic viscosity of an ethanol/glycerol mixture as a function of ethanol droplet diameter in a SBR at t_d = 10 s (33 vol% ethanol) by using CFD simulation.

5.3.4 BR at H_l = 0.14 m (33 vol% ethanol)

Initially at t = 0 two layers are formed due to the density and viscosity differences between ethanol and glycerol (s. Fig. 5.80). The mixing time depends on the mass of the liquid (pan cake) above the impeller. Large amount of ethanol above the impeller forms a thick layer and leads to a slow dispersion of the ethanol into the bulk as can be seen between $0 \leq t \leq 240$ s in Fig. 5.75 where the bulk viscosity decreases slowly from η_m = 1047 mPa s to η_m = 882 mPa s. The ethanol layer is initially thick and clear above the stirrer, so that the rotating movement of the mixture by the stirrer is only slowly transfered to the top surface of ethanol leading to a long mixing time in the BR. During the mixing process, the region of intermediate viscosity between the impeller and shaft (Fig. 5.80) as a result of an increasing laminar convection between ethanol and glycerol with the consequence of a

decrease of the mixture viscosity with time [69]. A vortex is formed behind the anchor impeller to diminish the buoyancy forces and to accelerate the mixing of ethanol with glycerol. A faster mixing is found between $240\,s \le t \le 300\,s$ where the mixture viscosity decreases from $\eta_m = 882$ mPa s to $\eta_m = 125$ mPa s. It needs a long mixing time (Fig. 5.75) when the final mixture viscosity and ethanol droplet diameter becomes constant (Fig. 5.76). The mixing time and the final mixture viscosity are found to be $t_m = 340$ s and $\eta_m = 122$ mPa s (Fig. 5.75), respectively.

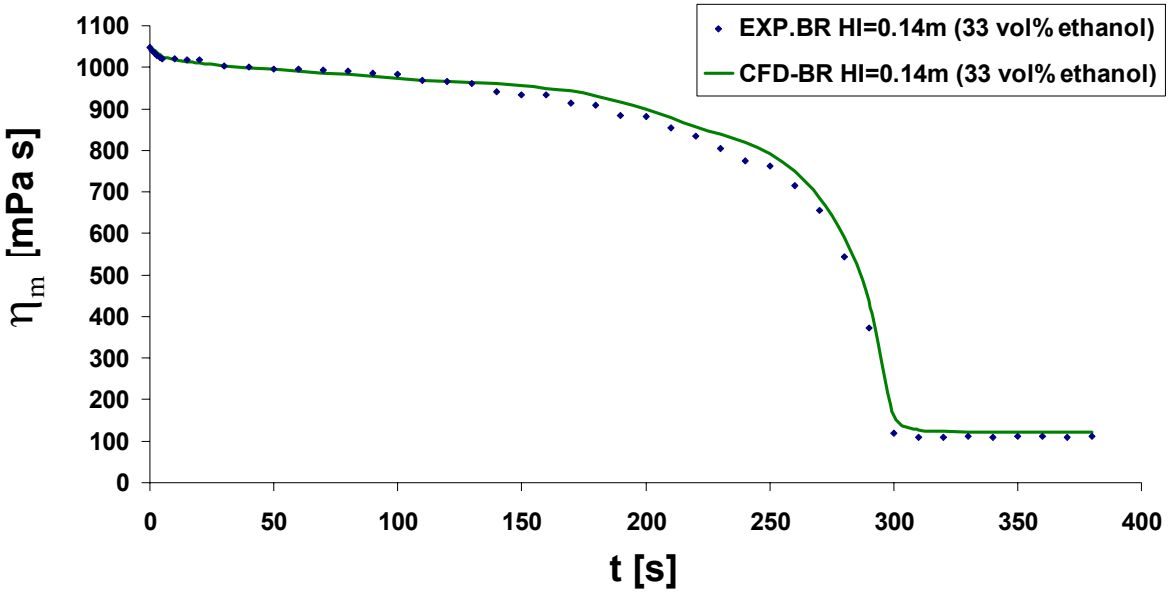

Figure 5.75: Mixture viscosity of an ethanol/glycerol as a function of time in a BR with $H_l = 0.14$ m (33 vol% ethanol), determined experimentally and by using CFD simulation.

For the mixing in the BR ethanol droplets may disperse in the stirrer region, the bottom of the vessel and the bulk liquid. In each region there is a chance that the ethanol droplets will be divided into smaller droplets or mixed into the bulk liquid. In addition, in each region the droplets have a chance to move to another zone [55]. The droplets may be divided by a physical contact with the stirrer which produces the highest shear forces. Therefore the transport of the liquid droplets occurs from the high velocity

region (stirrer) to the lower velocity region (shaft). The shear stresses are lower in the bulk liquid, but the droplets may be deformed further or be mixed completely. Fig. 5.76 shows that ethanol droplet diameter as a function of time in the BR also behaves as a time step function which predict the pan cake effect. For $0 \leq t \leq 138\,s$ the diameter of ethanol droplets remains constant (d_p = 0.2 mm) and there is no break up of the droplets. Therefore the mixing is caused by the gravitational forces and the shear forces of the stirrer (below the ethanol layer) which transport ethanol into the bulk glycerol (as explained above) from the tip of the impeller towards to the shaft. This leads to a circulation between the impeller and the shaft which enhance the mixing process. A small break up of the ethanol droplets is found from d_p = 0.2 mm at t = 138 s to d_p = 0.16 mm at t = 160 s. A large break up of the ethanol droplets is found between $160\,s \leq t \leq 190\,s$. Again a small break up of the ethanol droplet is found between $190\,s \leq t \leq 230\,s$ until a complete mixing is obtained at t_m = 340 s where no further decrease of the droplet diameter occurs.

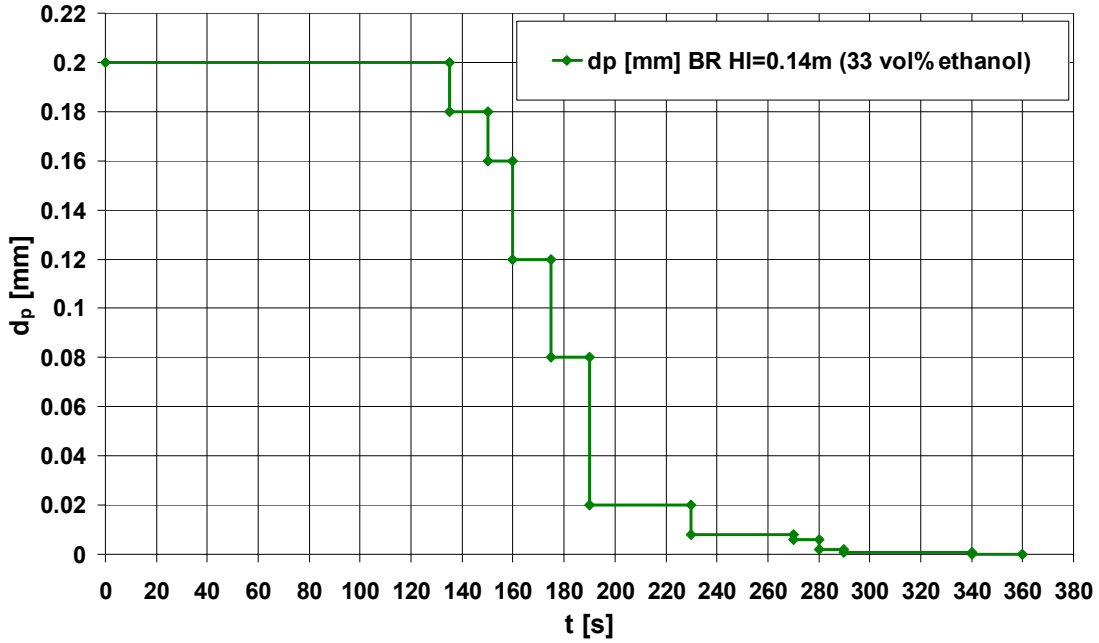

Figure 5.76: Calculated ethanol droplet diameters as a function of time (s. Chap. 5.3.5.4) in a BR with H_l = 0.14 m (33 vol% ethanol) by using CFD simulation.

By including Figs. 5.75 and 5.76 the mixture viscosity of ethanol and glycerol as a function of ethanol droplet diameter can be shown in Fig. 5.77.

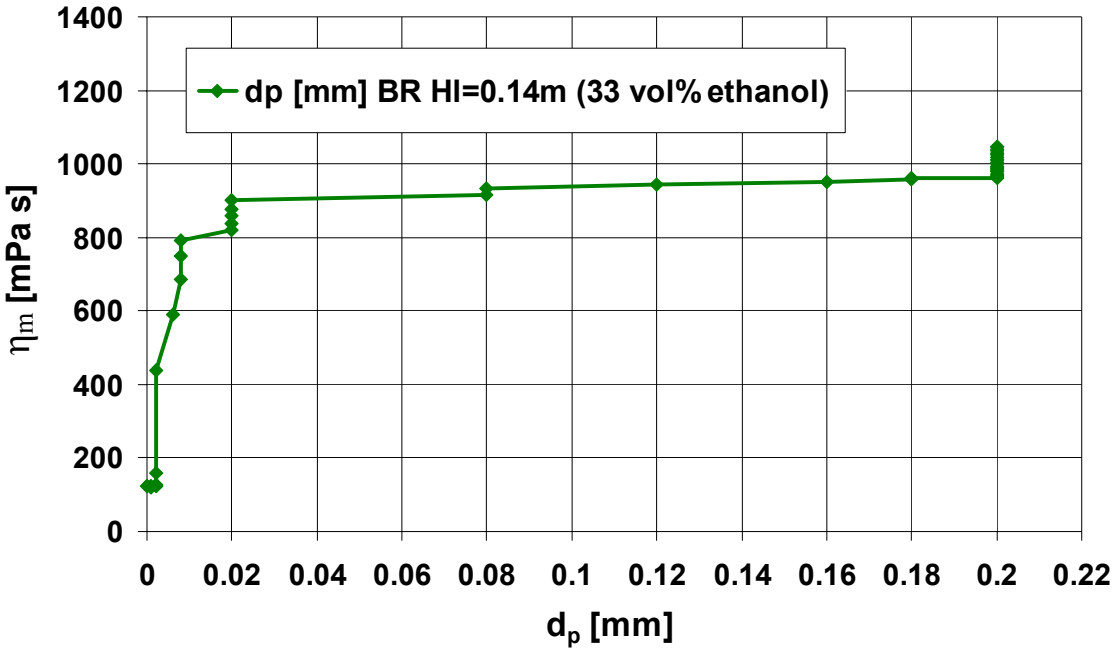

Figure 5.77: The dynamic viscosity of ethanol/glycerol mixture as a function of ethanol droplet diameter in a BR with H_l = 0.14 m (33 vol% ethanol) by using CFD simulation.

It is concluded that when the droplet diameter of ethanol decreases, the mixture viscosity decreases and so the velocity u_m of the liquid mixture increases. This means that the Reynolds number Re_m (s. Eq. 2-4) increases (Fig. 5.78-a). Reynolds number as a function of the d_p is a polynomial function of a fourth degree. The Reynolds number has no significant change for t < 150 s (Fig. 5.78-b) because here there is no break up of the ethanol droplets and very slow mixing between ethanol and glycerol occurs. Between 150 s ≤ t ≤ 200 s there is a small increase of the mixture velocity because the produced circulation between the shaft and impeller becomes larger and extends to the ethanol layer (pan cake) above the bulk mixture. The circulation leads to a higher deformation of the pan cake and to a break up of ethanol droplets and therefore a decreasing η_m and so a higher

Reynolds number is obtained. The break up of ethanol droplets happened because a larger mass of ethanol is exposed to the stirrer shear forces. For $t \geq 200$ s a larger break up of ethanol droplets occur leading to a further increase of the mixture velocity and Reynolds number Re_m until the mixture properties becomes constant at $t_m = 340$ s.

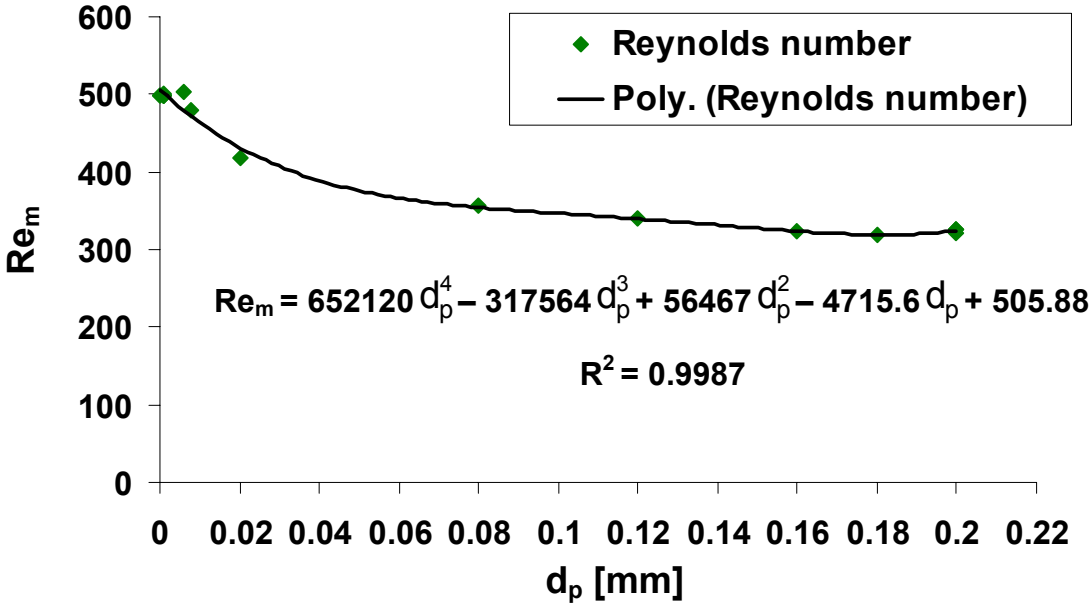

Figure 5.78-a: Reynolds number Re_m as a function (polynomial) of ethanol droplet diameter d_p in a BR with $H_l = 0.14$ m (33 vol% ethanol) and ω = 150 rpm by using CFD simulation.

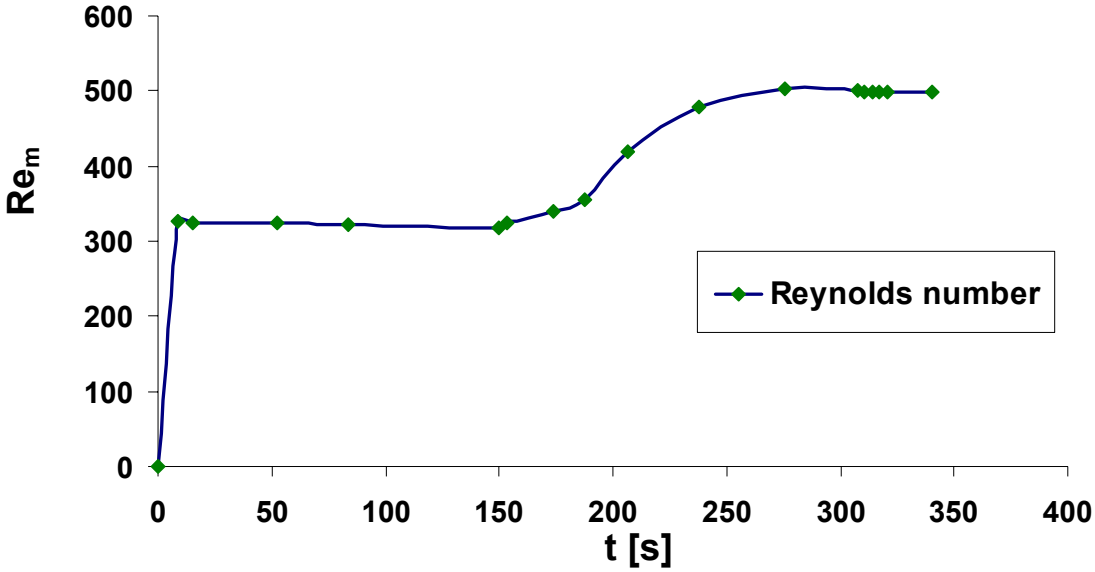

Figure 5.78-b: Calculated Reynolds number Re_m as a function of time in a BR with $H_l = 0.14$ m (33 vol% ethanol) and ω = 150 rpm by using CFD simulation.

The calculated ethanol mass fraction profile as a function of time at nine different positions in the BR near the shaft, in the middle between the shaft and the impeller and near the cylindrical wall can be shown in Fig. 5.79. Initially at t = 0 high ethanol mass fractions exist at the points above glycerol height of H_G = 0.1 m (P_3, P_4 and P_5). When the anchor starts to rotate, ethanol mass fractions decrease slowly for 0 < t < 150 s and decrease faster for t > 150 s until a complete mixing is obtained at relatively large t_m = 340 s. Ethanol mass fraction is zero at the points below glycerol level of H_G = 0.1 m (P_1, P_2 and P_6) at t = 0 and increases slowly for 0 < t < 200 s and increase faster for t > 200 s until the complete mixing is obtained at t_m = 340 s.

The points near the vertical blade of the impeller (P_1 and P_7) have the lowest mass fractions of ethanol because the mixing near the cylindrical wall of the vessel and in the impeller region is fast. Also the pushed ethanol by the impeller to these positions (P_1 and P_7) is completely mixed with glycerol due to the existence of the impeller high shear forces.

The points near the shaft P_2 and P_9 which are at the same height as that for P_1 and P_7, respectively have higher ethanol mass fractions because the mixing near the shaft is weak and the pushed ethanol by the impeller is slowly mixed with glycerol. It is concluded that the points which exist near the cylindrical wall and also near the impeller (P_1, P_3 and P_7) reach the mixing time faster than the points in the middle (P_5, P_6 and P_8) and last are the points near the shaft (P_2, P_4 and P_9).

The calculated distribution of ethanol mass fractions in all the nine points can explain the mixing behavior and flow velocity of ethanol in glycerol as a function of time from the tip of the impeller towards the shaft and then towards the cylindrical wall (Fig. 5.79).

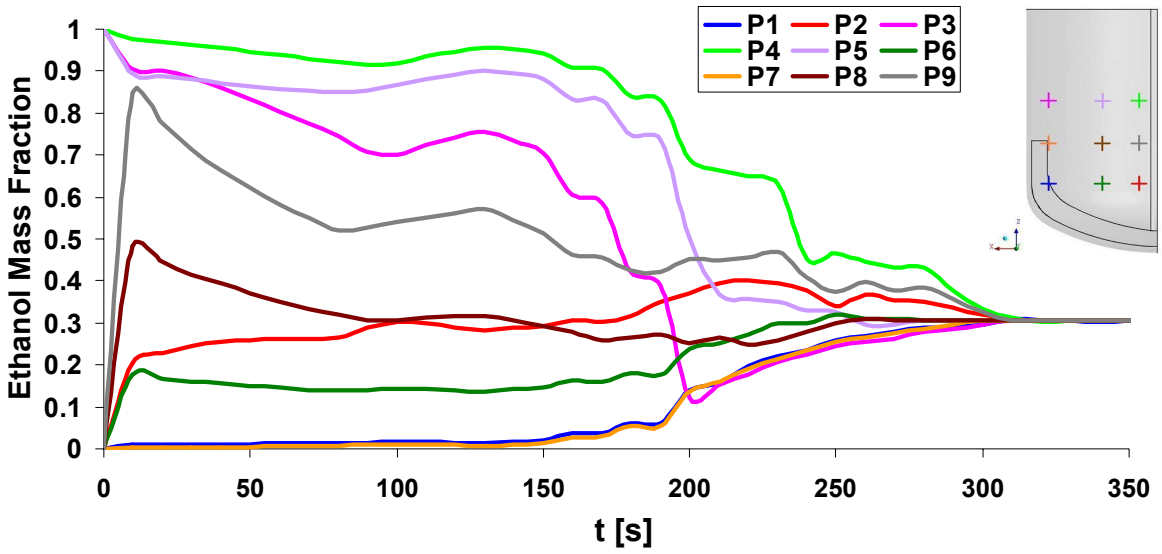

Figure 5.79: Calculated ethanol mass fraction as a function of time by CFD simulation at different positions in the BR with H_l = 0.14 m (33 vol% ethanol) and ω = 150 rpm.

The calculated dynamic mixing behavior of ethanol with glycerol by using the isosurface of ethanol mass fraction as a function of time shown in Fig. 5.80 (right) and the video visualization, shown in Fig. 5.80 (left). Initially at t = 0 two distinct layers appear, i.e. a pan cake is formed. When the impeller starts the rotation for t > 0, ethanol is pushed into glycerol and mixed from the cylindrical wall near the tip of the impeller to the shaft and then towards to the cylindrical wall leading to a symmetrical vortex around the shaft at the interface between ethanol and the bulk mixture for t = 50 s. This vortex (trombe) becomes larger at t = 100 s, so that the length and deformation of ethanol filaments increase leading to a fast convection of ethanol in the glycerol for t = 200 s. The visualized mixing behaviour and its CFD simulation in a BR with H_l = 0.14 m (33 vol% ethanol) are in a good agreement.

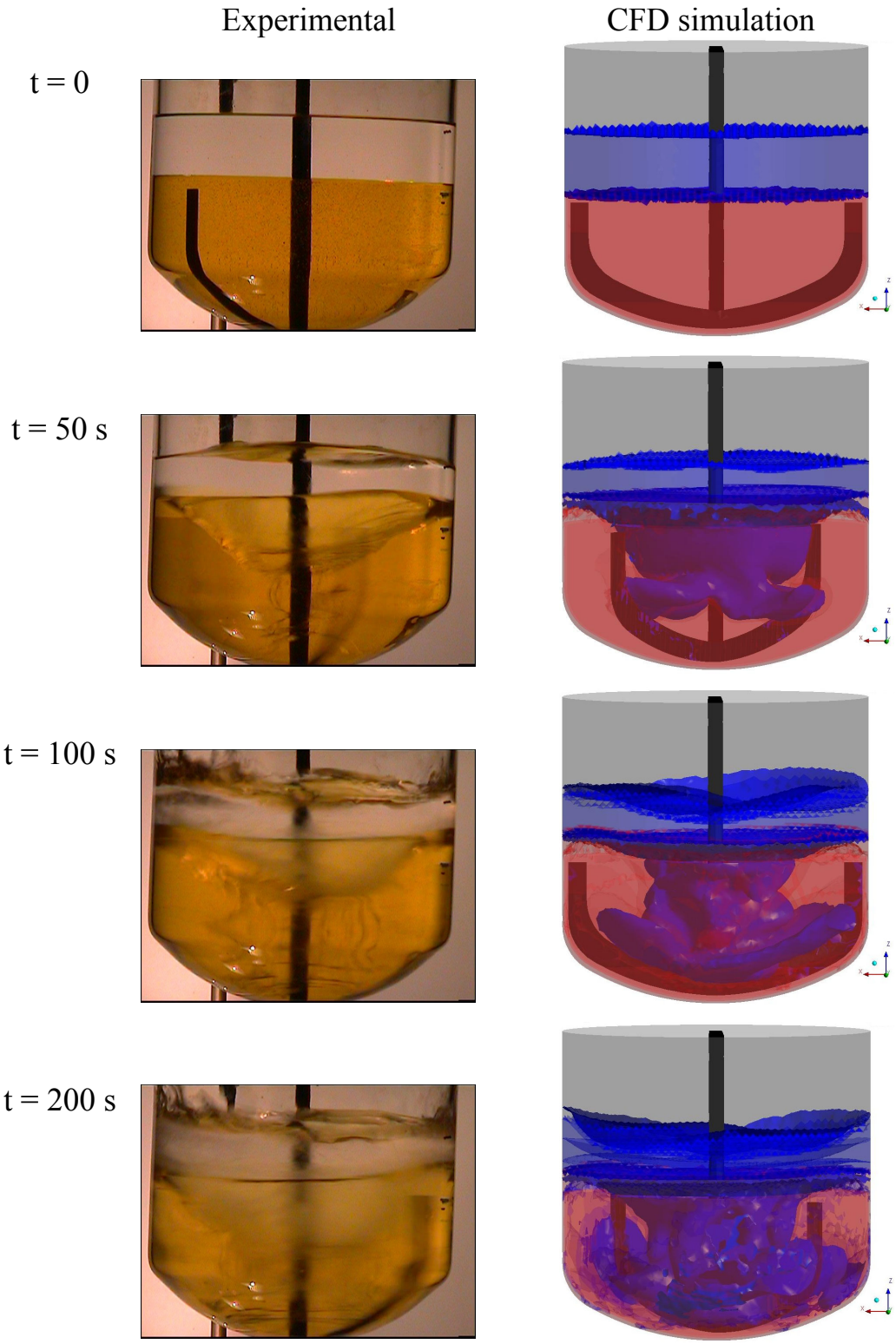

Figure 5.80: The dynamic mixing behavior of ethanol/glycerol mixture in a BR with H_l = 0.14 m and ω = 150 rpm, shown by video visualization (left) and CFD simulation (right) using an isosurface of ethanol mass fractions at different times between $0 \leq t \leq 200$ s.

The density field $\rho_m(x,z)$ of ethanol and glycerol mixture in a BR at t = 50 s is shown in Fig. 5.81 where a large mass of low density ethanol still exists above the bulk glycerol and uptil now a small mass of ethanol is mixed with glycerol. Therefore small mixture densities are found above the tip of impeller and large mixture densities are found below the tip of impeller. The calculated mixture density field (right) is very similar to the visualized dynamic mixing (left).

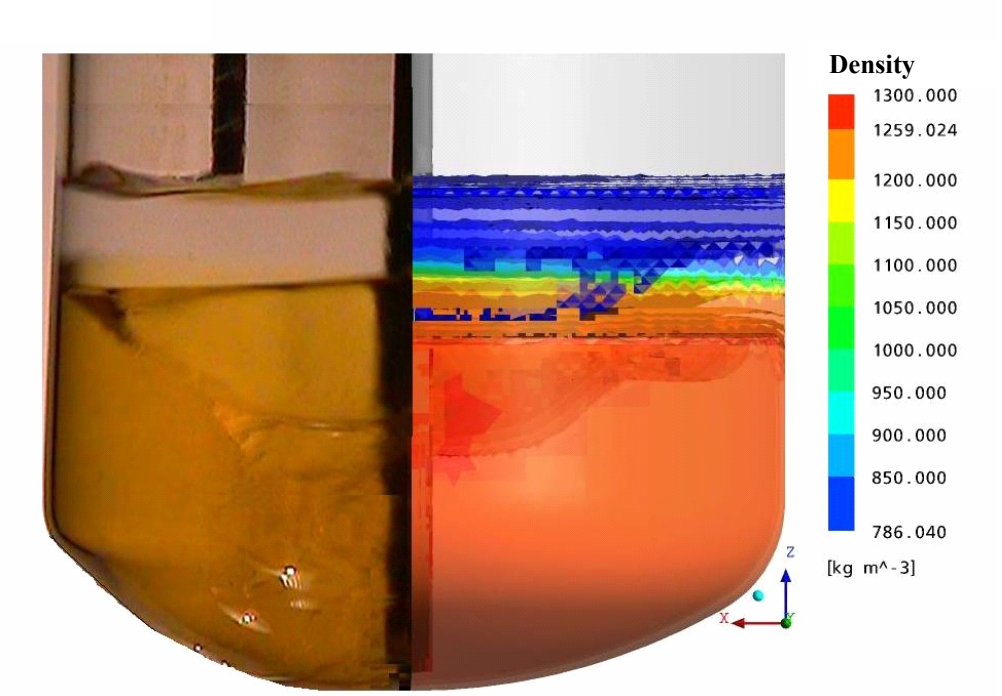

Figure 5.81: The density field of ethanol/glycerol mixture in a BR (H_l = 0.14 m) and ω = 150 rpm, by video visualization (left) and CFD simulation (right) using isosurfaces of the mixture density ρ_m, at t = 50 s.

The calculated flow velocity- and mixture viscosity fields of ethanol/glycerol as a function of time between $0 \le t \le 4.95$ s in a 3D BR by using sliding mesh method (s. Chap. 4.1.3.4.7) are shown in Figs. 5.82-a and 5.82-b. These fields can explain the dynamic mixing behaviour shown in Fig. 5.80. It can be seen that the circulation flow behind the impeller rotation (clock wise) exists at t = 0.45 s, 0.9 s and 2.25 s (Fig. 5.82-a) and at t = 2.7 s,

4.05 s and 4.5 s (Fig. 5.82-b). A good agreement with the experiment is found.

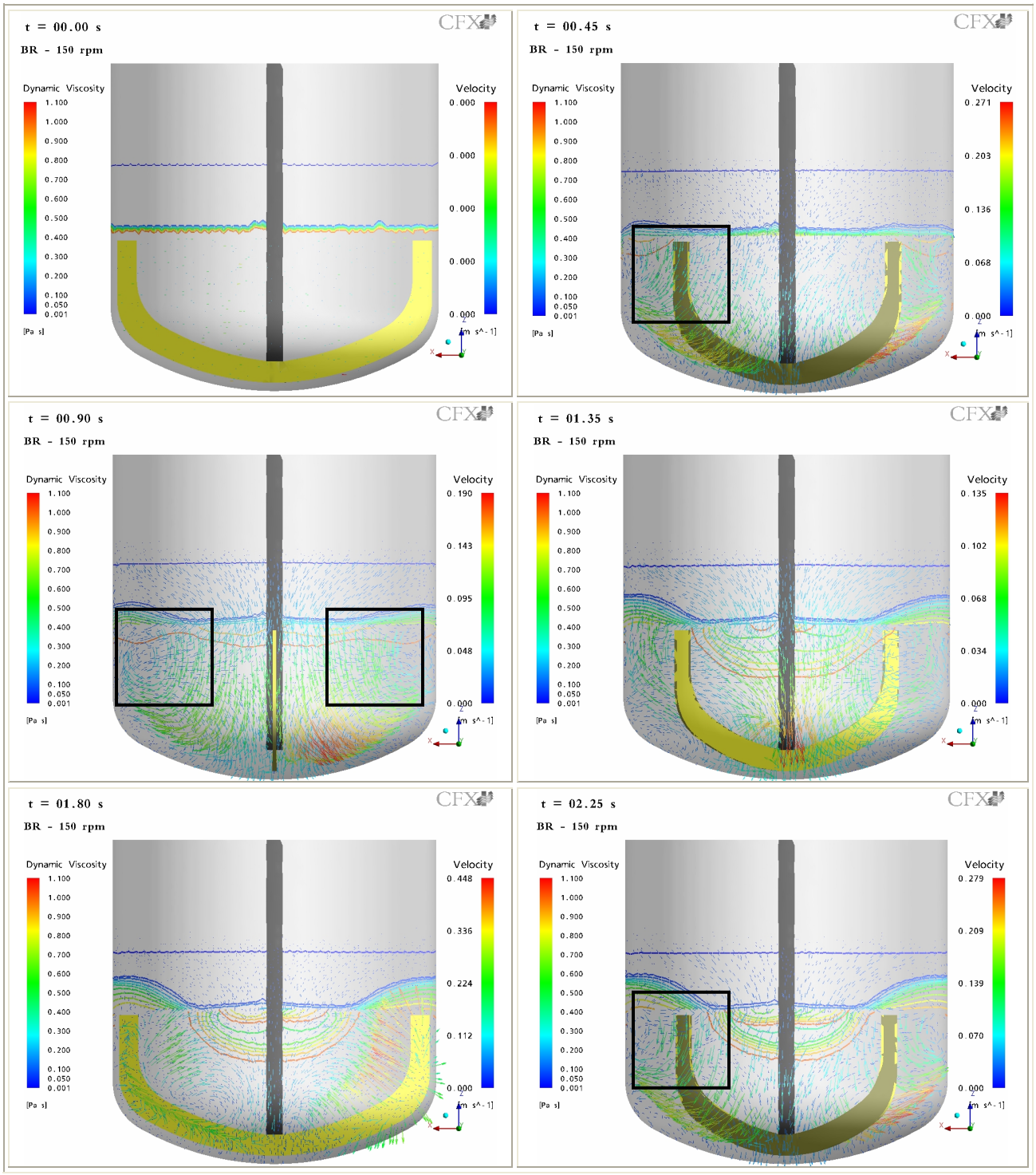

Figure 5.82-a: Calculated flow velocity- and mixture viscosity fields as function of time for ethanol/glycerol in a BR at ω = 150 rpm by using sliding mesh method.

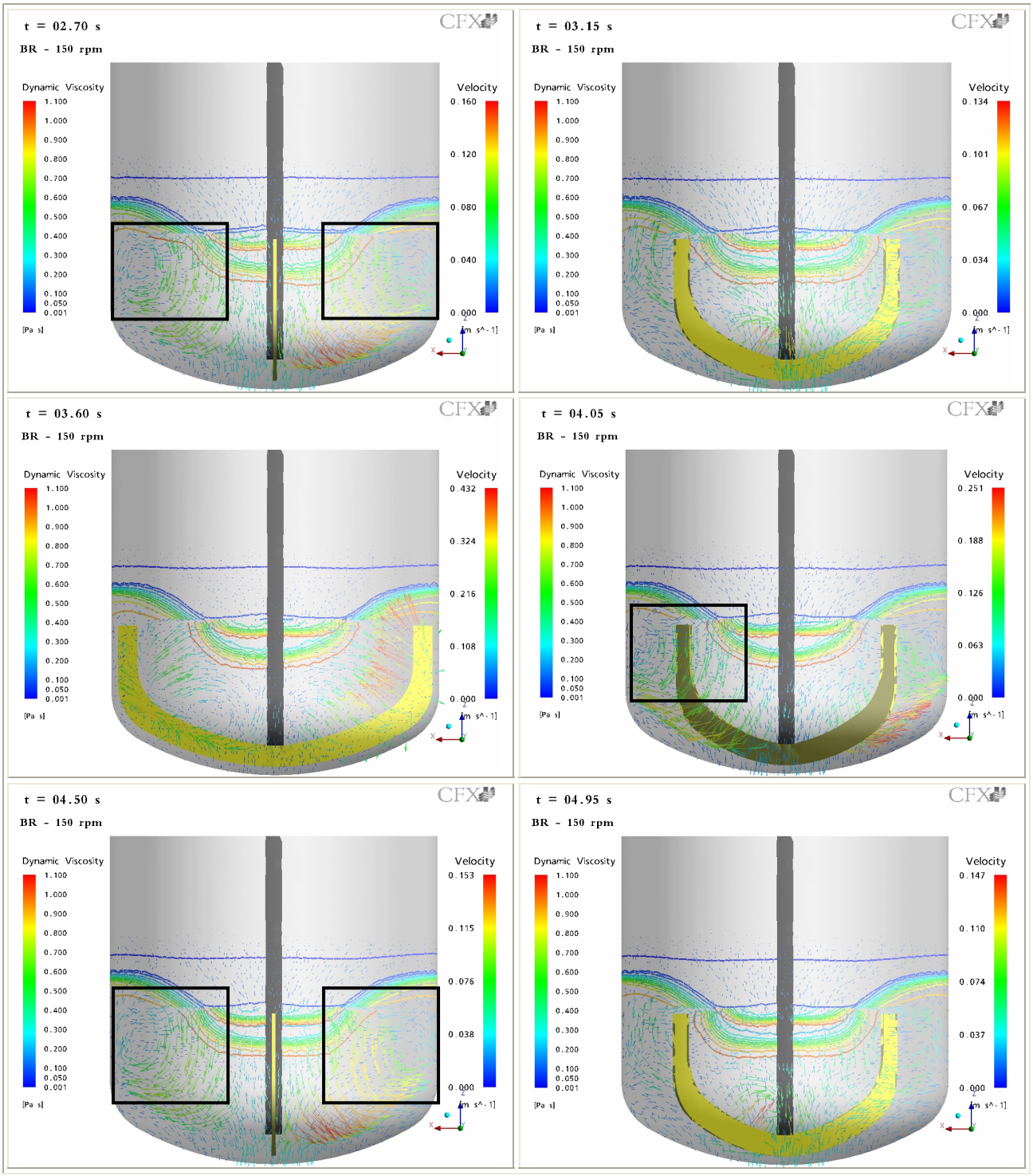

Figure 5.82-b: Calculated flow velocity- and mixture viscosity fields as function of time for ethanol/glycerol in a BR at ω = 150 rpm by using sliding mesh method.

The radial viscosity profile η_m (y) for ethanol and glycerol mixture in the BR at t = 100 s is shown in Fig. 5.83. The maximum mixture viscosities are found near the cylindrical wall at y = ± 0.078 m and decrease towards the shaft. The mixture viscosity at y = − 0.078 m is lower than that at y = 0.078 m because at this time the anchor is near y = − 0.078 m and transport a larger mass of ethanol to this position leading there to a local decrease of the mixture viscosity. Whereas a small mass of ethanol at the same time t = 100 s reaches to the position at y = 0.078 m leading to a local higher mixture viscosity because a weak effect by the impeller is present here. As a consequence ethanol is transported by the impeller towards to the shaft leading to a low mixture viscosity around the shaft. The viscosity at y = − 0.025 m is higher than that at y = − 0.05 m because a very weak mixing can be found in the centre of the formed circulation between the shaft and the impeller at y = − 0.05 m.

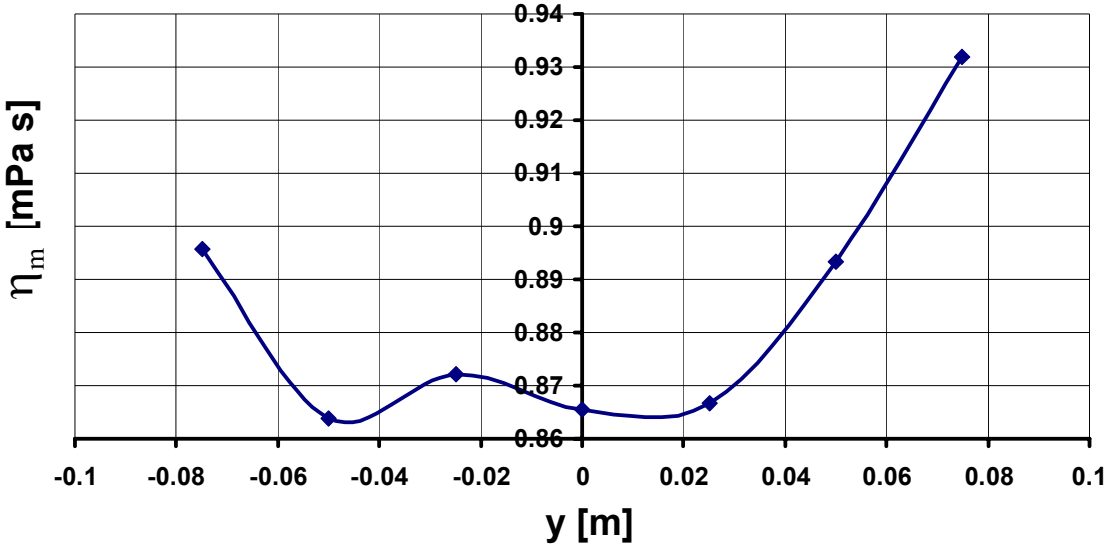

Figure 5.83: Radial viscosity profile for ethanol/glycerol mixture in y-direction for a BR, at t = 100 s.

The calculated and simulated mixture viscosity η_m of glycerol and ethanol as a function of time t for a SBR at t_d = 5 s and t_d = 10 s and for a BR with a total liquid height H_l = 0.14 m at ϑ = 21 °C and ω = 150 rpm are shown in Fig. 5.84. It is found that the mixing times t_m from the experiments and CFD simulations for the SBR at t_d = 5 s and t_d = 10 s are lower than that in the BR at H_l = 0.14 m because the dosage of ethanol gives additional kinetic energy to the bulk liquid leading to a faster break up of ethanol droplets and a larger contact area between ethanol and glycerol, then a faster mixing occurs. In the case of the SBR a similar sharp decrease of the η_m is obtained for t_d = 5 s and t_d = 10 s during the dosage, but a slower decrease of the η_m after the dosage is found for t_d = 10 s because the velocity of the bulk liquid in this case is lower than that for t_d = 5 s which leads to a slower break up of ethanol droplets and longer mixing time. It is concluded that when the dosage time in a SBR increases, then the mixing behavior becomes similar to that in the BR and a longer mixing time is required to get a complete mixing and a similar final mixture viscosity.

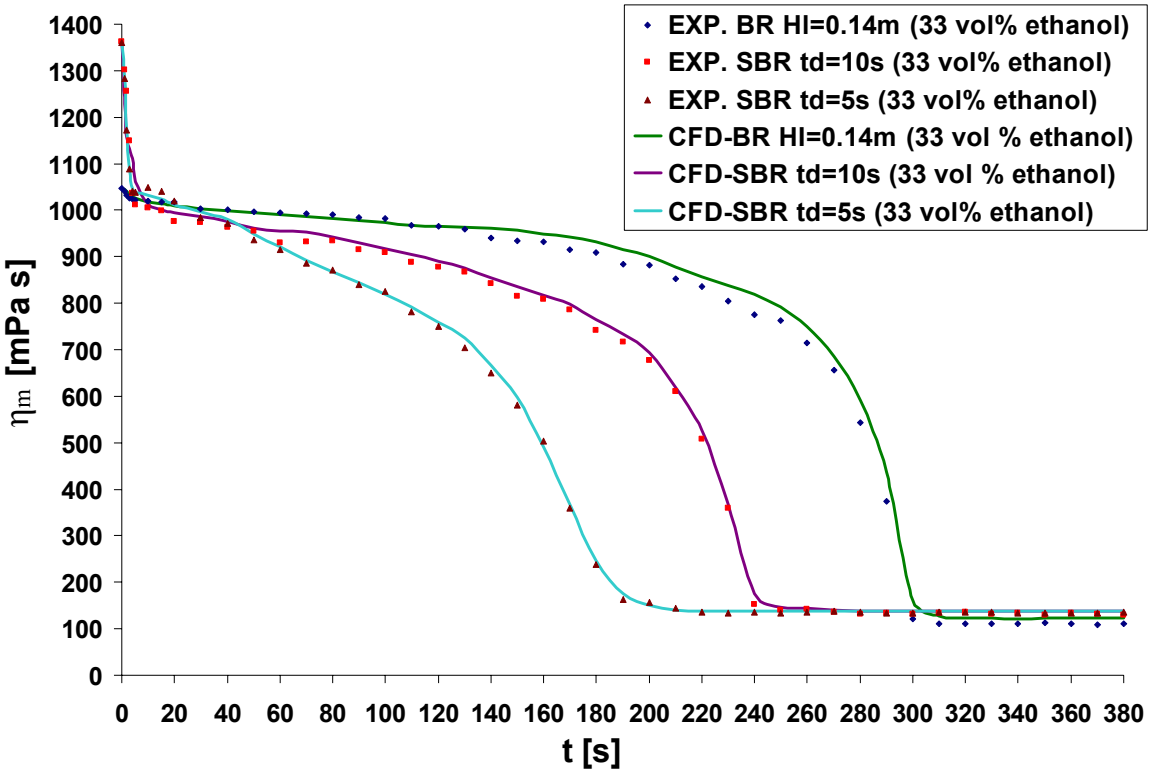

Figure 5.84: The mixture viscosity as a function of time for ethanol/glycerol (33 vol% ethanol) in a SBR with t_d = 5 s and t_d = 10 s and in a BR with H_l = 0.14 m at ϑ = 21 °C and ω = 150 rpm, determined experimentally and by using CFD simulation.

5.3.5 Step functions of ethanol droplet diameter for CFD simulations in SBR and BR

Ethanol droplet diameters d_p as a function of time are shown in Fig. 5.85 for SBR and BR. It is found that the break up of ethanol droplets starts from the beginning of the dosage in the SBR but it needs a long time to start the break up of the droplets at t = 130 s in the case of BR. A fast break up of the droplet diameter is found during the mixing process in the SBR at t_d = 5 s, whereas a slow break up of ethanol droplet diameter is obtained in the BR leading to a longer mixing time. In the case of a SBR for t_d = 10 s the number of ethanol droplet breaks up decreases and the droplet size reduction increases with time, in comparison to t_d = 5 s. So it can be concluded that with increasing dosage time t_d in the SBR the formation of the relatively

thick ethanol layer like in the BR is more and more realized. The ethanol droplet break up in the BR starts later (at t > 138 s) with a smaller number of breaks up but a larger droplet size reduction. The large droplet size reduction is connected with a sharp decrease of the mixture viscosity η_m (t), as can be seen from Figs. 5.71 and 5.84.

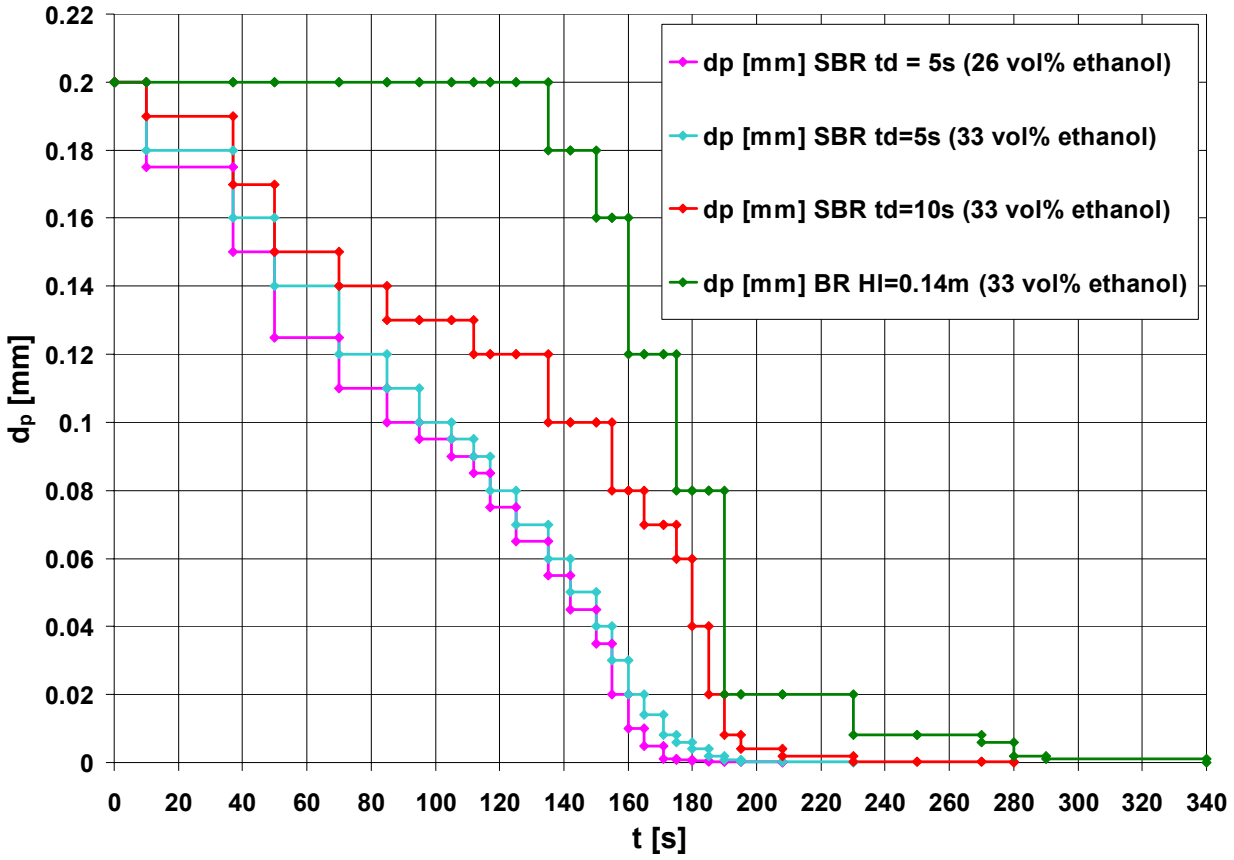

Figure 5.85: Calculated ethanol droplet diameter d_p as a function of time for SBR and BR, at ϑ = 21 °C and ω = 150 rpm.

The initial ethanol droplet diameter d_p at t = 0 is assumed to be 0.0002 m [120]. The break up of ethanol droplet in different time periods during the mixing in SBR and BR is calculated by using time step functions of η_m (t) including Eq. (4-31) in the CFD simulation. In Chap. 5.3.5.1 it is presented the break up of ethanol droplet diameter in different time periods until a

complete mixing is obtained when the mixture viscosity η_m remains constant and no further break up of ethanol droplets happens.

5.3.5.1 SBR at t_d = 5 s (26 vol% ethanol)

By using the measured viscosities $\eta_m(t)$ of the liquid ethanol/glycerol mixture as a function of time, the following validated step function is formulated.

Between $0 \le t \le 10$ s $\Rightarrow$ $d_p = 0.0002$ m

S1 = step(t/1.0[s]-0) *0.0002[m]

S2 = step(t/1.0[s]-10) *0.0002[m]

d_p ethanolSBR1 = S1-S2.

Where d_p ethanolSBR1 is ethanol droplet diameter in a SBR in the first time period of the mixing process.

Between $10.1\text{ s} \le t \le 37$ s $\Rightarrow$ $d_p = 0.000175$ m

S3 = step(t/1.0[s]-10.1) *0.000175[m]

S4 = step(t/1.0[s]-37) *0.000175[m]

d_p ethanolSBR2 = S3-S4.

Similar step functions are used for the following time periods:

Between $37.1\text{ s} \le t \le 50$ s $\Rightarrow$ $d_p = 0.00015$ m

Between $50.1\text{ s} \le t \le 70$ s $\Rightarrow$ $d_p = 0.000125$ m

Between $70.1\text{ s} \le t \le 85$ s $\Rightarrow$ $d_p = 0.00011$ m

Between $85.1\text{ s} \le t \le 95$ s $\Rightarrow$ $d_p = 0.0001$ m

Between $95.1\text{ s} \le t \le 105$ s $\Rightarrow$ $d_p = 0.000095$ m

Between $105.1\text{ s} \le t \le 112$ s $\Rightarrow$ $d_p = 0.00009$ m

Between $112.1\text{ s} \le t \le 117$ s $\Rightarrow$ $d_p = 0.000085$ m

Between $117.1\text{ s} \le t \le 125$ s $\Rightarrow$ $d_p = 0.000075$ m

Between $125.1\,s \le t \le 135\,s$ $\Rightarrow$ $d_p = 0.000065$ m

Between $135.1\,s \le t \le 142\,s$ $\Rightarrow$ $d_p = 0.000055$ m

Between $142.1\,s \le t \le 150\,s$ $\Rightarrow$ $d_p = 0.000045$ m

Between $150.1\,s \le t \le 155\,s$ $\Rightarrow$ $d_p = 0.000035$ m

Between $155.1\,s \le t \le 160\,s$ $\Rightarrow$ $d_p = 0.00002$ m

Between $160.1\,s \le t \le 165\,s$ $\Rightarrow$ $d_p = 0.00001$ m

Between $165.1\,s \le t \le 171\,s$ $\Rightarrow$ $d_p = 0.000005$ m

Between $171.1\,s \le t \le 175\,s$ $\Rightarrow$ $d_p = 0.000001$ m

Between $175.1\,s \le t \le 180\,s$ $\Rightarrow$ $d_p = 0.00000075$ m

Between $180.1\,s \le t \le 185\,s$ $\Rightarrow$ $d_p = 0.0000005$ m

Between $185.1\,s \le t \le 190\,s$ $\Rightarrow$ $d_p = 0.0000004$ m

Between $190.1\,s \le t \le 195\,s$ $\Rightarrow$ $d_p = 0.0000003$ m

Between $195.1\,s \le t \le 208\,s$ $\Rightarrow$ $d_p = 0.0000002$ m

Between $208.1\,s \le t \le 230\,s$ $\Rightarrow$ $d_p = 0.0000001$ m

5.3.5.2 SBR at t_d = 5 s (33 vol% ethanol)

In this case the validated step function $d_p(t)$ is formulated by the following relationships.

Between $0 \le t \le 10\,s$ $\Rightarrow$ $d_p = 0.0002$ m

S1 = step(t/1.0[s]-0) *0.0002[m]

S2 = step(t/1.0[s]-10) *0.0002[m]

d_p ethanolSBR1 = S1-S2.

Between $10.1\,s \le t \le 37\,s$ $\Rightarrow$ $d_p = 0.00018$ m

S3 = step(t/1.0[s]-10.1) *0.00018[m]

S4 = step(t/1.0[s]-37) *0.00018[m]

d_p ethanolSBR2 = S3-S4.

Between $37.1\,s \le t \le 50\,s$ $\Rightarrow$ $d_p = 0.00016$ m

Between	$50.1\,s \le t \le 70\,s$	$\Rightarrow$	$d_p = 0.00014$ m
Between	$70.1\,s \le t \le 85\,s$	$\Rightarrow$	$d_p = 0.00012$ m
Between	$85.1\,s \le t \le 95\,s$	$\Rightarrow$	$d_p = 0.00011$ m
Between	$95.1\,s \le t \le 105\,s$	$\Rightarrow$	$d_p = 0.0001$ m
Between	$105.1\,s \le t \le 112\,s$	$\Rightarrow$	$d_p = 0.000095$ m
Between	$112.1\,s \le t \le 117\,s$	$\Rightarrow$	$d_p = 0.00009$ m
Between	$117.1\,s \le t \le 125\,s$	$\Rightarrow$	$d_p = 0.00008$ m
Between	$125.1\,s \le t \le 135\,s$	$\Rightarrow$	$d_p = 0.00007$ m
Between	$135.1\,s \le t \le 142\,s$	$\Rightarrow$	$d_p = 0.00006$ m
Between	$142.1\,s \le t \le 150\,s$	$\Rightarrow$	$d_p = 0.00005$ m
Between	$150.1\,s \le t \le 155\,s$	$\Rightarrow$	$d_p = 0.00004$ m
Between	$155.1\,s \le t \le 160\,s$	$\Rightarrow$	$d_p = 0.00003$ m
Between	$160.1\,s \le t \le 165\,s$	$\Rightarrow$	$d_p = 0.00002$ m
Between	$165.1\,s \le t \le 171\,s$	$\Rightarrow$	$d_p = 0.000014$ m
Between	$171.1\,s \le t \le 175\,s$	$\Rightarrow$	$d_p = 0.000008$ m
Between	$175.1\,s \le t \le 180\,s$	$\Rightarrow$	$d_p = 0.000006$ m
Between	$180.1\,s \le t \le 185\,s$	$\Rightarrow$	$d_p = 0.000004$ m
Between	$185.1\,s \le t \le 190\,s$	$\Rightarrow$	$d_p = 0.000002$ m
Between	$190.1\,s \le t \le 195\,s$	$\Rightarrow$	$d_p = 0.0000008$ m
Between	$195.1\,s \le t \le 208\,s$	$\Rightarrow$	$d_p = 0.0000004$ m
Between	$208.1\,s \le t \le 220\,s$	$\Rightarrow$	$d_p = 0.0000002$ m
Between	$220.1\,s \le t \le 250\,s$	$\Rightarrow$	$d_p = 0.0000001$ m

5.3.5.3 SBR at t_d = 10 s (33 vol% ethanol)

In this case the validated step function $d_p(t)$ is formulated by the following relationships.

Between $0 \le t \le 10$ s $\Rightarrow$ $d_p = 0.0002$ m

S1 = step(t/1.0[s]-0) *0.0002[m]

S2 = step(t/1.0[s]-10) *0.0002[m]

d_p ethanolSBR1 = S1-S2.

Between $10.1 \text{ s} \le t \le 37$ s $\Rightarrow$ $d_p = 0.00019$ m

S3 = step(t/1.0[s]-10.1) *0.00019 [m]

S4 = step(t/1.0[s]-37) *0.00019[m]

d_p ethanolSBR2 = S3-S4.

Between $37.1 \text{ s} \le t \le 50$ s $\Rightarrow$ $d_p = 0.00017$ m

Between $50.1 \text{ s} \le t \le 70$ s $\Rightarrow$ $d_p = 0.00015$ m

Between $70.1 \text{ s} \le t \le 85$ s $\Rightarrow$ $d_p = 0.00014$ m

Between $85.1 \text{ s} \le t \le 112$ s $\Rightarrow$ $d_p = 0.00013$ m

Between $112.1 \text{ s} \le t \le 135$ s $\Rightarrow$ $d_p = 0.00012$ m

Between $135.1 \text{ s} \le t \le 155$ s $\Rightarrow$ $d_p = 0.0001$ m

Between $155.1 \text{ s} \le t \le 165$ s $\Rightarrow$ $d_p = 0.00008$ m

Between $165.1 \text{ s} \le t \le 175$ s $\Rightarrow$ $d_p = 0.00007$ m

Between $175.1 \text{ s} \le t \le 180$ s $\Rightarrow$ $d_p = 0.00006$ m

Between $180.1 \text{ s} \le t \le 185$ s $\Rightarrow$ $d_p = 0.00004$ m

Between $185.1 \text{ s} \le t \le 190$ s $\Rightarrow$ $d_p = 0.00002$ m

Between $190.1 \text{ s} \le t \le 195$ s $\Rightarrow$ $d_p = 0.000008$ m

Between $195.1 \text{ s} \le t \le 208$ s $\Rightarrow$ $d_p = 0.000004$ m

Between $208.1 \text{ s} \le t \le 230$ s $\Rightarrow$ $d_p = 0.000002$ m

Between $230.1 \text{ s} \le t \le 250$ s $\Rightarrow$ $d_p = 0.0000004$ m

Between $250.1 \text{ s} \le t \le 270$ s $\Rightarrow$ $d_p = 0.0000003$ m

Between $270.1 \text{ s} \le t \le 280$ s $\Rightarrow$ $d_p = 0.0000002$ m

Between $280.1 \text{ s} \le t \le 290$ s $\Rightarrow$ $d_p = 0.0000001$ m

5.3.5.4 BR at H_l = 0.14 m (33 vol% ethanol)

In this case the validated step function $d_p(t)$ is formulated by the following relationships.

Between $0 \leq t \leq 135$ s $\Rightarrow$ $d_p = 0.0002$ m

B1 = step(t/1.0[s]-0) *0.0002[m]

B2 = step(t/1.0[s]-135) *0.0002[m]

d_p ethanolBR1 = B1-B2.

Where d_p ethanolBR1 is ethanol droplet diameter in a BR in the first time period of the mixing process.

Between $135.1\text{ s} \leq t \leq 150$ s $\Rightarrow$ $d_p = 0.00018$ m

B3 = step(t/1.0[s]-135.1) *0.00018[m]

B4 = step(t/1.0[s]-150) *0.00018[m]

d_p ethanolBR2 = B3-B4

Similar step functions to that above for the droplet diameter of ethanol as a function of time are used for the following time periods:

Between $150.1\text{ s} \leq t \leq 160$ s $\Rightarrow$ $d_p = 0.00016$ m

Between $160.1\text{ s} \leq t \leq 175$ s $\Rightarrow$ $d_p = 0.00012$ m

Between $175.1\text{ s} \leq t \leq 190$ s $\Rightarrow$ $d_p = 0.00008$ m

Between $190.1\text{ s} \leq t \leq 230$ s $\Rightarrow$ $d_p = 0.00002$ m

Between $230.1\text{ s} \leq t \leq 270$ s $\Rightarrow$ $d_p = 0.000008$ m

Between $270.1\text{ s} \leq t \leq 280$ s $\Rightarrow$ $d_p = 0.000006$ m

Between $280.1\text{ s} \leq t \leq 290$ s $\Rightarrow$ $d_p = 0.000002$ m

Between $290.1\text{ s} \leq t \leq 340$ s $\Rightarrow$ $d_p = 0.000001$ m

Between $320.1\text{ s} \leq t \leq 360$ s $\Rightarrow$ $d_p = 0.0000001$ m

5.3.6 The modified CFD-Algebraic slip model (MASM) in comparison with Algebraic slip model (ASM) and the Transport model (TRM) in a SBR and a BR

The calculated dynamic viscosity of ethanol and glycerol mixture η_m as a function of time t when it is used the modified algebraic slip model (MASM), algebraic slip model (ASM) and the transport model (TRM) in the CFD simulations at ϑ = 21°C and ω = 150 rpm can be shown in Figs. 5.86 and 5.87 for SBR and BR, respectively. It is shown that alone the MASM developed in this work is able to describe realistic the measured mixture viscosity $\eta_m(t)$ as a function of time.

The final mixture viscosities for the SBR by using the MASM and TRM are η_m = 300 mPa s at t_m = 205 s and η_m = 267 mPa s at t_m = 60 s, respectively. The final mixture viscosities for BR by using the MASM and TRM are η_m = 122 mPa s at t_m = 340 s and η_m = 178 mPa s at t_m = 100 s, respectively. The calculated final mixture viscosities η_m have approximately the same values, whereas the calculated mixing times t_m are completely different. Especially the $\eta_m(t)$ behavior is quite different. The mixing time by using TRM is shorter than that by using MASM with a time difference of Δt = 145 s for the SBR and Δt = 240 s for the BR. The reason is that the transport model does not consider the density differences and the relative velocity between ethanol (upper layer) and glycerol (lower layer). For that the slow mixing process between $5.2\,s \le t \le 150\,s$ is not realized when the transport model is used to calculate the mixture viscosity η_m in the SBR and BR as can be seen in Figs. 5.87 and 5.88, respectively. However the MASM considers the buoyancy forces, the interphase mass

transfer and the relative velocity between ethanol and glycerol which depends on the ethanol droplet diameter $d_p(t)$ as a validated step function. Therefore the MASM describes the real mixing behavior between ethanol and glycerol compared to that determined from experiments in the SBR and BR. It is concluded from Figs. 5.86 and 5.87 that the calculated mixture viscosities $\eta_m(t)$ from TRM are not in agreement with that measured from the experiments in the SBR and BR, respectively.

The ASM shows a completely unrealistic $\eta_m(t)$ behavior, final mixture viscosity and mixing time for the SBR and BR in comparison with the MASM. The reason is that the ASM does not consider ethanol droplets break up as a function of time, in opposite to the MASM.

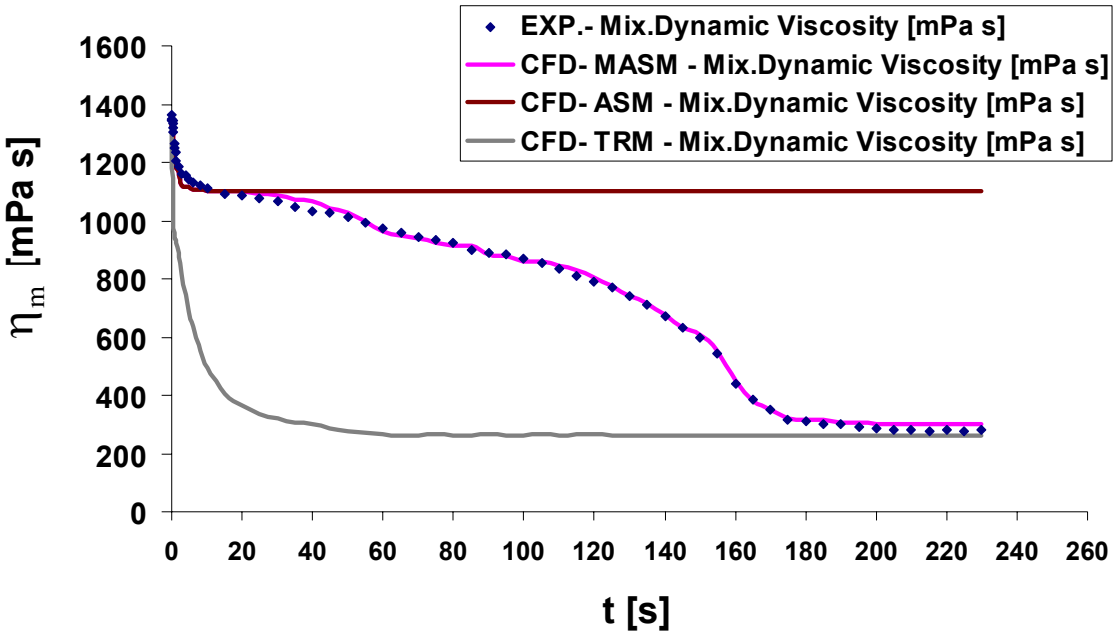

Figure 5.86: Mixture viscosity of the ethanol/glycerol as a function of time in a SBR at t_d = 5 s, determined experimentally and CFD-simulation by using the models MASM, ASM and TRM.

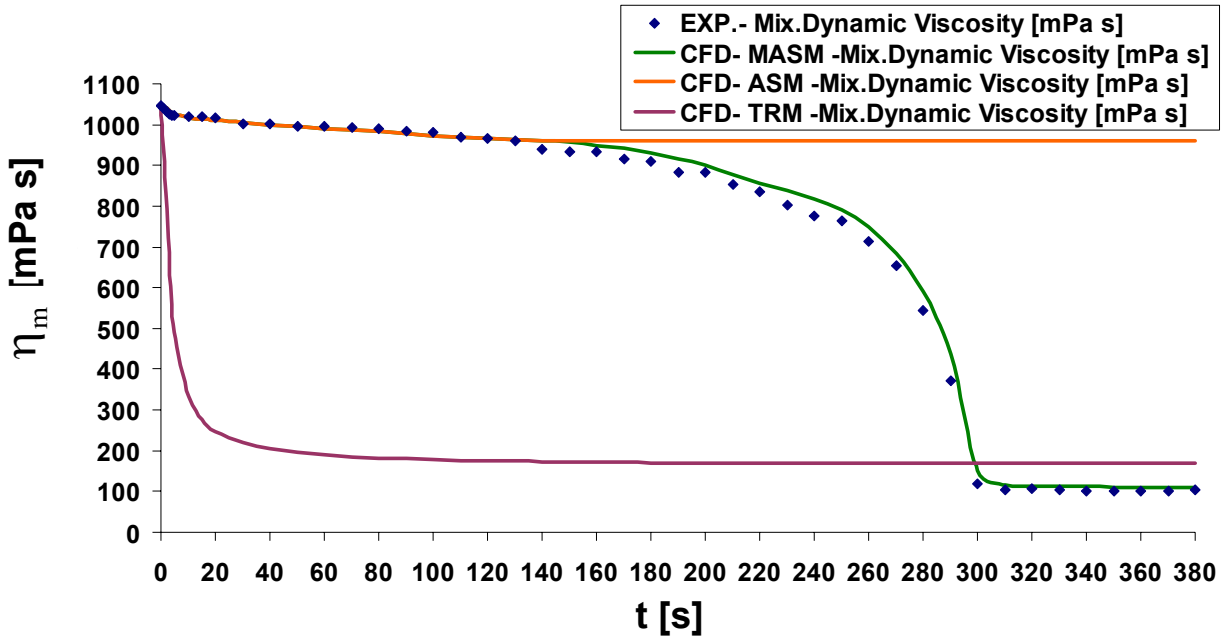

Figure 5.87: Mixture viscosity of ethanol/glycerol as a function of time in a BR with H_l = 0.14 m determined experimentally and CFD-simulation by using the models MASM, ASM and TRM.

5.3.7 Summary of the measured and calculated η_m and t_m

The measured and the calculated dynamic mixture viscosities η_m of ethanol and glycerol and mixing times t_m in a SBR and a BR are summarized in Tab. 5.2.

Table 5.2: The measured and CFD calculated mixture viscosity η_m and mixing time t_m for a SBR and a BR.

	EXPERIMENT			CFD-Simulation	
	Mixture Viscosity [mPa s]	Mixing Time [s]		Mixture Viscosity [mPa s]	Mixing Time [s]
		Torque method	Decolorisation Reaction		
SBR at t_d = 5 s (26 vol% ethanol)	279	208	206	300	205
SBR at t_d = 5 s (33 vol% ethanol)	134	222	-	138	220
SBR at t_d = 10 s (33 vol% ethanol)	130	282	-	137	280
BR with H_l = 0.14 m (33 vol% ethanol)	110	342	340	122	340
BR with H_l = 0.09 m (33 vol% ethanol)	135	20	17	-	-

6. CONCLUSIONS AND OUTLOOK

• ***Conclusions***

1. The mixing times and time dependent dynamic viscosities of the liquid mixture with different viscosities and different densities can be predicted by CFD simulation in a SBR and a BR and are in a good agreement with experimental values.
2. The new developed MASM in connection with a step function of the droplet diameter $d_p(t)$ predicts the mixing behaviour of these liquids.
3. Reducing the number of cells by a factor of 20 decreases the computational time of simulation by factor of 10, without remarkable change in the results.
4. The cell size should not exceed 0.015 m to get a good special resolution.
5. It is found that a dosage time of 5 s, an inlet tube diameter 0.023 m, anchor velocity of 150 rpm and the width of the horizontal blade of the anchor impeller of 0.015 m are the best operating conditions.
6. With a decolourisation and a torque method for determination of the time dependent mixture viscosities and the mixing times in a SBR and a BR, it is possible to validate the used CFD models.
7. For the SBR, a jet phenomenon during the dosage of ethanol plays a big role to get a fast mixing.
8. It is possible with CFD to predict the complex batch phenomenon (pan cake effect) in a BR for liquids with high viscosity difference and high density difference.
9. This thesis presents methods for recognition of more complex problems and alternative mixing designs for critical applications.

10. The high viscosity liquid mixture has also a great effect on an observed secondary flow field with an axial circulation behind the rotating impeller which can be predicted by CFD simulation.

Outlook

1. The mixing behavior of different liquid mixtures with different geometries and stirrers should be carried out.
2. It is assumed the investigated mixing phenomena also are happened in large scale vessel, the quantitative scale up relation ship could also be developed and carried out with suitable volume of liquids.
3. It is intended to investigate the mixing behavior for non-miscible liquids in a BR with different stirrer types and velocities.
4. The studied mixing processes are the first step to a CFD simulation of polymerization reactions including high viscosity effects.

7. REFERENCES

[1] Delaplace, G., Guerin, R., Leuliet, J., Torrez, C., Andre, C., *Sliding mesh method to simulate flow of highly viscous fluid in stirred tank agitated with helical ribbon impeller*, Proc.2th International Conference on Simulation in food and Bio industries (2002) 151-157.

[2] Nakamura, S., Brodkey, R., *Computational Flow Analysis for the Chemical Mixing Vessel with Impeller and Baffles*, ASME Fluid Engineering Summer Conference Boston, Massachusetts, June 11-15 (2000) 1-8.

[3] Myers, K., Ward, R., Bakker, A., *A Digital Particle Image Velocimetry Investigation of Flow Field Instabilities of Axial- Flow Impellers*, J. Fluid Eng. 119 (1997) 623-631.

[4] Battello, G., Grisafi, F., Micale, G., Brucato, A., *Flow Field In An Unbaffled Stirred Tank via Particle Image Velocimetry*, Dipartimento di Ingegneria Chimica dei Processi e dei Materiali e Laboratoroi INCA, Viale delle Scienze-90128 Palermo, Italy (1999) 1-6.

[5] Chemineer, *Computational Fluid Mixing (CFM)*, (2003) online in the Internet: http://www.Chemineer.com/technology.php

[6] Frank, T., *Eulerian Multiphase Flow Modeling, Phase Interaction Models*, ANSYS Germany (2004).

[7] Sveen, J., *New insights from Navier-Stockes modeling of free surface flows*, Dept. of Mathematics, University of Oslo., (2006) online in the Internet: http://www.math.uio.no/~jks/work.html

[8] Peixoto, S.M.C., Nunhez, J.R., Duarte, C.G., *Characterizing the Flow of Stirred Vessels with Anchor type Impellers*, Sao Paulo, BRASIL, ISSN 0104-6632, Braz. J. Chem. Eng. 17 (2000) 1-15.

[9] Ju, W., Huang, X., Wang, Y., Shi, L., Zhang, B.; Yuan, J., *An Investigation of the Flow Field of Viscoelastic Fluid in A Stirred Vessel*, 10th European Conference on Mixing, Elsevier Science B.V. (2000) 312-320.

[10] Delaplace, G., Torrez, C., Gradeck, M., Leuliet, J., André, C., *Flow of Newtonian and non-Newtonian fluids in an agitated vessel equipped with a non-standard anchor impeller*, 10th European Conference on Mixing, Elsevier Science B.V. (2000) 321-328.

[11] Dantecdynamic, *Particle equipment, Seeding particles for PIV and LDA measurements*, (2005) online in the Internet: http://www.dantecdynamic.com/PE/seeding/Index.html

[12] Dantecdynamic, *Imaging Systems*, (2005) online in the Internet: http://www.dantecdynamic.com/PIV/System/Index.html

[13] Haam, S.J., Brodkey, R.S., Fort, I., Vanecek, V., *Laser Doppler Anemometry measurements in an Index of Refraction Matched in The Presence of Dispersed Beads Part I*, Int. J. of Multiphase Flow 15 (1998) 279-285.

[14] Haam, S.J., Brodkey, R.S., *Motion of Dispersed Beads Obtained by Particle Tracking Velocimetry Measurements Part II*, Int. J. of Multiphase Flow 220 (1998) 485-537.

[15] Nakamura, S., Brodkey, R.S., *Computational and Experimental Study of the Fluid Flow in A Cylindrical Cavity with An Impeller Rotor at An Electric Location*, 3rd ASME/ JSME Joint Fluids Engineering Conference, San Francisco, California (1999) 1-6.

[16] Clifford, M.J., Cox, S.M., Finn, M.D., *Reynolds number effects in a simple planetary mixer*, Chem. Eng. Sci. 59 (2004) 3371-3379.

[17] Wörner, M., *Computational Modeling of Multiphase Flows*, International Summer School on "Computational Modeling of Combustion & Multiphase Flows in Energy Systems", Neptun-Olimp, Romania (2003) 1-35.

[18] Kvicinsky, S., Kueny, J., Avellan, F., Parkinson, E., *Experimental and Numerical Analysis of Free Surface Flows in a Rotating Bucket*, Proceeding of the XXlst IAHR Symposium on Hydraulic Machinery and Systems, Lausanne (2002) 1-7.

[19] Kvicinsky, S., Kueny, J.-L., Avellan, F., *Numerical and Experimental Analysis of Free surface Flow in A 3D non Rotating Pelton Bucket*, The 9th International Symposium on Transport Phenomena and Dynamics of Rotating Machinery, Honolulu, Hawaii, USA (2002) 1-8.

[20] Torrecilla, M., *Introduction to numerical simulation of fluid flows*, Technical University of Munich, Winter school, Russia (2004) 24-34.

[21] Frank, T., *Eulerian Multiphase Flow Modeling: Phase Interaction Models*, Ansys CFX, Otterfing, FZR-Dresden, Germany (2003).

[22] Frank, T., *Free Surface Flow Theory*, Chapter 1, Ansys CFX, Otterfing, Germany (2004).

[23] Kat chalmers, *The influence of complex rheology on mixing, reaction and control of stirred vessels*, (2005) online in the Internet: http://www.kat.chalmers.se/cpdc/tvproj.htm

[24] Cremer, H.W., *Chemical Engineering Practice*, Vol. 8, Butterworths Scientific Publications, London (1965).

[25] Zhao, Y., Brodkey, R.S., *On Representation of Complex Turbulent Flows*, (2005) online in the Internet: http://www.chbmeng.ohio-state.edu/~brodkey/RES_3D-Stereo

[26] Nakamura, S., Brodkey, R.S., *Direct and Large Eddy Simulation of the Three-Dimensional Unsteady Flows in the Counter-Jet Mixing Vessel*, ASME Fluids Eng. Summer Conference, Boston (2000) 1-7.

[27] Frank, T., *Flow Visualization Methods*, Ansys CFX Germany (2004).

[28] Kirk-Othmer, *Encyclopedia of Chemical Technology*, 3rd edition, Vol. 24, John Wiley & Sons, USA (2006).

[29] Perry, R.H., Green, D., *Perry's Chemical Engineers' Handbook,* 7th edition, McGraw-Hill (1997).

[30] Petersen, E.E., *Chemical Reaction Analysis*, Prentice Hall Inc., USA (1965).

[31] Smith, J.M., *Chemical Engineering Kinetics*, 3rd edition, McGraw-Hill (1987).

[32] Kalok C Lee, *An experimental investigation of the trailing vortex structure and mixing and mixing characteristics of stirred vessels*, (2005) online in the Internet: http://www.eee.kcl.ac.uk/mecheng/kcl/kclphd.html

[33] Miettinen, T., Laakkonen M., Aittamaa J., *The applicability of various flow visualization techniques for the characterization of Gas-Liquid in a mixed tank*, Helsinki University of Technology, Espoo, Finland, AIChE J. 48 (2002) 673-685.

[34] Kukura, J., Arratia, P.C., Szalai, E.S., Bittorf, K.J., Muzzio, F.J., *Understanding Pharmaceutical Flows*, Pharmaceutical Technology, 10 (2002) 48-72.

[35] Zalc, J.M., Szalai, E.S., Alvarez, M.M., Muzzio, F.J., *Using CFD to Understand Chaotic Mixing in Laminar Stirred Tanks*, AIChE J. 48 (2002) 2124-2134.

[36] Binding, D.M., Couch, M.A., Sujatha, K.S., *Experimental and numerical simulation of dough kneading in filled geometries*, J. of Food Eng. 58, Issue 2 (2003) 111-123.

[37] Mavros, P., *Flow Visualization in Stirred Vessels a Review of Experimental Techniques*, Trans IChemE 79, Part A (2001) 113-127.

[38] Zwart, P., *Numerical Methods for Multiphase Flow Models in CFX-5*, Ansys Canada, Waterloo, Canada (2004).

[39] Ekato, *Anchor impeller*, (2004) online in the Internet: http://www.ekato.com

[40] Hartmann, H., Derksen, J.J., Montavon, C., Pearson, J., Hamill, I.S.; Van den Akker, H.E.A., *Assessment of Large Eddy and RANS stirred tank simulations by means of LDA*, Elsevier Science (2003).

[41] Delaplace, G., Leuliet, J.C., Relandeau, V., *Circulation and mixing time for helical ribbon impellers. Review and Experiments*, Experiments in Fluids 28 (2000) 170-182.

[42] Delaplace, G., Torrez, C., Gradeck, M., Leuliet, J., André, C., *Tracer experiments- A way to validate computational fluid dynamic simulations in an agitated vessel,* Récents Progrés en Génie des Procédés 15 (2001) 77-84.

[43] Peters, D.C., Smith, J.M., *Mixing in anchor agitated vessels*, The Canadian J. Chem. Eng. 47 (1969) 268-271.

[44] Bujalski, W., Jaworski, Z., Nienow, A., *CFD Study of homogenization with dual Rushton turbines – Comparison with experimental results part II*, Trans. Inst. Chem. Eng. 80 (2002) 97-104.

[45] Zlokarnik, M., *Ullmanns Enzyklopädie der technischen Chemie*, Bd. 2, Kapitel Rührtechnik (1973) 63-73.

[46] Hiby, J.W., *Definition und Messung der Mischgüte in flüssigen Gemischen*, Chem.-Ing.-Tech. 51 (1979) 704-709.

[47] Landolt, Börnstein, *Zahlenwerte und Funktionen aus Physik und Chemie*, 6.Auflage, Bd.2, Teil 5, Springer Verlag, Berlin (1969).

[48] Merck, *Chemikalienkatalog*, (2004) online in the Internet: http://www.chemlin.de/markt/chemikalienkataloge.htm

[49] Peters, D., Smith, J., *Fluid flow in the region of anchor agitated blades*, Trans. Instn. Chem. Eng. 45 (1967) T360-T366.

[50] CFX-5 Tutorials Documentation, Tutorial 7, *Free Surface Flow Over a Bump*, (2005).

[51] Ferziger, J., Perić, M., *Computational Methods for Fluid Dynamics*, Springer- Verlag Berlin Heidelberg, Germany (1996).

[52] Abid, M., Xuereb, C., Bertrand, J., *Hydrodynamics in vessels stirred with anchors and gate agitators: Necessity of a 3-D Modelling*, Trans. IChemE 70, Part A (1992) 377-384.

[53] Rożeń, A., Baldyga, J., *Instability of coutte flow of two liquids differing in viscosity*, Task Quarterly, 3 (2003) 1-14.

[54] Ohta, M., Kuryama, M., Saito, S., *A two-dimensional model for the secondary flow in an agitated vessel with anchor impeller*, J. Chem. Eng. of Japan 18 No.1(1985) 81-84.

[55] Bouwmans, I., Van den Akker, H. E. A., *The influence of viscosity and density differences on mixing times in stirred vessels*, IChemE Symp Ser. 121 (1990) 1-12.

[56] Pasteur, *REACTOR BEHAVIOR*, (2005) online in the Internet: http://www.che.boun.edu.tr/che302/Chapter%2011.pdf

[57] Van De Vusse, J.G., *Mixing by agitation of miscible liquids-Part I*, Chem. Eng. Sci. 4 (1955) 178-200.

[58] Zlokarnik, M., *Einfluß der Dichte- und Zähigkeitsunterschiede auf die Mischzeit beim Homogenisieren von Flüssigekeitsgemischen*, Chem.-Ing.-Tech. 42 Nr.15 (1970) 1009-1011.

[59] Lodgsdon, J.E., *Ethanol*, Encyclopedia of Chemical Technology, New York, John Wiley & Sons, 4th Ed. 9 (1994) 812–860.

[60] Wikipedia, *Glycerol*, (2006) online in the Internet: http://en.wikipedia.org/wiki/Glycerol

[61] Process equipment globalspec, *Mixers*, (2006) online in the Internet: http://process-equipment.globalspec.com

[62] Clevelandmixer, *Mixing glossary of terms*, (2006) online in the Internet: http://www.clevelandmixer.com/files/pdf

[63] Parrinst, *Stirrer Options*, (2006) online in the Internet: http://www.parrinst.com/default.cfm

[64] Chemineer, *Advanced Impeller Technology for Superior Performance*, (2006) online in the Internet: http://www.chemineer.com

[65] Autoclave, *Impeller System*, (2006) online in the Internet: http://autoclave.en.ec21.com

[66] Engin.umich., *Semibatch*, (2006) online in the Internet: http://www.engin.umich.edu

[67] Hoogendoorn, C .J., Den Hartog, A. P., *Model studies on mixers in the viscous flow region*, Chem. Eng. Sci. 22 (1967) 1689-1695.

[68] Bouwmans, I., Bakker, A., Van Den Akker, H.E.A., *Blending liquid of differing viscosities and densities in stirred vessels*, Trans. IChemE 75, Part A (1997) 777-783.

[69] Smith, J. M., Schoenmakers, A.W., *Blending of liquids of differing viscosity*, Chem. Eng. Res. Des. 66 (1988) 16-21.

[70] Irving, J. R., *Viscosities of Binary Liquid Mixtures, A Survey of*

Mixture Equations, NEL Rep. No. 630 (1977).

[71] Shekhar, S.M., Jayanti, S., *Mixing of Pseudoplastic Fluids using Helical Ribbon Impellers*, Dept. of Chemical Engineering, Institute of Technology-Madras, Indian, AIChE J. 49, No.11 (2003) 2768-2772.

[72] Teodoro, E.-S., Edmundo, B.-D.L., Alberto, T., Tanguy, P.A., *Flow Patterns in RheologicaIly Evolving Model Fluids Produced by Hybrid Dual Mixing Systems*, Chem. Eng. Technol. 24 (2001) 913-918.

[73] Queimada, A.J., Marrucho, L.M., Coutinho, J.A.P., Stenby, E.H., *Viscosity and Liquid Density of Asymmetric n-alkane Mixtures: Measurement and Modeling*, The Fifteenth Symposium on Thermophysical Properties, Colorado, U.S.A, June 22-27 (2003).

[74] Hoyt, J.W., Sellin, R.H.J., *A Mirror and Tracer Method of 3-D Flow Visualization*, (2005) online in the Internet: http://www.odeweb.demon.co.uk

[75] Edward, L.P., Victor, A.A.-O., Suzanne, M.K., *HANDBOOK OF INDUSTRIAL MIXING SCIENCE AND PRACTICE*, U.S. (2004).

[76] Chemguide, *Ideal mixtures*, (2005) online in the Internet: http://www.chemguide.co.uk

[77] See.ed.ac., *Mixtures*, (2005) online in the Internet: http://www.see.ed.ac.uk/~jwp/procalcs/procalcs/mixtures

[78] Roeckl, Single, *Agitator types*, (2005) online in the Internet: http://roeckl-und-single.de

[79] Brauer, H., *Stirred vessel reactors*, Fundamentals of Bio-chemical Engineering, 2 (1985) 395-444.

[80] Bakker, A., LaRoche, R.D., Wang, M.-H., Calabrese, R.V., *Sliding Mesh Simulation of Laminar Flow in Stirred Reactors*, The Online CFM Book, February 15 (2000): http://www.bakker.org/cfm

[81] Wikipedia, *Miscible*, (2005) online in the Internet: http://en.wikipedia.org/wiki/Miscible

[82] Kraume, M., *Mischen und Rühren*, Wiley-VCH, Weinheim (2003).

[83] Zlokarnik, M., Chem.-Ing.-Tech. 39 (1967) 539-545.

[84] Tanguy, P. A., Lacroix, R., Bertrand, F., Choplin L., Brito de la Fuente, E., *Mixing of Non-Newtonian Viscous F1uids with Helical Impellers: Experimental and Three-Dimensional Numerical Studies* AIChE Symp. Ser. 286 (1992) 33-47.

[85] Tanguy, P. A., Thibault, F., Brito de la Fuente, E., *A New Investigation of the Metzner-Otto Concept for Anchor Mixing Impellers*, The Canadian J. Chem. Eng. 74 (1996) 222-228.

[86] Cranfield, *Computational Fluid Dynamics*, (2004) online in the Internet: http://www.cranfield.ac.uk/soe/cpd/ate-cfd.htm

[87] Käppel, M., *VDI-Forschungsh*, Nr. 578 (1976).

[88] Rohrlich, F., *Computer Simulation in the Physical Sciences*, PSA 2 (1991) 507–518.

[89] Abdennour, R., Ksouri, M., M'sahli, F., *Experimental Nonlinear Model Based Predictive Control for a Class of Semi-Batch Chemical Reactors*, Int. J. Adv. Manuf. Techn. 20, No. 6 (2002) 459-463.

[90] Spector, M., *Models and Theories*, British J. Philo. Sci. 16 (1965) 121-142.

[91] Hegselmann, R., *Modelling and Simulation in the Social Sciences from the Philosophy of Science Point of View*, Kluwer (1996) 77-100.

[92] Winsberg, E., *Simulations, Models and Theories: Complex Physical Systems and their Representations*, Philo. Sci. 68 (2001) 442-454.

[93] Bostrom, N., *Are you Living in a Computer Simulation*, Philo. Quarterly 53, No. 211 (2003) 243-255.

[94] Bremermann, H. J., *Minimum energy requirements of information transfer and computing*, Int. J. Theor. Phys. 21 (1982) 203-217.

[95] Raczynski, *The Benefits of computer simulation*, (2005) online in the Internet: http://www.raczynski.com

[96] Bertrand, F., Tanguy, P. A., Brito de la Fuente, E., *A New Perspective for the Mixing of Yield Stress Fluids with Anchor Impellers*, J. Chem. Eng. Japan, 29, No. 1 (1996) 51-58.

[97] Action energy, *Blending miscible liquids*, (2006) online in the Internet: http://www.actionenergy.org.uk

[98] Pip, N.J., Gül, N.Ö.-T., *Effects of physical property differences on blending*, Chem. Eng. Technol. 28, No. 8 (2005) 908-914.

[99] Irving, J. R., *Viscosities of Binary Liquid Mixtures: The Effectiveness of Mixture Equations*, NEL Rep. No. 631, 1977.

[100] CFX-5 Documentation, *Solver Theory*, (2005) 21-239.

[101] CFX-5 Documentation, *Solver Modeling*, (2005) 16-201.

[102] CFX-5 Documentation, *Introduction to CFX-5*, (2004) 94-104.

[103] CFX-5 Documentation, *Reference Guide*, (2004) 37-46.

[104] Ansys CFX-10 Documentation, *Multiphase Flow Modeling*, (2005).

[105] Ansys CFX-10 Documentation, *Basic Capabilities Modeling*, (2005).

[106] Ansys CFX-10 Documentation, *Materials and Reactions*, (2005).

[107] CFX-5 Documentation, *Solver Manager*, (2005) 2-10.

[108] CFX-5 Documentation, *Post*, (2005) 2-18.

[109] Ansys CFX-10 Documentation, *Fluid-Fluid interfaces*, (2005).

[110] Ansys CFX-10 Documentation, *GGI and MFR Theory*, (2005).

[111] Shamlou Ayazi, P., Edwards, M.F., *Power Consumption of Helical Ribbon Mixers in Viscous Newtonian and Non-Newtonian Fluids*, Chem. Eng. Sci. 40 (1985) 1773-1786.

[112] Metzner, A.B., Otto, R.E., *Agitation of Non-Newtonian Fluids*, AIChE J. 3 (1957) 3-12.

[113] Patterson, I.W.A., Carreau, P.J., Yap, C.Y., *Mixing with Helical Ribbon Agitators, Part II: Newtonian Fluids*, AIChE J. 25 (1957) 508-517.

[114] Frohn, A., Roth, N., *Dynamics of Droplets*, Springer (2000) 66-67.

[115] Patrick, P.M., Gary, M.H., *Fluorimetric Analysis on Individual Nanoliter sample Droplets*, Applied Spectroscopy 48 (1994) 956-958.

[116] Science World, *Drag Coefficient*, (2006) online in the Internet: http://scinenceworld.wolfarm.com/physics/DragCoefficient.html

[117] Tritton, D.J., *Physical Fluid Dynamics*, 2nd Ed. Oxford, England (1988).

[118] Kaiser, T., Roll, G. Schweiger, G., *Investigation of Coated Droplets by Optical Levitation*, J. Aerosol Sci. 27 (1996) 519-520.

[119] Hardalupas, Y., Taylor, A.M.K.P., Wilkins, J.H., *Experimental Investigation of Sub-millimeter Droplet Impingement on to Spherical Surfaces*, Int. J. Heat and Fluid Flow 20, No. 5, (1999) 477-485.

[120] Castanet, G., Lavieille, P., Lebouché, M., Lemoine, F., *Measurement of the Temperature Distribution within Monodisperse Combusting Droplets in Linear Streams using Two-color Laser-induced*, Exp. Fluids 35, No. 6 (2003) 563-571.

[121] Mulholland, J.A., Srivastava R.K., Wendt, J.O.L., *Influence of Droplet Spacing on Drag Coefficient in Nonevaporating, Monodisperese Stream*, AIAA J. 26 (1988) 1231-1237.

[122] Mie.Utoronto, *Computational Fluid Dynamics*, (2004) online in the Internet: http://www.mie.utoronto.ca/labs/MUSSL/cfd

[123] Hiraoka, S., Tada, Y., Kato, Y., *Model Analysis of Mixing Time Correlation in an Agitated Vessel with Paddle Impeller*, J. Chem. Eng. Japan 34, No. 12 (2001) 1499-1505.

[124] Micale, G., *CFD simulation of particle distribution in stirred vessels*, Trans. IChemE 78, A (2001) 435-444.

[125] Attila, R., Thomas, K., *Stability limits in binary fluids mixtures*, J. Chem. Phys., 122 (2005) 64507-64508.

[126] Ishii, M., *One-dimensional drift-flux model and constitutive equations for relative motion between phases in various two-phase flow regimes*, ANL 77 (1977) 47-48.

[127] M., Tavassalo, V., *On the Mixture Models for Multiphase Flow*, VTT Publications, (1996).

[128] John J. McKetta, *Encyclopedia of Chemical Processing and Design*, Marcel Dekker, Inc., New York, 62 (1997) 451-455.

[129] Schönbucher, A., *Thermische Verfahrenstechnik*, Springer, Berlin; 1. Auflage (2002).

[130] Mathematik, *Introduction to Computational Fluid Dynamics*, (2005) online in the Internet: http://www.mathematik.uni-dortmund.de

[131] Cranfield, *Computational Fluid Dynamics*, (2006) online in the Internet: http://www.cranfield.ac.uk/soe/cpd/ate-cfd.htm

[132] Bruce, W., Robert, E., *Liquid- Liquid contacting in unbaffled, agitated vessels*, AIChE J. 19 (2004) 304-312

[133] Kostin, I., Martion, M., Texier, R., *Modelling of Miscible Liquids with the Korteweg Stress*, EDP Sci. 37 (2002) 741-753.

[134] Jiao, C., Hötzl, H., *An Experimental Study of Miscible Displacements in Porous Media with Variation of Fluid Density and Viscosity*, Tran. Porous Media 54 (2004) 125-144.

[135] Chen, C., Wang, L., *Miscible droplets in a porous medium and the effects of Korteweg stresses*, Phys. Fluids 13 (2001) 2447-2456.

[136] Alargova, R.G., Bhatt, K.H., Paunov, V.N., *Liquid-Liquid Dispersion Technique*, Advanced Materials 16 (2004) 1653-1657.

[137] Stieß, M., *Mechanische Verfahrenstechnik 1*, 2. Auflage, Springer Verlag, Berlin (2002).

[138] Pahl, M.H., Wehry, T., *Mischer für hochviskose Medien*, Universität Paderborn (2004) online in the Internet: http://www-vt.upb.de/ahp/en/mitarbeiter/wehry/Mischer.pdf

[139] Takahashi, K., Arai, K., Saito, S., *Power Correlation for Anchor and Helical Ribbon Impellers in Highly Viscous Liquids*, J. Chem. Eng. Japan, 13 (1980) 147-156.

[140] Bakker, A., Gates, L.E., *Properly Choose Mechanical Agitators for Viscous Liquids*, Chemical Engineering Progress, 12 (1995) 25-34.

[141] Shekhar, S.M., Jayanti, S., *Mixing of Power Law F1uids Using Anchor's Metzner-Otto Concept Revisited*, AIChE J., 49 (2003) 30-52.

[142] Bakker, A., Fasano, J.B., *Turbulent Mixing and Chemical Reaction in Stirred Tanks*, The Online CFM Book, February 15 (2000): http://www.bakker.org/cfm

[143] Hardalupas, Y., Taylor, A.M.K.P., Wilkins, J.H., *Experimental investigation of Sub-millimeter droplet impingement on to spherical surfaces*, Int. J. Heat and Fluid Flow, 20, No.5 (1999) 477-485.

[144] Yoshida, M., Ito, A., Yamagiwa, K., Ohakawa, A., Abe, M., Tezura, S., Shimazaki, M., *Power characteristics of unsteadily forward-reverse rotating impellers in an unbaffled aerated agitated vessel*, J. Chem. Technol. and Biotechnol. 76, No.4 (2001) 383-392.

[145] Jones, P.N., Ozcan-Taskin, G.N., *Effects of Physical Property Differences on Blending*, Chem. Eng. and Technol. 28, Issue 8 (2005) 905-914.

[146] Bujalski, J.M., Jaworski, Z., Bujalski, W., Nienow, A.W., *The Influence of the Addition Position of a Tracer on CFD simulated Mixing Times in a Vessel Agitated by a Rushton Turbine*, Chem. Eng. Research and Design, 80 (2002) 824-831.

[147] Karcz, J., Szoplik, J., *An effect of the eccentric position of the propeller agitator on the mixing time*, Proceeding of the 30th International Conference of SSCHE, Poland, (2005) 135-144.

[148] Iguchi, M., Tsujino, R., Nakamura, K.-I., Sano, M., *Effects of Surface Flow Control on Fluid Flow Phenomena and Mixing Time in a Bottom Blown Bath*, Metallurgical and Materials Transactions, 30 B (1999) 631-655.

[149] Verschuren, I.L.M., Wijers, J.G., Keurentjes, J.T.F., *Mean Concentration and Concentration Fluctuations in a Stirred-Tank Reactor*, AIChE J. 48, No.7 (2002) 1390-1400.

[150] Anderson, D.M., McFadden, G.B., *Diffuse-Interface Methods in Fluid Mechanics*, Annual Review of Fluid Mechanics 30 (1998) 139-165.

[151] Espinosa, T., Brito, E., Thibault, F., Tanguy, P., *Power consumption with anchor mixers- effect of bottom clearance*. Chem. Eng. Comm. 157 (1997) 65-71.

[152] Kampinoyama, *Numerical analysis of flow of a Bingham fluid in an anchor impeller*, Int. Chem. Eng. 34, No. 2 (1994) 263-269.

[153] Dieulot, J., Delaplace, G., Guerin, R., Leuliet, J., Brienne, J., *Laminar mixing performances of a stirred tank equipped with helical ribbon*

agitator subjected to steady and unsteady rotational speed, Trans. IChemE J. 80, Part A (2002) 335-343.

[154] Guozhong, Z., Litian, S., Peiqing, Y., *CFD study of mixing process in Rushton turbine stirred tanks*, Third International Conference on CFD in the Minerals and Process Industries, CSIRO, Melbourne, Australia 10-12 December (2003).

[155] Zlokarnik, M., *Suitability of stirrers for the homogenization of liquid mixtures*, Chem.-Ing.-Tech. 39 Nr.9/10 (1967) 539-549.

[156] Rielly, C.D., Pandit, A.B., *The mixing of Newtonian liquids with large density and viscosity differences in mechanically agitated contactors*, 6th Europ. Conf. on Mixing, Pavia, Italy (1988) 69-74.

[157] Paschedag, A.R., Kassera, V., Sperling, R., *Aktuelle Entwicklung in der CFD für gerührte systeme*, Chem.-Ing.-Tech.79 Nr.7 (2007) 983-999.

List of Conference Abstracts

1. Al-Qaessi, F., Abu-Farah, L., Sudhoff, P., Schönbucher, A., *CFD Simulation of Multicomponent Mixture of Ethanol and Glycerol in Stirred SBR with Anchor Type Impeller*, Chem.-Ing.-Tech. 77 (2005) 1058. www.cit-journal.de
2. Al-Qaessi, F., Abu-Farah, L., Schönbucher, A., *CFD simulation for the dynamic mixing of different density and different viscosity liquids in stirred SBR and BR. – A preliminary study for the safety assessment of polymerisation reactions*, 8. Fachtagung: Anlagen-, Arbeits- und Umweltsicherheit, P04 (2006), ISBN 3-936415-48-X.
3. Al-Qaessi, F., Abu-Farah, L., Schönbucher, A., *Mixing times and secondary flow phenomena of glycerol with ethanol in SBR and BR – an experimental and CFD study*, Chem.-Ing.-Tech. 79, 9 (2007).

Publications in Preparation

1. Al-Qaessi, F., Abu-Farah, L., Schönbucher, A., *A new method to determine the mixing time in miscible liquids of different viscosities and densities*, AIChE Journal.

2. Al-Qaessi, F., Abu-Farah, L., Schönbucher, A., *The influence of a pan cake effect on the mixing time in miscible liquids of different viscosities and densities in a batch reactor*, AIChE Journal.

3. Al-Qaessi, F., Abu-Farah, L., Schönbucher, A., *Prediction of mixing times and time dependent mixture viscosities in miscible liquids of different viscosities and densities by CFD simulation*, AIChE Journal.

Oral Presentations

2007 Al-Qaessi, F. (presented), Abu-Farah, L., Schönbucher, A., "CFD-simulation of the dynamic mixing of liquids with different densities and viscosities in semi-batch and batch reactors"
Neujahrskolloquium des Fachbereichs Chemie und dem Ortsverband der Gesellschaft Deutscher Chemiker, University Duisburg-Essen, Essen-Germany.

2006 Al-Qaessi, F., Abu-Farah, L. (presented), Schönbucher, A., "CFD simulation for the dynamic mixing of different density and different viscosity liquids in stirred SBR and BR. – A preliminary study for the safety assessment of polymerisation reactions"
8. Fachtagung Anlagen-, Arbeits- und Umweltsicherheit, Köthen - Germany.

2005 Al-Qaessi, F., Abu-Farah, L. (presented), Schönbucher, A., "CFD Simulation of Multicomponent Mixture of Ethanol and Glycerol in Stirred SBR with Anchor Type Impeller"
DECHEMA/GVC - Jahrestagungen 2005, Wiesbaden, Rhein-Main-Hallen - Germany.

2005 Al-Qaessi, F., Abu-Farah, L., Schönbucher, A. (presented), "Experimental work and CFD-Simulation of mixing behavior in chemical reactors"

Albaath University, Faculty of Chemical and Petroleum Engineering, Homs-Syria.

2005 Al-Qaessi, F., Abu-Farah, L., Sudhoff, P. (presented), Schönbucher, A.,
"Reaction calorimeter investigations and computations of mixing processes in the SBR"
Neujahrskolloquium des Fachbereichs Chemie und dem Ortsverband der Gesellschaft Deutscher Chemiker, University Duisburg-Essen, Essen-Germany.

Posters

2007 Al-Qaessi, F., Abu-Farah, L., Schönbucher, A.,
"Mixing times and secondary flow phenomena of glycerol with ethanol in SBR and BR – an experimental and CFD study"
DECHEMA and VDI-GVC - ProcessNet-Jahrestagung 2007, from 16 – 18.10.2007, Aachen - Germany.

2006 Al-Qaessi, F., Abu-Farah, L., Schönbucher, A.,
"CFD simulation for the dynamic mixing of different density and different viscosity liquids in stirred SBR and BR. – A preliminary study for the safety assessment of polymerisation reactions"
8. Fachtagung Anlagen-, Arbeits- und Umweltsicherheit, from 9 – 10/11/2006, Köthen - Germany.

2005 Al-Qaessi, F., Abu-Farah, L., Sudhoff, P., Schönbucher, A.,
"CFD Simulation of Multicomponent Mixture of Ethanol and Glycerol in Stirred SBR with Anchor Type Impeller"
DECHEMA/GVC - Jahrestagungen 2005, from 6 – 8/9/2005, Wiesbaden, Rhein-Main-Hallen - Germany.

Curriculum Vitae

Name : Fawzi A. Hamadi Al-Qaessi

Place / Date of birth : Baghdad – Iraq / 03.08.1970

Academic Qualification

10/1988 – 06/1990	Technical Diploma in Chemical Industries from Department of Chemical Industries, Specialized in Operation of Industrial Units at Technical Institution of Baghdad, Ranked (1) from (198) students with average 82.577% in Baghdad-Iraq.
10/1991 – 06/1995	B.Sc. Degree in Chemical Engineering from the Chemical Engineering Dept. - College of Engineering at University of Baghdad in Baghdad-Iraq.
10/1998 – 06/2001	M.Sc. Degree in Chemical Engineering from the Chemical Engineering Dept. at the University of Jordan in Amman-Jordan.
10/2003 – 11/2007	Ph.D. Degree in Chemical Engineering from Institute of Chemical Engineering at University Duisburg-Essen – Campus Essen (Institut für Technische Chemie I in Universität Duisburg-Essen, Campus Essen) in Essen-Germany.
10/2003 – 10/2007	I have got a DAAD scholarship for the financial support of my doctorate study in the Institute of Chemical Engineering at University Duisburg-Essen – Campus Essen in Essen-Germany.

Scientific Biography and Work Experiences

10/1995 – 10/1998	Quality control, Design, Processing and Operating of Ethanol, Acetic Acid, Ethel Acetate, Citric Acid products and Recycling process of Plastics for private factory (AL-TAI BUREAU) in Baghdad - Iraq.
10/1996 – 10/1998	Lecturer, in Computer Programming Labs in two languages (FORTRAN 77 and QBASIC), six programs (Windows, MSDOS, AutoCAD R14, Internet, Microsoft PowerPoint, Word and Excel), the subject of Engineering Drawing and The Laboratory of Industrial Units for the subjects of Unit Operation, Math, Chemistry, Mass, Fluids and Heat Transfer, in the Chemical Engineering Dept.-College of Engineering at University Of Baghdad in Baghdad - Iraq.
10/1998 – 06/2001	Teaching Assistant, in Heat and Mass Transfer, Unit Operation Lab. (Math and Chemistry), Numerical Methods (FORTRAN77 and MATHLAB), Mass transfer, Thermodynamics and Computer Aided Design (simulation and modeling) in the Chemical Engineering Dept. at the University of Jordan in Amman-Jordan.
07/1999 – 08/2000	Chemical Engineer, Analysis and Design of Water Treatment at the Orient Water Treatment and Safety Est. in Amman - Jordan.

06/2000 – 06/2001	Chemical Engineer and Researcher, in Production of Activated Carbon from Date Stones using a Fluidized-Bed Reactor by using Zinc Chloride and Phosphoric Acid, in Department of Chemical Engineering-Faculty of Engineering Technology at Al-Balqa' Applied University in Amman - Jordan.
03/2002 – 10/2002	Chemical Engineer (Supervisor on installation and Maintenance the equipments of physically and chemically water treatment) in Water Treatment Department for Juma Almajed Est., in Dubai - United Arab Emirates.
10/2002 – 03/2003	Chemical Engineer and Researcher in Waste Water Treatment in the laboratory of Institute for Thermal Process Engineering at Technical University of Clausthal with Prof. em. Dr.-Ing. A. Vogelpohl, in Clausthal-Zellerfeld - Germany.